In-line powder flow behaviour measured using electrostatic technology

By Nik Yusuf Hill-Izani (N.Y. Hill-Izani)

School of Pharmacy, De Montfort University, United Kingdom

A thesis submission in partial fulfilment of the requirement for the degree of Doctor of Philosophy awarded by De Montfort University

Under the supervision of: Professor Geoff Smith

Second supervisors: Dr David Armitage; Dr Ahmet Orun

Month of submission: December 2019

Acknowledgements

I would like to express my gratitude to the following. My supervisor Professor Geoff Smith for providing his constant guidance, constructive advice and support throughout the entirety of this PhD. My second supervisor Dr David Armitage, for providing his expertise within the areas of powder flow and Fourier analysis, and for reviewing my chapters. And to Eugene Polygalov, for the design and provision of technical support regarding the EPFS technology, data-analysis and data-acquisition software.

Thank you to Steve Boswell of S3 Process Limited for his generous donation of materials and equipment, GEA Group for their loaning of the screw feeder, as well as to the team at Freeman Technology Limited for providing excellent technical support on the FT4 Powder Rheometer.

A big thank you to my father and mother, Nik and Sarah, for their financial and emotional support throughout the entirety of this PhD. I'm sorry this took so long. Also, to the rest of my family: Aishah, Anna, Lydia, Jacob, Eleanor, Humphrey and Millie, thank for your unending constant support through and through.

Thank you to my friends in my research group including: Bhaskar Pandya, Yowwares Jeeraruangrattana, Anand Vadesa, Pathum Wijesekara and Longinus Ogugua; all of whom have provided good advice and company. I wish you all the best in your endeavours.

A big thank you to the De Montfort University Pharmaceutics Technical team, including: Angela Ferguson, Anona Griffin, Jo Dickinson, Aasha Varia, Ian Fletcher, Peter Gibbs and Cathy Holmes; all of whom have provided technical support throughout my project and putting up with my occasional outrageous demands. Thank you to my friend Dr Rachel Armitage in the SEM department, who helped me obtain the SEM images for my research as well as being an excellent source of advice and emotional support. Also, many thanks to the De Montfort University Engineering department for manufacturing the bespoke equipment including the flow nozzles and the tablet-press scale EPFS.

And finally, thank you to all of my friends who have all supported me at different stages of my PhD: Neil Adams, Chelsey Edwards, Alex Chambers, Jack Laugher, Anna Aldersley, James Wright, Peter Baker, Christine Parker, Cara Wood, Christian Evans, Joe Braithwaite, Matthew Harding, Deepali Bij, Sarah Glynn, Karen Glasscock, Abigail Hood and Shabina Hossain Khaja.

Abstract

Within solid-dose manufacturing processes, powder flow and powder triboelectrification are critical to the quality of the final product. Off-line testers do not simulate the shear and packing conditions that a powder would experience in-process and may be unreliable in predicting in-line flow and charging properties, which are key components to successful formulation and process design.

In this work, a dual-electrode, electrostatic powder flow sensor (EPFS) was used to obtain electrostatic signals that were generated in response to the pattern of flow of pharmaceutical powders in two density modes: The first being powders in lean phase flow, generated by free-fall of the powder from the outlet of a screw-feeder. The second being dense phase flow, through either 19.1 mm I.D. stainless-steel pipe or at the outlet of a tablet-press hopper. Powders were selected from a range of low to high cohesivity so as to study the effect of powder cohesion on the flow pattern. Electrostatic signals were then analysed by three distinct signal processing methods (RMS signal averaging, cross correlation, and Fast-Fourier-Transform) with a view to determining certain characteristics of powder flow, i.e. mass flow rate; cohesivity; and triboelectrification.

In the first application a calibration was attempted to establish the link between the root-mean-square (RMS) of the electrostatic signal and the mass flow, as determined by the accumulation of mass on a balance placed below the screw-feeder (in the case of lean phase application) and the 19.1 mm i.d. pipe (in the case of dense phase application). In both cases it proved unsuccessful, owing to the instability in the electrostatic signal (i.e. its dependence on factors other than mass flow, for example inherent and induced charge fluctuations and moisture content). An alternative method for determining mass flow rate was proposed based on the second signal processing method, which involved the cross-correlation of signal from both sensors to determine the free-fall velocity. This method might work in future applications if combined with a suitable technique for determining the powder density.

In the second application, a Fast-Fourier-Transform (FFT) of the electrostatic signal to yield an FFT spectrum was used to establish whether this technique could determine aspects of powder cohesivity. A correlation in rank order of cohesivity was observed between the ratio of the summed or averaged amplitudes at the three principle frequencies to the summed or averaged of the baseline components respectively, and the cohesivity of the powders, as determined by off-line powder rheometry assessments of dynamic flow and bulk properties.

In the third application, the RMS signal normalised to the powder mass flow rate was used to study the time-dependent powder charging behaviour, which is induced by the transportation of the powder within the screw feeder. Characteristic relative charging profiles were obtained for each powder, which in some cases were coupled to charge-induced adhesion of the powder to the equipment.

In the last application, the RMS signal generated from the EPFS sensor located at the outlet of the hopper on a rotary tablet press was used to interrogate the dense-phase intermittent-flow resulting from the dosing of the tablet die. Those more cohesive powders gave a larger RMS signal at the lower electrode (relative to the upper electrode) whereas less cohesive powders had similar RMS signals at each electrode. While the exact explanation of this effect is currently unknown these results suggest that the technique might be useful in the determination of die filling as a function of the input material characteristics.

In summary, this work has provided some insight into the potential applications of EPFS for in-line measurement of powder flow and charging characteristics. Future work should focus on (i) developing an integrated sensor with an independent measurement of density to yield the powder mass flow using an inferential approach, (ii) co-use of techniques (such as Faraday-cup and charge decay analysers) to

validate the in-line charging behaviour, (iii) further exploration of the significance of the signal amplitude difference at the tablet press hopper outlet on the characteristics of the tablet compact.

Table of contents

List of Figures

List of Tables

Chapter 1. Introduction:

1.1. The fundamentals of fluid flow

The flow of gaseous, liquid and solid matter are facets of many ordinary day-to-day processes, widely used to describe their displacement across two different locations, although their individual flow characteristics are dependent on their fundamental intermolecular arrangement (Buckton 2007; Fay 1994). Gaseous and liquid flow can be categorised under the umbrella term “fluid flow”, although both express distinct characteristics due to the differences in their fundamental intermolecular interactions. Gases are characterised by very weak intermolecular forces (i.e. Van der Waals), a high degree of separation between neighbouring molecules which contributes to its high compressibility, and the ability to fully expand into a container (Buckton 2007; Nakayama 2018). On the other hand, in liquids, the intermolecular separation distance is significantly smaller, which results in a low compressibility and the ability to take on the shape of its container (Buckton 2007; Nakayama 2018). Furthermore, the constituent molecules are bound by stronger intermolecular forces which are strong but flexible, meaning that they can easily flow around neighbouring molecules, but remain linked due to the cohesive nature of the aforementioned forces. These bonds contribute towards the liquid surface tension; induced by attraction of the surface molecules at the free surface by those within the bulk and is defined by the tensile strength per unit length of the free surface (Nakayama 2018). Also, for both states of matter, viscosity plays in important role in their fluid dynamics. When two layers of a substance move against one another at different velocities (i.e. in parallel flow), a resistance is generated across the interfacial layers (shear plane) as a result of the viscosity of the substance, which then controls the rate of shear for any applied shear stress (Nakayama 2018). For gases and liquids, the viscosity is known to be proportional and inversely proportional, respectively, to the temperature of the substance (Nakayama 2018).

The properties of fluid flows such as volume, pressure, velocity, density, viscosity and temperature can be manipulated so as to establish a degree of control of their flow behaviour (Nakayama 2018). Two distinct fluid flow behaviours include laminar flow and turbulent flow, where the former regime describes the uniform movement of a fluid in smooth layers, whereas the latter develops chaotic velocity fields (Fay 1994; Nakayama 2018). The tendency for a fluid flow to develop either of the two regimes within a tube, is indicated by the Reynolds

number Re, where u = the average velocity, D = tube diameter and v = kinematic fluid viscosity (Equation 1), (Nakayama 2018).

$$Re = \frac{uD}{\mathrm{v}} \qquad \text{(Equation 1)}$$

Fluid flows can also contain more than one phase (e.g. gas-liquid and liquid-liquid), also known as multiphase flow (Liu, Li, et al. 2020). Depending on the dimensions of the conveying pipe, the flow velocity and field, as well as the proportion of gas to liquid components, one or more characteristic flow patterns can develop within the fluid flow, including plug, stratified, mist, churn, annular, bubbly and slug flow. Further information on these flow regimes can be found within the following articles (Kanin, et al. 2019; Soleimani and Hanratty 2003; Ye and Guo 2013; Zhang, Jinya, et al. 2016; Zhang, Zhennan, et al. 2019). Furthermore, should the aforementioned process parameters change, the flow patterns may transition between the different types (Soleimani and Hanratty 2003). Fluid flows have numerous applications, including common use as the conveying or fluidisation medium for solid/liquid matter within many industrial processes (e.g. metallurgical, refrigeration, power and pharmaceutical), (Bentham, et al. 2004; Lim, et al. 2014; Liu, Ni, et al. 2019; Qian, et al. 2014).

1.2. The fundamentals of the flow of powders

Compared to fluid flow, solid flow differs in a number of ways. However, it will be necessary to consider the fundamental nature of the solid in its static state before elaborating on its flow behaviour. In solid matter, the constituent atoms or molecules are arranged in a structure linked by rigid intermolecular bonds which do not possess the flexibility of fluid molecules. It is the degree of order in the solid structure which determines its crystallinity. Structures in which the atoms/molecules are tightly packed and arranged in a repeated pattern are classified as crystalline (Buckton 2007). On the other hand, solids which possess a high degree of disorder in their lattice structure are known as amorphous materials. Solids, including those utilised within industrial conveying processes, are known to range between crystalline and amorphous states, which ultimately define their physico-chemical properties (Buckton 2007).

In the aforementioned processes, solid material is typically handled in the form of a powder or a multiparticulate system (e.g. granules), comprised of millions of individual particles which interact with other particles within the bulk via fundamental inter-particular forces. The

following inter-particular interactions define the bulk characteristics of the powder (Capece, et al. 2016; Sarkar, et al. 2017; Yang, L., et al. 2015), and are described below:

a) Van der Waals: dipolar attraction between the particles, which are the strongest of the three forces.
b) Electrostatic: attraction due to charges accumulated on the particle surfaces.
c) Capillary: dipolar attraction or liquid bridging between particles due to the presence of moisture.

The magnitude of the aforementioned forces is in turn determined by the inherent physical and chemical properties of the constituent particles, which include but are not limited to: particle size and distribution, moisture content, particle shape (which influences the degree of interlocking with the bulk material), particle density, material chemistry (e.g. hygroscopicity, conductivity, resistivity), surface energy and surface roughness (Bentham, et al. 2004; Capece, et al. 2016; Liu, L. X., et al. 2008; Prescott and Barnum 2000; Sarkar, et al. 2017). Most notably, the relationship between the fundamental inter-particular forces and the inherent particle properties define the cohesive/adhesive nature of the powder, which are integral in defining their bulk and flow properties (Prescott and Barnum 2000). A powder which exhibits high cohesivity/adhesion, also known as “poor-flowing” or cohesive, is typically characterised by a high internal friction (resistance between bulk particles), high wall friction (resistance between the bulk particles and contacting surface), low bulk density and high compressibility. On the other hand, a powder which exhibits low cohesive properties, i.e. a “free-flowing” powder, is characterised in contrary to a cohesive powder (Prescott and Barnum 2000).

Unlike fluids (i.e. gases and liquids) the majority of powders do not readily flow. For a non-contained powder at rest (e.g. conical heap) the driving forces for flow (due to downward force of gravity being translated into lateral force) are balanced with the internal forces present within the material (i.e. internal friction) and the forces at the contact plane (i.e. surface friction). However, a powder can be encouraged to flow by applying a force with sufficient energy which is able to overcome these forces, resulting in the shearing of bulk structure (Staniforth and Aulton 2007). In this instance, the bulk structure is disrupted and the particles dislocate, which will be dependent on the nature, magnitude and extent of the applied stress and the qualities of the contacting surface (Prescott and Barnum 2000). In the majority of systems, powder flow can be expressed in terms of shear rate and shear stress. When a shear force is applied to powder, it creates a tangential component across a plane

which the particles will flow across should they be unable to withstand this component (Deleuil, et al. 1998; Jones and Pilpel 1966). The magnitudes of the shear stress, powder volume and the tangential component, dictate whether the powder will compact, dilate or flow without any changes in packing volume (Deleuil, et al. 1998).

Powder flow systems may either be considered as dense phase or lean phase, although this very much depends on the context of the system (e.g. pneumatic vs non-pneumatic systems). In pneumatic systems, the nature of the system is dependent on the ratio of powder loading to that of the conveyed air. Systems with high powder loadings are considered dense phase and systems with low powder loadings are considered lean phase (Alkassar, et al. 2019). For non-pneumatic systems the nature of the system is dependent on the packing of particles. For example, a system in which particles are packed very closely together with a high ratio of bulk powder volume to containing volume (i.e. hopper flow) can be considered a dense phase flow system (Anand, et al. 2009). These types of systems tend to experience very little dilation during flow. On the other hand, non-fluidised lean phase systems would be characterised in contrary to dense phase systems. In this case, particle packing and the ratio of the bulk powder volume to the containing volume is low (including when a containing volume is absent), whereas the degree of dilation is higher due to the increased free volume within the system (Feng, et al. 2020). Both dense phase and lean phase systems are widely-employed in powder conveying, with a few common systems described below.

1) Downwards flow due to gravity: In this scenario, the force of gravity induces a stress upon an unimpeded powder, enabling it to free-fall through air. The air resistance and the buoyancy of the powder are forces which counter the downward force due to gravity such that the rate of change of the powder velocity decreases until it reaches a steady-state, i.e. terminal velocity. Gravity is also the primary driving force in hopper and silo flows. However, the internal friction within the bulk powder under a consolidated state and the friction between the hopper walls and powder also act as resistance to the flow. At the opening of a hopper, the free surface of the powder is unimpeded, therefore should the force of gravity overcome the frictional forces present within the system, the powder will be able to flow out of the hopper. However, due to the presence of the aforementioned frictional forces, a velocity distribution is developed across the bulk of the powder, which are strongest nearer to the centre of the hopper and weakest nearer to the walls, thus resulting in a shear

stress developed at the interfaces between zones with different velocities (Prescott and Barnum 2000; Staniforth and Aulton 2007). Whilst inside the hopper, the flow is in dense phase due to the restriction imposed by the hopper opening (Anand, et al. 2009), whereas in free-fall, the powder is in lean phase as it is unimpeded and allowed to dilate (Feng, et al. 2020).

2) Flow due to a shearing mechanism: Here, the powder is conveyed along a pipe (e.g. screw feeder) or within a container (e.g. high shear mixer-granulator) by means of a dynamic shearing mechanism, which supplies sufficient energy into the system in order to induce and maintain flow. The shearing mechanism also induces a characteristic flow pattern in the powder which will be dependent on the material properties, the nature of the shearing mechanism (e.g. shear rate), the dimensions of the pipe/container and the quantity of powder conveyed (Cavinato, et al. 2013).
3) Flow due to pneumatic transport: The energy supplied by air flows, can be used to overcome the frictional forces within powders or solid material so that they may be conveyed throughout pipelines. Pneumatic flow can exist under dense phase (Cong, et al. 2011; Cong, et al. 2013; Jaworski and Dyakowski 2001) or lean phase configurations (Qian, et al. 2014), and can further experience transition between the two phases (Cong, et al. 2011; Cong, et al. 2013; Gao, et al. 2018). The nature of the flow regime is dependent on the powder material properties, the degree of powder loading, pipeline configuration (e.g. horizontal or vertical), airflow velocity, conveying pressure, permeability of powder to the conveying airflow (Cong, et al. 2011; Cong, et al. 2013; Gao, et al. 2018), as well as aerodynamic properties such as drag forces (Yang, Y., et al. 2019). Example flow regimes developed by powders under pneumatic conditions include stratified flow, suspension flow, plug flow, fluidized flow, annular flow, slug flow and settled layer flow (Cong, et al. 2011; Cong, et al. 2013; Jaworski and Dyakowski 2001).

It is evident that the nature of flow will be dependent on the conditions which the powder is conveyed under. The ability of a powder to flow in a given process is known as it's "flowability", which is described as multidimensional. Flowability describes the coupling between the material properties, the nature of the shear force(s), the packing conditions, the geometry and qualities of the contact plane and the environmental conditions (Prescott and Barnum 2000). All components must be accounted for when predicting the flow behaviour of a powder within a given process.

1.3. The fundamentals of powder charging and its influence on flowability

Another important but somewhat disregarded component of powder flow systems are electrostatic phenomena which are known to occur when two or more bodies contact, for example, in the form of abrasion, collision, sliding etc. (Matsusaka, et al. 2010). The exact mechanisms behind charge transfer are still poorly understood since it is challenging to observe these behaviours at the fundamental level. The proposed mechanisms for charge generation are attributed to either material, ion or electron transfer (Matsusaka, et al. 2010; Wong, et al. 2015). Material transfer theory describes the charge transfer across particle fragments between two surfaces. Ion transfer theory, which is much more obscure, describes the transfer of ions between contacting particles which arise due to interaction between the water adsorbed onto the particle surface and the material. However, out of the three mechanisms, electron transfer is the theory that is the most universally accepted. In this scenario, charge is transferred when one contacting body donates an electron to another, resulting in one charging more positively and the other charging more negatively (Karner and Anne Urbanetz 2011; Matsusaka, et al. 2010; Matsusyama and Yamamoto 2006). The capacity and magnitude for each body to charge is dependent on the work functions (i.e. the energy required to remove an electron off of a surface) and the capacitance between both contacting bodies (Matsusaka, et al. 2010).

Charging or triboelectrification of powders are considered adverse phenomena which develop under the conditions of flow. In the pharmaceutical industry, the majority of raw ingredients are handled in a powdered form. Pharmaceutical powders in particular have a propensity to trap and accumulate charge since many are organic materials with high degrees of resistivity ($>10^{13}$ Ωm), which increases their charge decay time (Wong, et al. 2015). Furthermore, many pharmaceutical manufacturing processes involve high-energy shearing mechanisms which subject the powder to numerous particle collisions. Although, the magnitude and propensity of powder charging is dependent on the nature of the particle collisions, (Šupuk, et al. 2012), the powder material properties and the environmental conditions (Rowley 2001; Wong, et al. 2015).

Powder charging can also impact its flowability during handling. Within a bulk powder, electrostatic attraction between particles can result in their agglomeration which can worsen its flowability (Pingali, et al. 2009). Furthermore, within a process (especially within those with extensive operating times), the charged powder may interact and adhere to the equipment

walls or flow mechanisms (Kaialy, et al. 2014), which may result in the loss of material such as expensive active pharmaceutical ingredients (APIs), (Peltonen, et al. 2018; Samiei, et al. 2017; Šupuk, et al. 2012).

In the most serious instances, powder charging can generate a spark within processes with high dust concentrations, which can result in a hazardous dust explosion (Eckhoff 2009; Glor 1985). As a safety precaution, processes which produce high dust concentrations such as milling and fluidised bed drying / coating must be connected to earth during operation. Although, there is some uncertainty as to whether earthing is at all effective in reducing all charges during processing e.g. in blending (Engers, et al. 2006).

Within pharmaceutical formulation and development, an extensive knowledge on the charging properties of powders is valuable, especially in respect to the processing conditions (Rowley 2001). This is because many powder material properties are known to impact powder charging which include but are not limited to: particle size and distribution (Šupuk, et al. 2012), particle shape (Kaialy, et al. 2014), surface roughness (Karner and Anne Urbanetz 2011), material chemistry (i.e. which impacts their hydrophobicity/hydrophilicity) (Šupuk, et al. 2012), and moisture content (Rowley and Mackin 2003). Unfortunately, there exists no standardised methodology for characterising powder charge, specifically within a pharmaceutical setting.

1.4. Importance of powder flow in pharmaceutical product manufacture

The quality of a pharmaceutical product is based on the alignment of its physical, chemical and (micro)-biological characteristics to specifications which guarantees medical efficacy and patient safety, as outlined within the Quality Target Product Profile (QTPP) (ICH 2009). Under the Quality by Design (QbD) paradigm, these characteristics are collectively classified as critical quality attributes (CQAs). Input variables (i.e. process parameters and material attributes) which may impact the CQAs are identified through a process known as risk assessment, which is normally undertaken early into the development process (ICH 2009). Experimentation is used to further study the relationship between the input variables and CQAs, which can be aided by multivariate analysis and design of experiment (DoE) tools (ICH 2009). Subsequently, a design space can be developed which expresses a combination of all material attributes and CQAs that assures product quality. From this, an operating space within the design space can be developed, which establishes the working limits and is translatable across multiple manufacturing equipment. This will be accompanied by a control strategy, which states the necessary measures required to ensure sufficient control over the CQAs (ICH 2009).

The powder flow properties (e.g. Hausner Ratio and Carr's Index) are considered CQAs and play an important contribution to the final product quality (Yu 2008). During the process of bulk material transfer, it is necessary that the raw material / intermediate products are able to flow between two or more locations in a uniform and well-controlled manner. Unfortunately, many powders do not process good flow properties and in-process flowability, which can resulting in adverse effects such as flow rate deviations, arching, rat-holing and flooding (Prescott and Barnum 2000). Consequently, a large portion of the pharmaceutical development cycle may be dedicated to improving the processability of a formulation, of which in-process flowability is a major component. This work may involve: the design and/or the selection of manufacturing equipment which may accommodate these poorly flowing materials; inclusion of a manufacturing step where the flow properties are improved by physical modification of the particles (e.g. granulation, spheronisation and extrusion); or reformulation, which may include the addition of diluent materials with good flow properties and flow aids (e.g. talc). However, even within a validated process, the CQAs may be susceptible to variability should the input material properties somehow alter, e.g. due to a change in material supplier.

Continuous manufacturing is a growing trend within the pharmaceutical industry, used to tackle the major limitations faced in traditional batch manufacturing, such as scaling difficulties as well as improving the process understanding, which is typically poor (Plumb 2005). This paradigm aims to unite all unit operations into a single continuous line, whereby the raw materials are introduced into the process and the output is the finished product, with no product intermediates present. The benefits of continuous manufacturing processes include: increased yields; reduced waste; cheaper product; improved process control; shorter processing times; reduced manpower; reduced time to market; and a lower commercial risk (Plumb 2005). However, as a trade-off, there is an added challenge to developing formulations and processes which are able to maintain uniform powder flow behaviour throughout the entire manufacturing line. Should input variability arise upstream and not be accounted for within the control strategy, this could result in CQA variation which ultimately could impact the product quality. Since continuous manufacturing lines are expected to produce several kilograms of product per hour (Simonaho, et al. 2016), it is critical that the control strategy is well developed so that product quality is consistently achieved throughout the manufacturing cycle. To meet these requirements, an extensive knowledge base is required which accounts for the material flow properties and their interactions with the process flow mechanisms.

1.5. Characterising powder flow properties

Powder flow characterisation techniques are used to assess the powder's flow response to a specific combination of shear conditions and equipment geometry. A number of off-line static and dynamic flowability testers are available, which are reviewed below.

1.5.1. Angle of repose

The angle of the repose indicates the degree of inter-particulate friction present within the powder (Beakawi Al-Hashemi and Baghabra Al-Amoudi 2018). In this test, the powder is poured through a funnel onto a base with a specific diameter so that it forms a cone. Two variations of the test exist, including the drained and dynamic angle of repose, which essentially determines the means of how the cone is formed. Regardless, the angle which the cone forms with the horizontal contact plane is known as the angle of repose θ (Fig. 1-1). In general, cohesive powders form steeper cones with a larger angle of repose (Table 1-1) (British Pharmacopoeia Commission 2019c), since their constituent particles possess higher internal friction and do not slide past each other easily. These powders tend to be characterised by lower particle size and sphericity, higher internal friction and particle roughness (Beakawi Al-Hashemi and Baghabra Al-Amoudi 2018). On the other hand, powders with better flow properties will form shallower cones will smaller angles of repose.

It is important to note that the angle of repose exhibited by the powder will be highly dependent on the test employed (Beakawi Al-Hashemi and Baghabra Al-Amoudi 2018; British Pharmacopoeia Commission 2019c). It has also been stated that the output parameters are only conclusive of flow behaviour observed in conditions similar to the given test (Beakawi Al-Hashemi and Baghabra Al-Amoudi 2018). Output variability can occur due to aeration and segregation effects that arise during the pouring of powder into the apparatus (British Pharmacopoeia Commission 2019c). Also, in some instances, the angle of repose has reportedly demonstrated insensitivity to changes in powder flowability caused by an alteration in the bulk moisture content (Emery, et al. 2009).

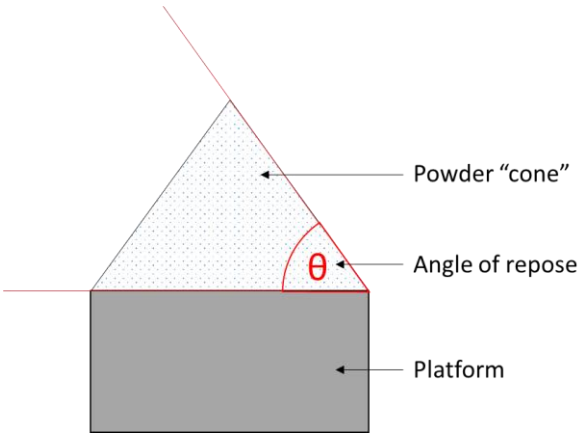

Fig. 1-1. Static angle of repose.

Table 1-1. Flowability and the corresponding angle of reposes [adapted from (British Pharmacopoeia Commission 2019c)].

Flowability	Angle of repose / θ
Excellent	25 - 30
Good	31 - 35
Fair	36 - 40
Passable	41 - 45
Poor	46 - 55
Very poor	56 - 65
Extremely poor	> 66

1.5.2. Flowability & flow through an orifice

Hoppers and silos are commonly used to deliver powder into pharmaceutical unit operations such as tablet presses. Within a hopper, the powder tends to exist in a consolidated state due to its weight under gravity exerting a load, which is mostly prominent nearer the aperture of the hopper. If a shearing mechanism such as an auger is not present, the shear force which induces flow will caused by the powder’s weight under gravity. Hopper flow is dependent on the inter-particulate friction and the particle-wall friction (i.e. the cohesive and adhesive forces respectively). If the powder’s weight under gravity is able to overcome both the cohesive and adhesive forces present at the free surface, the powder will yield and flow will occur. However, powders with high cohesion and adhesion properties have an increased tendency to form an arch which resists the gravity induced shear force, therefore resulting in zero flow (Baserinia, et al. 2016).

The flowability test assesses the capacity as well as the time taken for a powder with known mass to flow through a set of apertures (10, 15 and 25 mm) within a standardised apparatus

(British Pharmacopoeia Commission 2019b). Similarly, the flow through an orifice test measures the powder mass flow rate from hoppers, silos or containers (British Pharmacopoeia Commission 2019c). In both tests, the minimum aperture size which permits flow is identified and in case of the latter the consistency in the powder mass flow rate is determined. Like the angle of repose, both flowability and flow through an orifice tests are method dependant and thus the resulting flow behaviour will also be dependent on the flow conditions under which it was determined (British Pharmacopoeia Commission 2019c).

1.5.3. Carr's Index & Hausner Ratio

A bulk powder which is poured into a container typically contains a number of air pockets or voids which interfaces its constituent particles, where this state is known as its poured or bulk density V_{bulk}. Upon agitation, the particles can rearrange to occupy these voids, resulting in densification of the bulk powder. The degree at which the powder densifies is correlated to its flowability (British Pharmacopoeia Commission 2019c). These measurements are performed using a bulk / tapped density tester. Here, a powder sample with known mass is introduced into a graduated measuring cylinder and the initial volume V_{bulk} and bulk density ρ_{bulk} are recorded. After the sample is subjected to a pre-defined number of agitations or taps, the final volume V_{tapped} and tapped density ρ_{tapped} are determined. The change in density ρ is calculated using (Equation 2 and (Equation 3) (British Pharmacopoeia Commission 2019c). The powder's flowability is then determined by reading the values against the reference index (Table 1-2).

$$\mathrm{HR} = \frac{\rho_{\mathrm{tapped}}}{\rho_{\mathrm{bulk}}} \qquad \text{(Equation 2)}$$

$$\mathrm{CI} = \frac{\rho_{\mathrm{tapped}} - \rho_{\mathrm{bulk}}}{\rho_{\mathrm{tapped}}} \times 100\% \qquad \text{(Equation 3)}$$

Table 1-2. Flowability and the corresponding HR and CI values [adapted from (British Pharmacopoeia Commission 2019c)].

Flowability	HR	CI / %
Excellent	1.00 - 1.11	1 – 10
Good	1.12 - 1.18	11 – 15
Fair	1.19 - 1.25	16 – 20
Passable	1.26 - 1.34	21 – 25
Poor	1.35 - 1.45	26 – 31
Very poor	1.46 - 1.59	32 – 37
Extremely poor	> 1.60	> 38

CI and HR are useful for describing a powder's consolidation behaviour within a hopper, which can be further linked to its hopper flowability (Leturia, et al. 2014). Although, it has been argued that bulk / tapped density measures do not reliably replicate the compaction experienced by the material during the transfer operations (Prescott and Barnum 2000). CI and HR can also be used to assess the susceptibility of particulate materials to segregate due to vibration during storage or transport (Hastie 2015).

Some limitations of the technique are listed below. It is difficult to achieve consistent initial poured density, which impacts the reproducibility of the CI and HR values. Powder conditioning is typically restricted to more sophisticated dynamic flow testers (Leturia, et al. 2014). The outputs are highly dependent on the input variables such as the amount of energy introduced during testing (i.e. the number of taps) as well as the consistency in the particle properties (Li, Qin, et al. 2004). If segregation propensity is to be assessed, it must be ensured that the sample measured is representative of the total batch (Hastie 2015). Finally, like angle of repose, HR and CI have also both been reported to be insensitive to changes in the bulk moisture content (Emery, et al. 2009).

1.5.4. Characterising hopper flow behaviour

1.5.4.1. Predicting discharge mass flow rate through circular orifices

A number of models have been developed for the prediction of powder mass flow rate from hopper orifices. Many of these models are based on the equation developed by (Beverloo, et al. 1961). Here, the mass flow rate W of a powder with particle diameter d discharged from an orifice with diameter D can be inferred from (Equation 4), where the ρ_a is the bulk density, g is the acceleration due to gravity, the Beverloo constant k which is dependent on the particle size and shape constant C which lies within the range of 0.55 – 0.65 and is related to the geometry of the hopper, although for most applications C is treated as 0.58 (Calderón, et al. 2017; Oldal, et al. 2012). The component $(D - kd)$ is also known as the Weighardt's relationship of which mass flow rate is a function (Weighardt 1952). Beverloo, et al. (1961) reported a linear correlation between $W^{2/5}$ and the D, which when extrapolated to intercept the y-axis, yielded a value which correlated with kd. From this relationship, the effect of particle size and shape on the hopper outlet diameter may be studied and utilised for the design of hoppers (Anand, et al. 2008).

$$W = C\rho_a g^{\frac{1}{2}}(D - kd)^{\frac{5}{2}} \qquad \text{(Equation 4)}$$

However, correlations obtained from the Beverloo model are only applicable to particle systems with uniform size and shape distribution (which impacts the specific surface area and thus k), zero cohesion and within cylindrical flat-bottomed hoppers (Calderón, et al. 2017), as such many authors have expanded upon the original Beverloo equation so as to account for these effects. Brown and Richards (1965), presented a modified model for determining the discharge rate for powders in hoppers with a bases (Brown and Richards 1965). Here, the powder mass flow rate from an angled hopper $W_{angled\ hopper}$ can be derived from powder mass from rate predicted from a flat-bottom hopper $W_{flat-bottom\ hopper}$ with equivalent hopper and outlet diameter (Equation 5), where θ is the angle formed between the vertical hopper wall and the angled surface .

$$W_{angled\ hopper} = W_{flat-bottom\ hopper}\frac{1 - \cos\frac{3}{2}\theta}{\sin\frac{5}{2}\theta} \qquad \text{(Equation 5)}$$

Humby, et al. (1998), modified the Beverloo equation to account for differences in particle size distribution (Equation 6), where $Z(d_{eff})$ is coupled to the effective particle size distribution, η_d is the flowing packing density and C was assumed 0.58 (Humby, et al. 1998). The authors were able to predict the discharge rate for binary mixtures which were in good agreement with experimental results.

$$W = \mathrm{C}\rho_a \eta_d g^{\frac{1}{2}}[D - Z(d_{eff})]^{\frac{5}{2}} \quad \text{(Equation 6)}$$

Anand, et al. (2009), modified the Beverloo constant using the Bond number in order to predict the mass flow rate for cohesive powder flow within a rectangular hopper (Equation 7) (Anand, et al. 2009). Here, $1.9e^{0.3Bo}$ is substituted for k, which was derived via regression analysis of k vs Bond number. Also, C is treated as 1.03 due to the rectangular hopper geometry and the Weighardt function is adjusted to account for the length L_0 and width W_0 of the rectangular opening. The authors were also able to study the impact of hopper angle on mass flow rate for powders with different Bond numbers. The mass flow rate predicted using modified Beverloo equation were shown to deviate by a value of up to 10% from the mass flow rate predicted using Discrete Element Method (DEM). The authors state that sources error included difficulties in estimating the mass flow rate in DEM simulation when the flow was intermittent. Also, it was assumed that ρ_{flow} remained constant when in actuality, the flow density would expect to fluctuate with cohesion.

$$W_{flat-bottom\ hopper} = 1.03\rho_{flow} g^{\frac{1}{2}}[L_0 - (1.9e^{0.3Bo})][W_0 - (1.9e^{0.39Bo})\mathrm{d}]^{\frac{3}{2}} \quad \text{(Equation 7)}$$

The above studies represent non-exhaustive list of applications using Beverloo's equation. Further applications are given by (Ji, et al. 2019; Tangri, et al. 2019; Uñac, et al. 2012; Zaki and Siraj 2019).

Another method of modelling hopper mass flow rate is the "Minimum Energy Theorem" given by (Brown 1961; Brown and Richards 1970). Using Equation 8, the mass flow rate Q through a circular aperture D can be predicted. The authors state that Q will be dependent on the bulk density ρ_a and the hopper half-angle θ. Furthermore, they were able to demonstrate that the estimate values of θ for plane and cylindrical flow regimes were in good agreement with experimental data.

$$\frac{4Q}{\pi\rho_a g^{1/2}(D-k)^{5/2}} = \frac{(1-\cos\theta)^{1/2}}{2^{1/2}\sin^{3/2}\theta} \quad \text{(Equation 8)}$$

1.5.4.2. Shear cell testing

Shear cell testing is a commonly used flowability tester. Originally developed by Andrew Jenike (Jenike 1964), the operation of the tester is based on the shear force (load) required to induce failure in a consolidated powder. The traditional Jenike shear cell tester achieves this by slowly shearing two consolidated powder layers against one another using a lateral shear force (Ganesan, et al. 2008), whereas modernised variations of the instrument such as the annular/Schulze tester instead utilise a head with a set of small blades arranged radially (Schulze 2008). These blades are inserted into the consolidated powder sample and a rotational shear force is applied, creating a shear stress perpendicular to the applied force (Prescott and Barnum 2000), resulting in the movement of a mobile layer which is sheared against the static sample layer.

For annular testers, the testing routine involves pre-compacting the powder using a pre-defined load. The consolidated powder is then pre-sheared to achieve steady-state flow, after which by applying a constant shear force, the powder shear stress is increased until the powder yields, also known as the point of incipient failure. Pre-shear / shear testing is then repeated using varying loads. The points of incipient failure are plotted on a plot of shear stress vs shear force, in the form a yield locus (Leturia, et al. 2014).

Mohr's circle analysis is used to extract specific values from the yield locus (Freeman 2007; Koynov, et al. 2015; Leturia, et al. 2014; Zafar, et al. 2015). A small Mohr's circle is drawn, intersecting with the origin and lying tangential to the yield locus (see Fig. 1-2). The maximum point at which circle intersects the x-axis represents the maximum shear force at zero shear stress, known as the unconfined yield strength UYS. This represents the state of stress within the consolidated powder when unconfined, e.g. the exposed surface of an arch in a hopper (Koynov, et al. 2015). A second larger Mohr's circle is also drawn through the pre-shear data point whilst lying tangential to the yield locus. The maximum point at which circle intersects the x-axis represents the maximum shear force at zero shear stress is known as the major principle stress MPS. This represents the stress state of a consolidated powder whilst under confinement (Koynov, et al. 2015).

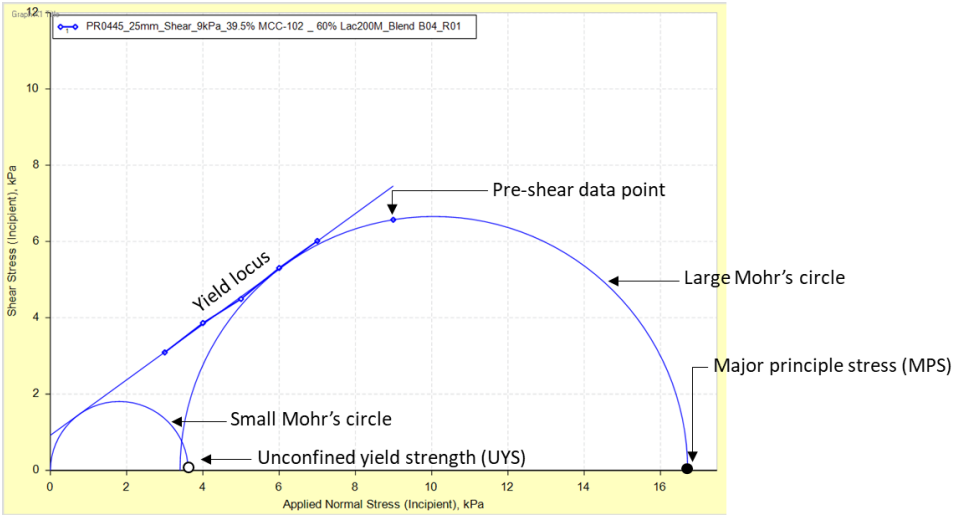

Fig. 1-2. Shear cell yield locus with Mohr's circle analysis.

A parameter known as the flow function coefficient FF is then determined by taking the ratio of the MPS to the UYS (Equation 9). Also, another useful parameter is the angle of internal friction φ, which is the angle formed between the yield locus as it intersects with the x-axis. The FF and AIF will generally be higher for cohesive powders which typically possess a higher degree of inter-particulate friction (Ganesan, et al. 2008; Prescott and Barnum 2000).

$$\mathrm{FF} = \frac{\mathrm{MPS}}{\mathrm{UYS}} \qquad \text{(Equation 9)}$$

The shear cell used to predict powder flow behaviour and mode within hoppers given that the stress and packing conditions between both are similar (Ganesan, et al. 2008; Prescott and Barnum 2000), and unlike CI and HR, demonstrate higher sensitivity to moisture content (Ganesan, et al. 2008). Typically, the FF is used to predict the hopper flowability of a powder, with refence against a specific flow index (Table 1-3).

Table 1-3. Flow index classification [adapted from (Jenike 1964)].

Flow Index	Flow characterisation
FF < 1	No flow
1 < FF < 2	Very cohesive
2 < FF < 4	Cohesive
4 < FF < 10	Easy flowing
10 < FF	Free-flowing

Unfortunately, shear cell testing outputs are often used as a universal test for flowability and as such, commonly misattributed to powder flow systems with unrelated shear and packing conditions. Shear cell testing is also limited in that it cannot always provide reliable data for powders that cannot be easily consolidated i.e. free-flowing powders (Koynov, et al. 2015) and is generally a time-consuming technique (Leturia, et al. 2014). Additionally, when characterising blends containing flow aids using annular type testers, there is a chance that the shearing layer may fully slip over the static layer due to added lubrication, resulting in measured shear stresses which are lower than the expected value.

1.5.4.3. Wall friction testing

Wall friction testing is similar in principal to shear cell testing, but instead characterises the degree of friction present between a powder and surface. The wall friction test can be performed using the Jenike shear tester which involves slowly applying a lateral force to a compressed powder resting on a coupon with a specific surface finish until it yields (Hancock 2019; Pillai, et al. 2007). Alternatively, the test can be performed using a rotating coupon, which is sheared against a pre-consolidated powder (Freeman 2007). In this scenario, a constant pre-defined normal stress is then applied to the powder and the shear stress is slowly ramped up until failure occurs. These measurements are then repeated by varying the normal stress. The steady-state shear stresses are recorded as a function of the respective normal stresses, from which a wall friction yield locus is generated (see Fig. 1-3). A line of best fit is regressed through the yield locus and is extrapolated to intersect with the origin. The angle that is formed between the line of best fit and the origin is known as the wall friction angle φ_w, a parameter used to characterise the friction between the powder and surface. Powders that flow worse against a surface tend to have higher WFAs and vice-versa (Hancock 2019). These values are typically used to predict how well a powder will flow on a given surface such as those present in a hopper and in the area of hopper design, can be used to predict the required steepness in order to achieve the desired mode of flow (Hancock 2019).

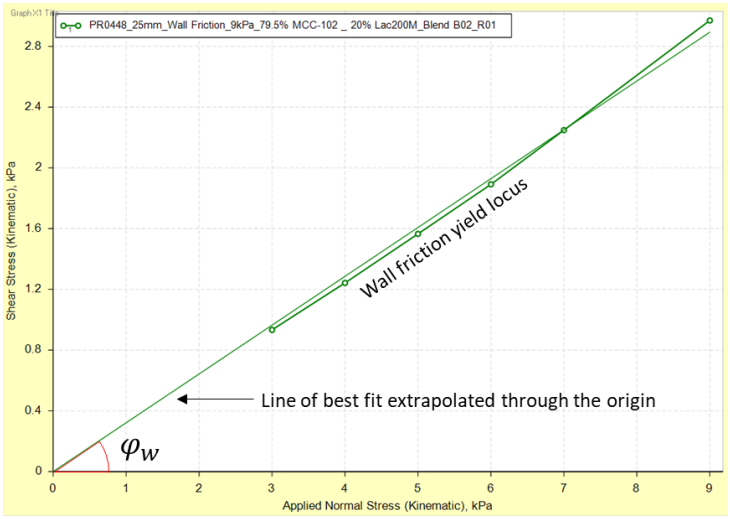

Fig. 1-3. Wall friction yield locus.

1.5.4.4. Uniaxial compression testing

The uniaxial compression test also characterises the shear properties of a consolidated powder (Fig. 1-4). The powder is initially consolidated to a desired density within a column, after which the column is removed and a normal stress is applied to the unconfined consolidated powder until it fractures. The normal stress at which fracture occurs is also known as the UYS, which is similar to that measured using the shear tester. The UYS is then determined for a range of normal stresses, from which a yield locus is generated. The FF can then be calculated by taking in the ratio of the applied normal stress to the UYS (Chen, et al. 2017).

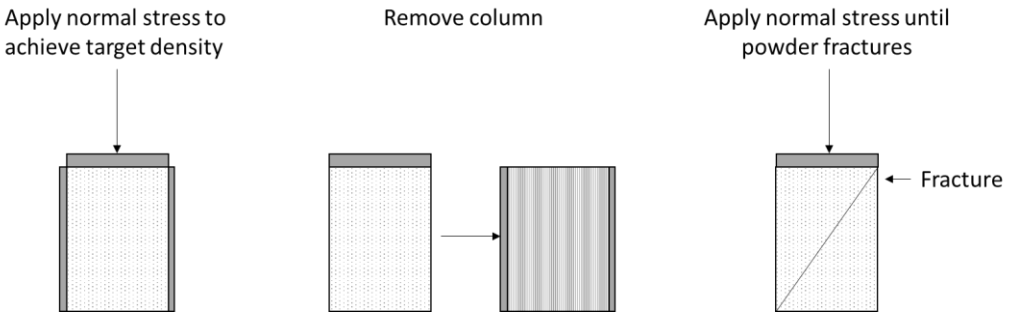

Fig. 1-4. Uniaxial compression test procedure.

The uniaxial compression test is a quick and simple test which is able to produce reproducible data. FF and UYS determined via uniaxial compression test have shown similarity to the same parameters obtained using the Jenike shear tester for powders that exhibit cohesive flow

properties. Although, for powders that demonstrated free-flowing properties, the uniaxial tester tended to underestimate the FF and UYS (Chen, et al. 2017).

1.5.4.5. Ball indentation

The ball indentation test characterises the powder hardness which is reflective of its flowability. In this test, a spherical ball indenter is used to penetrate a consolidated powder at increasing depths. The hardness of the powder is determined from the ratio of the maximum indentation load to the projected indenter surface area (Tirapelle, et al. 2019; Zafar, et al. 2015). The powder hardness has shown by the authors to be linearly correlated to the UYS parameter which is measured via shear testing and are related by a constraint factor (whose value is dependent on the particle properties). A few advantages of the ball indentation method include the ability to perform measurements using only a small quantity of powder and the capacity to perform measurements multiples on the same sample due to the small size of the indenter (Zafar, et al. 2017).

1.5.4.6. Hopper design based on shear and wall friction testing

Jenike (1964), developed a methodology based on shear and wall friction outputs for the analysis of stress profiles within hoppers (Jenike 1964). This process allows one to study the different hopper geometries that may or may not induce blockage; a key methodology in the design of hoppers. A key parameter involved in hopper design is flow factor ff, which indicates the quality of the flow channel present within the flow system. Generally, a smaller ff the better the flow channel formed, and when the critical stress $\overline{\sigma_1} > UYS$, the arch will fail and the powder will flow under gravity. ff is the ratio of the major consolidating stress σ_1 to the strength of a solid $\bar{\sigma}$ (i.e. the pressures which act on a dome or arch during obstruction). The σ_1 can be determined by measuring shear force at different loads (Prescott and Barnum 2000). $\bar{\sigma}$ is inferred from the φ_w measured at various hopper θ's for different material φ's, which indicates the combination in φ_w and θ' required to achieve desirable mass flow regimes and undesirable funnel flow regimes (Hancock 2019; Prescott and Barnum 2000). The lines for ff, as well as FF are plotted on the graph for $\bar{\sigma}$ against σ_1. The region where these lines intersect indicates the critical applied stress $\overline{\sigma'}$ to achieve gravitational flow without arching (Fig. 1-5), (Fitzpatrick, et al. 2004; Jenike 1964).

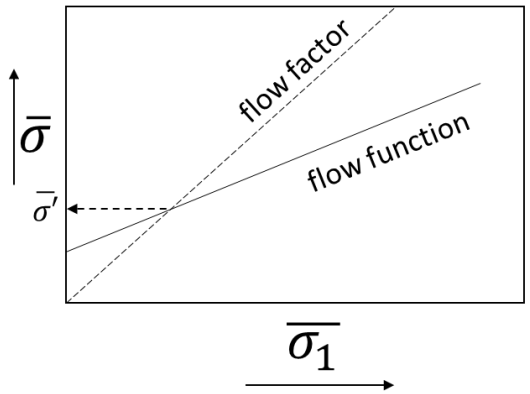

Fig. 1-5. Critical applied stress (CAS) derived from the intersection between the hopper flow factor and flow function, adapted from (Jenike 1964).

The critical outlet diameter B (i.e. the minimum orifice diameter which allows for the flow of powder without formation of a cohesive arch), can then be determined using (Equation 10), where ρ_a is the powder bulk density, g is the acceleration due to gravity and $H(\theta')$ is a hopper geometry function (Fitzpatrick, et al. 2004; Jenike and Leser 1965; Jenike 1964).

$$B = \frac{H(\theta')\overline{\sigma'}}{\rho_a g} \qquad \text{(Equation 10)}$$

Applications of Jenike's methodology for hopper design are described in the following articles (Fitzpatrick, et al. 2004; Ketterhagen, et al. 2009; Ketterhagen and Hancock 2010; Søgaard, et al. 2017; Xue, et al. 2019; Zhou, et al. 2020).

1.5.5. Dynamic powder flow testing

1.5.5.1. Sevilla powder flow tester / raining bed tester

The Sevilla powder flow tester attributes flowability to the tensile strength present within a fluidised powder bed. A powder with known weight is placed in a vessel with a permeable base and conditioned with fluidised air. Fluidised air is then applied to the top of the powder bed in order to achieve a compacted state at a pre-defined stress. The fluidised air is then injected into the base of the compacted bed until it fractures whilst the pressure drop across the powder bed is continuously recorded. The pressure drop at which failure occurs is known as the tensile failure stress (Zafar, et al. 2015).

The raining bed test operates under a similar principle to the Sevilla powder flow tester. The powder is initially conditioned inside a column via fluidisation and agitation in order to achieve a desired size fraction. The bed is then rotated by 180° so that the bed is suspended upside

down, although it does not fail since its weight under gravity is supported by the airflow. The airflow velocity is then slowly reduced until it reaches a critical velocity where the powder bed fails. Powder beds with a higher degree of inter-particulate cohesion are able to resist failure at lower air velocities due to an increased compact tensile strength (Zafar, et al. 2015). The tensile strength is derived from the pressure drop across the powder bed plotted against the rain-off velocity (Girimonte, et al. 2018).

1.5.5.2. Avalanche testing

Avalanche testing is an example methodology which utilises dynamic flow conditions in a similar stress state to angle of repose in order to assess the powder flow properties. Here, a powder is placed into a drum and is rotated at a slow velocity. As the powder bed reaches a critical angle, the inter-particulate cohesive bonds are unable to support the bed weight resulting in an avalanche and redistribution of the material across the base of the drum. A video camera is used to record the flow in real-time from which the avalanche time and angle may be determined from an average number of rotations (Krantz, et al. 2009; Nalluri and Kuentz 2010).

1.5.5.3. FT4 Powder Rheometer

Developed by Freeman Technology Ltd, the FT4 Powder Rheometer is a multi-purpose tester designed to characterise flow properties under dynamic flow conditions. A key accessory used in conjunction with this tester is a blade designed to induce variable shear conditions depending on its direction of rotation. Different flow properties are characterised based on the energy required for the blade to induce flow within the powder bed under different simulated flow conditions (Hare, et al. 2015). A single dynamic flow test can yield multiple parameters, each describing different aspects of the powder flow behaviour such as stability, flow rate sensitivity and average flow energy (Freeman 2007). An advantage of this tester lies in its automation and conditioning protocol which improves the reproducibility of its outputs. The conditioning protocol dilates the powder bed and breaks apart any agglomerates present, thus presenting a consistent starting point prior to flow testing. Aside from flow properties, the FT4 Powder Rheometer is also able to characterise bulk and shear properties such as compressibility, permeability, φ, and φ_w by substituting the blade with the appropriate accessory. Powder flow studies utilising this FT4 Powder Rheometer can be found in the following articles (Freeman 2007; Hare, et al. 2015; Koynov, et al. 2015; Krantz, et al. 2009; Leturia, et al. 2014; Nan, et al. 2017a; Nan, et al. 2017b; Tirapelle, et al. 2019).

1.6. Characterising powder charge properties

The standard method for determining the charge polarity and magnitude on powders is the Faraday Cup (British Standards Institute 1995; British Standards Institute 1996). The Faraday Cup (see Fig. 1-6), consists of a conductive inner cup which is connected to an electrometer. An outer cup serves to shield the inner cup from external electrical interference, whilst an insulation layer which interfaces both cups acts to prevent current leakage. The powder is charged externally before being placed into the inner cup (Šupuk, et al. 2012). The charged powder induces the flow of current across the cabling connecting the cup and the electrometer, biasing the inner cup with a voltage opposite to that on the powder. The charge Q is displayed on the electrometer as a voltage which is directly proportional to the powder charge in the cup. It is also common practice to simultaneously determine the mass of the measured powder by mounting the Faraday Cup on a balance. The specific charge of the powder Q/m can be determined by normalising the induced charge by the mass (Engers, et al. 2006; Šupuk, et al. 2012).

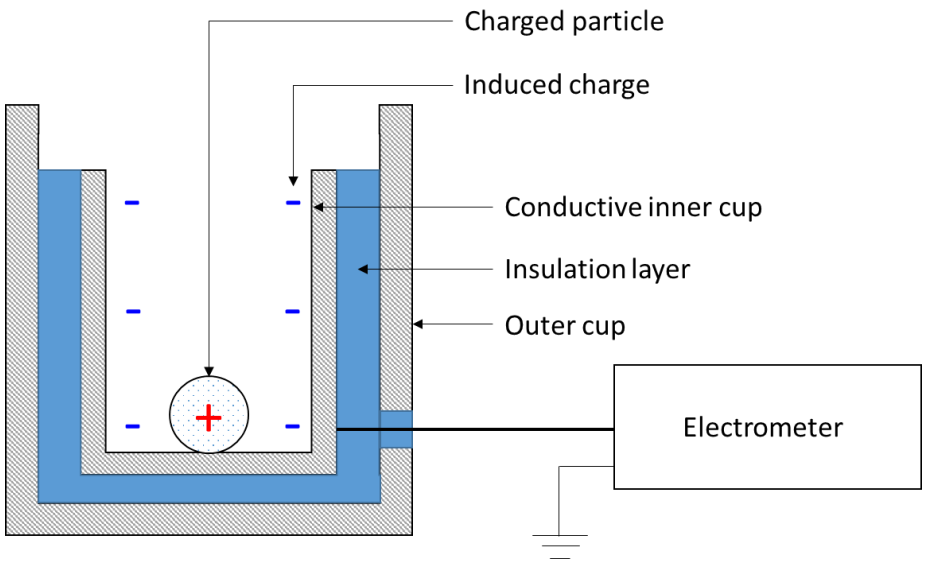

Fig. 1-6. Schematic of the Faraday Cup, adapted from (British Standards Institution 1996).

It is typical for powders to be ranked in order of their charge magnitude and polarity relative to other materials (Šupuk, et al. 2012). Known as a triboelectric series, this ranking is able to provide a simple indication on the relative chargeability of different powders, although they are considered to be highly empirical (Wong, et al. 2015) and are dependent on the conditions they were characterised under, including the techniques used to charge and feed the powder

into the cup (Shi, et al. 2017). As a result, triboelectric series of materials analysed across different labs may be ranked inconsistently to one another (Park, et al. 2008). Therefore, it is imperative that the charging and feeding techniques are kept consistent to ensure comparative data between materials. It is also recommended for the operator to be connected to an earthing source so as to prevent additional charging during the measurement process (British Standards Institute 1995; Karner and Anne Urbanetz 2011). Finally, the electrometer should be connected to an earthing source which is electrically quiet to avoid drift in the induced voltage reading.

A select number of studies have utilised the Faraday Cup for characterise charging properties of pharmaceutical powders (Ghori, et al. 2014; Rowley 2001; Šupuk, et al. 2012; Watanabe, et al. 2007). However, charge measurements (off-line or in-process) are not routinely performed in the pharmaceutical industry and therefore no standardised procedure specific to this industry exists for such as purpose outside of those stated by the British Standard Institute.

1.7. Limitations to off-line flowability and charge testing

Many of the flow testers reviewed above have enjoyed widespread use within the area of powder flow characterisation. Regarding the pharmaceutical industry in particular, the angle of repose, flowability / flow through an orifice, bulk / tapped density and shear cell are routinely employed as standard flowability tests (British Pharmacopoeia Commission 2019c). Typical practice within the industry is to select the simplest and least time-consuming tester. Their outputs are then used to universally describe the powder flowability within all processes, without consideration given to the differences between the shear conditions or equipment geometry (Prescott and Barnum 2000). This was a consequence of a powder flowability being considered an inherent property of the powder. For example, a powder which was characterised as cohesive by a tester would be expected to flow poorly in all processes. This is not actually the case, since powders are known to flow (or not) depending on the compatibility between the process shear conditions and the powder flow properties (Wang, Y., et al. 2017). The reality is that flowability is dimensionless and cannot simply be expressed using a single flow parameter (Prescott and Barnum 2000). It is also critical that when attempting to predict the in-process powder flowability based on off-line tester outputs, to consider the stress states between both process and tester. Stress states can either be static (e.g. a powder at rest) or dynamic (e.g. a fluidised powder) and under both, the flowability of the same powder may be characterised differently due to the variation in particle interactions and motions (Krantz, et al.

2009). Herein lies a major limitation in off-line testers, since they are mostly restricted to generating a singular stress state, from which a single flow parameter is yielded. This parameter is usually insufficient for predicting the in-process flow behaviour as the latter typically involves multiple interactions under dynamic flow conditions. Also, it is unsuitable to characterise an in-process powder flow which exhibits a dynamic stress state using a tester which is only able to simulate a static stress state and vice-versa (Krantz, et al. 2009). However, this does not mean flow parameters characterised using a static tester are not valuable. In fact, these parameters are still useful in building an understanding of a powder's response to specific conditions that may occur in a process (e.g. compression within a confined spice). However, in order to reliably predict how a powder will flow within any given process, measurements must be performed under representative stress states, shear conditions and environmental conditions, which is not feasible using current off-line flow testers.

For the measurement of charge, there are a number of limitations related to the standard Faraday Cup method. Firstly, the cup is only able to yield a single value of charge, regardless of the quantity of powder measured. This renders it impossible to determine the distribution of charge across a batch of powder. Moreover, the charge developed on a powder is highly dependent on how it was conditioned before measurement (e.g. material properties, and the technique used to induce triboelectrification). The triboelectrification process has been performed using different methods across literature which has included: shaking the powders within a container (Hussain, et al. 2013; Šupuk, et al. 2012); powder blending (Engers, et al. 2006); and conveying using a vibratory feeder and pneumatic air flows (Ndama, et al. 2011). Since each of these methods charge the powders in a different manner, it is unlikely that they will also develop charge in an identical manner, which is also an issue when attempting to predict the charging properties of a powder for a process application.

A more accurate method would be to employ the process itself as the charging medium (Engers, et al. 2006). However, the closed-ended nature of the Faraday Cup renders it challenging to integrate into in-process flows since its maximum capacity would be reached relatively quickly and often prior to the onset of adverse charging events. This would facilitate the need for an integrated cleaning regime. Alternatively, charge measurements may be performed in tandem with on-line sampling, however the sampling technique can reportedly induce unwanted further charging (Shi, et al. 2017). Finally, in order to measure the specific

charge of the powder, a balance is required to record the weight which is not easily installed into a process without impacting the nature of the flow.

1.8. Numerical simulations of powder flow systems

Numerical solution tools can be used to simulate multi-particulate flow systems in order to build a fundamental understanding of the flow behaviour at the particulate level. Discrete element method (DEM) is a computational tool originally developed by (Cundall and Strack 1979), which has seen further expansion over time. DEM solves the positioning, velocity and forces involved for each particle with respects to their neighbours and the equipment geometry (also treated as the boundary surfaces) at regular time intervals (Mukherjee, et al. 2018). These models are developed from a number of physical laws which can include Newton's 2nd and 3rd law, gravity, sliding and rolling friction coefficents (Ketterhagen and Hancock 2010; Mukherjee, et al. 2018; Pachón-Morales, et al. 2019; Tiscar, et al. 2019), air drag (Kretz, et al. 2016), plasticity and elasticity (Behjani, et al. 2019; Hou, et al. 2014; Kruggel-Emden, et al. 2007; Pachón-Morales, et al. 2019), friction (Kretz, et al. 2016), cohesive and adhesive interaction (i.e. electrostatic attraction, Van der Waals forces and liquid bridging) (Behjani, et al. 2019; Chan and Washino 2018; Hou, et al. 2014; Mukherjee, et al. 2018; Nwose, et al. 2012; Pachón-Morales, et al. 2019). DEM has been used to model flows in systems such as screw feeders (Hou, et al. 2014; Kretz, et al. 2016), blenders (Behjani, et al. 2019), hoppers (Ketterhagen and Hancock 2010; Zhang, T. F., et al. 2019) and die-filling in tablet presses (Nwose, et al. 2012). Also, DEM has also been combined with computational fluid dynamics (CFD), in order to study the effect of fluid flow on the motions of the particles (Nwose, et al. 2012). Some example applications of DEM-CFD include the modelling of flow within fluidised beds (Fries, et al. 2013), pneumatic conveyors (Zhao, H. and Zhao 2019), and an investigation into the role of airflow during die filling (Nwose, et al. 2012).

DEM is a powerful tool which is able to analyse and quantify kinetic parameters involved in complex flows that would be otherwise be impractical to obtain experimentally (Hou, et al. 2014). It is anticipated that with further development, DEM may be used in place of experimentally derived flow measurements, thus saving resources, costs and time. However, DEM has not yet become adopted for routine use within the pharmaceutical industry. A major limitation is the restriction on the number of particles and interactions that may be generated within a model before becoming too computationally intensive and increasing the simulation time (Berger and Hrenya 2014). Unfortunately, in order to avoid missing collisions between

particles, small time intervals are required which increases the number of collisions that need to be resolved (Garg, et al. 2012). Scaling laws can be incorporated into the model in order to reduce the number of particles in a system, although this comes at a cost of accuracy (Chan and Washino 2018; Tiscar, et al. 2019). It may also be possible to accommodate wider particle size distributions by addressing the issues faced with communication cost/time which can be achieved by improving the communication hardware (Berger and Hrenya 2014). There is also a limitation to the complexity in particle shapes and the broadness of the distribution in particles sizes that may be simulated. Irregular particles can be fashioned by clumping simple shapes such as spheres together, although these do not truly represent the real particles within the powder (Pachón-Morales, et al. 2019).

1.9. Measuring powder flow and charge *in-situ*

The predictability of powder flow measurements can be improved by obtaining them *in-situ* whilst the powder is under the influence of the process' shear conditions. A good example of a commercial device which can monitor the in-line mass flow rate is the loss-in-weight feeder, which is comprised of a screw feeder mounted on top of a load cell. The device can control the mass flow rate by constantly monitoring the loss-in-weight of powder dosed in reference to a set point. Moreover, through the use of a built-in feedback closed loop system, the output mass flow rate will always be matched by adjusting the screw speed when necessary (Singh, et al. 2015). Therefore, should disturbance be introduced to the system in the form of input flow or material property variation, the feeder should be able to compensate for this disturbance without impacting the output mass flow rate.

The loss-in-weight feeder is commonly integrated into many unit operations as a means of bulk transfer and are especially valuable within in the realms of continuous processing where consistent powder mass flow rates are critical in achieving end product CQAs. However, there are some limitations to these devices. For one, the necessity for the inclusion of a load cell renders it impractical to install the loss-in-weight feeder into multiple locations within the process. Secondly, the device does not usually record the mass flow data in real-time, meaning that a lot of valuable information on the in-process flow behaviour is lost.

There are many areas of the process where the powder flow behaviour may be impossible to measure using current commercial options. In order to reliably measure powder flow properties in these areas, the technologies would need to be able to access the flow and yield reproducible and accurate data in response to events such as flow disturbance and fluctuation,

i.e. different sampling volumes (Fonteyne, et al. 2015). Ideally, these technologies should be able to demonstrate sensitivity to different material properties such as particle / agglomerate size and moisture content, which is important since drift in these properties could act as precursors to a change in flow rate. As well, these technologies should be universally applicable to different types of powder flow regimes and should not change or impede the natural flow pattern (Fonteyne, et al. 2015), and should be robust in the hostile processing conditions (FDA 2004), e.g. resistance to fouling (Fonteyne, et al. 2015), temperature and humidity fluctuations and external inference such as vibration. These requirements would also be required for an *in-situ* measurement of powder charge. Although, these technologies must also demonstrate a capacity to quantify the charge without inducing additional charging effects on the powder. Finally, the technology should also be able to measure charge as a continuous parameter rather than a single measurement, in order to tracking powder charging as a function of time.

1.10. Introduction to process analytical technology (PAT) framework and tools

The Food and Drug Administration have developed a framework for the analysis and control of CQAs via Process Analytical Technologies (PAT) tools (FDA 2004). These tools can be divided into one of four following categories: a) multivariate tools that facilitate process design and understanding, which can also assist in the identification of input variables which are critical to the CQAS; b) process analytical tools, which are able to describe the physical, chemical or biological attributes in real-time based on a univariate measurement; c) process control tools, which establishes control over the CQAs through a combination of process monitoring and effective control strategies, in order to ensure quality in the final product; and d) continuous improvement, which feeds back the data collected during process monitoring across the entirety of the product lifecycle to improve the process and expand the knowledge base for the development of other processes (FDA 2004). The application of PAT tools can ultimately reduce production times, facilitate real-time release, reduce material wastage, reduce the energy footprint, facilitate automation and increase product yield (FDA 2004). PAT tools for in-line powder flow and charge analysis spans across a wide range of different technologies and are typically analysed via one or more of the following methods: a) measurement of the powder velocity in pneumatic flow regimes (Yan 1996); b) univariate calibration of a measured parameter against a flow characteristics / parameter such as mass flow rate (Yan 1996); and c)

determination of the powder mass flow rate μ, which is inferred from the chordal solids fraction β_c, the projected cross-sectional area A_c, the powder velocity V and the true density of the powder ρ (Equation 11), (Barratt, et al. 2000).

$$\mu = \beta_c A_c \rho V \qquad \text{(Equation 11)}$$

The following sub-sections will describe some of these technologies, including their principle of operation, as well as advantages and disadvantages with respect to their applicability to common pharmaceutical processes and powder flow regimes.

1.10.1. Near-infrared spectroscopy

Near-infrared spectroscopy (NIR), analyses the molecular bond vibration within the near-infrared region of the electromagnetic spectrum. Regarding powders, this technology has mainly been applied to analyse their in-line API / drug concentration during blending (Benedetti, et al. 2007), granulation (Fonteyne, et al. 2016; Vercruysse, et al. 2014), and within tablet press feed frames (De Leersnyder, et al. 2018; De Leersnyder, et al. 2019; Wahl, et al. 2014; Ward, et al. 2013). Although NIR is the most widely applied and researched PAT tool due to its relative availability (Fonteyne, et al. 2015), applications for powder flowability and flow property measurement have been reported less. Alam, et al. (2017), used an NIR tool to characterise the in-line flow behaviour of a cohesive and non-cohesive powder flowing through a tube based on the univariate response of the spectral absorbance to the powder stream thickness. A Partial-Least-Squares (PLS) model was used to quantify the acetaminophen (APAP) concentration present at different mass flow rates and tube angles, from which a design space was developed which indicated the acceptable ranges in both parameters so as to achieve the target powder stream thickness with the target APAP concentration (Alam, et al. 2017). On the other hand, Singh, et al. (2015), designed an NIR coupled feedback / feedforward control system in order to monitor the powder bulk density delivered by a screw feeder and a blender in real-time. This powder bulk density parameter obtained using a PLS calibration model for drug concentration was validated under different flow regimes. The NIR system was then integrated into system containing excipient feeders, a blender and a tablet press. The powder bulk density data was fed-forward in order to control downstream tabletting parameters, whilst the hopper fill level, blend composition and tabletting parameters was fed-back to control the API and excipient feeder parameters. The feedforward

/ feedback controller was shown to reject changes in the bulk density (induced by random disturbances), before it impacted the tablet and weight hardness properties (Singh, et al. 2015).

NIR is able to demonstrate good sensitivity to even discrete changes in the flowing powder bulk density, which favours an in-line application (Singh, et al. 2015). Since the powder flow behaviour is inferred from the drug / API concentration, it should be ensured that: the sampling window is large enough to detect discrete changes in these characteristics, the technique is able to interrogate multi-component blends, and a suitable measurement software capable of recording all process parameters is available (Fonteyne, et al. 2016). Careful considerations should also be made as to how the NIR sensor should be installed, so as to ensure accurate and reproducible measurement (Fonteyne, et al. 2016). Should the NIR sensor be installed so that it is in direct contact with the powder, then it will be susceptible to fouling which can impact the measurement accuracy. Alternatively, the NIR sensor can be installed outside of the pipework, where it is instead able to access the flow through a transparent pipe or window (Alam, et al. 2017; Singh, et al. 2015). Compared to the first setup, the latter configuration could require major modifications to be made to the processing equipment which may not be feasible in all instances, although it does protect the sensor from fouling. However, as a trade-off, the window is also sensitive to fouling, which would require a suitable (and preferably automated) cleaning protocol which does not impede the flow of powder. Singh, et al. (2015), did not incorporate a cleaning protocol in order to prevent fouling of their window, although their powders were presumably delivered in lean phase (i.e. from a screw feeder), meaning that the propensity to foul the window would have been lower (Singh, et al. 2015). Another disadvantage of this technology may be related to the density in the analysed flow regime. Alam, et al. (2017), reported a loss in detectability of the sensing element when a maximum bed thickness of 5 mm was achieved, which could imply incompatibility with incredibly dense phase flows such as those observed in hoppers (Alam, et al. 2017).

1.10.2. Radiometric attenuation

Radiation based strategies have been widely reported for non-intrusive in-line analysis of powder flow measurement. Radiometric sensors utilise a number of beams transmitted from a radioactive source, i.e. x or γ-rays (Yan 1996), which traverse the cross-sectional area of a pipe and interact with a single or multi-element detector. Generally, these sensors operate on the

principle of attenuation of radioactive waves, which obeys the Beer-Lambert law (Equation 12), where I and I_0 represents the intensity of the incident and transmitted waves, x is the thickness of material that passes through the waves and μ is a linear attenuation coefficient (Barratt, et al. 2000; Yan 1996).

$$I = I_0 e^{-\mu x} \qquad \text{(Equation 12)}$$

Flowing particles can attenuate the beam elements when they cross their path, thus interfering with the overall beam intensity detected by the element detectors. The degree of attenuation is proportional to the total solids thickness, from which the chordal solids fraction β_c and the projected cross-sectional area A_c may be derived. The particle velocity V can be calculated by applying a cross-correlation algorithm to two signals induced by the flow of powder generated by two sensors arranged in series (Fig. 1-7). Finally, the mass flow rate μ may be inferred from the product of the chordal solids fraction, projected cross sectional area, true density of the powder ρ and V (Equation 11).

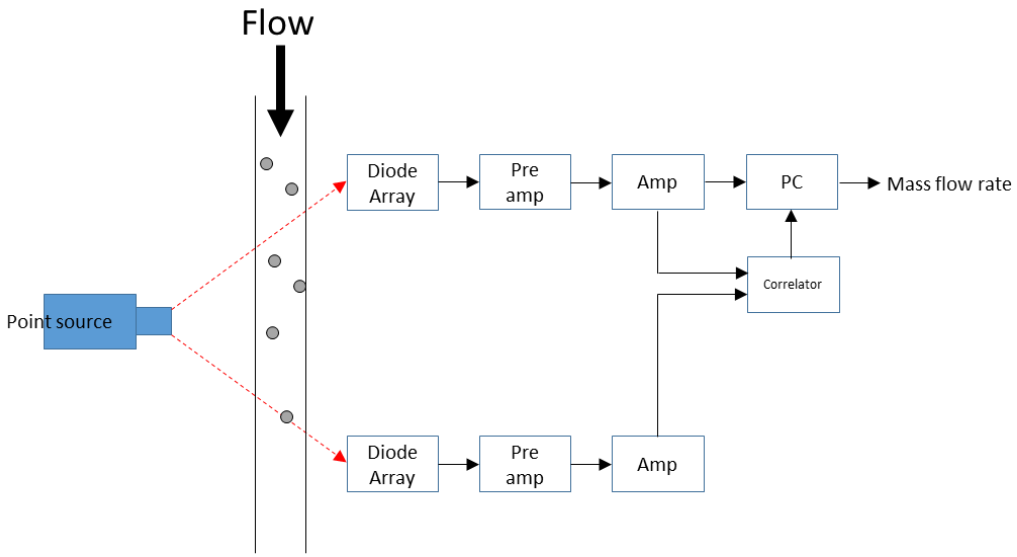

Fig. 1-7. Radiometric attenuation concept, adapted from (Barratt, et al. 2000).

Barratt, et al. (2000), used a radiometric sensor array to determine the mass flow rate of particles across four different locations within a pneumatic conveyor (Barratt, et al. 2000). The authors were able to detect fluctuations in the particle mass flow rate which was thought to be influenced by the changes in the particle flow dynamics between each location within the

conveyor pipeline. Although, in some cases, the mass flow rate was underestimated by a maximum value of 26 %. The authors attributed this to a degree of uncertainty in both solids fraction and velocity measurements. The former was thought to be induced by the in-homogeneity in the flow regime as well as the presence of dynamic bias. On the other hand, the latter was impacted poor signal modulation induced by dilute phase flows as well as the presence of a roping flow regime, which implied that the particle velocity was not consistent between both sensors. In fact, the accommodation towards in-homogenous flow distribution has been identified as the most prominent issue when integrating this technology for in-line flow measurement (Yan 1996). It has been suggested the system may be able to compensate for an in-homogenous flow distribution by increasing the number of beams within the sensor, thus facilitating an increased interrogation surface area. However, this would impose further costs on an already expensive piece of equipment (Yan 1996).

1.10.3.Microwave attenuation

Microwave attenuation is similar in principle to radiometric attenuation but instead utilises a microwave transmitter and receiver (Fig. 1-8), with solids flow producing an attenuation effect on the transmitted microwave signal (Yan 1996). Pang, et al. (2018), explored in-line mass flow measurement of powder delivered from a silo. The mass flow rate was inferred using (Equation 11), where the solids concentration was derived from the attenuation of microwaves due to the particle flow and the powder velocity was determined based on the Doppler shift in microwaves frequency due to their reflection off particles (Pang, et al. 2018). The technique was described applicable to both steady and un-steady flow regimes with relative deviation in the latter reported as high as 5.51 %. Although, the authors did highlight a few downsides to the technique. Firstly, high density flows reflected the majority of microwaves, resulting in a plateau effect between the current output and the predicted mass flow rate. The attenuation properties of the particles were also shown to be impacted by particle size and permittivity characteristics of the materials. Particles size > 706 µm resulted in a deviation > 50 % between the predicted and actual mass flow rate. This deviation also doubled in value for particles > 1563 µm. To prevent this effect, the authors suggested avoiding particle sizes significantly greater than the wavelength of the microwaves. Although many pharmaceutical powders tend to not possess particle sizes within the size range reported in this article, many cohesive powders do possess high agglomeration tendencies which may artificially induce a similar deviation effect. Finally, attenuation characteristics can also be impacted by fouling of the access port required for the microwave source to interrogate the powder flow (Yan 1996).

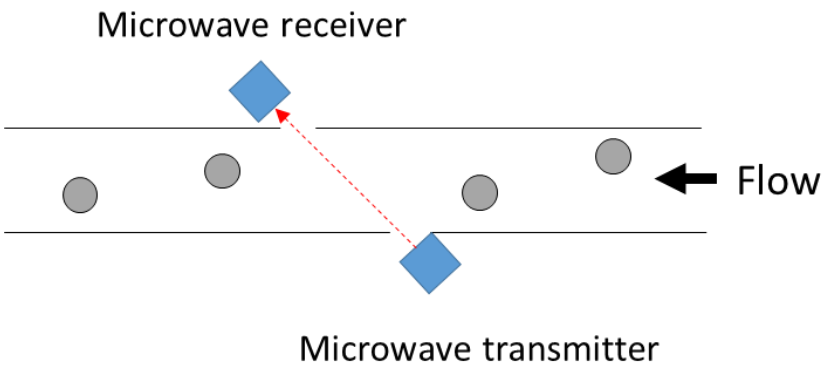

Fig. 1-8. Microwave attenuation concept, adapted from (Yan 1996).

1.10.4. Acoustic emission/attenuation

Acoustic emission technique involves the measurement of sound waves generated due to the impingement of flowing particles against each other and the walls of the equipment (Ruiz-Carcel, et al. 2018). Different types of particle interactions such as friction, impact and rolling produce characteristic high-frequency sound waves (Whiting, et al. 2018), which in turn are detected by acoustic emission sensors or microphones (Fig. 1-9). The intensity of the recorded sound waves can then be attributed to the powder mass flow rate (Ruiz-Carcel, et al. 2018), or the powder flow regime (Albion, et al. 2007).

Ruiz-Carcel, et al. (2018), estimated the mass flow rate of screw conveyed powders based on the sound characteristics extracted from the envelope of acoustic signals recorded using an acoustic emission sensor (Ruiz-Carcel, et al. 2018). Generalised norms (RMS signal) extracted from these envelopes at 2 second intervals were shown to correlate well with the conveying powder mass flow rate, with average errors reported no higher than 2.12 %. Also, the authors developed a density dependant calibration model based the generalised norms, intended to act as a universal model for the prediction of powder mass flow rate irrespective of the powder density and flow regime. This model reportedly produced accurate results for the range of densities tested, although further study was required in order to ascertain whether the model was also accurate for powder densities outside the tested range. Although, some disadvantages noted by the authors are given as follows. Firstly, very small particles < 25 µm are challenging to measure using this technique since they do not induce strong acoustic emission. Additionally, powder occlusion in the feeder can impact the transmission path, thus altering the acoustic characteristics of the impinging powders. Moreover, cohesive powders

can impact the screw filling properties which can lead to overestimation or underestimation in the mass flow rate. Depending on the process, occlusion and cohesion phenomena may be unavoidable when handling cohesive powders, which may limit the applicability of this technology.

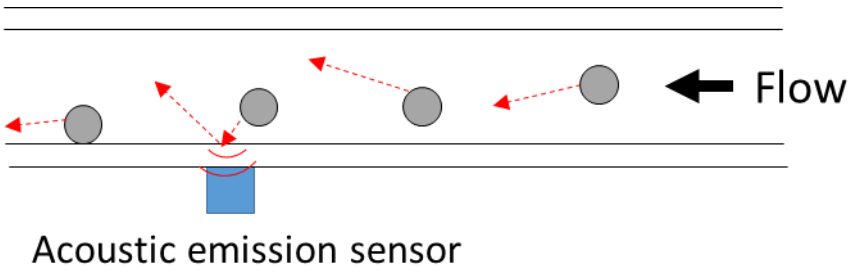

Fig. 1-9. Acoustic emission sensor concept.

Powder flow measurements may also be determined via acoustic attenuation principle. In this configuration, an acoustic source is positioned on the external wall of pipe which transmits a sound wave to a transducer located on the opposite wall. When powders pass through the sound wave, they induce an attenuating effect which can roughly be attributed to their concentration (Tallon and Davis 1997; Yan 1996). Tallon and Davis (1997), attempted to determine the powder mass flow rate μ of a pneumatically conveyed powder which was inferred from the solids concentration β_c measured via acoustic attenuation (based on the Beer-Lambert law), the solids velocity V obtained from cross-correlation of acoustic signals obtained from two microphones in series, the pipe area A_c and the solids density ρ (Equation 11), (Tallon and Davis 1997). The authors were able to establish a linear relationship between the attenuation coefficient and the powder mass flow rate, although they reported a 10 % difference in the attenuation relationship depending on the positioning of the microphones. Compared to acoustic emission, acoustic attenuation applications are frequently less reported, having been suggested only suitable in obtaining a relative measurement of solids concentration (Yan 1996). This is due to the dependency of the attenuation characteristics on consistent powder velocity and particle sizes, which could prove problematic for powders with wide particle size distributions and/or unstable flow regimes.

1.10.5. Digital imaging

Digital cameras have been used to measure in-line powder flow properties. In practice, a thin section of the powder flow stream is illuminated using a laser and detected using the digital camera which accesses the flow through a transparent port (Fig. 1-10). Through image processing, the number of pixels which comprise a single particle are counted to yield the equivalent diameter of each particle. The volumetric concentration of the flowing particles is determined from the pixels representing present powder flow within a cross-sectional slice and expressed as a percentage of the pixels present within the completed image (Qian, et al. 2015). It is also possible to quantify the particle size distribution within flowing solids (Carter, et al. 2005; Qian, et al. 2015), which may prove useful in determining potential deviations in the particle size due to interactions with the process flow mechanism. A few limitations regarding this technology have been identified by Carter, et al. (2005). Firstly, it is challenging for digital cameras to discriminate between particles when their concentration is high. This results in particle overlapping which may develop uncertainties in the measured particle size or count. Like NIR, digital cameras require the transparent port or window so that the camera may interrogate the flow. Not only does this require additional modification to be made to pipework but the port is also susceptible to fouling. However, this may be prevented by integrating an air purging system into the process (Qian, et al. 2015).

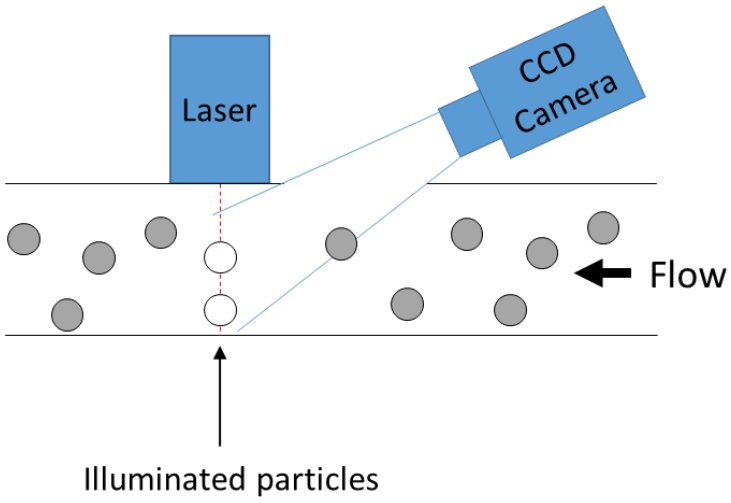

Fig. 1-10. Digital imaging concept, adapted from (Carter, et al. 2005).

1.10.6. Capacitance sensors

Capacitance sensors are a non-intrusive electrical based methodology which characterises the powder flow based on the material di-electric properties. These sensors are simple in structure (Yan 1996), typically comprising of two or more electrodes which span wall of a pipe. When particles enter the sensing region of the sensor, they induce a change in capacitance C by a magnitude which is directly or indirectly proportional to the solids' concentration (Li, Jian, et al. 2015; Yan 1996). The relationship is described by (Equation 13), where ε_0 is the permittivity of free space, ε is the permittivity of the powder, whereas A_p and d represent the area and separation distance of the electrodes respectively (Yan 1996; Yanagida, et al. 2000).

$$C = \varepsilon_0 \varepsilon A_p / d \qquad \text{(Equation 13)}$$

Capacitance sensors have been used to measure solids concentration in different flow regimes including: for powders conveyed within a pneumatic hose (Li, J., et al. 2015; Yanagida, et al. 2000); pneumatic flow regimes (Li, et al. 2015); and fluidised bed dryers (Tortora, et al. 2004; Wiesendorf and Werther 2000). These technologies are attractive since they are low in cost and can be easily integrated without major modifications required to be made to the pipework (Yan 1996), although they must be calibrated to the pipe material (Li, et al. 2015). Capacitance sensors tend to be disadvantaged by an in-homogeneous distribution in spatial sensitivity, which can result in measurement errors (Li, et al. 2015; Yan 1996). Baseline drift in the measuring circuit may occur due to fluctuations in the temperature and moisture (Hu, et al. 2006). Also, measurement errors may occur due to the fouling of the sensor, as well as the presence of an in-homogeneous solids' distribution (Hu, et al. 2006; Yan 1996).

Hu, et al. (2006), studied a number of approaches to improve the robustness of a capacitance-based technique by designing an array of multiple capacitance sensors with aim of improving the homogeneity in the spatial sensitivity, so as to reduce the impact of solids distribution in-homogeneity (Hu, et al. 2006). Moreover, the authors developed a measuring circuit based on correlated double sample technique, which reduced the baseline drift induced by temperature and moisture changes. A ± 5% linearity was reported between the predicted mass flow rate derived from the solids concentration and the actual mass flow rate, at different experimental temperatures (40 °C and 100 °C) and different material moisture contents (1 and 1.5 %).

1.10.7. Electrical capacitance tomography (ECT)

Electrical capacitance tomography (ECT) analyses the permittivity distribution induced by flowing solids. The sensor typically comprises of multiple capacitance electrodes which span the diameter of a pipe. Like capacitance sensors, ECT sensors respond to powder flow due to change in capacitance within their sensing region, however, the capacitance changes are converted to voltage signals which are then transferred to a computer. Image reconstruction techniques are then applied in order to analyse the permittivity distribution due to the solids flow across the cross-sectional area of the sensing region (see Fig. 1-11), (Sun, et al. 2008). These tomographic images are divided into a set of pixels, with each representing a solids concentration region. The average value of these pixels is equivalent to the overall volumetric solids concentration for that cross-section (Sun, et al. 2008).

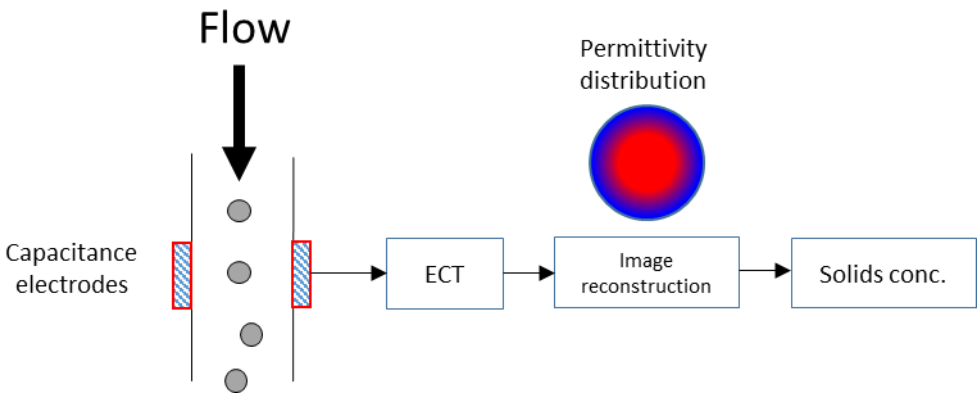

Fig. 1-11. ECT sensor concept, adapted from (Sun, et al. 2008).

Jaworski and Dyakowski (2001), investigated the morphology of dense phase pneumatic flow regimes using two ECT sensors, in which they were able to qualify the flow pattern, including the presence of phenomena such slug flow (Jaworski and Dyakowski 2001). The powder mass flow rate was also quantified (Equation 11), where the solids concentration was derived from the permittivity distribution and the solids velocity was derived via cross-correlation. ECT sensors benefit from a simple structure and low cost (Sun, et al. 2008). However, like capacitance sensors, they suffer from poor spatial sensitivity and susceptibility to in-homogeneous solids' distributions (Sun, et al. 2008). Additional disadvantages include the inability to interrogate small volume flows and the limited spatial resolution of images due to averaging across the finite length of the electrodes (Jaworski and Dyakowski 2001).

1.10.8. Electrostatic sensors for the measurement of powder flow characteristics

Electrostatic-induction or electrostatic sensors are a widely applied and researched type of flow technology whose measurement principle is based on the triboelectrification of particles developed under the conditions of flow (Coombes and Yan 2015). When the electrified particles move into close proximity to that of an electrode, the electric field generated by their surface charges capacitively induces the flow of current on the electrode. This current is then detected via external measurement electronics, which typically comprises of a transimpedance amplifier (that acts as an A/D converter), as well as a data-acquisition device (Fig. 1-12). This current is converted into a voltage signal where it is digitised and stored inside a computer (Li, et al. 2015). The signal magnitude will be sensitive to input variables which influence a powder's in-process charging. These include moisture content, particle size distribution, particle shape, as well as factors related to the processing equipment such as surface roughness (Qian, et al. 2012).

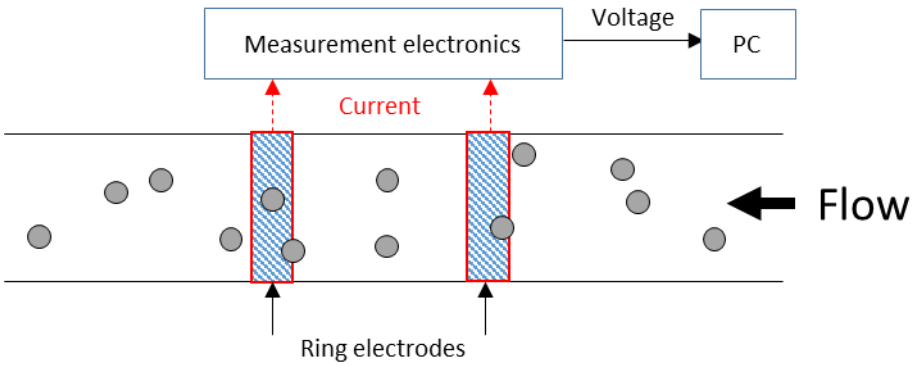

Fig. 1-12. Electrostatic sensor concept, adapted from (Carter, et al. 2005).

Electrostatic sensors are a promising flow technology given their low cost, simplistic structure, ease of installation, non-intrusive nature and capacity for rapid data acquisition. Additionally, the signal output is resistant to any powder accumulation to the electrodes, meaning that no cleaning protocol is required (Qian, et al. 2014; Yan 1996). Although, it should be acknowledged that the technology is not without its disadvantages. Like the capacitance sensor, electrostatic sensors also possess an in-homogeneous spatial sensitivity and are impacted by non-uniform solids' distributions. In these instances, powders which traverse

nearer to the electrode wall will induce a stronger current, whereas the opposite is true for those that traverse within the centre of the cross-sectional sensing region, leading to flow rate over/under-estimations (Qian, et al. 2012). In addition, the induced current is also highly sensitive to the material properties which impact the powder's charging capacity. Consequently, the unpredictability in the powder's charging behaviour can induce variability in the measured flow parameters (Carter, et al. 2005). Regardless, it remains one of the most widely researched technology due to its capacity for in-line measurement of solids' concentration, mass flow rate and velocity flow parameters.

Solids concentration measurements using electrostatic sensors are occasionally reported within literature. This parameter is typically derived from the overall charge detected by the electrostatic sensor at any given time, usually via the root-mean-square (RMS) of the electrostatic signal (Coombes and Yan 2015). In theory, the RMS is proportional to the concentration of particles within the sensing region provided that the material properties which impact charge remain consistent (Carter, et al. 2005). However, due to the unpredictable nature of the powder charging properties, it is generally considered impossible to quantify the solids concentration based on the RMS signal alone (Coombes and Yan 2015). Regardless, a relative solids concentration can provide qualitative information on behaviour such as the flow regime and the solids distribution.

The geometry of the electrodes is important in defining the relative solids concentration. Arc-shaped electrodes interrogate a smaller but localised region within the cross-section of a pipe, but when combined to form a circular array, the distribution in the solids concentration can be analysed (Li, et al. 2015). On the other hand, ring shaped electrodes interrogate a larger cross-sectional area and are thus able to detect more charges. However, this only provides a relative measurement of the overall solids concentration as opposed to a distribution (Li, et al. 2015).

Unfortunately, the inconsistent relationship between charge and solids concentration is also translated to the powder mass flow rate (Carter, et al. 2005). Although, Qian, et al. (2014), utilised an electrostatic sensor array for the in-line metering of pulverised fuel flow rate within pneumatic flows (Qian, et al. 2014). The solids concentration was inferred from the electrostatic signal RMS, which when combined with the velocity measurement, the powder mass flow rate was derived (Equation 11). The authors initially evaluated the performance of the technique using a lab-scale pneumatic conveyor, where they reported -9 to 6.6 % in errors between the predicted and reference mass flow rate. Following this, the authors integrated

the technology into a power plant in which they monitored the mass flow rate, velocity and fuel distribution over the course of 24 hours. As well, the response of mass flow rate and velocity to the fluctuations in coal loadings which occurred during a specific time-frame were also observed. Although, it is important to note that the authors did not evaluate the predicted mass flow rate against the true mass flow rate within the powder plant trials. Another concern is related to the geometry of the electrodes used within the sensor array, which were arc-shaped. These types of sensors yield flow information generated within localised regions of the pipeline, although their individual sensing regions do not tend span a large cross-sectional area of the pipe, meaning that there may have been regions present in which the powder flow lay undetected.

On the other hand, velocity measurements are perhaps the most widely reported of electrostatic based in-line applications. These measurements are achieved using an electrostatic sensor array containing two or more electrodes. When particles flow past both electrodes in succession, an electrostatic signal is generated for each, which should be nearly identical in nature but slightly displaced by a function of time. Cross-correlation algorithms can be applied in order to determine the degree of similarity between both signals, indicated by a correlation coefficient expressed as a function of time. The time value corresponding to maximum the cross-correlation coefficient will be indicative of the relative time delay between both signals τ_m at maximum similarity. The velocity V_c of the flowing particles can then be determined by taking the ratio of the electrode separation distance L to the time lag (Equation 14), (Coombes and Yan 2015).

$$V_c = \frac{L}{\tau_m} \qquad \text{(Equation 14)}$$

Electrostatic sensor velocity measurements are robust since the signal time delay is immune to factors such as moisture variation. As such, these measurements have enjoyed a wide degree of application, particularly for the characterisation of particle velocity in pneumatic conveyed pulverised fuel within the powder industry (Coombes and Yan 2015). Since velocity measurements have been studied extensively for many years, recent studies have focused on to optimising the sensor and/or measurement-electronics system design, in order to improve the accuracy and reproducibility in results. A number of these applications have been reviewed below.

Coombes and Yan (2015), studied the powder velocity of pneumatically conveyed powders within a vertical and a horizontal pipeline (Coombes and Yan 2015). The authors utilised a unique type of electrostatic array which spanned the diameter of the pipeline, thus enabling measurements across the entire cross-sectional area of the powder velocity as well as relative powder concentration (attributed to the RMS of the electrostatic signal). This sensor configuration was able to: determine the flow distribution across the cross-section of the pipe; determine the stability in the flow based on the correlation coefficient; and detect presiding flow regimes such as roping flow. Although, there is a concern regarding the intrusive nature of this technology. Since the authors only measured dilute phase flows, there was a lower tendency for the natural flow regime to be impeded. However, this would not likely be true for dense phase flows.

Qian, et al. (2012), also measured the solids concentration and velocity of pneumatically conveyed pulverised fuel, whilst attempting to tackle some of the roadblocks involved with velocity measurements, primarily the applicability to in-homogeneous solid distribution and the ability to accuracy determine discrete changes in velocity (Qian, et al. 2012). To this end, the authors developed two four-sensor arrays (arc and ring types), which were able to yield six velocity values via correlation computation and then combined to yield a final velocity via data fusion technique. Data fusion was shown to improve the consistency in the measured solids velocity, although this came at the cost of increasing the complexity in the sensor structure and measurement system, which can complicate the modification of the pipework and thus incur additional costs. Also, given that the velocity was acquired during post-processing, there was no comment on whether the data fusion technique would increase the processing time when determining the velocity parameter. This would be critical since near-instantaneous presentation of data is required for real-time measurement of powder flow. Finally, no comment was made on the size of the datasets used for cross-correlation.

Li, et al. (2015), compared the differences in velocity and concentration profiles of pneumatically conveyed particles detected within local regions and across the pipe cross-section, achieved using arc array and ring electrode sensors respectively (Li, et al. 2015). The arc electrodes were able to interrogate the flow of particles when they traverse within their localised sensing region, which enabled analysis of the powder velocity distributed across the pipe-cross section. This was particularly valuable in the instances when in-homogeneous solids distribution was present. Although the authors were unable to identify the differences in

charge distribution due the low sensing volume of the individual arc sensors, they were able to reliably determine the velocity (since cross-correlation coefficient > 0.85), the velocity distribution and even detect the presence of unstable flow regime in some cases. The mean velocity results for the ring sensor were considerably higher which was facilitated by a larger sensing area. Although, these results were considered more accurate (indicated by a cross-correlation coefficient > 0.9), due to higher degree of flow interrogation. From this study, it was clear that both types of sensors possessed their respective strengths and drawbacks, although from the perspective of a pharmaceutical application, it appears a ring sensor may be more beneficial as the increased degree of interrogation facilitates higher accuracy velocity measurements. Moreover, flow stability identification may not be a major issue simply because pharmaceutical flows regimes do not typically utilise pneumatic flow regimes, aside from fluidised bed dryers. Also, any interruptions to flow would be easily identifiable by changes to the charge signal.

Since electrostatic sensors have proven to be a reliable method in determining the in-line powder velocity, they have been combined with technologies which are able to independently measure the solids concentration, so that the in-line mass flow rate may be inferred.

Li, et al. (2015), utilised an integrated capacitance-electrostatic sensor in order to predict the mass flow rate of particles conveyed in dilute phase (up to 8 % concentration), via inferential technique (Equation 11), (Li, et al. 2015). The authors utilised a helical capacitance sensor in order to obtain an improved spatial sensitivity. Calibrations were performed on particle flows carried on a conveyor belt and within a gravitational rig delivered from a silo. Measurement errors between the predicted and actual mass flow rate ranged from -2 to 4 % for the conveyor belt and -3 to 8 % within the gravitational rig. Although, the increased error observed in the latter equipment was attributed to velocity overestimation due to the configuration of the electrostatic sensors which were displaced by a considerable distance. As a result, the powder was thought to accelerate between these two points resulting in an averaging effect on the velocity measurement. The authors do state that this problem can be resolved by installing electrode pairs at both points, thus reducing the electrode separation distance and yielding a more representative velocity measurement. Regardless, the increase in the error was not considered substantial.

Sun, et al. (2008), inferred the mass flow rate of pneumatically conveyed solids (Equation 11), via integrated ECT-electrostatic sensor measurement of solids concentration and velocity

respectfully (Sun, et al. 2008). The predicted mass flow rate measurements were reported with errors no higher than 5 %. However, it should be noted that the authors utilised a cyclone separator to redistribute the solids towards the capacitance sensor wall as a means to compensate for its poor spatial sensitivity, which may not be applicable in all processes.

Wang, S., et al. (2016), performed a two-part study in which they developed an optimised ECT-electrostatic sensor design for the localised measurement of powder flow rate, velocity and solids concentration (Wang, S., et al. 2016). This was achieved via simulation experiments using three different flow regimes (core, stratified and annular flow). The authors then obtained experimental measurements of the flow parameters in response to 'frozen rope' flow induced using a moving conveyor belt. Localised solids concentration measurements were predicted with errors < 10.43 %, local solids velocity was predicted with standard deviations than 0.42 and the relative error in the measured vs a reference solids mass flow ranged from -19.6 to 14.9 %. It is important to mention that these measurements were not performed using real powders, therefore applicability of the technique to in-line flows can still be considered an uncertainty.

Carter, et al. (2005), measured the in-line solids concentration and velocity measurements obtained using combined digital camera and electrostatic sensor technique in order to infer the powder mass flow rate (Equation 11), (Carter, et al. 2005). The errors in the predicted mass flow rate were reported no greater than 6 %, although it should be noted that these were performed on dilute phases using concentrations no greater than 2 % of the total volume. The authors do state that densified flows > 3 % in concentration would result in overlapping of particles, resulting in overestimation of the particle solids concentration. This could be problematic within a pharmaceutical sitting since many related processes typically involve flows with higher volumetric concentrations (e.g. hopper flow). It is also uncertain whether cohesive effects such as agglomeration may also result in similar particle overlapping issues at all.

1.10.9. Electrostatic sensors for the measurement of powder charging characteristics

Electrostatic sensors have also been reported in characterisation of the charging behaviour of powders whilst under the conditions of flow. Typically, the powder charge is indicated by the relative amplitude or RMS of the electrostatic signal (Gao, et al. 2018). Compared to the Faraday Cup, the electrostatic sensor is able to monitor the charge as a continuous parameter across a batch of particles without impeding or altering the nature of the flow regime (Zhang, Wenbiao, et al. 2018), rendering it perfectly suitable to capturing the charging behaviour induced only by the process. However, it is important to note that unlike the Faraday Cup, the electrostatic sensor is only able to measure the relative powder charge for a number of reasons: a) the sensor does not discharge the powder during measurement; b) the sensor possess an in-homogeneous spatial sensitivity; and c) the induced charge is amplified via the measurement electronics. However, as a trade-off, the electrostatic sensor possesses a somewhat unique capacity to detect the onset and progression of dynamic charging phenomena. Compared to flow applications, in-line charge analysis via electrostatic sensors are less commonly reported. Regardless, the few articles describing these applications have been reviewed below.

Hussain, et al. (2013), have used an electrostatic sensor to characterise the bipolar charging on different particulate materials (Hussain, et al. 2013). The authors initially charged the powders within a plastic container that was exposed to a vibration source, after which they carefully deposited the particles on an individual basis whilst recording the electrostatic charge. The charging trends in glass beads, PVA1600, silica sand and olivine sand were shown to agree with reference triboelectric series. Moreover, the charge and polarity distribution in glass bead/PVA1600 and silica sand/olivine sand blends were also characterised. Although bipolar charge measurement is certainly valuable, it is unlikely that this methodology is applicable for in-line use. This is because particles tend to flow in clusters or streams, meaning their measured net charges may result from them compounding together or even neutralising each other. It is also unfeasible to introduce a methodology for separating the particles since it could disturb the flow and induce further charging. In relation to this statement, the author's use of a vibratory feeder may very well have contributed to the measured charges on the particles.

Gao, et al. (2018), characterised the pulverised coal charging behaviour (indicated by the RMS signal) and flow regime within a pneumatic conveyor, using a combined electrostatic-ECT sensor (Gao, et al. 2018). Furthermore, two different conveying gaseous media were utilised in this study: carbon dioxide and nitrogen. Different conditions in the laminar flow were induced based on the input conveying pressure. The authors found that the charge intensity of the fuel was dependant on the conveying pressure and permeability to the conveying gas. At lower pressures, the pulverised coal was shown to charge more in carbon dioxide compared nitrogen. On the other hand, at higher pressures, the coal was shown to charge more intensely in nitrogen. Since the coal was more permeable to carbon dioxide, it possessed a higher tendency to disperse at higher conveying pressures, thus reducing the number of collisions. Due to the reduced permeability of the coal to nitrogen, the particles flowed in closer proximity with regards to one another, resulting in an increased number of collisions. The authors also found that the RMS was negatively correlated with the change in volume concentration, although this was more prominent in carbon dioxide than nitrogen. This article clearly shows the impact of the flow conditions nature on the powder charging behaviour, although the authors have only performed these measurements using a single material and have not yet explored the impact of other material properties and environmental conditions.

Zhang, et al. (2018), investigated the powder charging (using the RMS signal) in response to change in moisture content due to fluidised bed drying (Zhang, et al. 2018). The authors utilised an arc electrode array to measure the charge and velocity of hydrated powders within a localised region of the fluidised bed dryer at different air velocities. Samples were periodically removed from the equipment and their moisture content was determined using a halogen moisture balance. The authors identified a negative correlation between the powder charge and moisture content until the latter equilibrated. After this point, the powder began losing charge. A model was then developed which predicted the value of the in-line moisture content via the RMS signal, and two coefficients related to the powder velocity. Using this model, the authors were able to predict the in-line moisture content within ±15 % to that of the sampled moisture content. This study was valuable since it provided further insight into the powder charging trends in response to the change in moisture under these specific drying conditions, which otherwise would be difficult to characterise using a Faraday Cup. There is also a potential for the development of an in-line moisture content meter, although applicability to non-fluidised bed process is currently unknown.

Shi, et al. (2017), investigated the effect of powder charging behaviour on particle motions as well as the capacity to characterise particle charge to mass ratios using an arc electrode array within fluidised beds (Shi, et al. 2017). Using a liquid anti-static agent, the authors were able to vary the level of powder charge between experiments. Geldart B and D particles were shown to reduce in velocity by 26 % and 50 % respectively in response to powders charging to a saturated level. The loss in velocity was attributed to electrostatic attraction between particles. Moreover, the authors characterised the charge to mass ratio of the particles at different velocities and compared them to on-line charge measurements using a Faraday Cup, where both parameters showed a positive correlation. The authors reported errors between the charge to mass ratio measurements at no greater than 40 %, which was attributed to two factors: a) Faraday Cup sampling method was thought to induce additional charging on the powders; and b) the Faraday measurements were only sampled within a localised region, whereas the electrostatic sensor interrogated a large cross-sectional area. It is important to note that charge to mass ratio measurements obtained using the electrostatic sensor were derived from a relative solids concentration measurement, therefore there may be a degree of uncertainty in the authors results which would have been dependent on how the particles were distributed within the sensing region. In relation to this statement, the authors did not comment on the spatial sensitivity of their arc shaped electrodes.

1.11. Gaps in the knowledge

The value of PAT and electrostatic sensors for powder flow parameter analysis has already been emphasised within this literature review, although it is evident that many applications described have been towards pneumatic conveying processes using materials relevant to the power industry. Pharmaceutical processes tend to incorporate a broader range of shear and packing conditions which in turn yield different flow regimes. Common examples include dense phase hopper flow, dense phase intermittent through via dosing valve, lean phase screw feeder flow, fluidised bed flow, etc. Moreover, the types of powders and blends handled in pharmaceutical process spans a more extensive range of material and flow properties than those typically used in the power industry. Therefore, it is critical that the flow behaviours developed within these systems are fully understood to facilitate formulation and process design. However, to the author's best knowledge, electrostatic sensors have not yet been integrated for a pharmaceutical flow application.

Accounts of charge measurements of pharmaceutical powders have been reported (Šupuk, et al. 2012), although in almost all cases these were not performed in tandem with representative in-process charging conditions and were characterised using a Faraday Cup whose disadvantages have already outlined. In comparison to the Faraday Cup method, applications of electrostatic sensors for in-line powder charge measurement have rarely been reported except in fluidised bed dryers (Shi, et al. 2017; Zhang, et al. 2018) and pneumatic flow regimes (Gao, et al. 2018). So far, electrostatic sensors are one of the only in-line technologies which have demonstrated the capacity to characterise for both real-time flow and charge measurement simultaneously. From a PAT standpoint, the technology is attractive given its cost-effectiveness, simple structure, non-intrusiveness, ease of installation and robustness of the signal output to fouling (Qian, et al. 2014; Yan 1996). There is also an added research and developmental value to this technology in the facilitation and expansion upon the understanding of flow and charging characteristics that occur in process.

1.1. Aims, objectives and thesis structure

The aim of this work was to study the in-line flow and charging characteristics using an electrostatic powder flow sensor (EPFS) of powders conveyed under different flow regimes. Patterns present within the electrostatic signal were extracted, analysed and then used to ascertain the specific in-line flow properties / behaviour exhibited by the powder under the different shear conditions. The study objectives are defined below.

- Determine the relationship between the RMS of the electrostatic signal / powder velocity against the powder mass flow measured in-line under different flow conditions and in turn assess the feasibility of a calibration between the two parameters.
- Investigate the relationship between the powder flow pattern and the cohesivity of the flow powders using Fast-Fourier Transformation (FFT) algorithms.
- Assess the in-line charging behaviour exhibited by a number of pharmaceutical powders when conveyed using a twin-screw feeder.
- Study the hopper flow behaviour exhibited by blends with variable levels of cohesivity during the operation of a tabletting process.

The thesis structure is set out below. Chapters 4 through 6 have been drafted as papers for future publication, but have been adapted to the formatting of this thesis.

Chapter 1 – Introduction

Chapter 2 – Technology overview

Chapter 3 – Feasibility study for predicting in-line powder mass flow rate from electrostatic flow parameters using an electrostatic powder flow sensor (EPFS).

Chapter 4 – Qualitative determination of powder cohesivity by means of an electrostatic powder flow sensor (EPFS) coupled with Fast-Fourier-Transform (FFT) algorithms.

Chapter 5 – Investigation into the relative charging characteristics of a number of screw-conveyed pharmaceutical powders using an in-line Electrostatic Powder Flow Sensor (EPFS).

Chapter 6 – A first look into the application of an electrostatic powder flow sensor (EPFS) for the qualitative study of intermittent flow regime typically present within dense phase gravitational flows such as tablet press hoppers.

Chapter 7 – General discussion and conclusions

Chapter 2. Technology overview:

2.1. Description of the EPFS technology and the external circuit

The EPFS technology consists of a sensing element which is housed within a 100 mm diameter industrial-scale stainless-steel pipe (Fig. 2-1). The pipe has been modified using flanges in order to accommodate the sensing element as well as two SMA bulkheads (which sit on opposite ends on the exterior of the top flange) which connect to an external circuit. The sensing element is comprised of two enamelled copper wires, shaped to form rings 100 mm in diameter. Each electrode is housed within an individual plastic (acetal) ring which lie flush against the interior wall of the stainless-steel pipe, where they are separated with respect to another by an approximate height of 15 mm. Each SMA bulkhead is connected to a single electrode. These connections are isolated from external environment using a brass sheath in order to protect them from dust accumulation.

In this project, two additional EPFS' are used depending on the powder flow application (Fig. 2-2). The dimensions of these EPFS are scaled down in their diameter with respect to that of the industrial-scale EPFS. Although, it is important to note that the electrode spacing length is kept consistent between each design (± 1 mm). The second version of the EPFS possesses an interior wall and electrode ring diameter of 19.1 mm and is designed to attach to the base of a pipe so that it may interrogate dense phase gravitational flow. The third EPFS possess an interior wall and enamelled copper wire (Rowan Cable Products Ltd), shaped into a ring electrode to form an internal diameter of ~ 28 mm. The electrode separation distance for this electrode was slightly smaller at 14 mm, although this was not considered critical since cross-correlation work was not performed using these related outputs. This sensor interfaces a tablet press hopper and feeder.

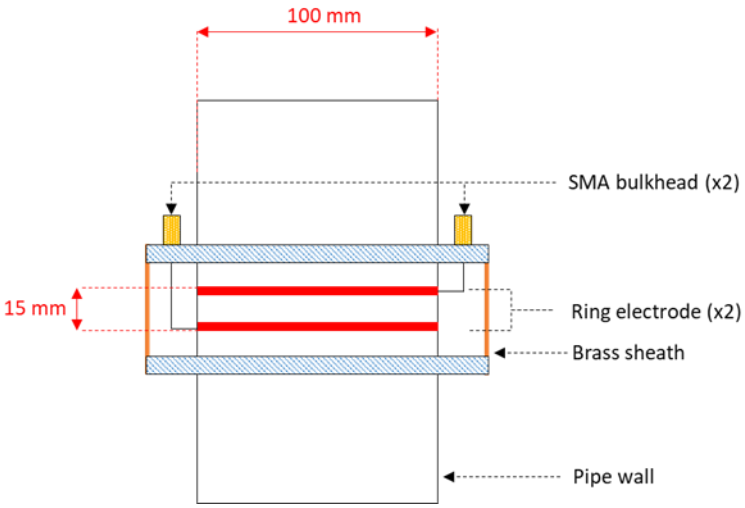

Fig. 2-1. General schematic of the industrial-scale EPFS structure.

Fig. 2-2. a) Industrial-scale EPFS; b) lab-scale EPFS; c) tablet press hopper EPFS.

The EPFS connects to the aforementioned external circuit (Fig. 2-3). This consists of a highly sensitive two-channel transimpedance amplifier (TIA), (Lyosense, De Montfort University) which functions as both a power supply and a current to voltage converter with amplification properties. The TIA is then connected to a data acquisition device (DAQ) (Model N° NI-USB-6212, National Instruments, United Kingdom), which then connects via USB to a PC with the appropriate hardware driver installed (NI-DAQmx Core Runtime 9.7.5, National Instruments).

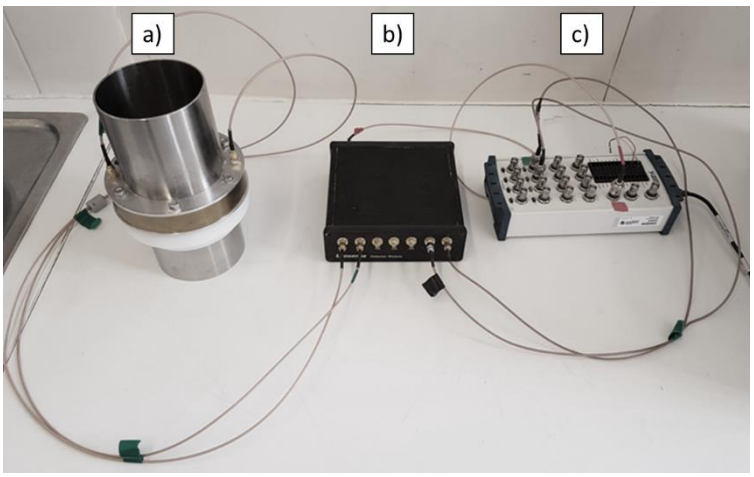

Fig. 2-3. EPFS and external circuitry including a) EPFS; b) TIA; and c) DAQ.

The overall measurement system is completed by an electronic balance (Excellence, Model XS2002S, Mettler Toledo) (Fig. 2-4), used to capture the weight of flowing powder or tablets. The balance is based off a solid-state sensor and therefore has an instantaneous response time.

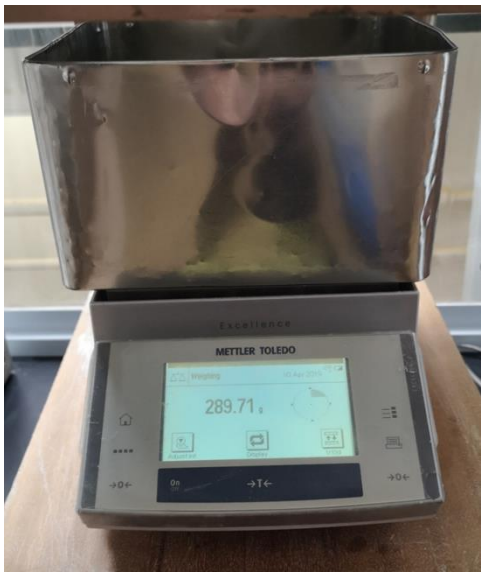

Fig. 2-4. Mettler Toledo balance with mounted container.

2.2. Principle of operation

The operation of the EPFS technology is based on the fluctuation in current which is induced by the movement of charges present on the surface of particles as they pass within the vicinity of the electrode pair. There exists a sensing volume or region adjacent to the immediate

proximity of each electrode where they are responsive to the moving charges (Ma and Yan 2000). If for example, a positively charged particle enters this sensing region, its electric field will induce the flow of electrons (current) via capacitive induction. These will be attracted from the external circuit towards the electrode and in doing so forming a negative bias (voltage) on the latter (Ma and Yan 2000). The current and voltage generated due to charges moving into the sensing region and reaching the same horizontal plane as the electrode is illustrated by wave "A" in Fig. 2-5. However, since the particle is under the conditions of flow, these events are only transient. As the particle leaves the sensing region, the current flows in the opposite direction, the voltage is discharged and the circuit is returned to its neutral state (illustrated by signal "B" in Fig. 2-5). The induced current and voltage are directly proportional to the net charges present within the sensing region. Moreover, for a single measurement of net charge, a positive and negative fluctuation will be present within the current response due to the aforementioned charging and discharging behaviour (Ma and Yan 2000). The spatial sensitivity of the electrodes will be dependent on its geometry (Qian, et al. 2012). For the EPFS, the electrode geometry and thus the degree of sensitivity were not studied in-depth. However, it can be confirmed that the EPFS is sensitive to particles traversing the centre of the cross-section and the walls.

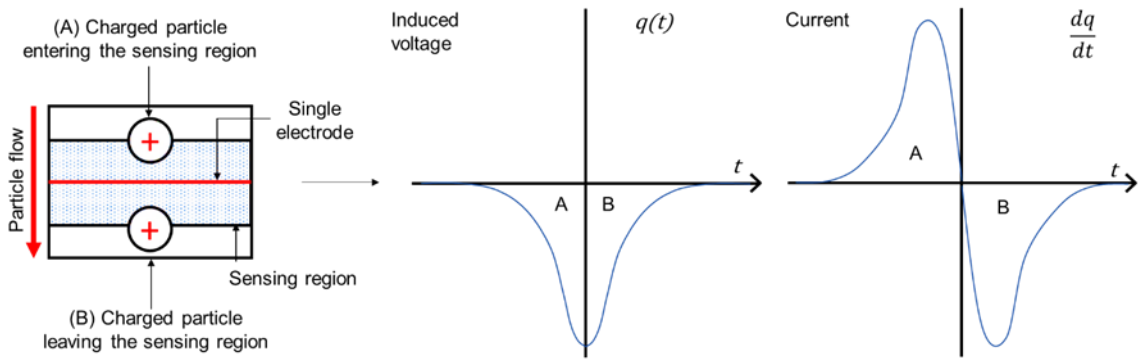

Fig. 2-5. Capacitive induction in response to the movement of a single charged particle for a single electrode, adapted from (Ma and Yan 2000).

For a multi-particulate system, the net charge will dependant on the total magnitude and polarity of charges present within the sensing region. For example, multiple charges with the same polarity may induce a stronger current, whereas two identically charged particles with opposite polarity may neutralise and fail to induce a current. The induced current is also

impacted by the electrode's spatial sensitivity, with charges located within the centremost region inducing a weaker current compared those nearer the wall (Qian, et al. 2012). Realistically speaking, the net charge and thus the induced current will fluctuate due to the aforementioned spatial sensitivity, the constant entry and exit of particles, their nature of flow (e.g. particle trajectory), as well as the stochastic charge distribution across their surfaces. Consequently, this randomness in the net charge results in a noise-like alternating current. The output current is normally undetectable due to attenuation caused by the large capacitance between the electrodes in respect to the grounded sensing element. The sensitive two-channel TIA is used to amplify and convert the analog current into a voltage signal. Each channel is equipped with an individual operational amplifier which possesses an inverting input and a gain of 1 pA per volt. Fig. 2-6, shows a schematic of a single electrode connected to a channel containing an operational amplifier. For a positively charged particle which attracts electrons towards the electrode, the output voltage will be positive in polarity and vice-versa.

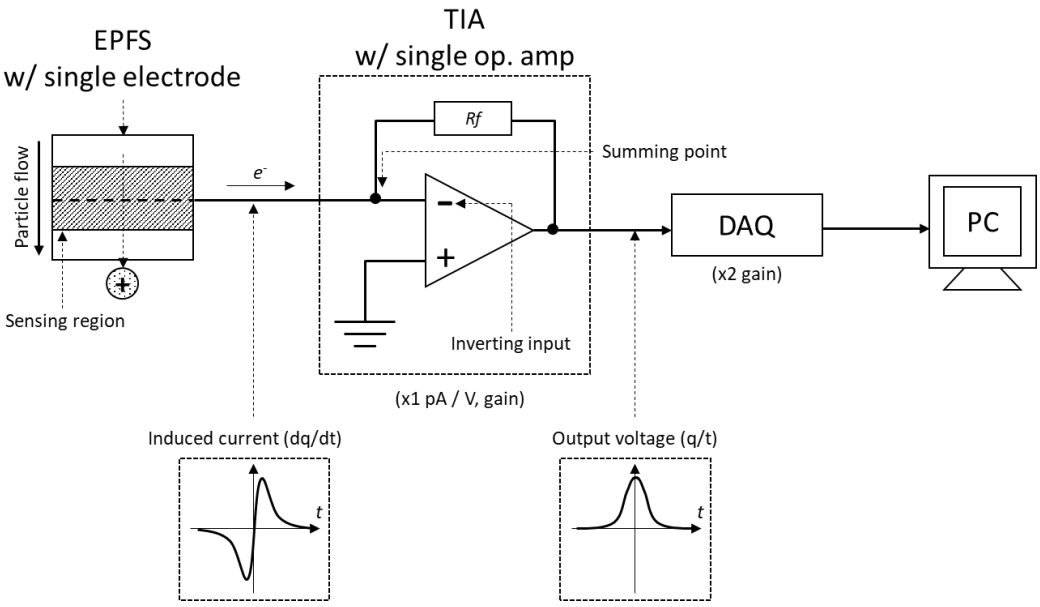

Fig. 2-6. Operation of the inverting operational amplifier.

Each voltage channel output from the TIA is connected to an individual input pin to the DAQ, where they are amplified (by a gain of x2), digitised and stored as comma separated values files (.csv) on a PC. A single measurement yields two voltage signals (one per electrode) which are expressed in millivolts (mV). Since the bottom electrode is displaced by a height of 15 mm

with respects to the top electrode, the voltage signals registered by both electrodes for the same particle(s) are also displaced by a time delay but otherwise should be completely identical. Although, upon further inspection of the data, it was found that the signals do in fact differ in magnitude (although not in their profile shape). These differences were caused by the slight variation in tolerance between the gigaohm range feedback resistors; stated up to 30 %. Therefore, it was ensured that each electrode was always connected to the same channels between experimental repeats.

Two additional notes are included within this sub-section:

- Firstly, it should be noted that the overall EPFS measurement system is immune to particle adhesion to the interior wall within the sensing region, i.e. stationary charges (Ma and Yan 2000). Whilst the voltage developed on the electrode is impacted by the stationary charges, the fluctuation in current (which the measurement principle is derived from) is only affected by charges moving past the electrode. This is an important property since it allows the EPFS to function normally in the presence of adhesive powders (e.g. due to triboelectrification) or within environments where the particle flow may be chaotic.

- Secondly, this type of sensing technology has been classified under a number of terminologies including electrostatic, electrodynamic and triboelectric (Ma and Yan 2000). The term electrostatic has been the most used across literature, given that it adequately describes the technology without creating misconceiving the reader on the nature of the measurement principle. Hereafter, the term electrostatic signal is adopted in place of voltage signal to avoid confusing the reader.

2.3. Data-acquisition software

Both electrostatic and gravimetric measurements are recorded simultaneously using customised data-acquisition software developed using a Borland C++ package. As mentioned in the previous sub-section, each measurement is saved using a .csv format. Each file contains the following time series: the electrostatic signals per electrode; the RMS of the electrostatic signal recorded by Channel 2 on the TIA; and the cumulative weight.

Fig. 2-7a-b, illustrates the cumulative weight and raw electrostatic signal as a time series. The cumulative weight is recorded at a frequency of 20 Hz (i.e. 1 datum per 0.05 s) which is defined by the manufacturers setting. The electrostatic data is recorded at a frequency 2 kHz (i.e. 1 datum per 0.5 ms), which was suitable for: i) capturing any discrete changes made in the

powder flow; and ii) capturing enough data points for signal averaging. Take note of the powder flow onset and stopping points in both graphs which clearly illustrates the dependency of the electrostatic signal on the flow of powder. Fig. 2-7c, shows the electrostatic signal with a low pass filter applied which removes any background interference present in the signal. Fig. 2-7d-f, illustrate the procedure whereby the RMS signal is determined, which is automatically calculated by the data-acquisition software after a measurement cycle is completed. This is achieved by taking the "average deviation from the mean" across a set of electrostatic data points that are accumulated within a single period between two weighing points. Fig. 2-7d, shows a data subset within a 0.05 s period which contains exactly 100 electrostatic data points. The absolute value of these data points is determined and then averaged, which yields a single RMS data point (Fig. 2-7e), this provides a measure of the charge magnitude for this particular time window. This is repeated across the entire electrostatic dataset, thus yielding the complete RMS signal (Fig. 2-7f). Note, that the "average deviation from the mean" is substituted for the actual RMS of the electrostatic signal given that calculating the latter requires unacceptably lengthy processing times (i.e. squaring and taking the square root of such large datasets). The "average deviation from the mean" is an appropriate substitute for the true RMS since both are close in value for noise-like data. The precise terminology for this parameter would be the "absolute value of the average deviation from the mean" (i.e. AVMDM) which may create confusion for some readers. Hereon after, the terminology RMS is adopted for convenience and due to the ubiquity of the term in electrostatics.

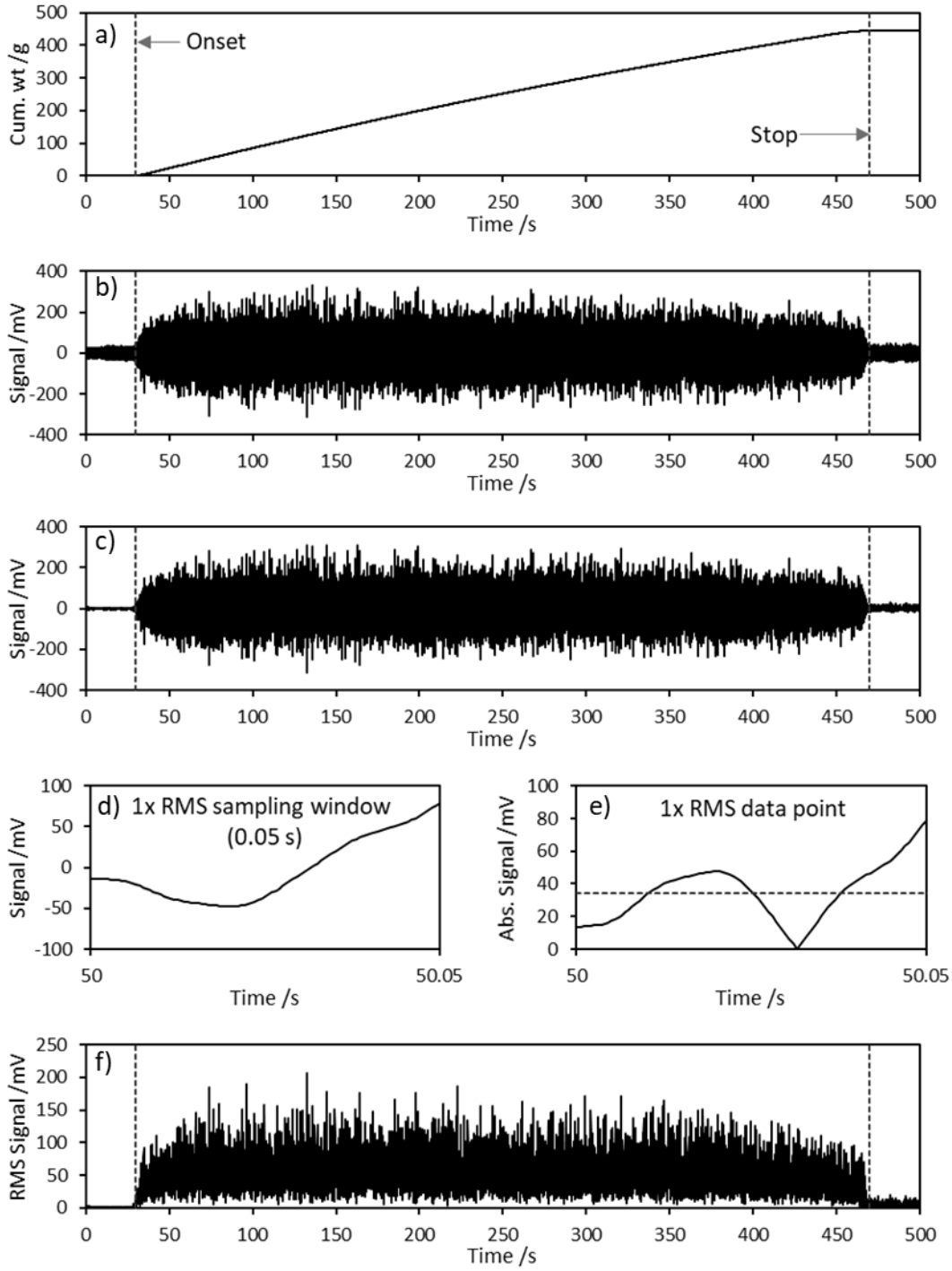

Fig. 2-7. Datasets measured for a screw conveyed Avicel PH102 NF at 40 rpm which include: a) weight signal; b) top electrostatic signal (unfiltered); c) top electrostatic signal (filtered at 50 Hz and 100+ Hz); d) top electrode RMS sampling window; e) calculation of a single RMS data point; and f) top electrode RMS signal (filtered at 50 Hz and 100+ Hz).

2.4. Data-analysis software

Prior to analysis, electrostatic datasets are initially processed using data-analysis software developed using a customised Borland C++ package. The software can apply noise-filtering, Fast-Fourier analysis and cross-correlation algorithms in order to isolate flow components, assess the signal periodicity and analyse velocity parameters, respectively. The Fast-Fourier Transform (FFT) algorithm was obtained from an open-source database (SDL Component Suite – Fourier, Epina Software Labs). In order to apply the FFT function, a time window within the electrostatic signal is selected within the software (Fig. 2-8). The "FFT Only" function is applied which returns the FFT of the electrostatic signal or its FFT spectrum (Fig. 2-9).

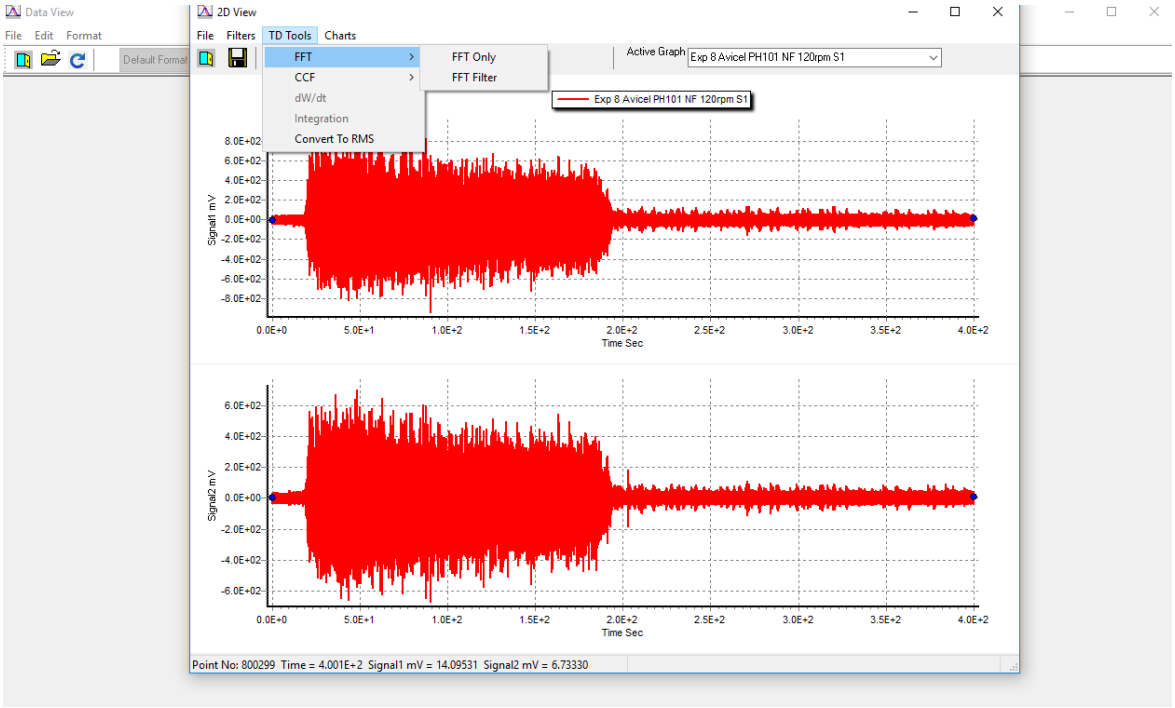

Fig. 2-8. Selecting an electrostatic dataset in order to apply FFT / cross-correlation. The two signals are recorded by the top and bottom electrodes in response to the flow of screw conveyed Avicel PH101 NF at 120 rpm.

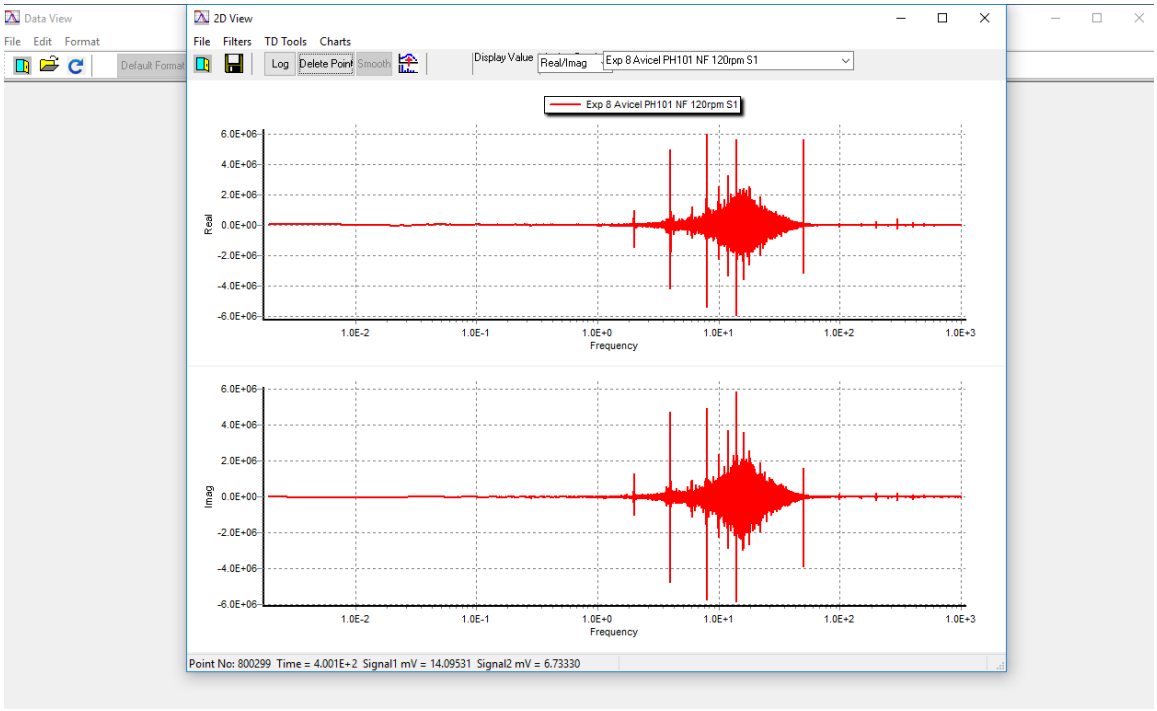

Fig. 2-9. FFT of the electrostatic signal recorded for screw conveyed Avicel PH101 NF at 120 rpm.

Fig. 2-10a, shows the electrostatic response when the screw feeder is run without powder. Fig. 2-10b, shows the same electrostatic signal converted into the frequency domain. There are mainly frequency components at 100 Hz+. Also, usually present in the FFT spectrum is a frequency component at 50 Hz which is attributed to the electrical mains interference, although due to the amplitude of the higher frequency components the amplitude of the smaller 50 Hz component is not easily visible. These graphs demonstrate that the frequency components associated with the feeder are predominantly are high in frequency, whereas the frequency components associated with powder flow, as shown in Fig. 2-9, are much lower in frequency (<50 Hz).

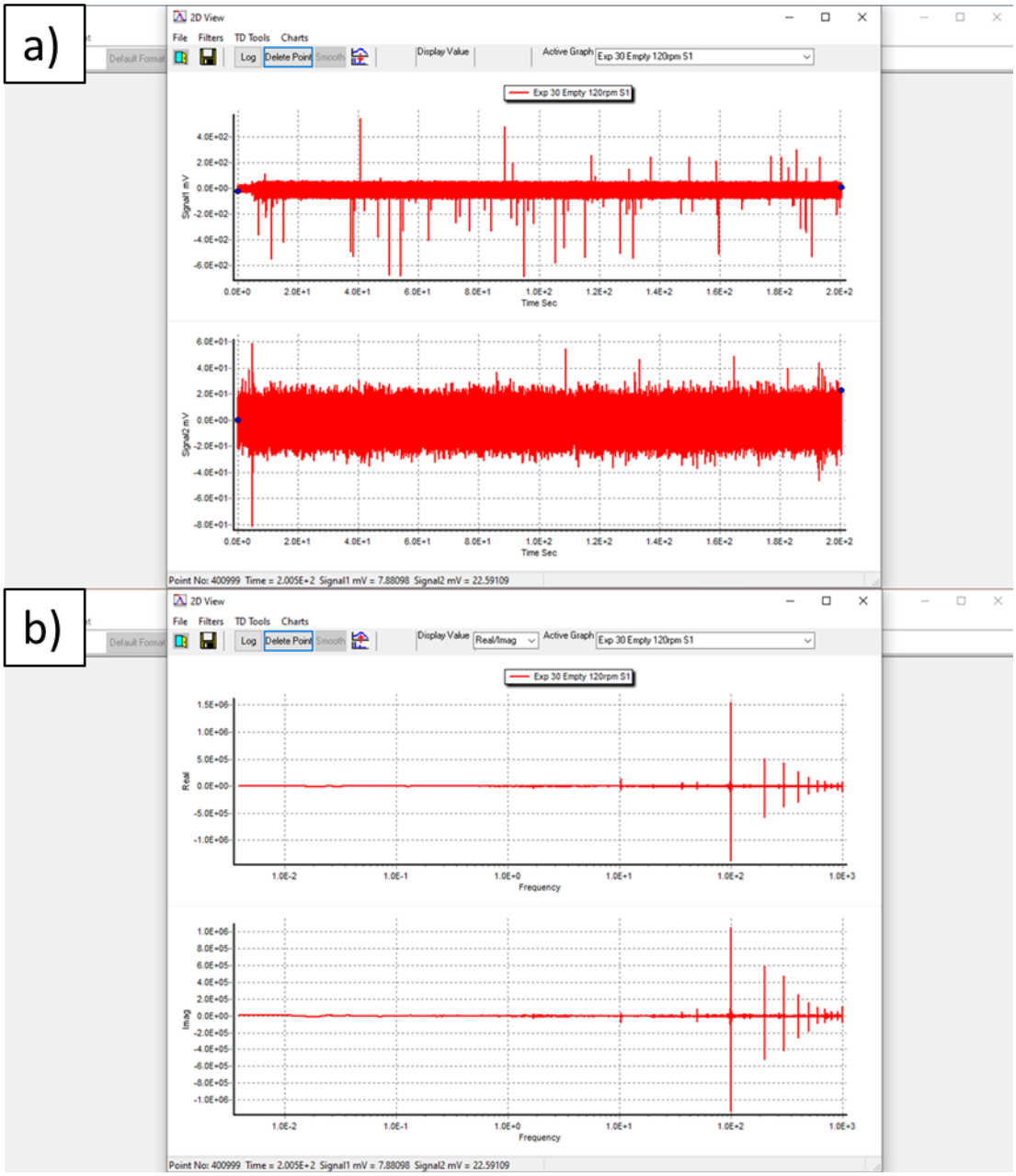

Fig. 2-10. a) electrostatic signals and b) FFT signal recorded for the empty screw feeder run at 120 rpm.

Noise-filtering can be applied in order to isolate the electrostatic response due to powder flow from interference, e.g. due to screw-feeder vibration. To achieve this, within the FFT spectrum, a frequency window containing the frequency components associated with the interference is selected (Fig. 2-11). An inverse FFT algorithm is then performed which transforms the spectrum into the time domain whilst filtering out the electrostatic data associated with the highlighted frequency components (Fig. 2-12). Aside from noise-filtering, FFT algorithm is used

for analysis of the periodicity in powder flow patterns, which is further elaborated on in Chapter 4.

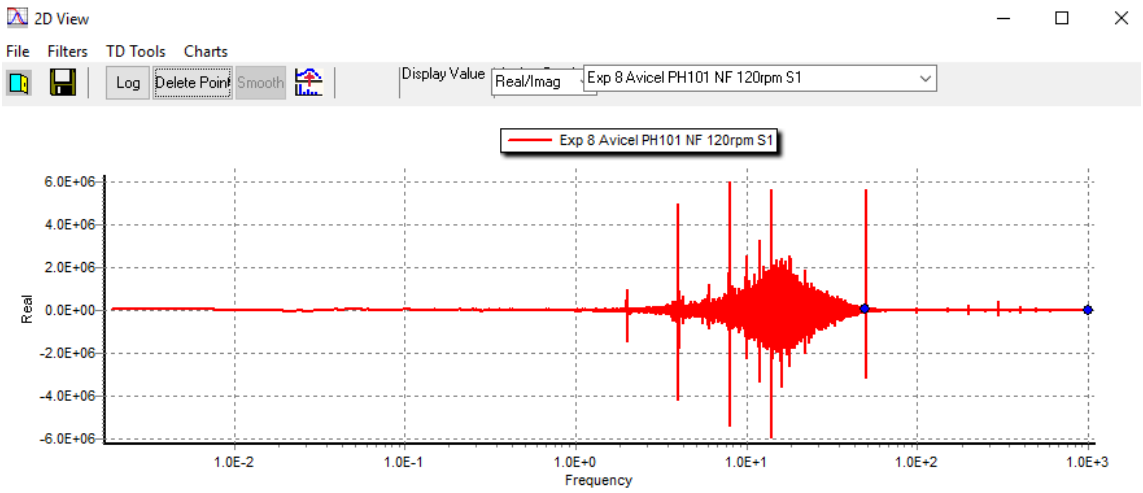

Fig. 2-11. FFT of the electrostatic signal with frequency components at 50 – 1000 Hz selected.

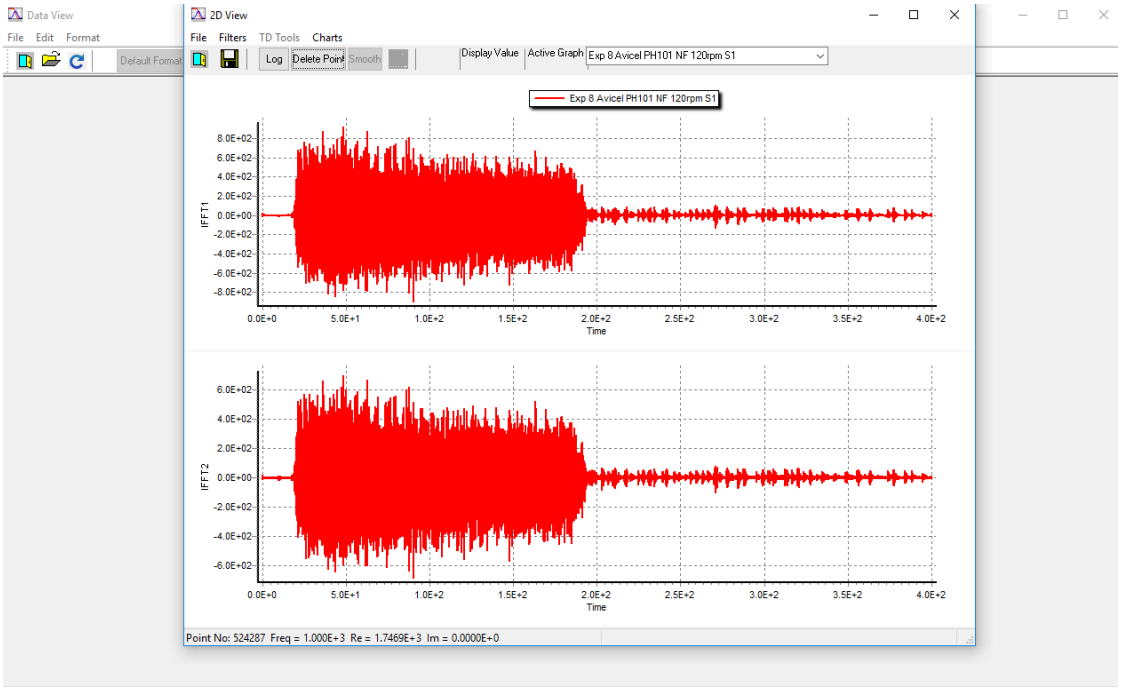

Fig. 2-12. Electrostatic signal with frequency components at 50 – 1000 Hz filtered out.

Cross-correlation analysis is performed by applying to a selected dataset, the function given by (Equation 15). Here, r = the cross-correlation factor calculated for each time series x_i and y_i, where i = 0, 1, 2….n-1. Furthermore, mx and my represent the respective means and d is equivalent to the delay.

$$r(d) = \frac{\sum_i [(x_i - mx) * (y_{(i-d)} - my)]}{\sqrt{\sum_i (x_i - mx)^2} \sqrt{\sum_i (y_{(i-d)} - my)^2}} \quad \text{(Equation 15)}$$

The software automatically calculates the cross-correlation function (CCF) against time. The point of maximum CCF represents the time difference CCF at which the signals are most correlated. The correlation velocity V_c is then determined by taking the ratio of the electrode separation length L to the time lag τ_m (Equation 14). The software can apply cross-correlation across multiple intervals or pre-defined length, which outputs a velocity time series.

Chapter 3. Feasibility study for predicting in-line powder mass flow rate from electrostatic flow parameters using an electrostatic powder flow sensor (EPFS):

3.1. Introduction

The critical quality attributes (CQAs) of a pharmaceutical solid dosage form are dependent on the interaction between the inherent flow properties of the excipients and API and the manufacturing equipment (Yu 2008). Therefore, it is critical that the process and formulation are well designed and understood with regards to their impact on in-process flowability, so that reproducible bulk transfer can occur between and within unit operations. This understanding can be facilitated through the application of PAT techniques to different types of process flow conditions (FDA 2004). In the majority of pharmaceutical operations, powder mass flow rate is typically used to quantify the amount of material that is flowing/conveying during bulk transfer operations. Currently technologies such as loss-in-weight feeders which are capable of reproducibly controlling the powder mass cannot be installed into all areas of the manufacturing process. Furthermore, these devices do not usually record the mass flow data which would otherwise be invaluable towards mechanistic understanding and continuous improvement of the process (FDA 2004). PAT applications for mass flow measurement reported in literature have typically been achieved using integrated technologies, which separately quantify the solids concentration and velocity (Carter, et al. 2005; Li, et al. 2015; Sun, et al. 2008; Wang, et al. 2016). Electrostatic sensors have remained the technology for the in-line measurement of velocity given the general robustness of the technology, excellent reproducibility in the measured parameter and immunity to fouling (Qian, et al. 2014; Yan 1996), although, it is expected that integrated applications require more development time and costs compared to a single sensor. However, in-line applications using the solitary electrostatic sensor have only ever been reported for the analysis of powder velocity (Coombes and Yan 2015; Li, et al. 2015; Qian, et al. 2012). Furthermore, univariate calibration of charge against powder mass flow rate is rarely ever reported. It is expected that this is related to the unpredictability in the charges that develop on powders which makes calibration challenging (Carter, et al. 2005). Although, Qian, et al. (2014), were able to infer the mass flow rate from the RMS and solids velocity yielded using an electrostatic sensor array (Qian, et al. 2014). The authors found that the predicted mass flow rate was comparable to a reference

measurement with only -9 to 6.6 % in error. A univariate calibration would be ideal as it helps keep the cost of the sensor low and its structure simple. So far, there have been no reports on the univariate calibration of powder charge or velocity against mass flow rate, specifically regarding powders flow regimes that are typical within pharmaceutical processes (e.g hopper flow and screw feeder flow). The aim of this work was to assess the feasibility of obtaining an in-line calibration of powder mass flow rate against EPFS parameters. These parameters included: i) the RMS of electrostatic signal, and ii) the powder velocity, obtained via cross-correlation of the electrostatic signals. These measurements were performed on two different flow regimes – dense phase gravitational flow and lean phase screw feeder flow. Particular focus was placed on: a) the relationship between the powder mass flow rate and the aforementioned flow parameters; b) the reproducibility in the flow parameters with respect to the mass flow rate; and c) the limitations of the technology with respects to the flow regime.

3.2. Materials

This study utilised five pharmaceutical excipients typically used as fillers or disintegrants (see Table 3-1). These powders were selected from a range of free-flowing to cohesive, since powder cohesivity is known to impact the screw filling efficiency (Yadav, et al. 2019). Each powder was stored and used whilst under ambient conditions.

Table 3-1. Details of the powder excipients. Conditioned bulk density was recorded using the FT4 Powder Rheometer for n=6 samples (see Chapter 4.3.2).

Material	Manufacturer/Supplier	Nominal particle size as stated by manufacturer /µm	Mean conditioned bulk density (g/mL)
Lactose #316 Fast flo	Foremost	106	0.61 ± 0.2 %
Lactose 200M EP	Blackburn Distributions	75	0.53 ± 1 %
Avicel PH101 NF	FMC Biopolymer	50	0.32 ± 0.5 %
Avicel PH102 NF	FMC Biopolymer	100	0.35 ± 0.2 %
Maize starch EP	JM Loveridge	N/S*	0.49 ± 1 %

*N/S = *not specified*

3.3. Method

3.3.1. Moisture analysis

Moisture content was measured by loss-on-drying for all powders, except for Avicel PH101 NF using conditions stated in the British Pharmacopoeia (British Pharmacopoeia Commission

2019d; British Pharmacopoeia Commission 2019e; British Pharmacopoeia Commission 2019f). The method used is given by (British Pharmacopoeia Commission 2019a). The weight of each sample ranged from the 0.5 – 1 g depending on the pharmacopoeia specifications. These were dried in the oven for the specific drying times. The procedure was slightly modified since the powders gradually gaining weight during cooling. Therefore, after being removed from the oven, each sample was cooled in a desiccator for 10 minutes, which was pre-conditioned at ~ 0 %RH using 2.5 - 5.0 mm molecular sieve beads (Type 4A, Fisher Scientific). Due to insufficient sample size, the moisture content of Avicel PH101 NF was instead determined via thermo-gravimetric analysis (TGA) (Pyris 1, PerkinElmer), using a drying rate of 5 °C/min within a range of 30 - 200 °C.

3.3.2. Dense phase flow experiment

Fig. 3-1, shows the dense phase gravitational flow rig, which comprised 1000 mm stainless-steel cylindrical pipe with an internal diameter of 19.1 mm. The lab-scale EPFS was fixed to the bottom of the pipe. A small brass nozzle with a polished inner cone angle of 40° was attached to the base of the EPFS. A selection of nozzles was available, with aperture diameters of 4.2, 4.5, 4.8, 5, 5.4, 10 and 15 mm. A flow stopper was fixed to the pipe to control the onset/stop of powder flow. The top electrode was connected to Channel 1 on the TIA and the bottom electrode connected to Channel 2. The pipe was also earthed to the TIA in order to reduce the generation of static charge on the outer pipe, which was induced by the particles continuously rubbing against the pipe wall. This was to ensure that the RMS signal magnitude was primarily dictated by the given powder mass flow rate and not by any increase in charge gained by the powders over time. Although the earthing process prevented this static charge build-up, it did not remove all charges on the particles, meaning that it was still possible to obtain an electrostatic signal for the powder flow. The completed rig was suspended above the solid-state balance by ~100 mm. A powder collection tray was mounted on the balance.

For the dense phase gravitational flow experiments, Lactose #316 Fast Flo was selected as it was the only powder capable of flowing through the pipe without causing blockage. With the flow stopper obstructing the nozzle aperture, the powder was gradually fed into the pipe until the latter was completely full, which was done to achieve as consistent a poured density as possible. By releasing the stopper, the powder was allowed to flow from the pipe onto the balance until fully emptied whilst recording electrostatic and gravimetric measurements using the EPFS and balance respectively. These measurements were thrice repeated for each nozzle,

using a fresh sample of powder each time. Between each repeat experiment, the pipe, flow regulators and EPFS were cleaned using ethanol. Note, that these preliminary experiments were not performed under controlled conditions.

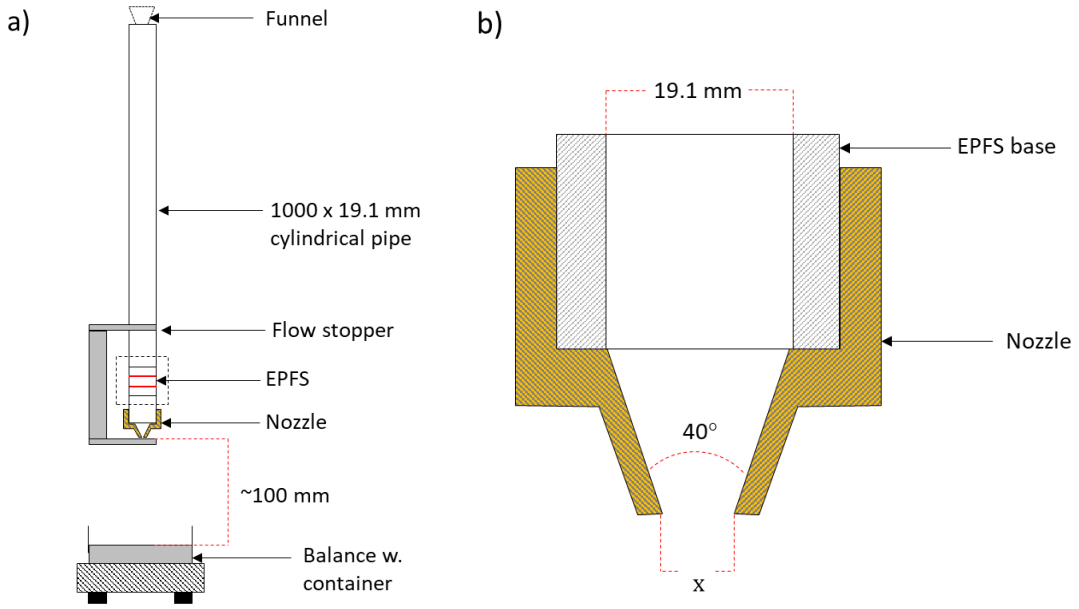

Fig. 3-1. Dense phase flow apparatus schematic diagrams of the: a) dense phase gravitational flow rig and b) the brass nozzle.

3.3.3. Lean phase flow experiment

Fig. 3-2, shows a schematic of the lean phase flow experimental setup, which comprised of a volumetric twin-screw feeder (T20, Coperion K-Tron, United Kingdom). The feeder was equipped with two 300 mm concave screws (10 mm thread pitch) and an agitation blade which ensured constant feed of powder to the screws. The feeder was mounted on top of an anti-vibration platform to dampen the noise induced by the gearbox motor (although noise-filtering was still required to be applied during the data-processing step). The industrial-scale EPFS and solid-state balance were installed on an isolated rig beneath the terminal of the screw feeder barrel. These were connected to the remaining components of the EPFS measurement system which were housed on a platform isolated from the feeder. The top electrode was connected to Channel 2 on the TIA and vice-versa (so that the top electrode was indicated by Signal 1 in the data sets). The effect of separation distance between the EPFS and barrel terminal was not studied at this point as the rig was fixed in height, although it was assumed that the distance travelled by the powder in this setup was too short for the periodicity in the flow pattern to be impacted. This would need confirmation in a future study, especially when utilising pipes which are longer in length.

The screw speed of the empty feeder was established after which it was switched off. 500 g of a given powder was dispensed and carefully loaded into the hopper (to minimise tribo-electrification due to handling). The screw feeder was switched on and the powder could convey until the hopper was emptied whilst recording electrostatic/gravimetric measurements using the EPFS and balance respectively.

Upon completion of a single measurement, the barrel and screws were disconnected from the feeder and together with the EPFS, were cleaned using ethanol. Measurements were performed using screw speeds of 40, 80, 120, 160 and 200 rpm and were thrice repeated for per screw speed. Note that environmental conditions were also uncontrolled for these experiments. However, temperature and relative humidity were recorded using a probe (TinyTag, Gemini Dataloggers). The ambient temperature and relative humidity ranged from 16.2 - 20.5 °C and 37.5 - 47.4 % respectively.

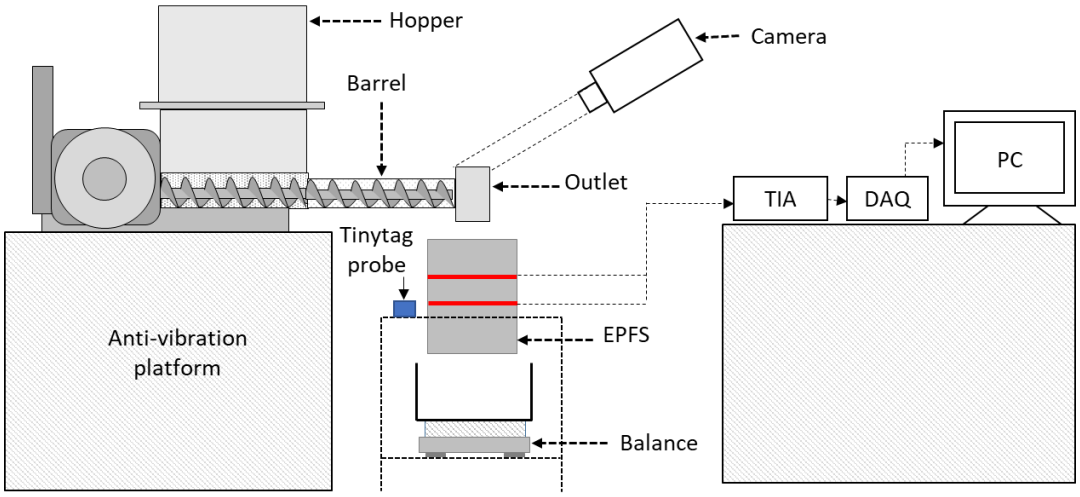

Fig. 3-2. Lean phase flow regime experimental setup.

3.4. Raw signal and data processing

The raw electrostatic signal obtained from all of the lean phase experiments were noise-filtered using the procedure described in Section 2.4, where frequency components at 50 Hz and >100 Hz were filtered out. The former components were attributed to electrical noise in the mains circuit whereas the latter was attributed to vibration induced by the screw feeder motor. This low-pass filtering procedure was not necessary for the dense phase datasets.

For both dense and lean phase experiments, the RMS of the electrostatic signals attributed to the top and bottom electrodes were manually determined in Microsoft Excel using the

procedure described in Section 2.3. Afterwards, the RMS and gravimetric profiles were reconstructed in Microsoft Excel, where the mass flow rate μ was then determined from the latter across 0.5 s intervals using the equation for linear regression (Equation 16), in which series x = time and series y = weight.

$$\mu = \frac{\sum_{i=1}^{n}(x_i - \bar{x})(y_i - \bar{y})}{\sum_{i=1}^{n}(x_i - \bar{x})^2} \qquad \text{(Equation 16)}$$

Also, the RMS signal was averaged over each 0.5 s interval, where each individual RMS data point was adjusted to a baseline value. The baseline was determined by taking the average of a 5 s section of the RMS signal attributed to zero powder flow. The average baseline value was then subtracted from each RMS data point. The resulting RMS and mass flow profiles are shown below in Fig. 3-3. Both RMS and gravimetric profiles were then truncated to isolate the datasets associated with the flow of powder. Note, that in mass flow profile are two large spikes in mass flow. These were a result of data-processing and not thought to be attributed to any real powder flow effects.

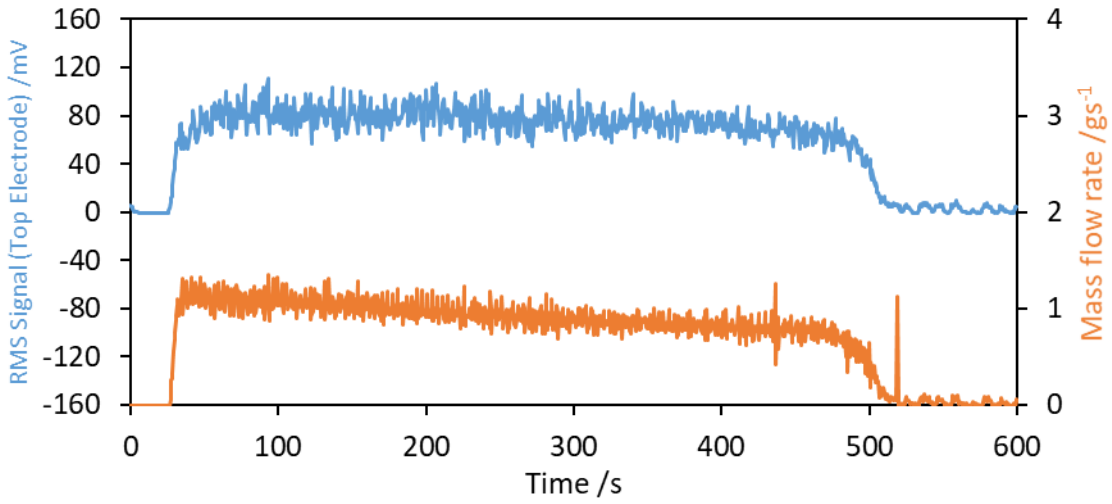

Fig. 3-3. Mass flow profile (determined via linear regression over 0.5 s intervals) and the corresponding RMS signal (averaged over 0.5 s intervals), recorded for Avicel PH101 NF that was screw-conveyed at 40 rpm.

The powder velocity was determined via cross-correlation algorithm in the data-analysis software using the cross-correlation algorithm (Equation 15) described in Section 2.4. In this case, cross-correlation was performed across consecutive 0.5 s sequences of electrostatic data. Fig. 3-4, shows the alignment between both signals.

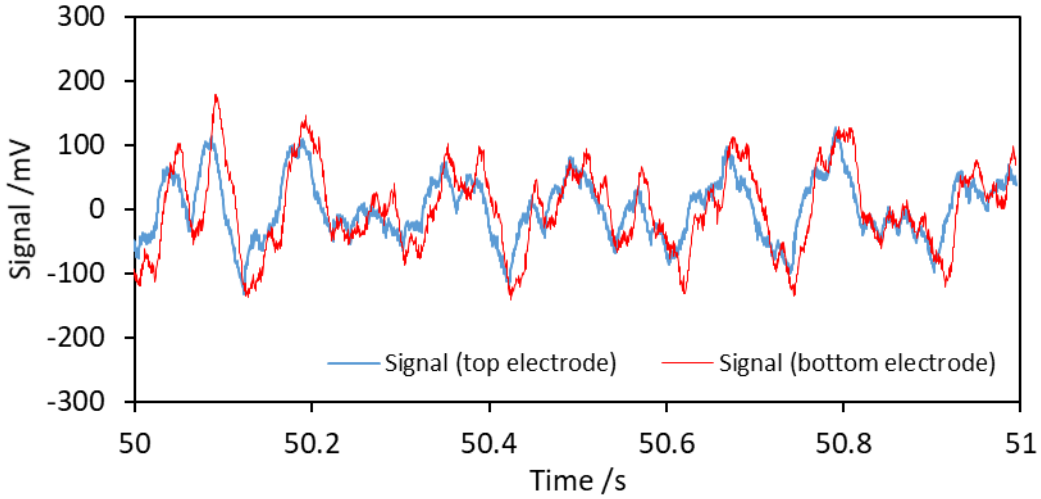

Fig. 3-4. Individual electrostatic signals recorded by the electrode pair in response to Lactose #316 Fast flo conveyed at 200 rpm. The graph is zoomed into a 1 s window so as to visualise the time delay.

The powder velocity profiles were reconstructed as a time series within Microsoft Excel (Fig. 3-5), which required adjustment using a time factor (which was equivalent to the maximum time point in the velocity time series divided by the maximum time point in the corresponding RMS/mass flow profile). Each velocity profile was truncated to the same time window as their corresponding RMS/mass flow profiles (shaded in red). The velocity profile also contained noise which occurred when attempting to apply cross-correlation to sections of the electrostatic signal which respond to zero powder flow, i.e. the electrostatic background noise, hence the large fluctuation in regions. These noisy regions were isolated out during further analysis.

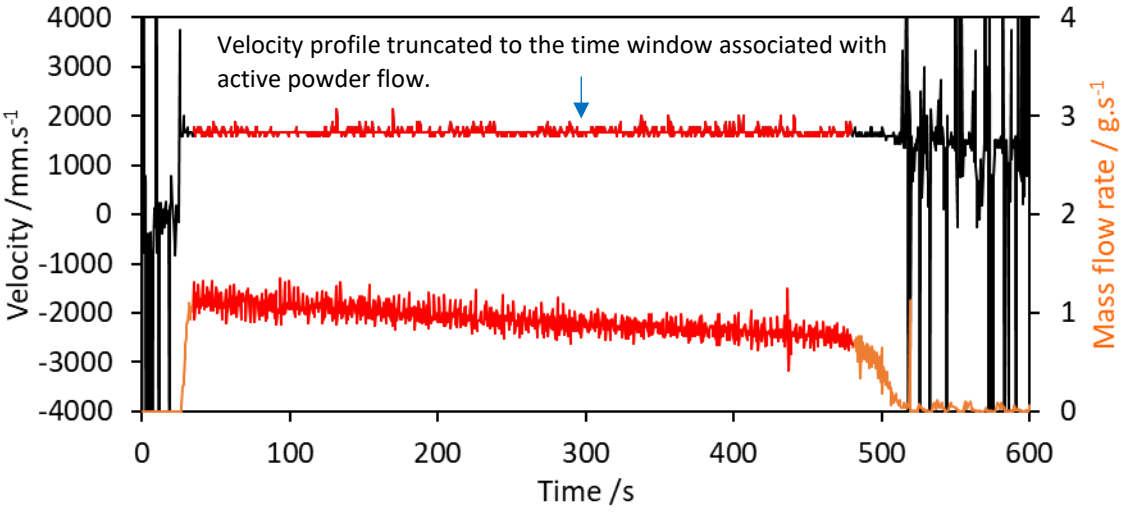

Fig. 3-5. Velocity profile (top) and mass flow profile (profile) recorded for recorded for Avicel PH101 NF that was screw-conveyed at 40 rpm. The regions shaded in red are associated with active powder flow.

3.5. Results and discussion

3.5.1. Dense phase flow experiment

3.5.1.1. Univariate analysis of the in-line dense phase mass flow vs RMS signal

Fig. 3-6, shows typical mass flow and RMS profiles for Lactose #316 Fast flo, flowing under dense phase gravitational flow conditions. The response of both parameters to active powder flow is indicated by the shaded regions in both profiles. The two large black spikes in the profiles are indicative of the transition between zero movement in the sensing region to active powder flow and vice-versa, i.e. sudden charging and discharging of the EPFS.

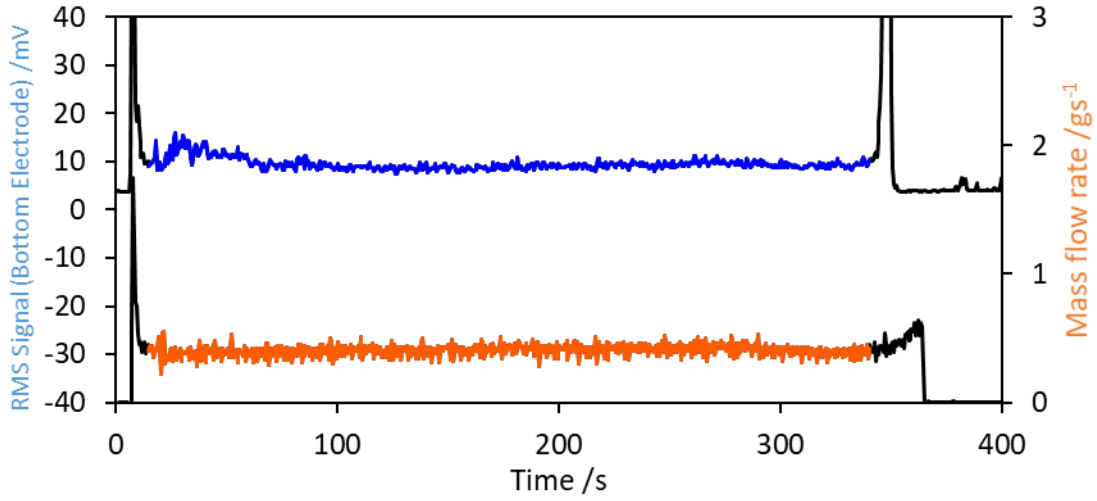

Fig. 3-6. Typical RMS and mass flow profile for Lactose #316 Fast flo, flowing through the pipe with a nozzle aperture of 4.2 mm. The regions shaded in blue and orange represent the RMS and mass flow data respectively, which were recorded in response to active powder flow.

Fig. 3-7, shows the linear relationship between the increasing nozzle aperture diameter and the mean gravitational mass flow rate (averaged from the respective truncated mass flow datasets) for each of the individual experimental repeats. Note, that the linear trendline did not intersect with the origin which suggests that a minimum aperture diameter existed which permitted gravitational flow. Error bars were also generated for each data point by taking the standard deviation of its respective truncated mass flow dataset.

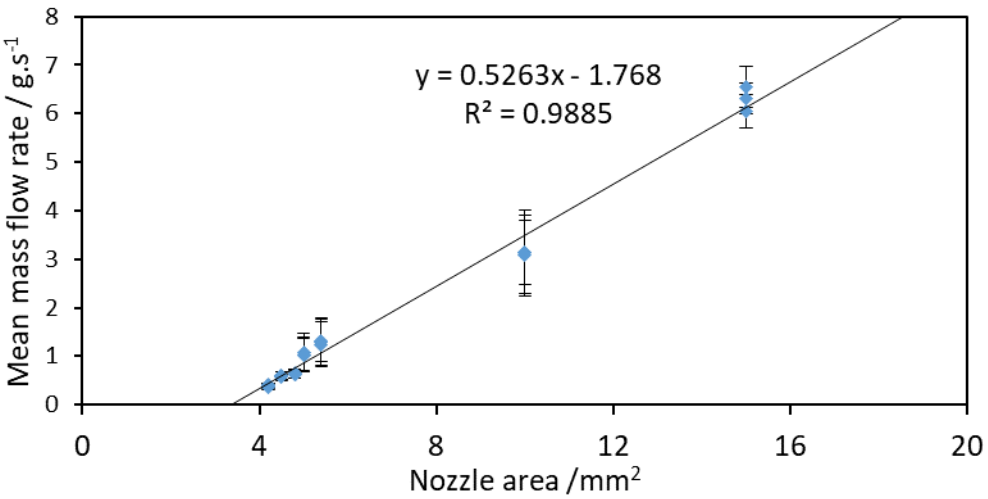

Fig. 3-7. Mean mass flow rate as a function of nozzle aperture diameter (n=3).

For the smallest nozzles (4.2 – 4.8 mm) and the 15 mm nozzle, the variation in mass flow rate was lower than 15 %, whereas for the larger nozzles (5 – 10 mm), the variation in the mass flow rate ranged from 21 - 37 %. These values, was well as their respective mass flow profiles (Fig. 3-8a-g) indicated that the powder flowed in a steady-state manner for the smallest nozzles and the 15 mm nozzle. Whereas for the 5 – 10 mm nozzles, the mass flow was more intermittent. These behaviours were also somewhat reflected within their respective RMS signal profiles. For the flow through the 4.2 mm (Fig. 3-8a) and 15 mm nozzle (Fig. 3-8g), the corresponding RMS signals were also relatively stable (standard deviation = 11 – 23 %). For the flow through the 4.5 mm and 4.8 mm nozzles, the corresponding RMS signals were more variable (standard deviation = 28 – 37 %). As well, the profiles indicated a loss in charge over time (Fig. 3-8b-c). The RMS signals recorded for flow through the 5 mm and the 5.4 mm nozzles showed a similar intermittent profile to their corresponding mass flow profiles, although the RMS increased over time until the end of its respective run, indicating that the powder gained charge over time (Fig. 3-8d-e). Standard deviation in these RMS signals ranged from 36 – 43 %. However, for the flow through the 10 mm nozzle, which was less erratic in terms of mass flow, the standard deviation in the RMS signal was lower at 19 – 25 %, suggesting that flow in these experiments were not erratic enough to induce additional charge on the powder like the those run through the 5 and 5.4 mm nozzles. These RMS and mass flow outputs were also consistent with those exhibited by the second and third samples; located in Appendix 1a-g and Appendix 2a-g respectively.

As reported in literature, changes made to the powder flow regime can alter the contact nature of particles in powder flow system, which can alter the triboelectrification behaviour (Gao, et al. 2018). In this case, the large fluctuation in the mass flow rate might indicate an erratic nature within the flow regime due to the powder bed repeatedly slowing down and speeding up, which may have altered the nature in the particle-particle/particle-wall contacts via increased abrasive movement or even increased the number of contacts, actions which are known to contribute towards increased triboelectrification (Gao, et al. 2018; Telko, et al. 2007). Also, the reduction in consistency in the mass flow and charging behaviour upon the transition from 5.4 to 15 mm nozzles suggests that an increase in nozzle aperture past a critical diameter resulted in greater dilation of the powder bed thus enabling it to flow in a more homogenous manner compared to flow through the 5 mm and 5.4 mm aperture nozzles.

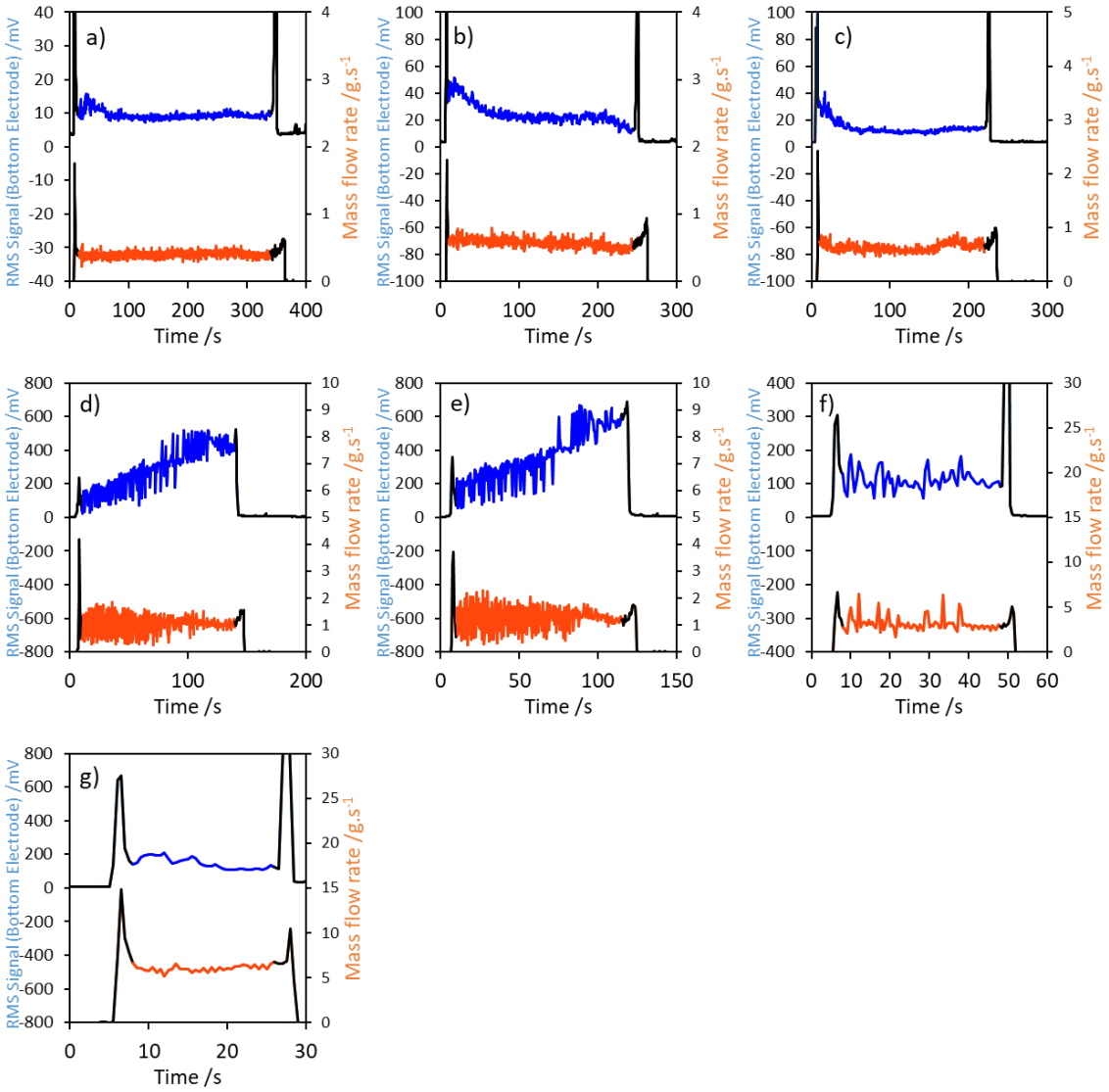

Fig. 3-8. Mass flow and RMS profiles recorded for the first runs of Lactose #316 Fast flo flowing through a pipe with nozzle apertures of: a) 4.2 mm; b) 4.5 mm; c) 4.8 mm; d) 5 mm; e) 5.4 mm; f) 10 mm; and g) 15 mm. The regions shaded in blue and orange represent the RMS and mass flow data respectively, which were recorded in response to active powder flow.

Fig. 3-9, illustrates the relationship between the mean RMS and the mean mass flow rate measured per repeat of powder for each nozzle. A linear trendline with an R^2 value of -0.492 was fit through the data, indicating significantly poor predictability in the mean RMS with respect to the mass flow rate. It is possible that two separate trends existed in the data associated with the 4.2 – 5.4 mm and the 10 – 15 mm nozzles, indicating a possible change in flow regime arising from the lack of control in the flow and packing conditions between increasing nozzle sizes. The flow behaviour adopted by the powder would have been heavily dependent on the available space provided by the nozzle aperture, the consistency and nature

of the packing density, the variation in the particle properties and the surface properties of the pipe (Babout, et al. 2013). Since the only force acting on the powder would have been gravity, the aforementioned material and process variables would have had a greater impact on the variability in the mass flow rate compared to a flow regime which utilises an input shear force. Another limitation was the unpredictability in the powder charging behaviour which could either be inherent or induced during handling or under the conditions of flow. It has been shown in these experiments that differences in the exhibited flow behaviour can induce unwanted charging on the powders. Based on these results, it was concluded unfeasible to calibrate the EPFS RMS signal against mass flow rate for dense phase flow systems.

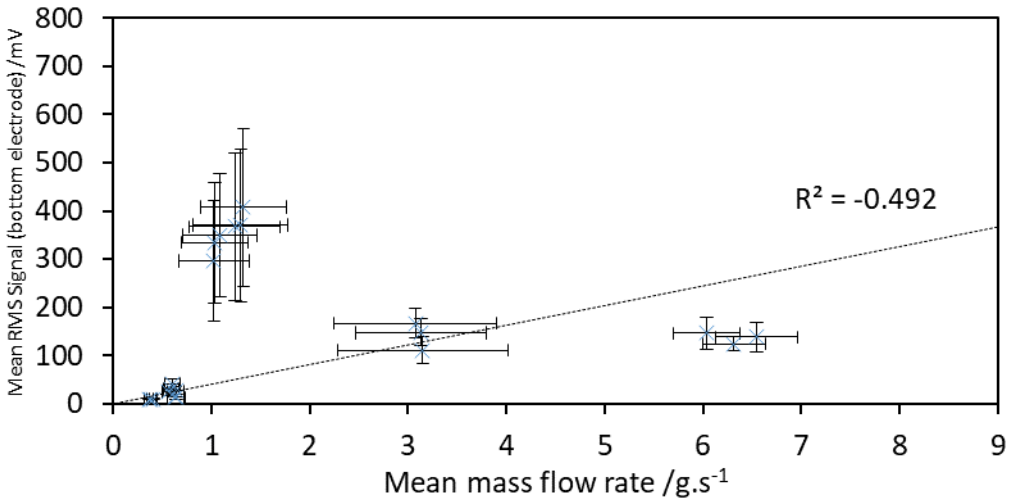

Fig. 3-9. Relationship between the mean mass flow rate and the mean value for the RMS signal for individual repeats of Lactose #316 Fast flo, flowing under dense phase gravitational flow through nozzles with aperture diameters of 4.2 – 15 mm.

3.5.1.2. Univariate analysis of the in-line dense phase mass flow vs powder velocity measurements

Cross-correlation analysis was attempted for the electrostatic signals recorded for dense phase flow. Fig. 3-10a, shows an example velocity and mass flow profile for Lactose #316 flowing through the 4.2 mm nozzle, which contained numerous positive and negative velocity fluctuations that reached the saturation limit of the EPFS ($\pm 3 \times 10^4$ mm.s^{-1}) which were mostly prominent within the first 200 seconds of the experiment. These fluctuations decreased in number as the pipe emptied. It was initially thought that the larger fluctuations implied movement of particles between both electrodes at very high velocities, however, as evident by the mass flow profile, which remained fairly homogenous throughout the entire run, this was

not the case. By closely analysing the electrostatic signals recorded by both electrodes at the beginning of the run, it was observed that both possessed erratic signal inductions which occurred at almost the same time points (Fig. 3-10b). In this case, since the delay between these inductions were very small, the resulting velocity determined via cross-correlation was unrealistically large. However, as the pipe flow moved closer to an empty state (~+200 s), these velocity fluctuations appeared to decrease, which were caused by the reduced similarity between the signals at latter time points (Fig. 3-10c). The temporal change between the RMS signal inductions from similar to dissimilar was thought to be reflective of shift in the powder flow regime. Where the inductions were temporally similar, it was thought that the entire powder bed moving downwards at once, thus inducing signals on the electrodes at the same time points. Whereas, the loss of similarity indicated powder moving past the electrodes at different velocities. In dense phase flows such as hoppers, velocity fields are known to develop. Kumar, et al. (2020), shows that when a hopper was nearer to full capacity, the majority of the particles flowed at a uniform velocity, except within the localised region of the outlet where velocity fields were more variable (Kumar, et al. 2020). At this region, the fasted moving section was concentrated within the centre and the slowest moving section was located nearest to the walls due to particle-wall friction, i.e. core flow regime. However, as the hopper emptied, the faster moving sections present within the velocity profiles transitioned higher up length of the powder bed, thus resulting in the velocity distribution forming across the entire powder bed. In this study, it was thought that this change in velocity distribution was the reason why the electrostatic signal inductions became dissimilar.

Nevertheless, these observations rendered prediction of powder mass flow rate via powder velocity measurements unfeasible for dense phase flow. For cross-correlation to be possible, the flow would need to be dilute enough so that particles which enter the top electrode sensing region first are also the first particles to subsequently enter the bottom electrode and so-on. This would allow the time delay to be distinguishable between both signals. For very dense powder flows, it is unlikely that velocity measurement via cross-correlation would be applicable.

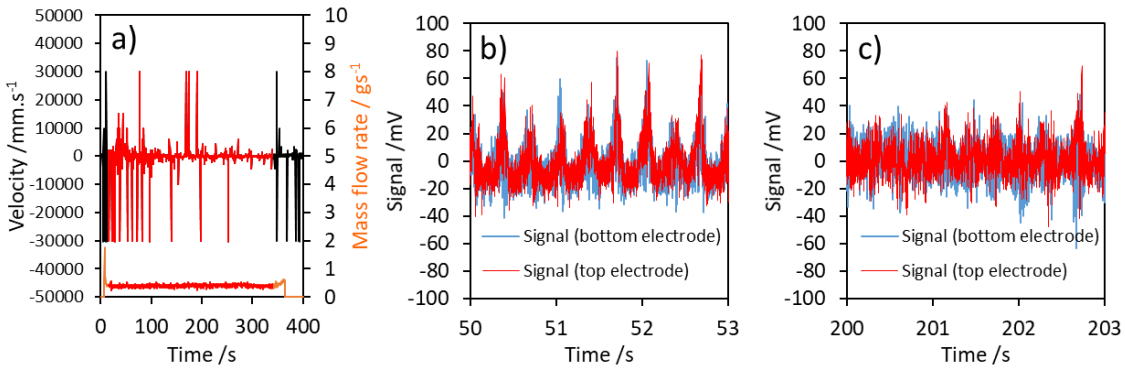

Fig. 3-10. a) Velocity and mass flow profile for Lactose #316 Fast flo, flowing through the 4.2 mm nozzle. The region shaded in red is associated with active powder flow. b) Corresponding electrostatic signals registered by the electrode pair, zoomed in to a 50 - 53 s time window. c) Corresponding electrostatic signals registered by the electrode pair, zoomed in to a 200 - 203 s time window

3.5.2. Lean phase flow experiment

3.5.2.1. Univariate analysis of the in-line lean phase mass flow via the RMS signal

Fig. 3-11a-e, shows a typical RMS and mass flow profile recorded for the five powders conveyed using a twin-screw feeder. The regions shaded in blue and orange represent the RMS and mass flow data sets attributed to active powder flow, whilst the regions shaded in black associated with the increase or reduction in active powder flow due to loading and emptying of the barrel respectively. Compared to the dense phase experiments, the screw feeder was able to establish better control over the powder mass flow rate. Although, for the majority of powders (excluding Lactose #316 Fast flo), a drift in the mass flow rate was observed over time. This was attributed to a loss in screw-filling efficiency due to the hopper gradually becoming emptier over time, although at this point it was expected for the RMS signal to decrease proportionally with the mass flow rate.

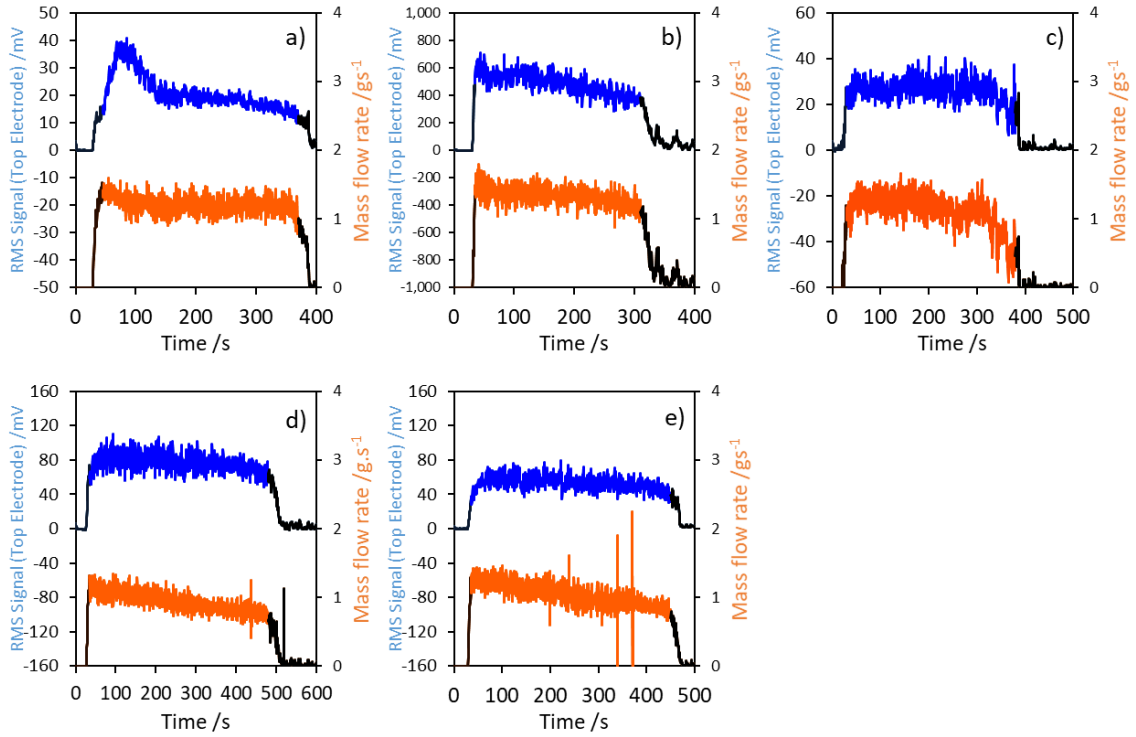

Fig. 3-11. Typical RMS and lean phase mass flow profiles for: a) Lactose #316 Fast flo; b) Lactose 200M EP; c) maize starch EP; d) Avicel PH101 NF; and e) Avicel PH102 NF. These datasets were generated in response to each powder having been conveyed using a twin-screw feeder at 40 rpm. The regions shaded in blue and orange represent the RMS and mass flow data respectively, which were recorded in response to continuous feeding.

Fig. 3-12a-e, shows the relationship between the mean RMS and mean mass flow rate for the individual samples of screw conveyed powders at 40 – 200 rpm. Compared to the dense phase results, an improved linear relationship was observed between the mean RMS and mass flow rate using this configuration (R^2 = 0.8361 - 0.9543), thus confirming the importance of an input shear mechanism for achieving repeatable flow rates. For Avicel PH101 NF, Avicel PH102 NF and maize starch EP, the standard deviation in RMS was as high as 22 %, whereas for the lactose monohydrate powders, standard deviation was as high as 36 %.

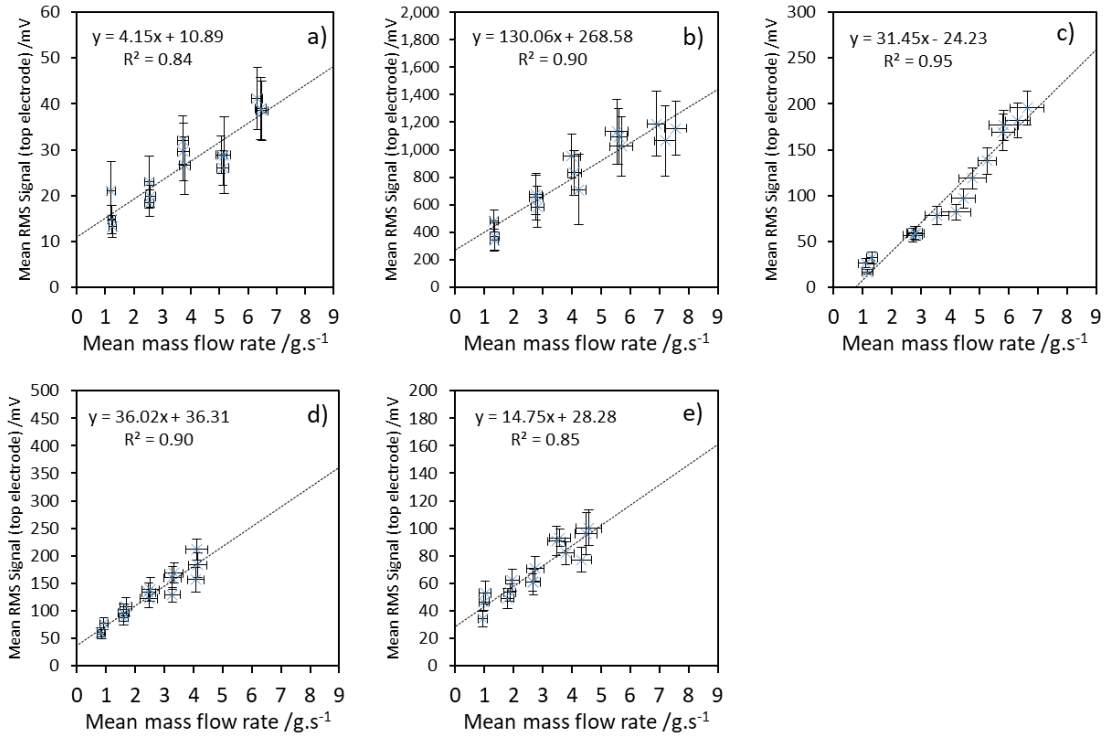

Fig. 3-12. Trends between the mean RMS and mean mass flow rate for individual samples of: a) Lactose #316 Fast flo; b) Lactose 200M EP; c) maize starch EP; d) Avicel PH101 NF; and e) Avicel PH102 NF, conveyed through the twin-screw feeder at speeds of 40 – 200rpm.

Fig. 3-13a-e, plots the individual RMS and mass flow datasets against each other to assess the drift in the former. The data points were also colour coded so as to indicate the mode of flow with respects to the barrel loading as follows: black = barrel loading; blue = continuous feeding; and light blue = barrel emptying. Moreover, a red line was crudely traced over these plots in order to show the trajectory in RMS signal data points over time, which was made in reference to the corresponding time series. The drift in RMS could be qualitatively studied by observing the shape in the continuous feeding profile, as well as the relative placement of the barrel loading and emptying profiles with respects to each other. In the maize starch EP profiles (Fig. 3-13c), the RMS data points associated with the continuous feeding stage were relatively clustered together. As well, the respective barrel loading and emptying region trajectories appeared to overlay, suggesting that the powder charge and mass flow rate was relatively stable during feeding. In the Avicel PH101 NF and PH102 NF continuous feeding profiles (Fig. 3-13d-e), an initial rise followed by a gradual decline in RMS was shown. Also, the mass flow rate was shown to reduce upon the completion of barrel loading and upon the onset of barrel emptying. It is because of this that their barrel loading and emptying profiles

did not overlay in the same manner as maize starch EP. In this instance, these effects were either coupled to a loss in mass flow rate or the loss of powder charge, although at this stage it is uncertain as to which effect was dominant. The Lactose #316 Fast flo profile (Fig. 3-13a), was shown increase in RMS immediately upon the onset continuous feeding but sharply decreased as it moved towards the onset of the barrel emptying period. Here, it was thought that a rapid charging and subsequent loss in charge effects were captured during feeding. Finally for Lactose 200M EP, (Fig. 3-13a-b) the RMS was shown to continuously decrease upon the onset of continuous feeding, with hysteresis observed between the barrel loading and emptying regions. Since the mass flow rate appeared relatively consistent during this period, the decrease in RMS was attributed to a loss in charge on the powder.

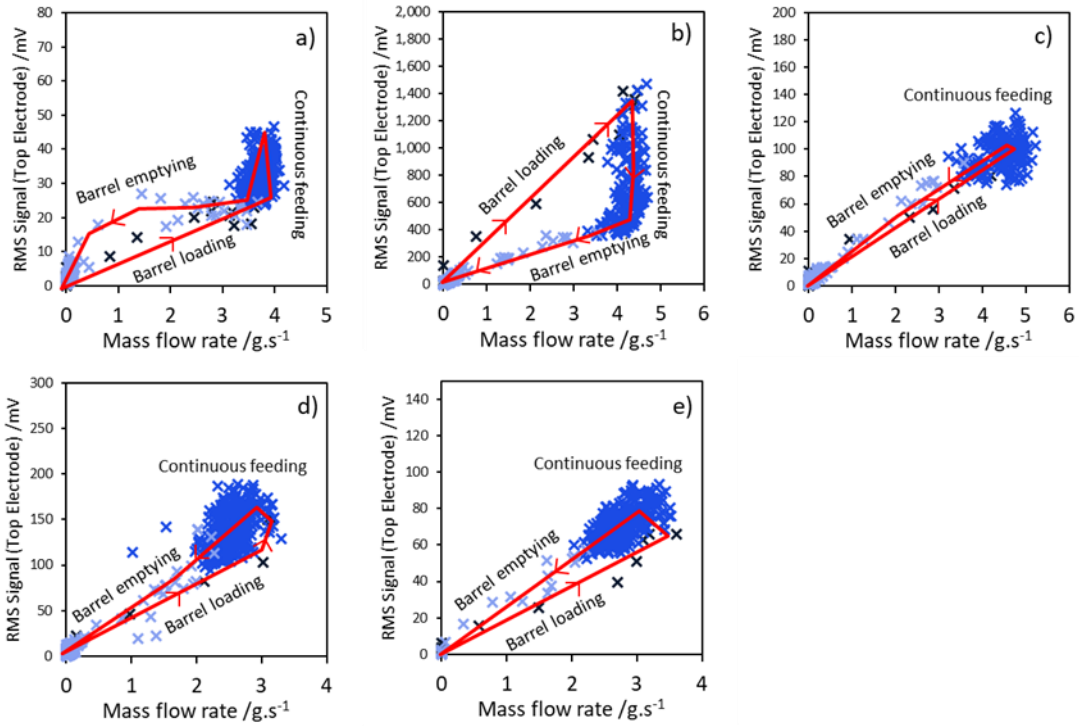

Fig. 3-13. RMS profiles as a function of the mass flow rate for individual samples of: a) Lactose #316 Fast flo; b) Lactose 200M EP; c) maize starch EP; d) Avicel PH101 NF; and e) Avicel PH102 NF, conveyed through the twin-screw feeder at a speed of 120rpm. The red line crudely traces the direction at which the data points evolved over time. Black data points represent barrel loading, blue data points represent continuous feeding and light blue data points represent barrel emptying.

For all of the powders, the variation in RMS may have been caused by a number of factors including: drift in the induced charge over time; drift in the mass flow rate/ flow regime (Gao, et al. 2018); and drift in the hopper fill volume. The inherent/induced charge on the powder would have also been susceptible to the differences in moisture content between each

material as water is known to contribute to the leakage of charge (Rowley and Mackin 2003). Lactose #316 Fast flo and Lactose 200M EP were both low in moisture content, whereas Avicel PH101 NF, Avicel PH102 NF and maize starch EP were higher in moisture content (Table 3-2). It could be that the presence of higher moisture contents in the latter powders discouraged the development of large variations in charge, whereas the lactose monohydrate powders were more susceptible to variation for the opposite reason. Aside from moisture, variability in other material properties such as particle size, shape and surface roughness may have also influenced differences in the charging nature between each powder (Wong, et al. 2015).

Table 3-2. Moisture content determined for each powder (n=3).

Material	Measured moisture content /%w/w
Lactose #316 Fast flo	0.4 ± 13 %
Lactose 200M EP	0.1 ± 42 %
Avicel PH101 NF	4.5 ± 4 %
Avicel PH102 NF	4.3 ± 4 %
Maize starch EP	12 ± 0.4 %

3.5.2.2. Analysis of the in-line lean phase flow via the powder velocity

Fig. 3-14a-e, shows the measured trend in the mean velocity and mass flow rate for the screw conveyed powders at screw speeds of 40 – 200 rpm. Each parameter was determined by taking the average value of the respective data points contained within the continuous feeding region. For each powder conveyed at each screw speed, the velocity measurements demonstrated insensitivity to the powder mass flow rate. Although, these powder velocities were very reproducible across all mass flow rates / screw speeds (standard deviation <2 %). Based on these observations, it was thought that any propulsion exerted by the screw feeding mechanism onto the depositing powder may have deteriorated due to the effect of drag in air, presumably reaching terminal velocity. However, it should be stated that the sensor was not repositioned at different heights with respect to the barrel terminal in order to confirm the drop in powder velocity.

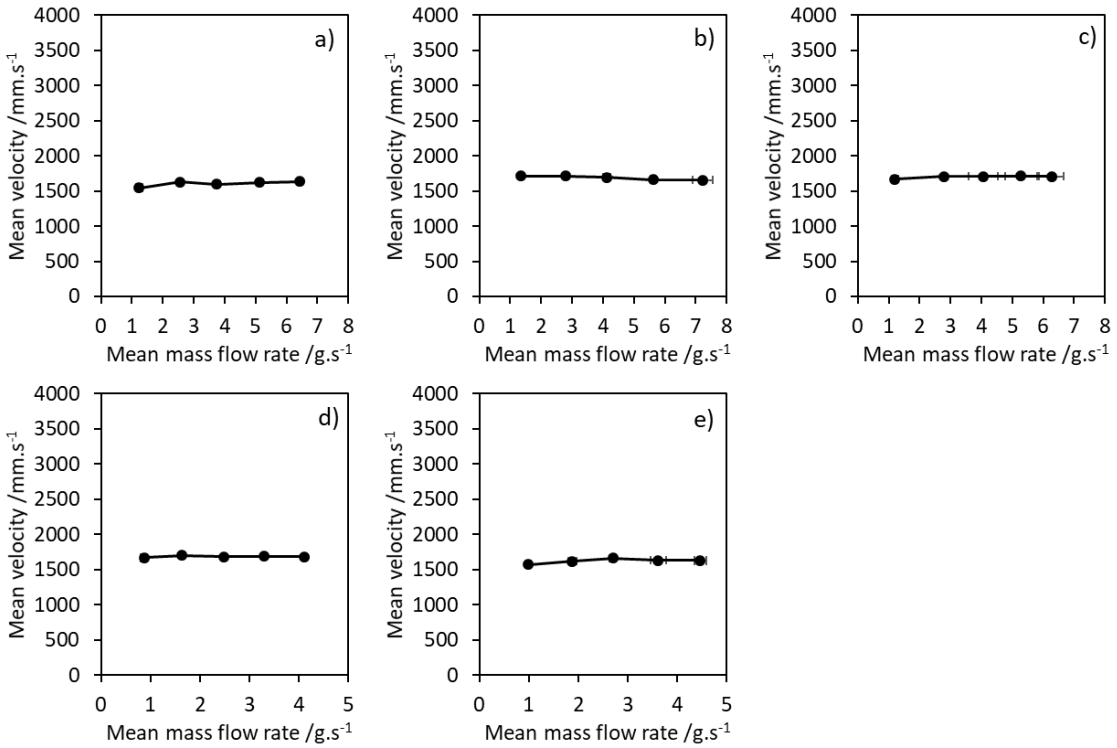

Fig. 3-14. Trends between the mean settling velocity and mean mass flow rate for individual samples of: a) Lactose #316 Fast flo; b) Lactose 200M EP; c) maize starch EP; d) Avicel PH101 NF; and e) Avicel PH102 NF, conveyed through the twin-screw feeder at speeds of 40 – 200rpm (n=3).

Table 3-3, organises each of the powders in terms of their mean settling velocity across the different screw speeds, although it should be noted that it was uncertain whether these were also their terminal velocities. Interestingly, the powders that achieved higher settling velocities were those that exhibited higher agglomeration tendencies. Fig. 3-15a-e, shows the packing differences for each material. Lactose #316 Fast Flo and Avicel PH102 NF exhibited very little agglomeration and deposited as a stream of individual particles, Avicel PH101 NF showed signs of loose agglomeration and Lactose 200M EP and maize starch EP were shown to pack and deposit as large plaques.

Table 3-3. Mean settling velocities calculated across the five different screw speeds for each powder (n=5).

Material	**Mean settling velocity across the five screw speeds /mm.s^{-1}**
Maize starch EP	1702 ± 1
Lactose 200M EP	1689 ± 2
Avicel PH101 NF	1684 ± 1
Avicel PH102 NF	1623 ± 2
Lactose #316 Fast flo	1607 ± 2

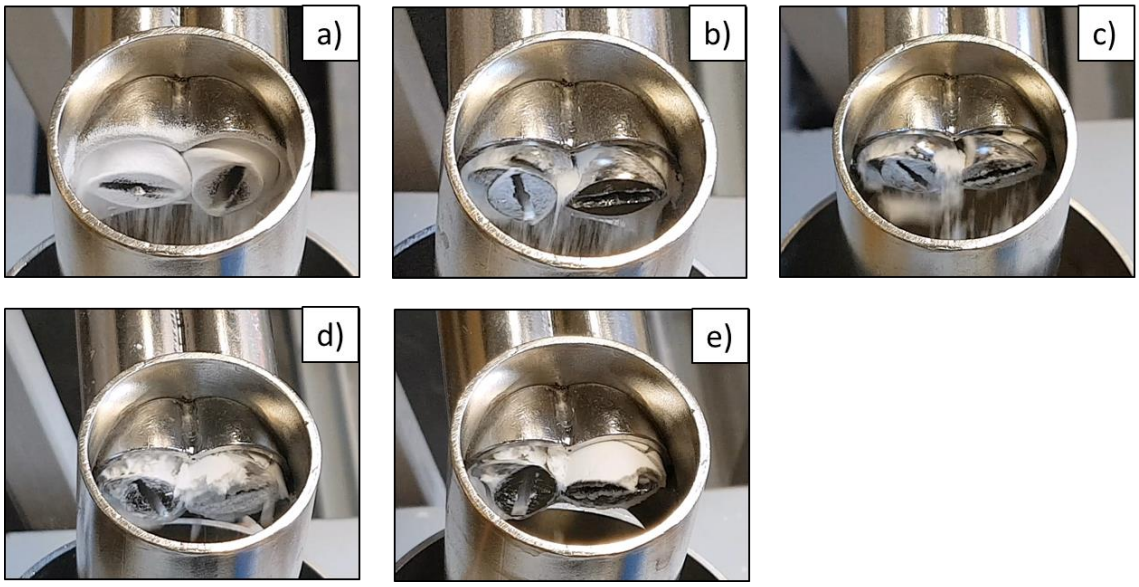

Fig. 3-15. Packing behaviour exhibited by the following powders in the screw feeder, a) Lactose #316 Fast flo, b) Avicel PH102 NF, c) Avicel PH101 NF, d) Lactose 200M EP, and e) maize starch EP.

An attempt was made in order to explain the relationship between settling velocity and packing behaviours. As described by (Equation 17), where g equals the gravitational acceleration and C_D equals the drag force; the terminal velocity V_T achieved by a settling particle or mass with density ρ within a fluid with density ρ_a, will increase with its equivalent circle diameter D_{CE} (Freret-Lorgeril, et al. 2019). Although, this relationship assumes that the particles had reached terminal velocity when entering the EPFS sensing region and that the change in the ρ due to agglomeration had less of an effect on V_T compared to the increase in D_{CE}.

$$V_T = \sqrt{D_{CE}\frac{4g(\rho - \rho_a)}{3\rho_a C_D}} \qquad \text{(Equation 17)}$$

Ultimately, for a lean phase flow using a screw feeder, the powder velocity cannot be directly calibrated against the powder mass flow rate. However, it might be possible to obtain the powder mass flow rate using an inferential technique, which combines the velocity measurements with an independent measure of powder density, solids concentration and

cross-sectional area (Carter, et al. 2005; Li, et al. 2015; Sun, et al. 2008; Wang, et al. 2016). It also would be necessary for these settling velocity measurements to be validated against a reference technology to ascertain the accuracy to the true powder velocity.

3.6. Conclusions

In this study, the feasibility of calibrating the EPFS flow parameters against the in-line powder mass flow rate was investigated. For dense phase gravitational flow regime, it was not practical to predict the in-line powder mass flow rate using the RMS signal given the dependency of the latter parameter on the flow regime adopted. Moreover, it was not possible to derive the powder velocity via cross-correlation given the absence of a time delay between the electrostatic signals recorded by the top and bottom electrodes. For lean phase flow, the RMS signal was demonstrated a relatively linear relationship with the powder mass flow rate, although this was specific to each given powder. However, the RMS signal was shown to drift during the continuous feeding stages of the experiments, with powders such as Lactose 200M EP and Lactose #316 Fast flo being especially susceptible. Additionally, the trend in the relationship between the RMS with the mass flow rate appeared to be dependent on the degree of packing each powder underwent in response to the screw feeding mechanism and the confined conditions of the barrel. It was possible to derive reproducible powder velocity measurements under lean phase conditions (where standard deviation was no higher than 2 %). However, the powder velocity was shown insensitive to the mass flow rate, which was thought to be related to the deterioration in propulsion exerted onto the powders by the screw feeder, due to their buoyancy in air. Interestingly, the velocity differences exhibited by the powders also appeared to be coupled to their agglomeration tendencies within the screw feeder. A future application could explore an integrated sensor which is able to infer the powder mass flow rate using an independent measurement of solids concentration and the EPFS velocity measurements. However, the velocity measurements do need to be validated against a reference technology, a task which was not addressed within this work. Velocity measurements can easily be achieved from time required for the particles to travel between two points captured using digital cameras. However, it is important that the region in which both the electrostatic and camera measurements are taken are consistent, otherwise some velocity discrepancies may be present due to differences in particle acceleration between both regions (Li, et al. 2015). Finally, this study also identified the sensitivity of the electrostatic

signal to the charge variation on the powders. This provided the basis for the work presented in Chapter 5, in which the EPFS was applied for the in-line measurement of dynamic powder charging properties.

Chapter 4. Qualitative determination of powder cohesivity by means of an electrostatic powder flow sensor (EPFS) coupled with Fast-Fourier-Transform (FFT) algorithms.

4.1. Introduction

The powder flow regime that develops within in a process will adopt a specific pattern which is related to the interaction between the material flow properties and the equipment shear and packing conditions. This can be seen in the study performed by Gao, et al. (2018), where the pneumatic flow regime was dependent on the amount of powder loaded into a pipe as well as the permeability of the material to the conveying gaseous media. Although the flow regime is typically a qualitative descriptor of the powder flow behaviour and doesn't necessary provide information on the bulk transfer parameters, flow outputs such as powder velocity are very much dependant on the type of flow regime adopted (Jaworski and Dyakowski 2001). Therefore, there could lie a potential value in the monitoring and even control of a powder flow regime enabled via in-line PAT techniques and control strategy. Moreover, flow regime analysis can also facilitate further process understanding, which can be fed back into continuous formulation and process design improvement as described by PAT framework (FDA 2004).

Powder flow properties or behaviour are typically characterised using off-line testers, some of which include: angle of repose, flow through an orifice, bulk/tapped density, shear cell (British Pharmacopoeia Commission 2019c), as well as dynamic methods such as the FT4 Powder Rheometer (Freeman 2007). Unfortunately, in-process powder flow regimes are not easily characterised using current off-line techniques since the shear and packing conditions are usually not comparable between both scenarios (Krantz, et al. 2009). Numerical solutions such as Discrete Element Method (DEM) can be effective tools for simulating and observing complex flow regimes that normally would not be feasible in-process, with an example account given by Hou, et al. (2014), who simulated three different cohesive powder flow regimes within a screw feeder model (Hou, et al. 2014). DEM is a cost-effective option which allows for the control, analysis and manipulation of specific particle and kinetic parameters, which would normally be impossible to obtain experimentally (Hou, et al. 2014). However, DEM is graphically limited by the number of particles that may be modelled as well as the

variety in their size (Berger and Hrenya 2014) and shape distributions (Pachón-Morales, et al. 2019). Options such as scaling law can reduce the complexity of a model at the cost of accuracy (Chan and Washino 2018; Tiscar, et al. 2019).

Ideally, flow regime analysis and characterisation should be performed in-process, where the powder flow develops naturally in response to the process flow mechanism. PAT technologies can interrogate these flow regimes and thus provide the qualitative information on how these behaviours develop and respond to input variables. Examples of PAT tools which have been used to qualitatively characterise or otherwise detect changes in powder flow regimes include NIR (Alam, et al. 2017), acoustic emission (Albion, et al. 2007) and ECT based technologies (Gao, et al. 2018). Electrostatic sensor operation is based on the induction of a current due to electrification of particles (Coombes and Yan 2015). These technologies could potentially act as good measurements of flow regime since the current output is highly sensitive to the flowing solids distribution or concentration (Qian, et al. 2012). Moreover, electrostatic sensors are attractive as PAT given their non-intrusiveness, low cost and simple structure (Qian, et al. 2014; Yan 1996). A few authors have reported on the in-line measurement of solids concentration by monitoring the change in the output RMS of the electrostatic signal (Coombes and Yan 2015; Li, et al. 2015; Qian, et al. 2014). Also, a few authors have also utilised frequency domain analysis on the electrostatic data in order to determine flow parameters and qualify flow characteristics. Zhang, J., et al. (2012), utilized Hilbert-Huang transform algorithm combined with back propagation neural network to differentiate between roping and stratified flow regimes of three-phase coal/biomass/air flows to a 100 % success rate (Zhang, Juan, et al. 2012). Li, Jian, et al. (2012), developed a spatial filtered method for an electrostatic sensor matrix, incorporating Fourier analysis as a means to measure the local particle velocity measurement in gravity flows (Li, Jian, et al. 2012). In the frequency spectra recorded for the flows of three types of particulates, the authors identified characteristic peak frequencies (which were related to the particle distribution and velocity) and from these were able to determine the local particle velocity with up to 11.1 % standard deviation. Finally, Fu, et al. (2018), used FFT to partly analyse the particle motion characteristics in pneumatically conveyed coal (Fu, et al. 2018). The authors reported a positive correlation between the peak frequencies of the FFT spectra, the air velocity and by extension the particle velocity, although particle distribution and fluctuations in the particle velocity resulted in non-linear effects.

As of yet, there has not been an attempt to characterise the flow regime developed by pharmaceutical powders under the shear conditions of a process, using electrostatic sensors. The aim of this work was to study these exact qualities using methodology based on an electrostatic powder flow sensor (EPFS) coupled with FFT analysis. Moreover, the effect of powder cohesivity on the resulting flow regimes was also investigated. These flow regimes were achieved using a twin-screw feeder since related factors such as packing behaviour, screw fill volume and feed factor were all reported to be significantly impacted by powder cohesion properties (Yadav, et al. 2019). Also, this work was supplemented using dynamic flow parameters and bulk properties, characterised off-line using an FT4 Powder Rheometer.

4.2. Materials

Five pharmaceutical powders were used in this study including: spray-dried lactose monohydrate (#316 Fast flo); a milled grade of lactose monohydrate sieved to 200 Mesh (200M EP, Blackburn Distributions); two grades of micro-crystalline cellulose (Avicel PH101 NF and Avicel PH102 NF); and maize starch (EP, JM Loveridge). Each powder was used "as received" (i.e. stored and used under ambient conditions).

4.3. Methods

4.3.1. Scanning electron microscopy (SEM) imaging

Samples of each powder were sputter coated with 15 nm of gold using a rotary pump coater (Q150RS, Quorum). Afterwards, the SEM images were taken using an EVO LS 15 model microscope (Zeiss), (accelerated voltage = 20 kV).

4.3.2. Flow characterisation using the FT4 Powder Rheometer

The impact of powder cohesivity on its flowability was characterized off-line using the FT4 Powder Rheometer (Freeman Technology Ltd, United Kingdom) which is capable of analysing characteristics of powder flow under dynamic conditions as well as other bulk properties (Fig. 4-1a). The FT4 Powder Rheometer offers good reproducibility in results due in part to system automation and an in-built conditioning protocol which standardizes the powder sample between each measurement. The tests performed in this study: stability & variable flow rate (VFR); compressibility; and permeability; were selected since their dynamic shear and packing conditions were considered similar to those in a screw feeder (i.e. flow due to a rotating shear

force, compression and agglomeration). The three tests are briefly explained below, which were followed per the standard procedure. More information can be found in the following articles (Freeman 2007; Leturia, et al. 2014).

Stability & VFR test, measured the dynamic characteristics of powder flow based on the resistance (i.e. the flow energy) of the particles against the rotating blade (Fig. 4-1b). This test was carried out using the specialized 23.5 mm blade on a 25 mm x 25 mL conditioned sample of powder. The blade was able to induce high stress bulldozing or low shear flow conditions during downwards and upwards movements respectively (Freeman 2007). For the stability portion of the test, the downwards flow energy was measured across seven cycles with a tip speed of 100 $mm.s^{-1}$. For the VFR portion, the tip speed was gradually decreased over four cycles (100, 70, 40 and 10 $mm.s^{-1}$). For both test portions, the upwards flow energy was measured at a constant tip speed of 40 $mm.s^{-1}$. **Compressibility test,** measured the volume change experienced by a powder under compression (Fig. 4-1c). This test was carried out on a 25 mm x 15 mL sample of conditioned powder using a vented piston which applied a series of normal stresses from 1 to 15 kPa. **Permeability test,** measures the change in porosity of a powder due to compression (Fig. 4-1d). This test was carried out on a 25 mm x 15 mL sample of conditioned powder, fitted with a permeable base connected to an air flow flowing at 2 $mm.s^{-1}$. The sample was compressed from 1 to 15 kPa using the vented piston whilst maintaining a constant air flow. For each normal stress, the change in pressure drop (PD) across the powder bed (mBar) was recorded. Stability & VFR measurements were repeated six times per powder, whereas compressibility and permeability measurements were repeated three times per powder.

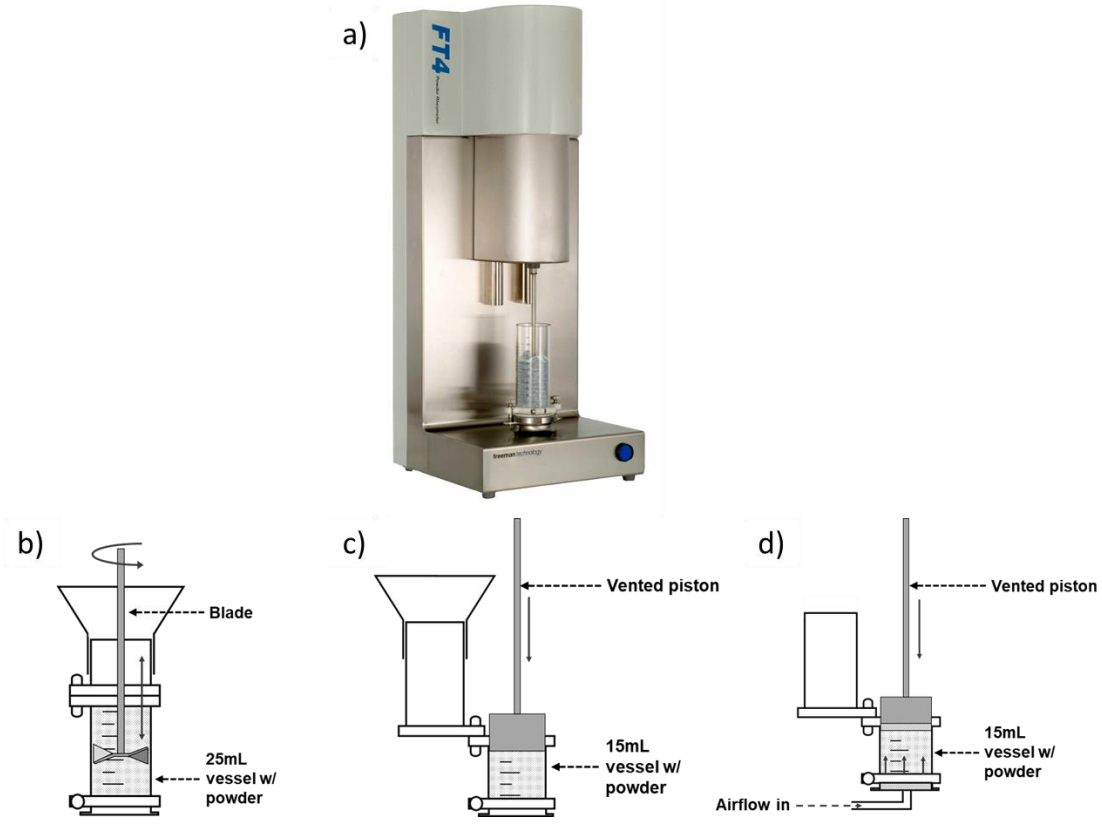

Fig. 4-1. a) FT4 Powder Rheometer (photo courtesy of Freeman Technology Limited); b) Stability & VFR test schematic; c) Compressibility test schematic; and d) Permeability test schematic.

4.3.3. Electrostatic measurements of powder conveyed using the twin-screw feeder

The experimental rig used in this study comprised of a volumetric twin-screw feeder (T20, K-Tron, United Kingdom) equipped with concave-type screws (300 mm length, double-start threads and 10 mm thread pitch). The twin-screw feeder was mounted on an anti-vibration platform to minimize any interference induced by the screw feeder motor on the EPFS cabling. The TIA and DAQ were installed onto a separate platform, approximately 1 m away from the feeder. Also, the EPFS was installed directly below the feeder outlet by approximately 16 cm with a tared container mounted on a balance which collected the following powder and recorded the cumulative mass. The top electrode was connected to Channel 2 on the TIA and vice-versa (so that the top electrode was indicated by Signal 1 in the data sets).

The screw speed of the empty twin-screw feeder was firstly set to 40 rpm before switching off. 500 g of powder was then dispensed and loaded into the hopper. The screw feeder was

switched on, allowing the powder to flow from the outlet whilst recording the electrostatic and gravimetric responses with the EPFS and balance respectively. Measurements were repeated three times, each using a fresh sample of powder. Also, between each repeated measurement, the barrel, hopper and screws were removed from the feeder and cleaned using ethanol. Note, that experiments were not performed under controlled conditions.

4.4. Raw signal and data processing

The raw electrostatic signal was low-pass filtered of frequency components which occurred at 50 Hz and >100 Hz (see Section 2.4). The filtered electrostatic data was then converted into the frequency domain using the FFT procedure (see Section 2.4). Here, it was ensured that the FFT sampling window for each dataset powder was kept consistent at 100 seconds, where it was assumed that the number of depositions made per screw turn within each dataset was relatively consistent. Additionally, the FFT sampling window was selected based on stability in the respective mass flow rate for the same powder, which was important since drifting mass flow rates may impact the charge density and thus the FFT signal amplitude. Within the same 100 second time window, the associated cumulative weight profile was fitted with a 2^{nd} order polynomial (Fig. 4-2a). The mass flow rate for this truncated window was then determined from this polynomial trendline, with the mass flow being considered stable if its gradient did not exceed ± 0.001 (Fig. 4-2b). This threshold was decided by repeated adjustments made to the truncating window to different periods of the weight profile, including where the mass flow rate was less consistent. Note, that although the time windows were selected so that mass flow rates between repeats were mostly close in value, there were some instances where this was not feasible.

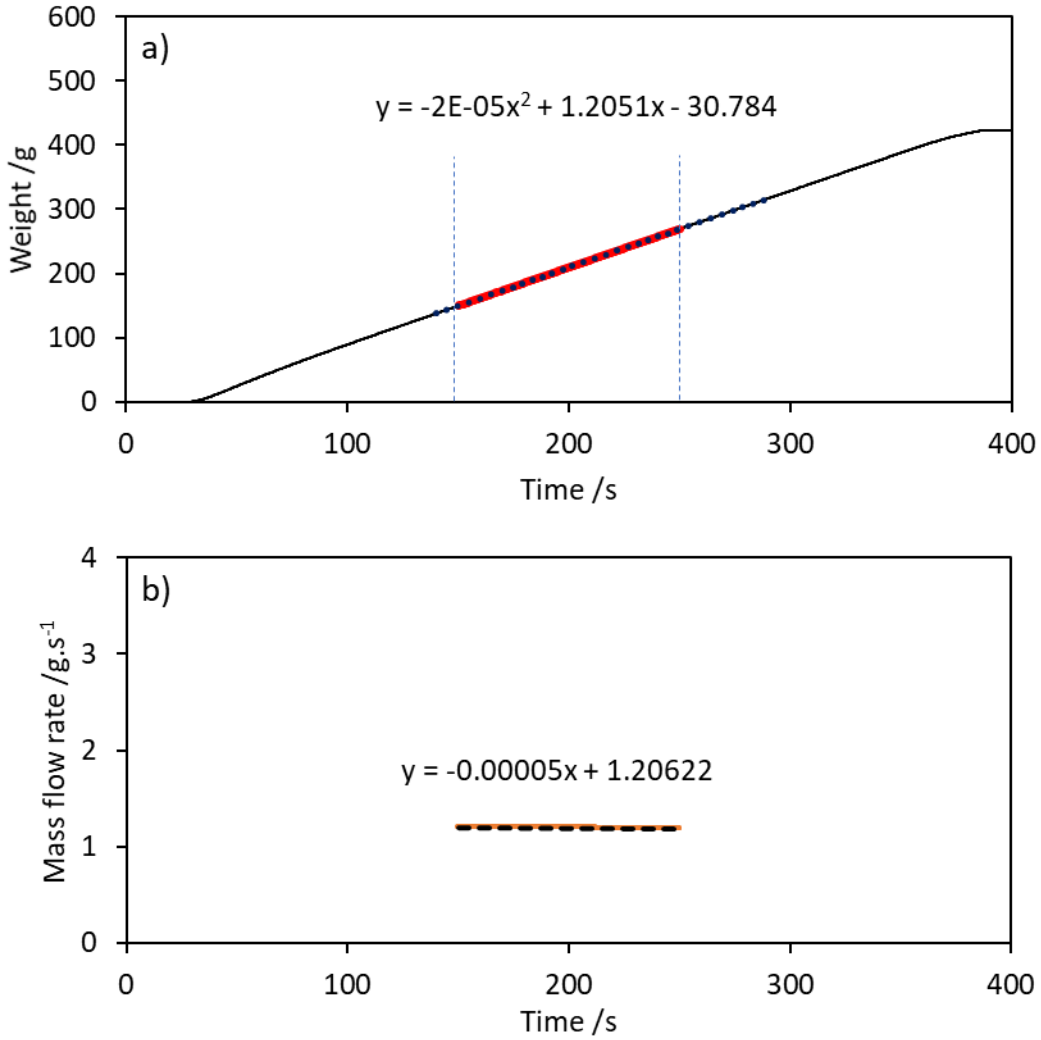

Fig. 4-2. a) Cumulative weight profile (truncated to 100 s) fitted with 2nd order polynomial, and b) derivative of the 2nd order polynomial with a fitted linear trendline (gradient < ± 0.001). This data was recorded in response to Lactose #316 Fast flo, screw conveyed at 40 rpm.

The resulting FFT signal comprised of two parts, one real r and one imaginary i, which refer to the charge and loss components of the electrostatic signal respectively, from which the magnitude of its vector a is determined (Equation 18).

$$a = \sqrt{r^2 + i^2} \qquad \text{(Equation 18)}$$

4.5. Results and discussion

4.5.1. Flow characterisation using the FT4 Powder Rheometer

4.5.1.1. Bulk property analysis using the FT4 Powder Rheometer

Fig. 4-3, shows the change in the compressibility percentage (CPS) of each powder with increasing normal stress. Cohesive and poor-flowing powders typically contained a high portion of entrained air pockets (i.e. higher void fraction) to which surrounding particles could relocate when exposed to a normal stress which resulted in a significant reduction in volume (Leturia, et al. 2014), as was the case for Lactose 200M EP, maize starch EP and Avicel PH101 NF (max. CPS = 26.22 %, 19.55 % and 17.51 % respectively). The better flowing powders (Avicel PH102 NF and Lactose #316 Fast-flo) were comparatively more resistant to compression (max. CPS = 11.1 % and 5.77 % respectively), probably due to an increased natural packing state and smaller bulk void structure. These results follow a similar trend to the compressibility index which was calculated by taking the ratio of the powder density compressed at 15 kPa and the conditioned bulk density (Table 4-1). Powders with a lower compressibility index indicated a worse flowing powder and vice-versa (Vasilenko, et al. 2011).

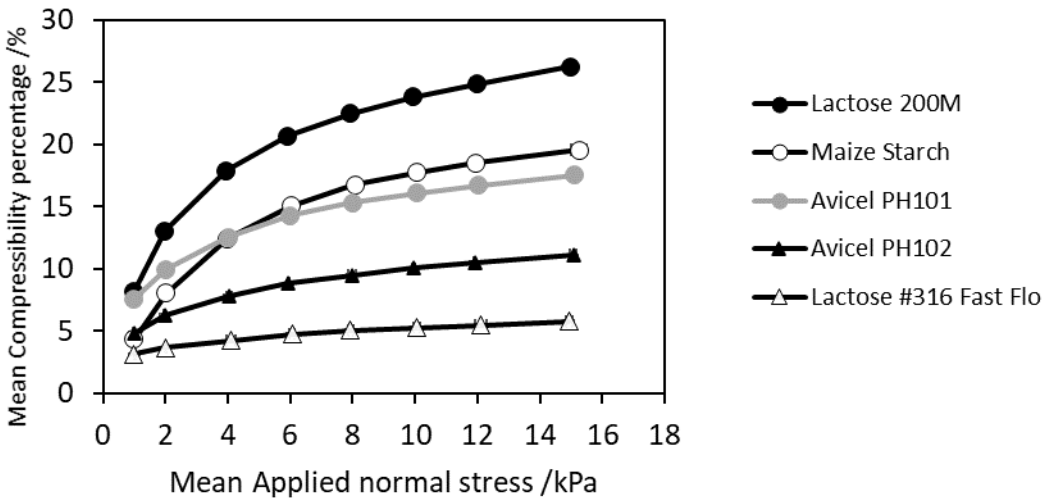

Fig. 4-3. Compressibility results (n=3).

Table 4-1 Compressibility Index calculated for each powder (n=3).

Material	Compressibility Index
Lactose #316 Fast Flo	17.34 ± 1.81 %
Avicel PH102 NF	9.01 ± 0.41 %
Avicel PH101 NF	5.71 ± 0.75 %
Maize Starch EP	5.12 ± 1.17 %
Lactose 200M EP	3.81 ± 0.43 %

Fig. 4-4, shows the change in pressure drop (PD) across the powder bed of each powder with increasing applied normal stress. Generally, based on the permeability profiles, each powder could be divided into two categories when consolidated: powders that remained relatively permeable and powders that drastically became more impermeable. The latter was true for the cohesive powders, with Lactose 200M EP and maize starch EP exhibiting high PD values of 3.34 and 1.81 mBar respectively at the minimum applied normal stress of 1 kPa, which further increased by 128 % and 195 % respectively at 15 kPa. This indicated a significant reduction in the void fraction for the already impermeable powders since their smaller particle size (see Fig. 4-5d-e) would have allowed them to pack more efficiently than coarser particles, thus forming a more densified powder bed (Hertel, et al. 2018; Zakhvatayeva, et al. 2018). This densification would have increased the resistance of the powder bed to the airflow since a greater proportion of particles make contact with the latter (Hertel, et al. 2018). Comparatively, Lactose #316 Fast flo, Avicel PH102, and Avicel PH101, were more permeable, as indicated by the lower PD values (0.52, 0.6 and 0.89 mBar at 1 kPa). Furthermore, at 15 kPa their PD values increased only by 6 %, 25 % and 27 % respectively, suggesting very minor changes made to the void structure when compressed, which was expected given that their particles were coarser (see Fig. 4-5a-c) and in the case of Lactose #316 Fast flo, smoother (Hertel, et al. 2018).

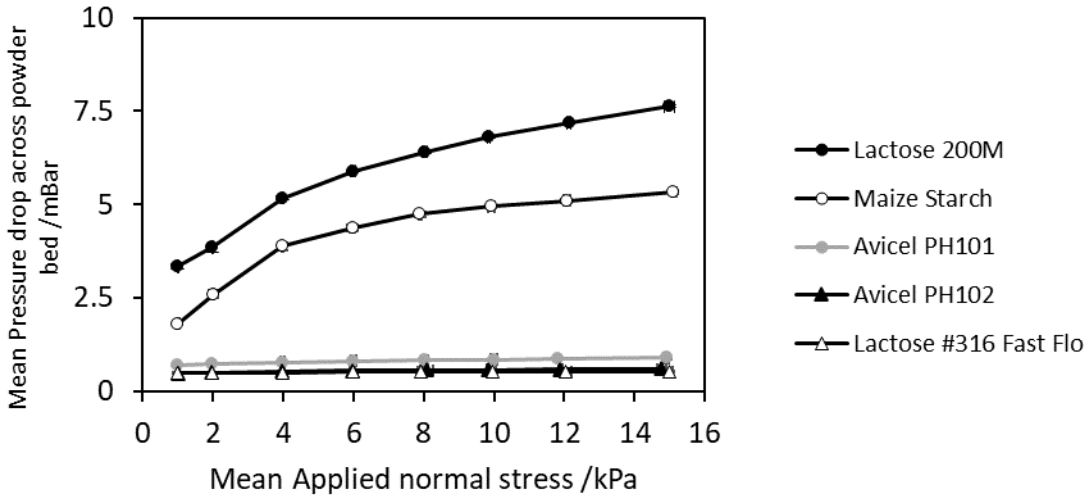

Fig. 4-4. Permeability results (n=3).

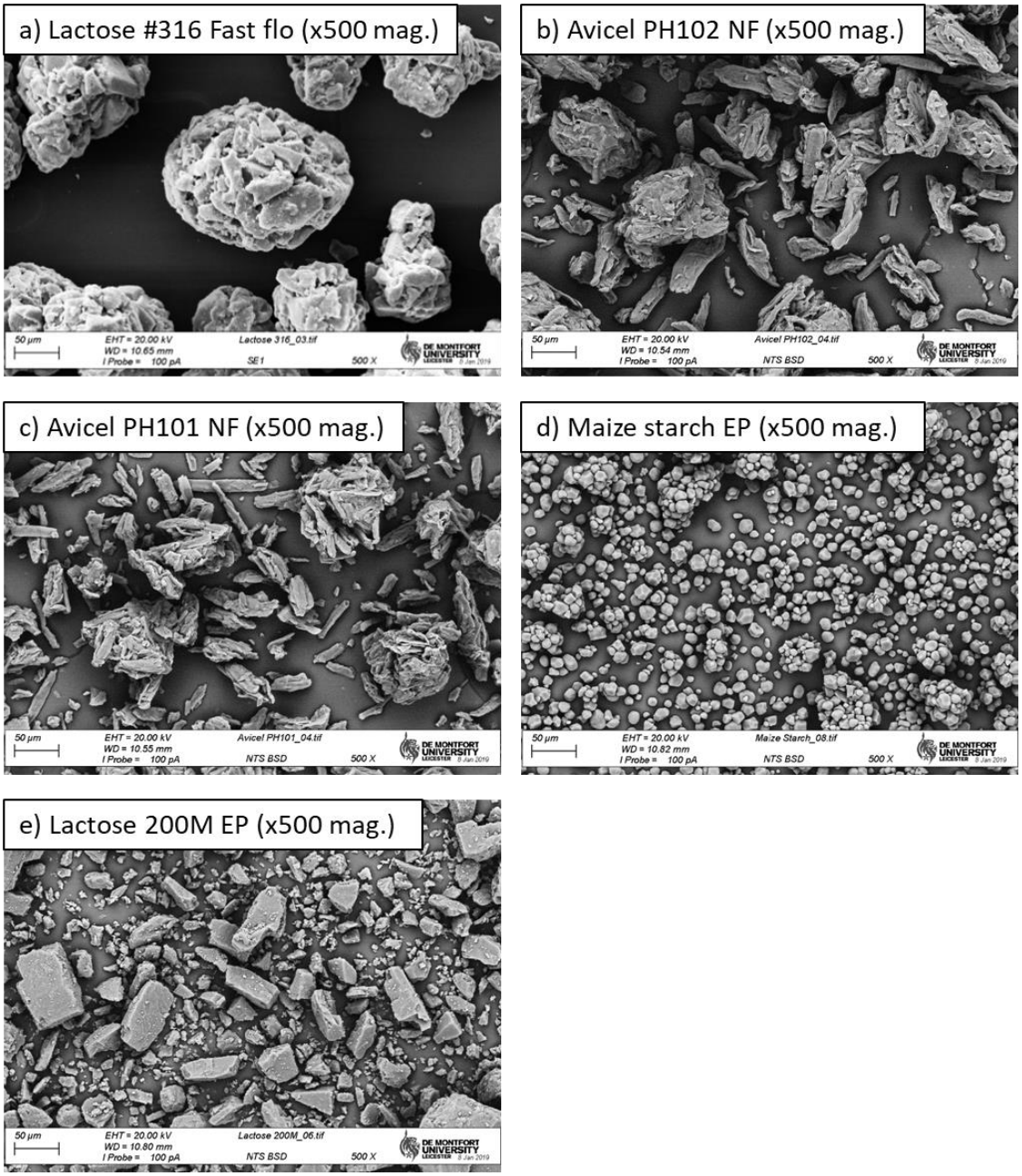

Fig. 4-5. SEM images of: a) Lactose #316 Fast Flo; b) Avicel PH102 NF; c) Avicel PH101 NF; d) maize starch EP and e) Lactose 200M EP, with magnifications stated.

4.5.1.2. Dynamic flow property analysis using the FT4 Powder Rheometer

Fig. 4-6, shows the flow energy profiles recorded for each powder recorded under stable and variable flow rates. Each datum was indicative of the total flow energy measured as the blade moved downwards through the sample. The flow parameters derived from these flow profiles are shown in Table 4-2.

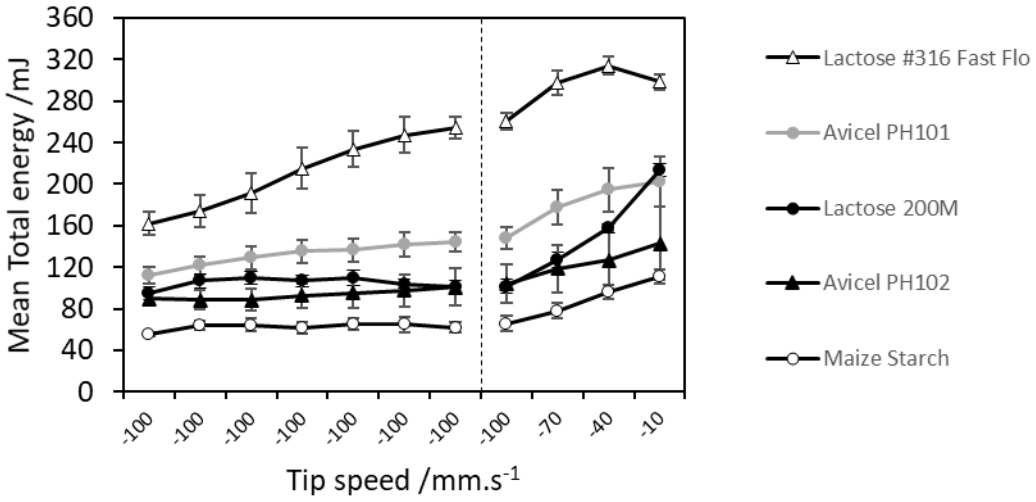

Fig. 4-6. Flow energy profiles under stable and variable dynamic flow conditions (n=6). Note: negative tip speed refers to rotation of the blade in the counter-clockwise direction.

Table 4-2. Stability & VFR dynamic flow parameters recorded for each powder (n=6). Standard deviation is expressed as a percentage. BFE = basic flow energy, SI = stability index, FRI = flow rate index, SE = specific energy, CBD = conditioned bulk density.

Material	Mean BFE, /mJ	Mean SI	Mean FRI	Mean SE, /mJ.g^{-1}	Mean CBD, /g.mL^{-1}
Maize starch EP	61.71 ± 8 %	1.11 ± 9 %	1.72 ± 12 %	6.48 ± 6 %	0.49 ± 1 %
Avicel PH102 NF	100.78 ± 18 %	1.11 ± 11 %	1.36 ± 7 %	4.55 ± 11 %	0.35 ± 0.2 %
Lactose 200M EP	101.25 ± 6 %	1.06 ± 3 %	2.12 ± 5 %	7.05 ± 5 %	0.53 ± 1 %
Avicel PH101 NF	144.38 ± 6 %	1.29 ± 4 %	1.36 ± 6 %	6.6 ± 10 %	0.32 ± 0.5 %
Lactose #316 Fast flo	253.99 ± 4 %	1.57 ± 5 %	1.15 ± 2 %	4.45 ± 2 %	0.61 ± 0.2 %

Cohesive powders were typically characterised by lower BFE and SI values, as well as higher SE and FRI values (Freeman 2007). BFE values indicated the mean demand in energy needed to achieve in for each of the powders, with Lactose #316 Fast flo being particularly intensive (mean BFE = 253.99 %) and maize starch being the least (mean BFE = 61.71 %). However, Avicel PH101 NF and PH102 NF were comparable to Lactose 200M EP in their measured BFE values, which might be attributed to their lower bulk densities. Interestingly, Avicel PH101 NF required more energy to achieve flow than Avicel PH102 NF, which may be attributed to additional particle interactions and bulk properties, such as the effect of particle shape increasing interlocking and friction (Freeman 2007).

The shape of the flow energy profiles showed the powder's response to stable and variable flow rates. Lactose 200M EP, maize starch EP and Avicel PH102 NF demonstrated consistent rheology under stable conditions, whilst Avicel PH101 NF and especially Lactose #316 Fast flo experienced effects similar to shear thickening in non-Newtonian fluids over repeated test cycles. SI values were used as markers of the stability in the powder rheology, where values that tended towards 1 indicated a more stable flowing powder as stated in (Freeman Technology 2010), which was generally true for the more cohesive powders and vice-versa.

Under variable flow rates, all powders experienced a marked increase in resistance to the rotating blade as it decreased in rotational tip speed. For Lactose 200M EP, maize starch EP and Avicel PH102 NF, this response was relatively linear, with the first powder showing a dramatic increase in flow energy with decreasing blade tip speed compared to the latter two, indicating high flow rate sensitivity. In contrast, the VFR flow energy profiles recorded for Avicel PH101 NF and Lactose #316 Fast flo were shown to plateau and slightly decrease in value, indicating a reduced flow rate sensitivity with decreasing tip speed. FRI values can be used to rank the flow rate sensitivity of each powder, with values that tended towards 3 indicating more flow rate sensitive powders as stated in (Freeman Technology 2007), which was true for the more cohesive powders as opposed to the free-flowing powders.

Stability and flow rate sensitivity can be related to the compressibility and permeability bulk properties of each powder as reported by (Freeman 2007; Leturia, et al. 2014). Under constant flow rate, free-flowing powders were indicated to have become more efficiently packed and interlocked over repeated test cycles, thus increasing the number of particles moved and consequently, their resistance to the blade. Under variable flow rates, free-flowing powders

did not experience such drastic changes in bulk density and void fraction, meaning that the overall resistance against the blade remained unaltered, especially at lower flow rates. On the other hand, cohesive powders naturally contained a large number of air pockets which collapsed when exposed to a shear stress, resulting in a stiff plaque of powder with high inertia. As a result, these powders could be easily entrained to the motion of the blade and thus flowed consistently with the given flow rate. Also, since their particle size was generally small, a lower number of particles were moved by the blade when compared to the coarser materials, meaning that the powder flow rate was less likely deviate from that of the blade (Freeman 2007; Leturia, et al. 2014).

Flow energies measurements obtained during upwards testing were used to investigate powder cohesivity effects. In this scenario, the blade moved in the upwards direction, the powder was unconfined, and the shear stress generated was low. Consequently, the weight of the powder on the blade acted as the major source of resistance which was further compounded by any cohesive forces present in the sample (Freeman 2007; Leturia, et al. 2014). SE values indicated the flow energy required during this testing, where SE < 5 = low cohesion and 5 < SE < 10 = moderate cohesion (as stated in FT4 documentation on specific energy). Lactose #316 Fast-flo and Avicel PH102 NF were classified as low cohesion powders, whereas Lactose 200M EP, maize starch EP and Avicel PH101 NF were classified as moderately cohesive. Interestingly, Avicel PH101 NF yielding a higher SE value compared to maize starch (6.6 mJ/g and 6.48 mJ/g respectively), despite being less cohesive. In the case of the former, it may be that the resistance to flow during upwards testing was also exacerbated by other particle-particle and particle-wall interactions which may include interlocking due to irregular particle shapes (Fig. 4-5c). It is worth noting that depending on the flow parameter, Avicel PH101 NF exhibited traits of both a cohesive and a good flowing powder, indicating its borderline flowability.

Table 4-3, summarizes the results from these bulk property and dynamic flow tests and thus characterizes the cohesivity of each powder based on these results. In general, cohesive powders (Lactose 200M EP and maize starch EP) were characterized by: high bulk compressibility; low bulk permeability; low input flow energy in a high stress confined environment; high input flow energy in a low stress unconfined environment; good flow stability; and good flow rate sensitivity. Non-cohesive powders (Avicel PH101 NF, Avicel PH102

NF and Lactose #316 Fast flo) were generally characterized with contrasting qualities to the cohesive ones.

Table 4-3. Powder cohesivity characterized based on FT4 parameters. CPS = compressibility percentage, PD = pressure drop across the powder bed, BFE = basic flow energy, SI = stability index, FRI = flow rate index, SE = specific energy.

Material	Cohesivity classification	CPS, /%	PD, /mBar	BFE, /mJ	SI	FRI	SE, /mJ.g^{-1}
Lactose 200M EP	Moderately cohesive	High	High	Moderate	~1	(1.5 < x < 3.0)	> 5
Maize Starch EP	Moderately cohesive	Moderate	High	Low	>1	(1.5 < x < 3.0)	> 5
Avicel PH101 NF	Fair-flowing	Moderate	Very low	Moderate	> 1	< 1.5	> 5
Avicel PH102 NF	Fair-flowing	Moderate	Very low	Moderate	> 1	< 1.5	< 5
Lactose #316 Fast flo	Free-flowing	Low	Very low	High	> 1	< 1.5	< 5

4.5.2. Flow characterisation via FFT analysis of the electrostatic signals

4.5.2.1. Qualitative relationship between the FFT spectrum and powder cohesivity

Fig. 4-7, shows a typical FFT spectrum recorded for one of the powders which was conveyed using the twin-screw feeder at a screw speed of 40 rpm. Each FFT spectrum typically contained two key features: 1) discrete harmonics and a continuous baseline containing numerous frequency components. Both features reflected the different types of depositions present within the flow pattern that developed as a result of the powder interaction with the screw feeding mechanism, which is explained below.

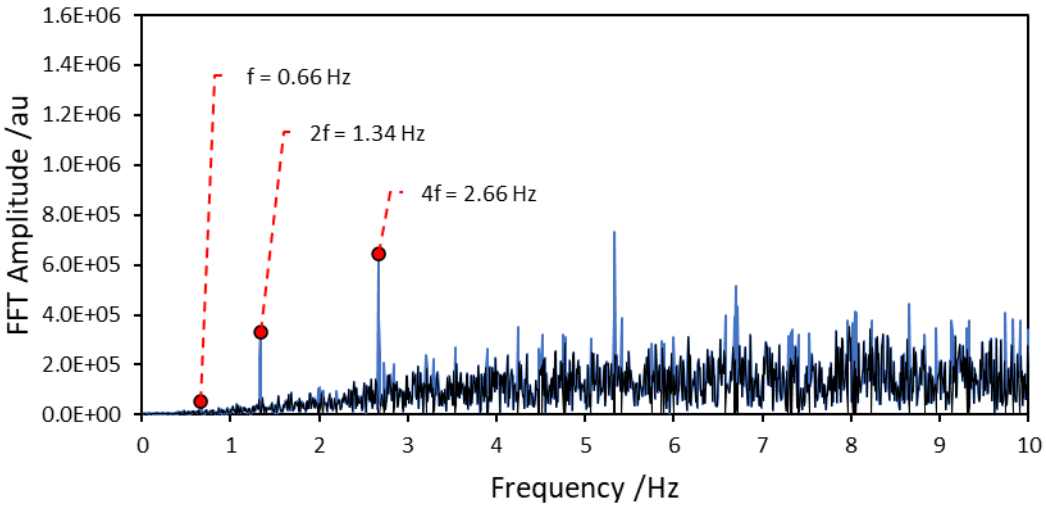

Fig. 4-7. FFT spectrum (magnified to a 0 – 10 Hz window) recorded for a maize starch EP conveyed at 40 rpm using a twin-screw feeder. Important harmonics are labelled in multiples of ("f") and the baseline is shaded in black.

The leftmost harmonic in each FFT spectrum is defined by a fundamental frequency *f* and by extension the screw speed in rps (0.66 Hz and 0.66 rps respectively for the above example). This meant that there was reoccurring element present in the electrostatic signal induced by powder flowing past the EPFS at that given frequency. Since it took a single screw approximately 0.66 s to complete a 360° rotation, it was strongly implied that this reoccurring element was induced by a powder deposition made at that same point of a screw's orientation with every full turn completed. Also present in the FFT spectrum are higher order harmonics of the fundamental frequency, which were coupled to the design of the screws as well as the screw speed. Each screw possessed two threads, the components responsible for conveying the powder down the barrel (Fig. 4-8a). These screw threads terminate at the barrel outlet, with one thread positioned at 180° with respects to the other. Consequently, this meant that a single powder lot could be deposited each time the screw completed a 180° turn, or two lots could be deposited for a completed full 360° rotation (Fig. 4-8b). Thus, these depositions accounted for the harmonic made at double the fundamental frequency, i.e. *2f*. Additionally, the screw feeder used two screws which were offset to the other by an angle of 90°. This meant that a powder lot could be deposited each time a single screw completed a 180° turn, which due to their positioning, effectively resulted in a deposition made every 90° turn of the screw combination. This yielded a harmonic at a frequency four times greater than the fundamental frequency, i.e. *4f*.

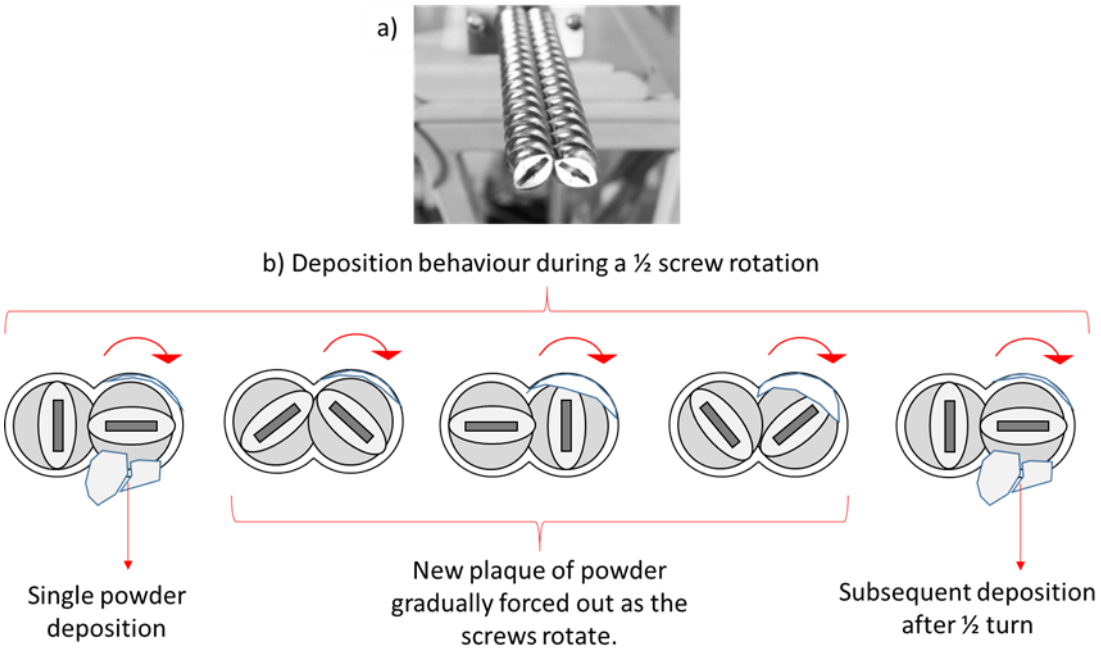

Fig. 4-8. a) twin-screw design and b) illustration describing the deposition of a large plaque of powder every half turn of the screws.

The harmonics: *f*, *2f* and *4f*, were thought to be the primary indicators of the periodic element within the powder flow pattern. Other harmonics such as *3f*, *5f* and *6f* can also appear in the FFT spectrum, although these were not found to be related to any real powder depositions and instead thought to result as a by-product during the FFT procedure (i.e. fitting multiple harmonics to non-integer cycles and fitting sine wave profiles to non-sinusoidal discharge profiles).

The remaining feature in the FFT spectrum is the baseline, which is a densified collection of frequency components present across a wide frequency range. These were connected to powder depositions lacking a periodic element. This feature appeared to possess a modality in its distribution which was typically strongest around ~10 Hz for all powders, which may indicate that non-periodic depositions made around this frequency were the most common. These baseline shapes are remarkably similar to the FFT spectra reported by (Fu, et al. 2018), which were also shown to be linked to their respective particle velocities.

Fig. 4-9a-e, shows the FFT spectrum recorded for each of the screw-fed powders, arranged in order from non-cohesive to most cohesive based on FT4 outputs (see Table 4-3). In each spectrum, the *2f* harmonic was always distinguishable, whereas the *f* and *4f* harmonics were

occasionally absent, although this was mostly only true for the higher cohesivity powders. Additionally, with the increase in powder cohesivity the relative amplitudes of the harmonics become smaller with respects to the baseline, suggesting that non-cohesive powders tended to develop more periodic components within their powder flow pattern compared to cohesive ones.

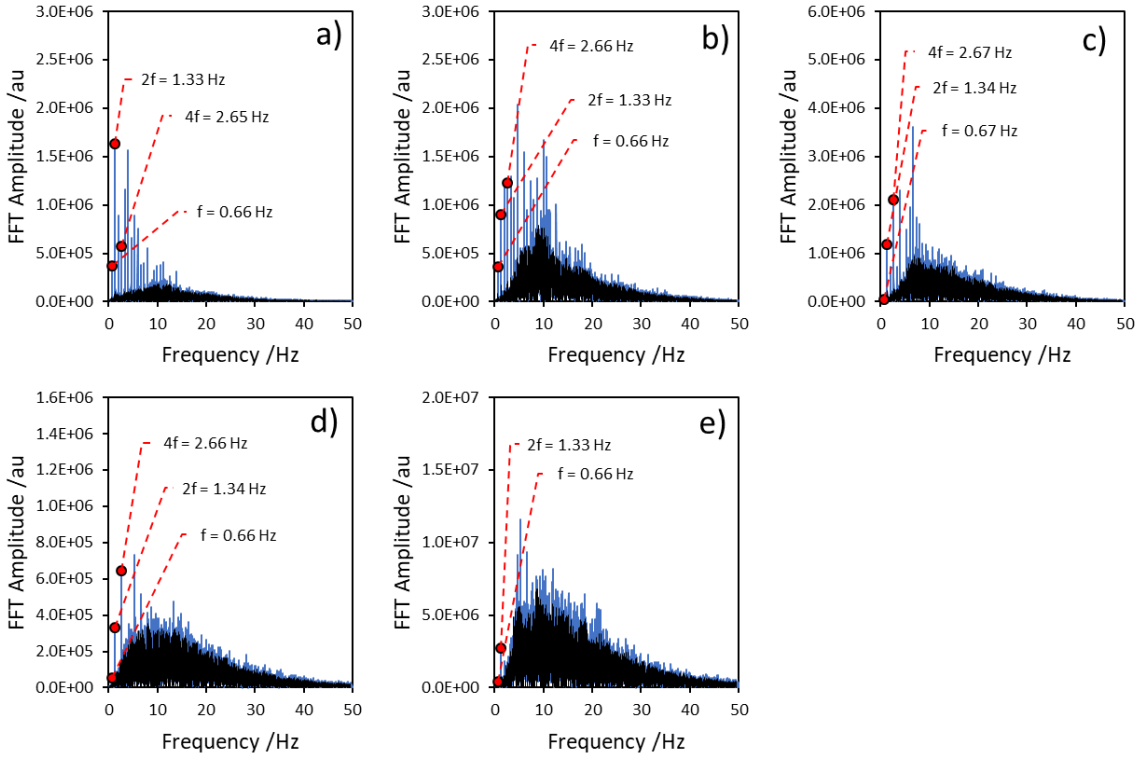

Fig. 4-9. FFT spectra of the electrostatic signals recorded for powders conveyed using a twin-screw at 40 rpm including: a) Lactose #316 Fast flo; b) Avicel PH102 NF; c) Avicel PH101 NF; d) maize starch EP; and e) Lactose 200M EP.

Fig. 4-10a-e, shows images taken from video recordings of the experiments, clearly illustrating the packing behaviour due to the differences in cohesivity between each powder. Lactose #316 Fast flo, flowed in a fluid-like fashion with no signs of agglomeration present. Avicel PH102 NF flowed in a similar manner to the previous powder, although this powder did show signs of loose agglomeration. Avicel PH101 NF demonstrated elevated agglomeration compared to Avicel PH102 NF, although these plaques of powder did not appear to hold their structure at the barrel terminal. Finally, Lactose 200M EP and maize starch EP, flowed almost exclusively as large agglomerates, which unlike Avicel PH101 NF, held their shape for a brief period after leaving the barrel.

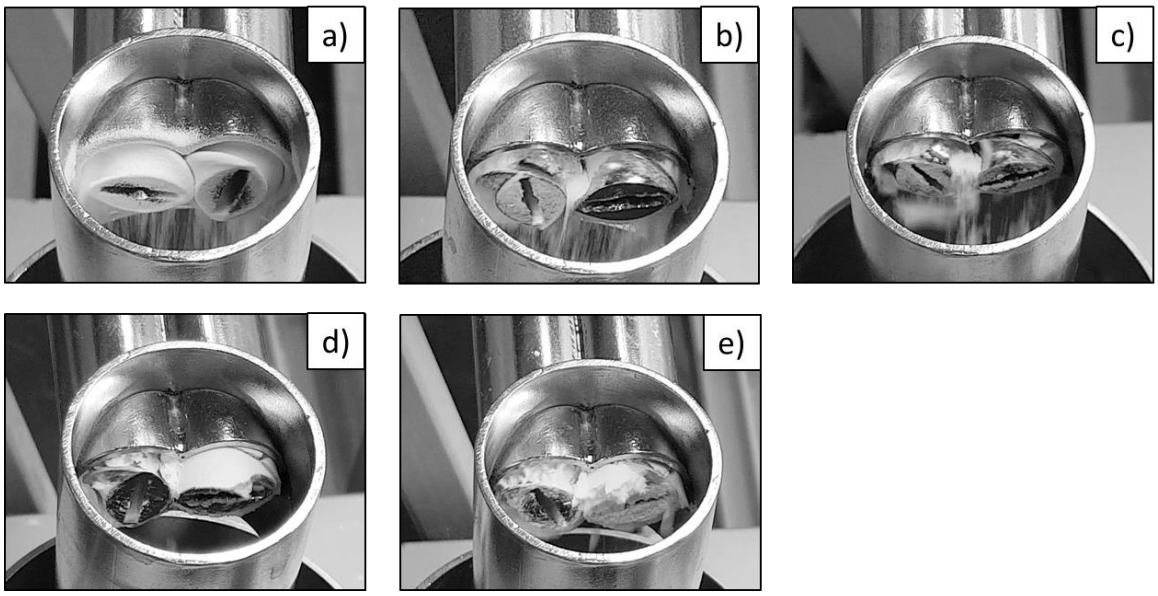

Fig. 4-10. Screw feeder powder deposition images of: a) Lactose #316 Fast flo; b) Avicel PH102 NF; c) Avicel PH101 NF; d) maize starch EP; and e) Lactose 200M EP.

Next, the method used to extract values from the FFT spectrum data and qualify the respective flowing powder cohesivity is elaborated. Here, the powder cohesivity based on the ratio of the harmonic to baseline frequency components, i.e. periodic to non-periodic powder depositions. To achieve this the following two-step filtering procedure was then applied in order to isolate the baseline from the FFT spectrum:

a) First filter: All FFT values with magnitude greater than the mean of all FFT values in the entire spectrum plus an *n* number of standard deviations were removed, where *n* = 3 for Lactose #316 Fast flo and *n* = 6 for the remaining powders.
b) Second filter: For the dataset with the above data applied, across consecutive 100 data point intervals, FFT values with a magnitude greater than the mean of all FFT values within that respective interval plus 2 standard deviations were removed.

Subsequently, the harmonics were obtained by subtracting the baseline dataset from the original FFT spectrum per frequency interval, then the important harmonics (*f*, *2f* and *4f*) were isolated by truncating the data to narrow frequency windows.

To the best of the author's knowledge, no standardised procedure current exists in literature for filtering harmonics and baseline from an FFT spectrum. Previous attempts at studying

features of the FFT spectra included: taking the moving average across the baseline and determining its area under the curve, or by studying the change in baseline shape, with attempts to link both to powder cohesivity. However, the above procedure was decidedly the most suitable method since it considered both the periodic and non-periodic components of flow.

Two indices were developed: the first from the ratio of sum of the important harmonics to total sum of baseline frequency components (Equation 19), and the second from the ratio of the average value of the important harmonics to the average value of the baseline frequency components (Equation 20), classified as $\mathrm{FPI}_{(\mathrm{sum})}$ and $\mathrm{FPI}_{(\mathrm{avg})}$ respectively, where FPI = flow periodicity index.

$$\mathrm{FPI}_{(\mathrm{sum})} = \frac{\text{Sum of harmonics } (\mathrm{'f'}, \mathrm{'2f'} \,\&\, \mathrm{'4f'})}{\text{Sum of all baseline components}} \qquad \text{(Equation 19)}$$

$$\mathrm{FPI}_{(\mathrm{avg})} = \frac{\text{Average of harmonics } (\mathrm{'f'}, \mathrm{'2f'} \,\&\, \mathrm{'4f'})}{\text{Average of all baseline components}} \qquad \text{(Equation 20)}$$

Fig. 4-11a-b, organizes each powder in ascending order of mean $\mathrm{FPI}_{(\mathrm{sum})}$ and $\mathrm{FPI}_{(\mathrm{avg})}$ value respectively. In both instances, FPI values that tended towards zero indicated cohesive powder flow (i.e. less periodic depositions/harmonics with respects to non-periodic depositions/baseline), and vice-versa. The rank orders in mean $\mathrm{FPI}_{(\mathrm{sum})}$ and $\mathrm{FPI}_{(\mathrm{avg})}$ correlated well with the flowability data in Table 4-3 and deposition images Fig. 4-10a-e, confirming that these indices are likely to be driven by powder cohesivity. Based on this data, preliminary thresholds could be proposed to characterize the flowability of each powder based on the respective $\mathrm{FPI}_{(\mathrm{sum})}$ and $\mathrm{FPI}_{(\mathrm{avg})}$ values. For cohesive powders, these were < 0.005 and 10 respectively. For poor/fair-flowing powder, $\mathrm{FPI}_{(\mathrm{sum})}$ and $\mathrm{FPI}_{(\mathrm{avg})}$ values were within the range of 0.005 - 0.01 and 10 - 20 respectively. For very free-flowing powders, $\mathrm{FPI}_{(\mathrm{sum})}$ and $\mathrm{FPI}_{(\mathrm{avg})}$ were > 0.01 and > 20 respectively. However, it is acknowledged that these index thresholds are based on the data obtained for a small selection of powders which is the main limitation of this approach. As such, it will be necessary to expand these measurements by accommodating a higher number of powders across a wider range of flow properties. As well, a comment is provided on the role of moisture and its impact electrostatic outputs. Although moisture

content is known affect the amount of charge on the powder (Rowley and Mackin 2003), it was not expected to largely impact the frequency-based outputs since these were mainly driven by temporal factors (i.e. periodicity in flow). Regardless, there are two instances where it would be expected for moisture content to impact the output electrostatic signal: i) where the moisture content change leads to a change in powder cohesivity, and ii) where the moisture content becomes elevated to a degree that the powder is unable to charge due to low surface resistivity.

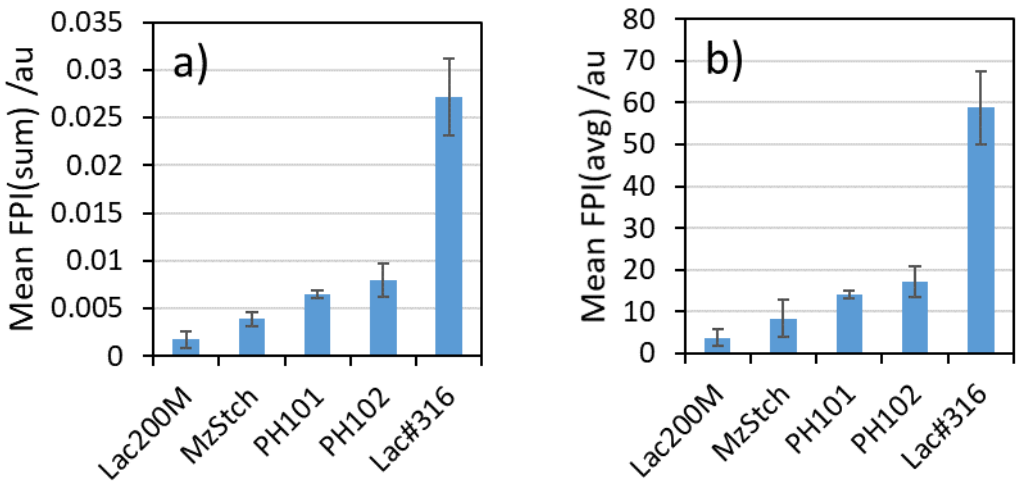

Fig. 4-11. a) Mean $FPI_{(sum)}$ and b) mean $FPI_{(avg)}$, determined for each powder (n=3).

The student's t-test was applied to the data in order to ascertain whether the yielded FPI values were significantly different from each other, where $p < 0.05$ (see Table 4-4 and Table 4-5). In most instances, the differences in FPI values between each powder were shown to be statistically significant, thus suggesting that powder cohesivity had a real effect on the periodic/non-periodic data. The only exception was observed for Avicel PH101 NF with respect to Avicel PH102 NF, where $p > 0.05$, which seemed to imply that their periodic/non-periodic distributions were similar in nature; unsurprising given their similarities in dynamic flow characteristics (Table 4-3). Although, this was not the case when comparing the slight differences in their bulk properties (Fig. 4-3, Fig. 4-4 and Table 4-1) and their observed packing behaviours (Fig. 4-10b-c). This could suggest a lack of sensitivity in the FPI values to powders which express alike flow patterns due to similar levels in cohesivity.

Table 4-4. Results from the student's t-test for the $FPI_{(sum)}$ values. p < 0.05. Non-significant interactions are coloured white.

	Maize Starch	Avicel PH101	Lactose 200M	Lactose #316	Avicel PH102
Maize Starch		0.0054	0.0295	0.0006	0.0197
Avicel PH101	0.0054		0.0012	0.0009	0.2316
Lactose 200M	0.0295	0.0012		0.0004	0.0053
Lactose #316	0.0006	0.0009	0.0004		0.0016
Avicel PH102	0.0197	0.2316	0.0053	0.0016	

Table 4-5. Results from the student's t-test for the $FPI_{(avg)}$ values. p < 0.05. Non-significant interactions are coloured white.

	Maize Starch	Avicel PH101	Lactose 200M	Lactose #316	Avicel PH102
Maize Starch		0.0054	0.0295	0.0006	0.0197
Avicel PH101	0.0054		0.0012	0.0009	0.2316
Lactose 200M	0.0295	0.0012		0.0004	0.0053
Lactose #316	0.0006	0.0009	0.0004		0.0016
Avicel PH102	0.0197	0.2316	0.0053	0.0016	

The following paragraph attempts to relate the FFT outputs with the powder flow, with particular emphasis given on the connection between powder cohesivity, packing behaviour and the periodicity in flow pattern. The packing behaviour within the barrel was determined by the ability of each powder to agglomerate, retain their agglomerated state due to cohesive strength and expand to occupy the volume of the barrel. The compressibility and permeability results could be used to identify which powders were most and least likely to exhibit these characteristics (see Fig. 4-3 and Fig. 4-4). Incidentally, the rank order in CPS and PD was the same as the FPS values, which supported the link between these characteristics and periodicity in the flow pattern (Table 4-6). One would expect that the cohesive powders would retain the periodicity of the rotating screw mechanism, which was inferred by the FRI and SI outputs from the FT4 Powder Rheometer, where cohesive flow was shown to be dependent on the input stress. Moreover, provided that this input stress remained consistent, the flow rate should have also remained consistent. However, it was expected that the FRI and SI outputs were mostly likely only relevant to the flow behaviour when the powder was conveyed

throughout the barrel, not during deposition. As shown in the video recordings, when the powders began to deposit from the barrel, they exhibited characteristic behaviours which depended on their cohesivity and previous interactions within the barrel. Cohesive powders retained their plaque form developed due to compression within the barrel. Upon exiting the feeder, the plaques were able to retain their shape for a short period of time until their weight overcame their cohesive strength. It was thought that this random delay in deposition from the screws corresponded to the non-periodic components within the FFT spectra recorded for the cohesive powders. In contrast, since non-cohesive powders possessed a lower propensity for agglomeration, these were more likely to deposit immediately upon reaching the barrel terminal, thus retaining the periodicity of the rotating screws. This behaviour may be seen as analogous to the fluid motion of water flowing out of an Archimedes screw. The SE values were thought to describe the tendency for powders to retain their agglomerated state upon deposition whilst under the conditions of dynamic flow and in an unconfined state. Cohesive powders which scored higher in SE were more likely to hold their structure under gravity compared to non-cohesive ones. Although, it should be acknowledged that the shear conditions between the barrel terminal and dynamic flow tester within FT4 Powder Rheometer were likely to be different. In both devices, the powder was forced to move by the shear mechanism and their resistance to deposition was the result of the cohesive forces. However, in case of the rheometer, the measured resistance (i.e. the SE values) was also compounded by friction between the powder bed and the split cell wall. Moreover, both devices conveyed the powders in different directions. The differences between these shear conditions were likely the reason why SE and FPI values were ranked differently in cohesivity (Krantz, et al. 2009).

An additional comment should also be made when comparing the rank orders obtained for the SE, CPS, PD and both FPI values (Table 4-6). Although each parameter was ordered generally in the same manner with respect to powder cohesivity, neither showed a good correlation when plotted against each other, which was no doubt due to the differences in the shear conditions used to characterise each flow parameter (Krantz, et al. 2009). Despite the lack of correlation, each flow parameter can be used understand the impact of powder cohesivity on the flow behaviour at different stages of the process, i.e. CPS and PD for describing the packing behaviour, SE for understanding the deposition behaviour, and FPI for describing the flow periodicity in the depositing powders.

Table 4-6. Cohesivity rank order based on FFT parameters, FT4 parameters and bulk properties.

Cohesivity ranking	$FPI_{(sum)}$, /au	$FPI_{(avg)}$, /au	SE, /mJ.g^{-1}	CPS, /%	PD, /mBar
Cohesive	Lactose 200M EP	Lactose 200M EP	Lactose 200M EP	Lactose 200M EP	Lactose 200M EP
	Maize Starch EP	Maize Starch EP	Avicel PH101 NF	Maize Starch EP	Maize Starch EP
	Avicel PH101 NF	Avicel PH101 NF	Maize Starch EP	Avicel PH101 NF	Avicel PH101 NF
	Avicel PH102 NF	Avicel PH102 NF	Avicel PH102 NF	Avicel PH102 NF	Avicel PH102 NF
Free-flowing	Lactose #316 Fast flo	Lactose #316 Fast flo	Lactose #316 Fast flo	Lactose #316 Fast flo	Lactose #316 Fast flo

The final part of this discussion briefly examines the relevance of this technology to the powder handling within industry and its potential applicability to real time powder flow measurements. There may be a potential application used to capture changes in the flowing powder cohesivity as an early indication of product failure, induced by, for example the uptake of moisture or variation in the powder flow properties (i.e. particle size), or in systems where fouling contributes to agglomeration and thus a change in flow pattern. However, it must be stated that the output flow parameters are entirely dependent on periodicity being present within the flow pattern. Consequently, this prevents the applicability of the technology for cohesivity measurement to alternative common modes of flow such as dense phase hopper flow and pneumatic flow. There may be an application for this technology within continuous manufacture, since screw feeders are widely employed as a medium for dispensing, blending and conveying between processes.

4.6. Conclusions

In this work, a methodology was developed to characterize differences in pharmaceutical powder flow regimes based on their inherent cohesivity. These were derived from an electrostatic signal, measured using an EPFS, which was capacitively induced by the powder surfaces charges under the conditions of flow. Fast-Fourier-Transformation (FFT) algorithms were used to convert the signal into the frequency domain (FFT spectrum), which contained frequency components linked to the periodicity in the respective flow pattern. It was found that the intensity of specific frequency components showed a trend with the powder cohesivity. Free-flowing powder flow contained a stronger periodic components (harmonics),

whereas cohesive powder flow contained stronger non-periodic components (baseline). Through further analysis, two FFT flow indices, $\mathrm{FPI}_{(\mathrm{sum})}$ and $\mathrm{FPI}_{(\mathrm{avg})}$, were developed based on the relative differences in intensity between the harmonics and baseline components. These were thought to be related to the powders packing properties within the feeder and their resistance to deposition under gravity (or lack of), due to their cohesive strength developed under a compressed state. FFT indices and FT4 parameters (SE, CPS and PD) were shown to rank the powders in very similarly orders of cohesivity, although it should be stated that the latter were treated as predictive of the flow adopted by the powders in the screw feeder rather than during deposition. Instead, these were used to develop understanding on the packing and deposition behaviours exhibited in-process. With further development, it is anticipated that the information yielded using this technology may be used to predict and/or detect the onset of adverse effects in the powder flow, induced by the changes in the powder cohesivity, e.g. blockages propagated by agglomeration.

Future work should focus on areas not covered in this work, most notably particle sizing techniques. The scope of this study primarily covered the relationship between the powder, its packing properties and the FFT flow parameters. At this stage, the inherent particle size was not characterised since it was likely that these sizes would alter within the screw feeder, either due to fracture or agglomeration. An in-line measurement of the particle size would be more relevant since they could capture the agglomerate size, which is more relevant to the FFT measurement. A commercial technology that could be applied for this purpose is the Eyecon$_2$ (Innopharma Labs), a PAT based on digital imaging which can report particle size and shape characteristics under the conditions of flow. Cohesivity measurements via FFT should also be expanded using a broader range of powders with different flow properties. These experiments should identify the technology failure modes, which include but are not limited to: the compatibility of the material with respects to the electrostatic measurement principle; the maximum flow concentration that may be interrogated using this method; and the maximum/minimum amount of charge that may be detected by the EPFS. Flow characterisation tests should also be expanded, including shear cell testing which may be relevant in describing the capacity for the consolidated powders to yield once they reach the barrel terminal. DEM may also be used to assess the particle interactions in the barrel which cannot be observed experimentally. In these models, the effects of the powder cohesivity on the particle motions and compaction properties may be studied.

Chapter 5. Investigation into the relative charging characteristics of a number of screw-conveyed pharmaceutical powders using an in-line Electrostatic Powder Flow Sensor (EPFS).

5.1. Introduction

Charging or triboelectrification of powders is ubiquitous within all processes that handle them since they often involve numerous particle collisions. Although, their effects may not be noticed until they adversely impact the nature of flow or the performance of the process. For example, charging can induce cohesive interactions within the powder, due to electrostatic attraction between the particles. Electrostatic attraction may also occur between the charged particles and the contact surface of processing equipment (Peltonen, et al. 2018; Samiei, et al. 2017). Both of these effects can potentially result in the deterioration of a powder's in-process flowability or cause adhesion of API/excipients to the processing equipment (Kaialy, et al. 2014), both of which can impact the final product CQAs downstream. Powder charging can also induce a spark within processes with high dust concentrations (e.g. fluidised bed dryers), resulting in catastrophic explosions (Eckhoff 2009; Glor 1985). To address these adverse effects, steps can be taken in order to prevent or otherwise reduce the quantity of charge generated within a process. These can include earthing of the equipment (Engers, et al. 2006) and incorporating anti-static excipients (Engers, et al. 2006; Lumay, et al. 2019).

A powder's charging capacity is typically predicted using the Faraday Cup technique, which comprises of a conductive cup connected to an electrometer (British Standards Institute 1995; British Standards Institute 1996). The typical method involves charging the powder externally (e.g. by shaking in a container), and then feeding it into the cup whereby the surfaces charges induce a potential difference on the inner cup surface which is subsequently detected by the electrometer (Lumay, et al. 2019; Samiei, et al. 2017). Moreover, by normalizing the charge to the powder weight, its specific charging capacity may be determined (Engers, et al. 2006; Matsusaka, et al. 2010; Šupuk, et al. 2012). Materials are typically organised into a series of relative chargeability and polarity, known as a tribo-series (Šupuk, et al. 2012; Watanabe, et al. 2007; Wong, et al. 2015), which are generally useful in ascertaining the chargeability of powders (Karner and Anne Urbanetz 2011), although they are largely empirical (Wong, et al. 2015), and highly dependent on the manner and conditions under which they were charged and measured.

There are also a couple of major disadvantages to the Faraday Cup method itself. Firstly, it is closed ended in nature, meaning that a limited quantity of powder may be interrogated until its maximum capacity is reached. This limited design also serves to impede the natural flow behaviour of the powder within a process. On-line sampling techniques may be able to extract powder directly from the process but this can actually induce further charging (Shi, et al. 2017). Additionally, the Faraday Cup is only capable of yielding a single static value of charge per measurement of powder, requiring emptying and cleaning protocols to be established in order to sample new powders. As a result, it also is challenging to predict the onset of charging phenomenon in real-time using the standard method.

It is important to recognise that charging is a very much a dynamic process, one which is dependent on the number and nature of collisions involved, as a function of time (Gao, et al. 2018; Šupuk, et al. 2012). Therefore, in order to predict a powder's propensity for charging in a given process, the test methodology should also simulate similar process shear and packing conditions. Moreover, given that the process of charging can also be time-dependent, powder charge should also be characterised as a continuous parameter. Unfortunately, no standardised method can quantify the dynamic charging behaviours of powders.

Electrostatic sensors, whose principle of operation are based on the electrification of particles (Coombes and Yan 2015), have been used to analyse the real-time charging properties of powders as a continuous parameter in processes such as pneumatic conveyors (Gao, et al. 2018; Qian, et al. 2017), and fluidised bed dryers (Shi, et al. 2017; Zhang, et al. 2018). However, in-line charge measurement techniques for pharmaceutical processes have rarely been reported.

The aim of this work was to study the dynamic charging characteristics of five different pharmaceutical powders using an EPFS. A volumetric twin-screw feeder was selected as the conveying device given that it involves a vigorous flow mechanism which is suitable for inducing powder triboelectrification. A relative measurement of the powder charge was obtained by normalizing the RMS of the electrostatic signal against its mass flow rate in order to yield the charge per gram per second, which could be monitored as a time series.

5.2. Materials

The details of the pharmaceutical powders used in this study are listed in (Table 5-1). Each powder was stored at ambient conditions and used “as received”.

Table 5-1. Excipient details.

Material	Trade name	Manufacturer	Nominal particle size stated by the manufacturer /µm
Lactose monohydrate (spray-dried)	Lactose #316 Fast-flo	Foremost / Kerry	106
Lactose monohydrate	Lactose 200M EP	Blackburn distributions	75
Microcrystalline cellulose	Avicel PH102 NF	FMC Biopolymer	100
Microcrystalline cellulose	Avicel PH101 NF	FMC Biolpoymer	50
Maize starch	Maize Starch EP	JM Loveridge	N/S*

*N/S = information not supplied

5.3. Methods

5.3.1. Moisture analysis

It was initially intended for the moisture content for the non-crystalline materials to be determined via thermo-gravimetric analysis (TGA) (Pyris 1, PerkinElmer). The moisture content of Avicel PH101 was characterised using temperature range of 30-200°C and drying rate of 5°C. However, following these measurements, the TGA instrument was out of service. For the remaining powders, their moisture content was assessed using their specified oven drying conditions stated in the British Pharmacopoeia (British Pharmacopoeia Commission 2019d; British Pharmacopoeia Commission 2019e; British Pharmacopoeia Commission 2019f). The method used (British Pharmacopoeia Commission 2019a), was slightly modified since the powders tended to gain weight during cooling. Instead, once the dried samples were removed from the oven, they cooled in a desiccator for 10 mins, which was conditioned at ~ 0 %RH using activated 2.5 – 5.0 mm molecular sieve beads (Type 4A, Fisher Scientific). Oven drying method was not performed for Avicel PH101 NF since only a limited sample size was available.

5.3.2. SEM imaging

Scanning-electron-microscopy (SEM) images of each powder were taken prior to screw conveying, with additional SEM images obtained for Lactose #316 Fast flo after experimentation. Each sample was sputtered coated with 15 nm of gold using a rotary pump coater (Q150RS, Quorum). The SEM microscope used was an EVO LS 15 model (Zeiss) and images were taken using an accelerated voltage of 20 kV.

5.3.3. Electrostatic measurements of powder conveyed using the twin-screw feeder

The powder conveying component of the rig comprised of a volumetric twin-screw feeder (T20, Coperion K-Tron), which was mounted on an anti-vibration platform, designed to minimize the vibration induced by the screw feeder gearbox on the EPFS cabling that resided within the near vicinity. A smaller stand was installed beneath the outlet of the screw feeder which housed the EPFS and the balance. The TIA and DAQ were installed on a separate platform away from the EPFS. The top EPFS electrode was connected to Channel 2 on the TIA and vice-versa (so that the top electrode was indicated by Signal 1 in the data sets). Additionally, a video camera mounted on a tripod was used to record footage of the powder depositing from the feeder outlet.

The screw speed was set to 40 rpm with the screw feeder in an empty state. 500 g of a material was dispensed into a metal tray and careful loaded into the feeder hopper to minimize charging. It was also ensured that the hopper lid was in place to prevent any aeration of the powder bed during feeding. The electrostatic/gravimetric measurement and video camera recordings were executed simultaneously, with the screw feeder switched on approximately five to ten seconds afterwards. The measurement run was sustained until the hopper was emptied of powder. Measurements were repeated three times per material using a fresh quantity of powder. Also, between experimental repeats, the screw feeder and its parts were cleaned using ethanol.

It is important to state that there was no means to control the temperature and relative humidity, therefore all experiments were performed under ambient conditions. Each set of experiments were performed on separate days per material, during which a temperature and

humidity probe (View 2, TinyTag) was used to record the ambient conditions of the lab. Table 5-2, shows the range in the minimum temperature and humidity measured during the course of the repeated experiments of each powder. Since the powders were conveyed under the same storage conditions and the experiment duration was short at 8-10 minutes each, it was not expected for the moisture content to drastically change during the short experimental periods.

Table 5-2. Range in the environmental conditions recorded during electrostatic/gravimetric experiments for each powder.

Material	Temperature range /°C	RH humidity range /%
Lactose #316 Fast flo	18.3 – 18.9	38 - 42
Lactose 200M EP	17.4 – 17.7	37.5 – 43.5
Avicel PH101 NF	18.9 – 19.9	39.5 – 44.9
Avicel PH102 NF	20.2 – 20.5	44.9 – 45.9
Maize starch EP	16.2 – 16.5	44.4 – 47.4

5.4. Raw signal and data processing

The raw electrostatic signals were low-pass filtered of frequency components at 50 Hz and >100 Hz, using the procedure described in Section 2.4. The RMS of the electrostatic signals were calculated for the filtered signals using the procedure described in Section 2.3. In Microsoft Excel, the mass flow rate was determined from the cumulative weight data (Fig. 5-1a), by applying the equation for linear regression (Equation 16), across consecutive 0.5 s intervals (Fig. 5-1b). Note. that in this particular mass flow profile two large spikes were present at 339.5 and 371 s, which seemed to indicate a transient loss in mass flow rate. In actuality these spikes were negative gradients which arose during data-processing and were considered artifacts, although these were not filtered out. In the filtered RMS data (Fig. 5-1c) the data points were averaged over 0.5 s intervals in order to align the dataset with that of the mass flow rate profiles (Fig. 5-1d). In doing so, the density of the RMS signal was reduced, enabling the trend in the data to be easily visualized. Furthermore, in order to account for a potential baseline effect, the mean RMS amplitude was determined for zero powder flow (i.e. the signal measured prior to switching on the screw feeder), which was then subtracted from

each RMS data point. Subsequently, at each time point the RMS was normalized against the corresponding mass flow rate (Fig. 5-1e), which was expressed in millivolts per gram per second ($mV.g^{-1}.s$), i.e. the charge per gram per second. It is important to recognise that the normalised signal provided a relative measure of specific charge, given the in-homogeneous spatial sensitivity of the electrodes and the flowing solids distribution (Qian, et al. 2012). Also, note that the terminology, normalized RMS and relative powder charge are synonymous and are thus used interchangeably throughout this chapter. Attention is also directed to a specific feature of these profiles, where the normalized RMS signal fluctuates between very large and small values at the latter time points when mass flow rate is essentially zero. However, small quantities of residual powder within the screw feeder hopper were occasionally dosed, in which case the mass flow rate slightly increased very briefly. When normalising the corresponding RMS values by the low mass flow rates, the result was a significantly large normalised RMS value. These regions were truncated out during data-processing.

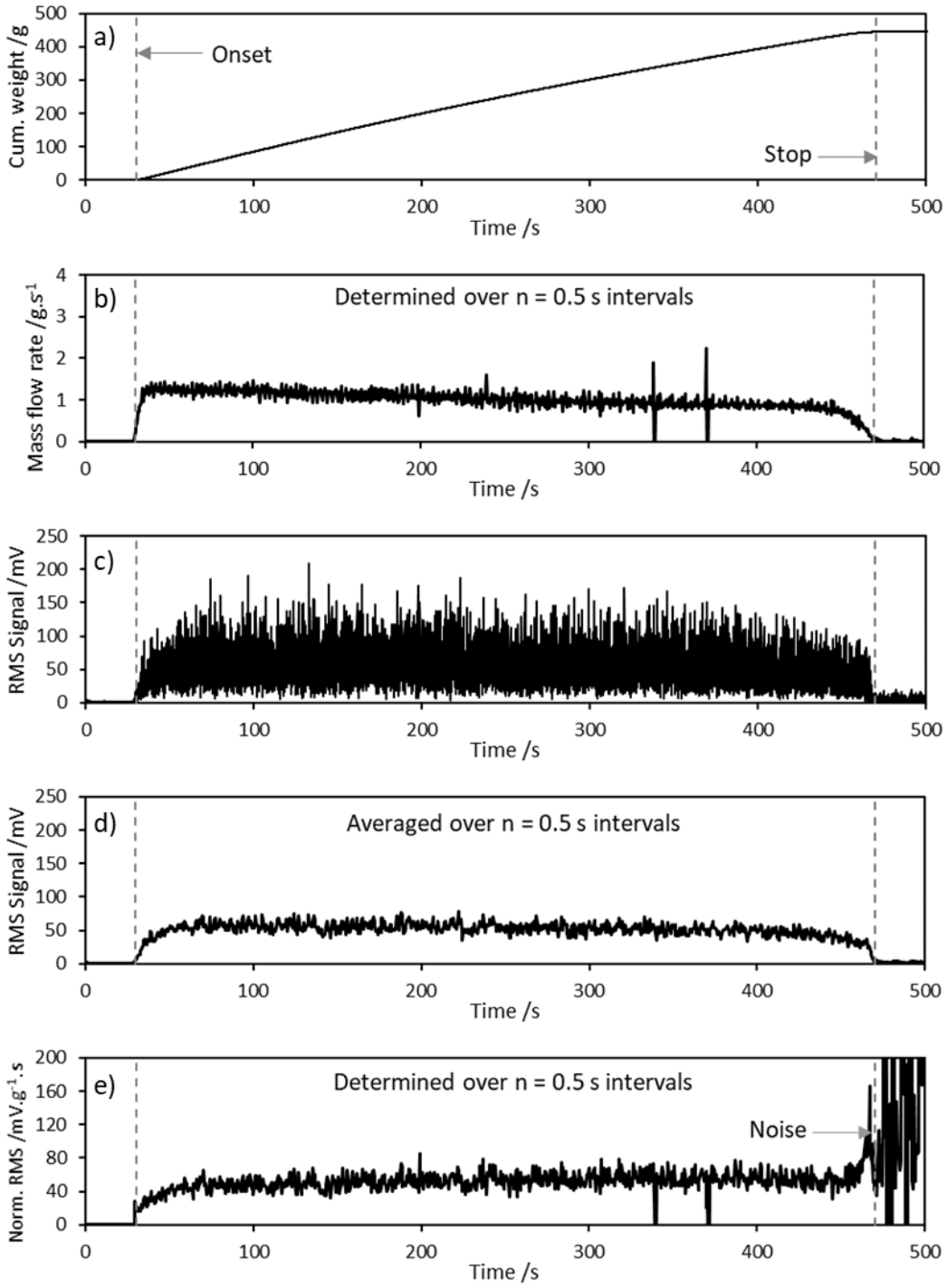

Fig. 5-1. Datasets yielded for Avicel PH102 NF screw conveyed at 40 rpm, which include: a) cumulative weight; b) mass flow rate; c) filtered RMS signal; d) filtered RMS averaged over 0.5 s intervals; and e) RMS signal normalized against the mass flow rate.

5.5. Results and discussion

Fig. 5-2a-c, shows relative charging profiles and the corresponding mass flow data recorded for the first experimental runs of Avicel PH101 NF, Avicel PH02 NF and maize starch EP. Also, profiles for the second and third experimental repeats per powder can be found in Appendix 3-Appendix 5 respectively. Each dataset was divided into three sections according to the degree of powder loading in the barrel. The first section of the graphs (coloured black), was associated with the powder quickly filling the free space in the barrel, thus achieving a continuous feed of powder (i.e. "barrel loading" stage). The second section (coloured dark grey), was attributed to a continuous feed of powder delivered by the screws c (i.e. "continuous feeding" stage). The last section (coloured light grey), indicated the reduction in mass flow rate due to the emptying hopper (i.e. "barrel emptying" stage). In some instances, particularly for the microcrystalline cellulose powders, the powder mass flow rate gradually reduced over time due to depleting powder in the hopper and feed into the barrel. This was a consequence of the volumetric feeder being unable to compensate for the change in hopper fill level over time, although this was expected to be reflected in the RMS signal proportionally. For the microcrystalline cellulose powders, the relative powder charge was observed to have rapidly increased in magnitude within ~25 – 45 seconds into the continuous feeding stage (Fig. 5-2a-b). Subsequently, the relative powder charge either stabilized over time or the relative charging rate was gradually reduced. Overall, the relative powder charge increased by ~13-14 % for Avicel PH101 NF, and ~11 to 14% for Avicel PH102 NF. For maize starch EP, one sample behaved similarly to the microcrystalline cellulose powders (see Appendix 5), whereas the two remaining samples were shown to a gradually increase in relative charge across entire duration of the experiment, with an example of the latter shown in Fig. 5-2c. The total increase in relative charge for maize starch EP samples ranged from ~10-12 %.

Fig. 5-3a-c, shows two sets of images per powder, taken from video recordings of the respective experiments, in an attempt to investigate the impact of charging on the powder adhesion. These were time-stamped according to the onset of the continuous feeding stage and the end time point at which of the powder ceased to further accumulate onto the screws and barrel (i.e. adhesion end point). Initially, attempts were made to identify these key events using ImageJ (National Institute of Health), although this was concluded unfeasible since it was impossible to isolate in the image the white particles from white light reflected on the barrel surface. Therefore, the adhesion onset and end time points were arbitrarily chosen, based on the absence in visual change in powder adhesion onto the screw feeding parts in the video

recordings. For the microcrystalline cellulose and maize starch powders, a small degree of powder was observed to accumulate on the faces and pitches of both screws early into the continuous feeding stage. Cross-referencing these images against the relative charging profiles at these time points showed somewhat of a temporal alignment between adhesion of powder to the feeder and powder charging, although it cannot be stated with certainty that the latter was induced by the former. This is because particles, especially finer ones, already possessed a propensity to adhere to the equipment surfaces. At this stage, it was also difficult to gauge whether powder charging impacted the mass flow rate, since any deterioration in mass flow rate may have been compounded or even obscured by the natural drift in mass flow rate induced by reducing hopper fill level over time; a consequence of volumetric feeding.

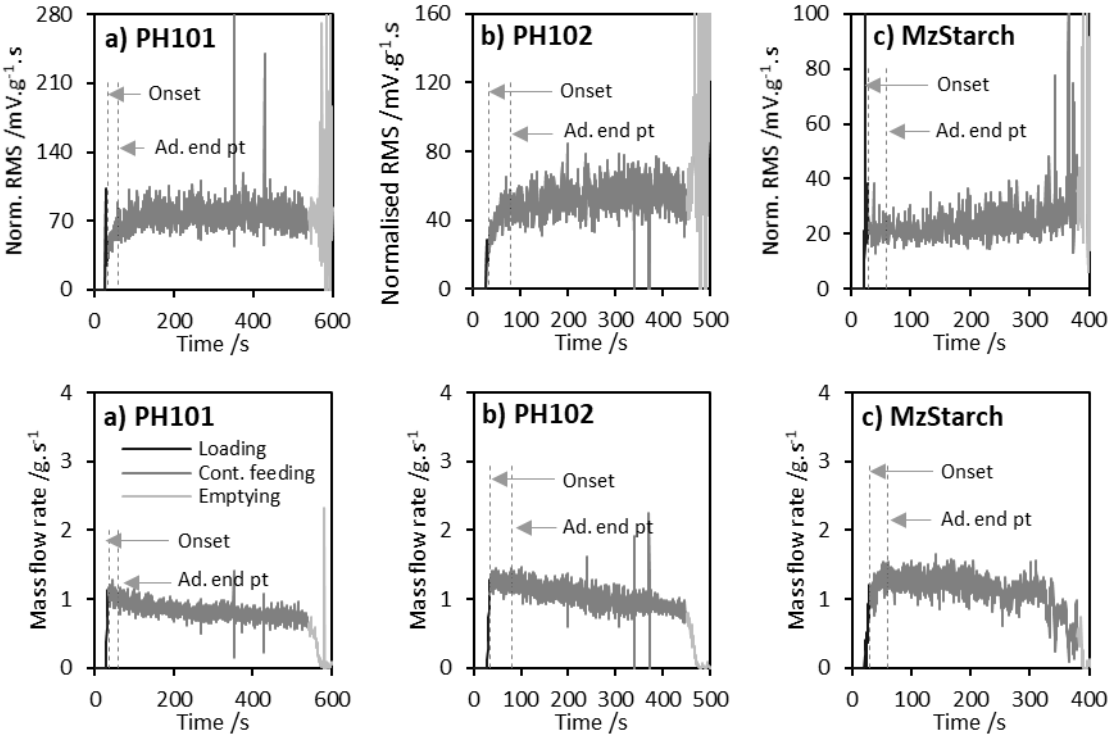

Fig. 5-2. (Top) relative charging profiles and (bottom) mass flow profiles for a) Avicel PH101 NF, b) Avicel PH102 NF, and c) maize starch EP. Annotated time points are linked to the time marked images below (see Fig. 10). Onset = the onset of continuous feeding stage, Ad.end point = apparent adhesion end point.

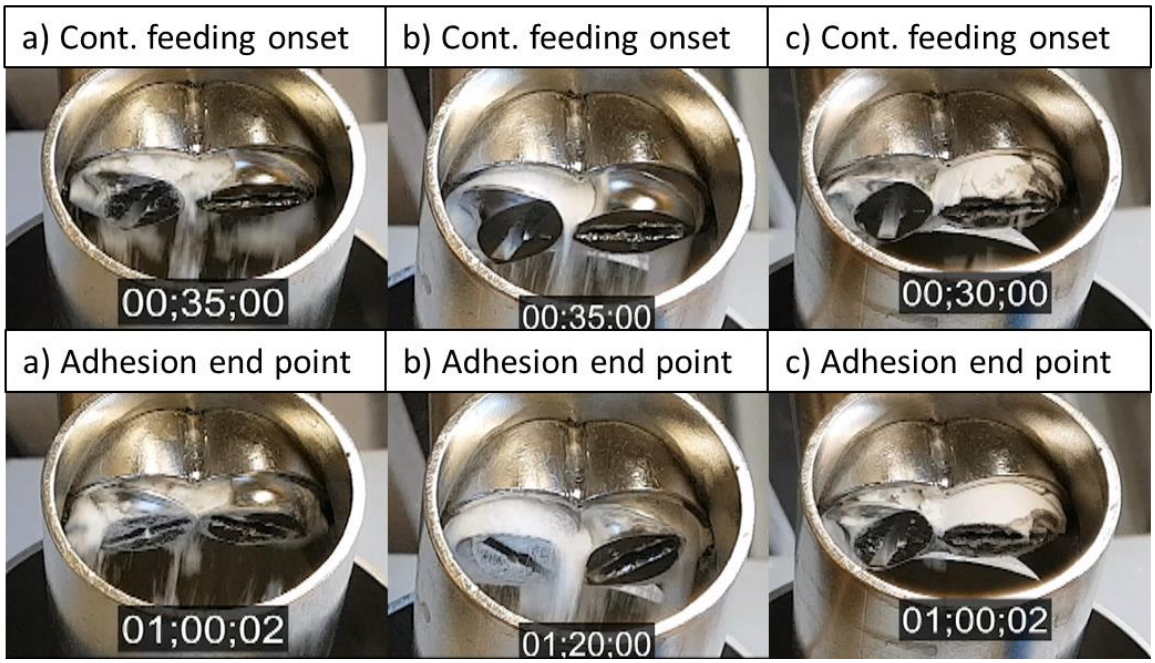

Fig. 5-3. Images taken of: (top) the onset of the continuous feeding stage and; (bottom) the apparent end point of powder adhesion to the screws, for a) Avicel PH101 NF, b) Avicel PH102 NF, and c) maize starch EP.

The lactose monohydrate powders charged differently compared to the other powders. A sample relative charging and mass flow profile for Lactose 200M EP is shown in (Fig. 5-4), with the remaining experiment repeats shown in Appendix 6. For this powder, the normalized RMS reduced in magnitude across the entirety of the continuous feeding stage, which was thought to be attributed to the powder gradually accruing less charge against the feeding mechanism. The loss in relative charge increased from a minimum of ~15 to a maximum of ~54%, across the three samples measured in succession. The reduction in the relative powder charge did not appear to impact the degree of powder adhesion over the course of the experiment (Fig. 5-5), nor its mass flow rate. One important observation accounted for during cleaning of the feeder, was the discovery of a sticky residue on the screws after conveying each sample, most likely induced by the abrasion of these sugar particles.

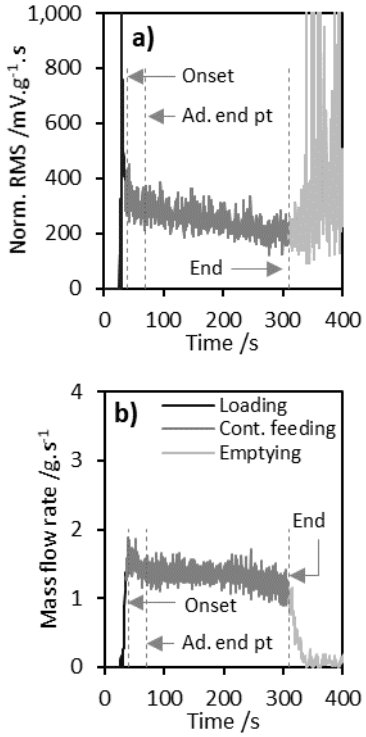

Fig. 5-4. a) relative charging profile and b) mass flow profile, recorded for Lactose 200M EP conveyed using the twin-screw feeder at 40 rpm. Annotations indicate the different stages of powder flow, which are linked to the images below (see Fig. 12). Onset = the onset of continuous feeding stage, Ad.end point = apparent adhesion end point, End = end of the continuous feeding stage.

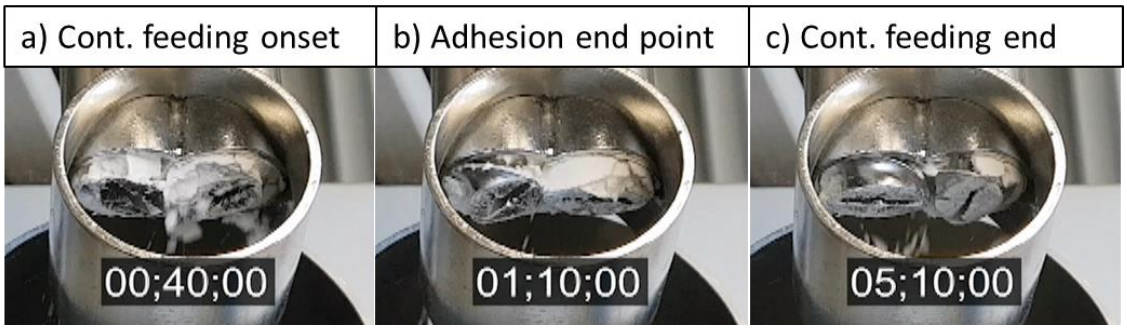

Fig. 5-5. Images indicating different stages of powder flow, taken from a video recording of Lactose 200M EP conveyed using the twin-screw feeder at 40 rpm.

Fig. 5-6a-c, shows the relative charging and mass flow profiles for three samples of Lactose 316 Fast flo. The relative charging profiles for these samples, capture a sudden increase in charge effect early into the continuous feeding stage. For the first sample (A), the onset of this phenomena was observed between ~40 and 100 s, where the normalized RMS increased by ~45 %. Subsequently, the normalized RMS was observed to have undergone a stabilization

period, decreasing in magnitude by ~43 % between 100 s and 140 s. Afterwards, the normalized RMS decreased by a total of 73 % until the barrel emptying stage was reached at around 370 s, which was a similar to that exhibited by Lactose 200M EP. With each successive sample (recorded in the order of sample A-C), the magnitude of the sudden triboelectrification effect was shown to decrease. The maximum normalized RMS recorded for samples B and C were ~ 46% and ~55 % lower than that of sample A respectively, indicating loss in chargeability with repeated measurements. Currently, it is unknown what the exact cause of this effect was, although a possible explanation for this effect is given later in the discussion.

The differences between the relative charging profiles could be seen in the video recordings of the powder flow (Fig. 5-7a-c). For all samples, powder was shown to gradually adhere to the screws upon the onset of the continuous feeding stage. Compared to the other powders, Lactose #316 Fast flo was shown to completely adhere to the screw faces and pitches, as well as the interior and sections of the exterior of the barrel. For sample A, the end point for the powder adhesion was ~ 140 s (i.e. the onset of the stabilization period after the sudden charging effect), afterwards no more powder was visibly shown to adhere to the equipment for the remainder of the experiment. For samples B and C, there appeared to be a gradual loss in powder adhered to the screws which persisted for the remainder of the experiment (Fig. 5-8). This may be related to the lower relative charges recorded for samples B and C compared to sample A at these time points suggesting that a minimum induced charge exists for the powder to maintain its adhesion to the screws.

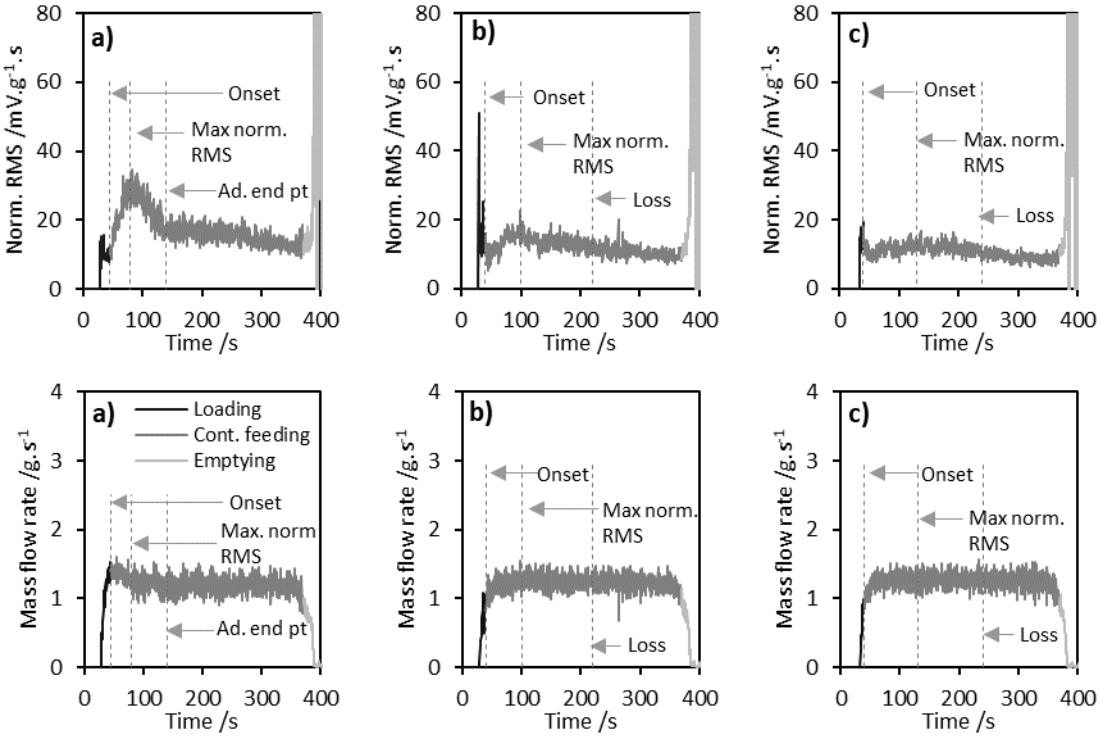

Fig. 5-6. (Top) relative charging profiles and (bottom) mass flow profiles for three samples of Lactose #316 Fast flo (Samples A, B and C). Annotated time points are linked to the time marked images below (see Fig. 14). Onset = the onset of continuous feeding stage, Max. norm. RMS = time at max. norm RMS, Loss = time point at the onset of apparent loss in powder adhesion.

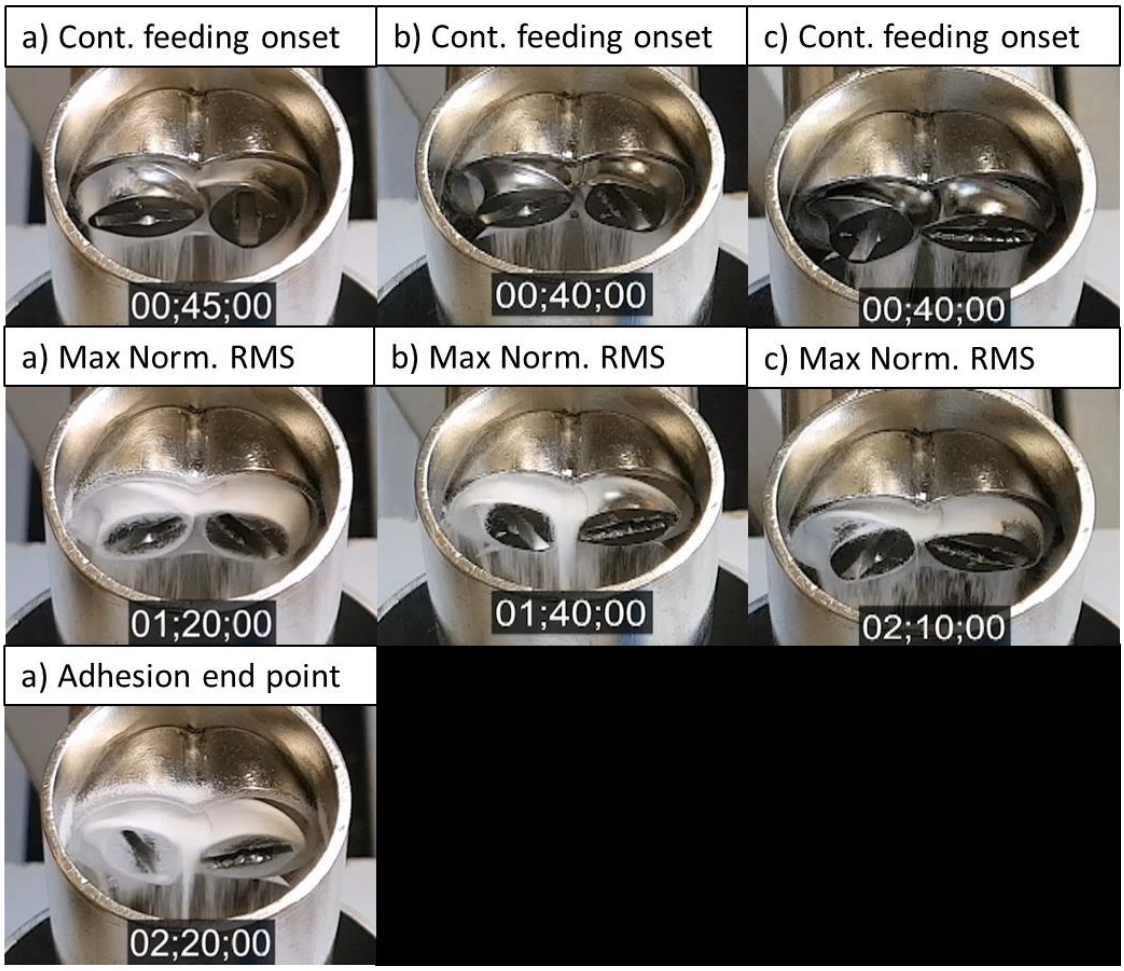

Fig. 5-7. Images taken from recordings of screw conveyed Lactose #316 Fast flo, samples A-C depicting: (top) the onset of the continuous feeding stage; (middle) approximate time point at the maximum normalized RMS; and (bottom) the apparent adhesion end point for sample A only.

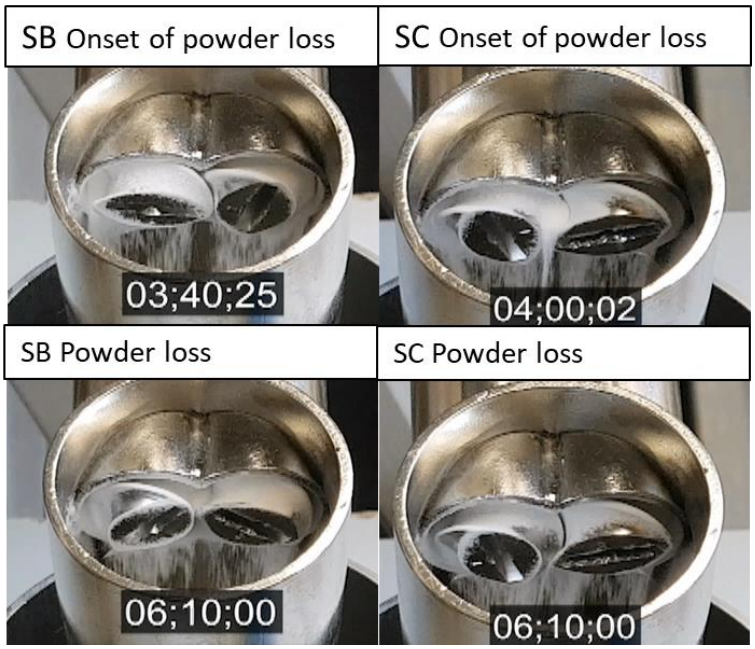

Fig. 5-8. Images taken from recordings of screw conveyed Lactose #316 Fast flo, samples B and C depicting: (top) apparent onset of powder loss (bottom) the powder loss at the end of each experiment.

A narrative is provided to explain the mechanisms behind the charging characteristics for each powder, with an attempt to link to the material properties, process parameters and equipment properties. There definitely appeared to be material dependent effect, observed by the propensity for the lactose monohydrate powders to charge less (including Lactose #316 Fast flo after the charging step), and for the microcrystalline cellulose and maize starch powders gain charge. In literature, it has been reported that the materials used in this study typically develop negative charges due to contact with stainless-steel (Eilbeck, et al. 2000; Lumay, et al. 2019; Peltonen, et al. 2018; Šupuk, et al. 2012). Therefore, one would have expected for each powder to have exhibited an increased relative normalized charge over extended screw conveying time. Given that the relative powder charge for newly dosed powder followed a similar charge trend given by the preceding doses, it was suggested that the conditions within the twin-screw feeder or the properties of the bulk material were somehow changing over time (whether these be the initial charge or other material properties).

The behaviour of Lactose #316 Fast flo was the simplest to explain in terms of its charge gaining characteristics. It was thought that the charging characteristics of this powder were facilitated by particle fracture due to the feeding mechanism, where increased friction and shearing are known to induce charging effects (Telko, et al. 2007). Fig. 5-9a-d, shows the SEM images taken of the Lactose #316 Fast flo particles after experimentation was completed,

where particle fracture by the loss in sphericity of the particles and increase in the number of fines.

The resulting size reduction and change in particle morphology led to an increase in effective surface area and charge density (Kaialy, et al. 2014), thus resulting in particle adhesion to the screws. Once the screws became fully coated, all subsequent doses of powder began to contact the coating particles more than the stainless-steel, which was thought to result in the powder charging less over time. Eilbeck, et al. (2000), reported a similar observation, whereby the charging magnitude of lactose monohydrate particles conveyed within a cyclone apparatus reduced in response to the accumulation of adhered lactose particles against the stainless-steel walls. As well, Murtomaa, et al. (2002), reported a loss in net charge for many different pharmaceutical powders as they slid over a glass surface with different levels of occlusion formed using the same powder (Murtomaa, et al. 2002). The authors also mention that when two like materials contact, they tend to only generate small quantities of charge. Based on the electron transfer theory (Matsusaka, et al. 2010; Wong, et al. 2015), lower charges may have been generated between like powders because their difference in work function could be smaller compared to a powder and metal. This theory also explains as to why Lactose 200M EP charged less over time. Since the powder was found to leave an adhesive residue on the screws, this effectively allowed newer doses of powder to charge against itself more so than the metal screws. However, as evident by its relative charging profile (Fig. 5-4), this loss in charge was observed immediately upon the onset of continuous feeding, which implies the powder coating process occurred sooner into the screw conveying procedure than Lactose #316 Fast flo, which initially required the particle fracture to induce the necessary charging conditions. Also, the loss in overall chargeability exhibited by the Lactose #316 Fast flo across the experimental repeats may be related to this effect. It may be possible that the adhered material was not completely removed from the screws during the cleaning procedure. Consequently, when the subsequent batch was conveyed through the feeder, its constituent particles were forced to contact against the residue and thus did not charge to the same degree as if it were conveyed against pure stainless-steel. If this was indeed the cause of this effect, an alternative solvent would have to be incorporated into the cleaning procedure. These powders are soluble in water but any residual moisture will also affect the overall chargeability of powders conveyed after cleaning. Therefore, a sufficient drying procedure would need to be incorporated to ensure the complete removal of moisture.

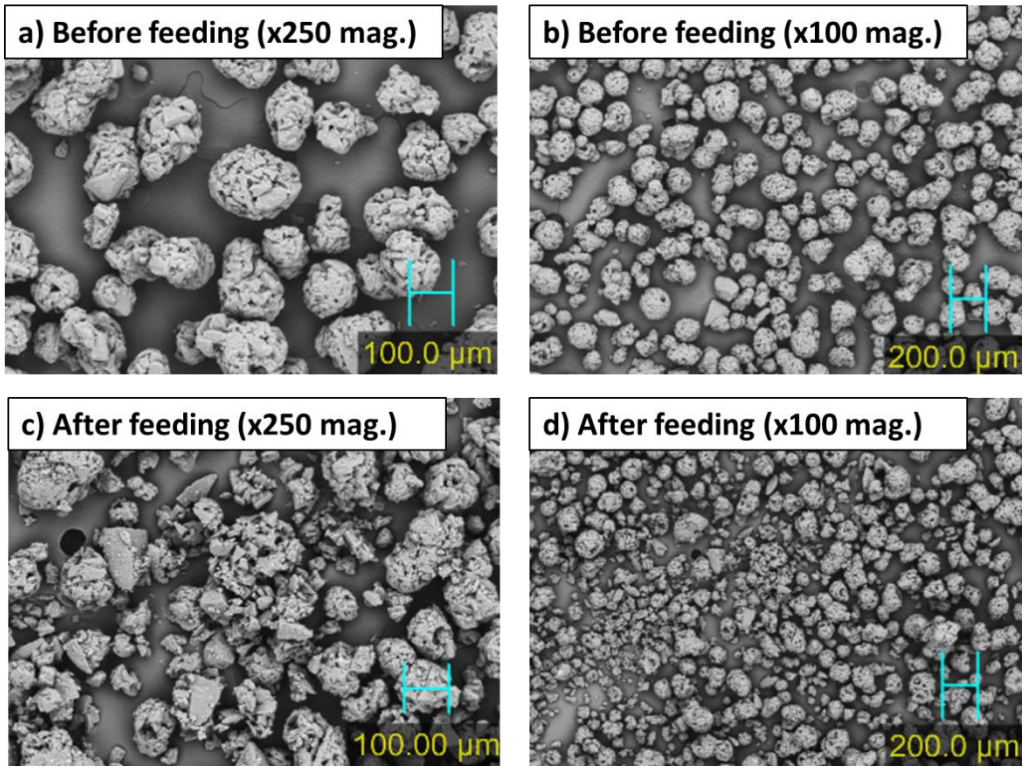

Fig. 5-9. SEM images of Lactose #316 Fast Flo collected before screw conveying at: a) x250 magnification and b) x100 magnification, and after screw conveying at: c) x250 magnification and d) x100 magnification.

For the remaining powders (microcrystalline celluloses and maize starch), it was thought that the absence of the particle fracture and adhesion phenomena allowed them to accumulate charge against the stainless-steel unhindered (i.e. small change in the number and nature of particle-metal contacts). The reduction in the charging rate for these some of these powders may be related to the constituent particles reaching a charge saturation limit (Chowdhury, et al. 2018). This may have been facilitated by an increase in the hopper residence time, thus increasing the exposure of the powder to the action of the agitator blade, resulting in the powders entering the barrel with an elevated initial charge. This hypothesis was based on reports in literature which stated that pre-charged particles follow a similar charging trend for the given material regardless of their initial charge (Chowdhury, et al. 2018; Matsusyama and Yamamoto 2006; Watanabe, et al. 2007). However, do note these were based on impact charge measurements and may not be translatable to the observations in this study, especially given the elevated complexity in the number and types of particle interactions observed during screw feeding.

The relative charging differences between each powder were also compared in order to provide an indicator of their susceptibility to triboelectrification under these experimental

conditions. A 6-order polynomial trendline fitted to the continuous feeding section of the relative charging profiles (Fig. 5-10). The initial and final normalised RMS values were determined by substituting x with the time values for the onset and stop in the continuous feeding sections respectively. Finally, the average of these initial and final normalised RMS values was determined for each powder.

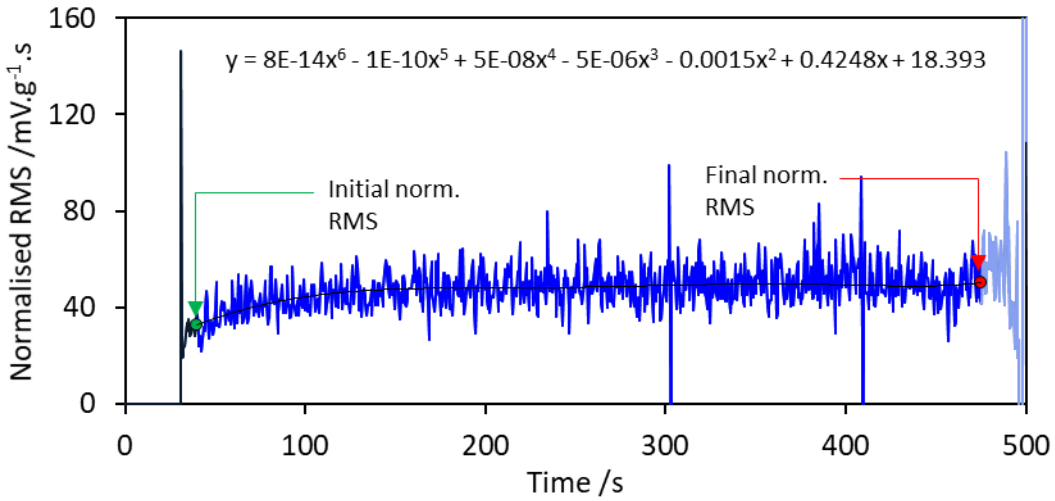

Fig. 5-10. Initial and final normalised RMS values derived from the normalised RMS profile.

The mean initial and final relative charges for each powder are illustrated in Fig. 5-11. For the microcrystalline cellulose and maize starch powders, the final relative charge was greater than the initial relative charge, whereas the opposite was true for Lactose 200M EP. On the other hand, the initial and final relative charges were shown very close in value for Lactose #316 Fast flo.

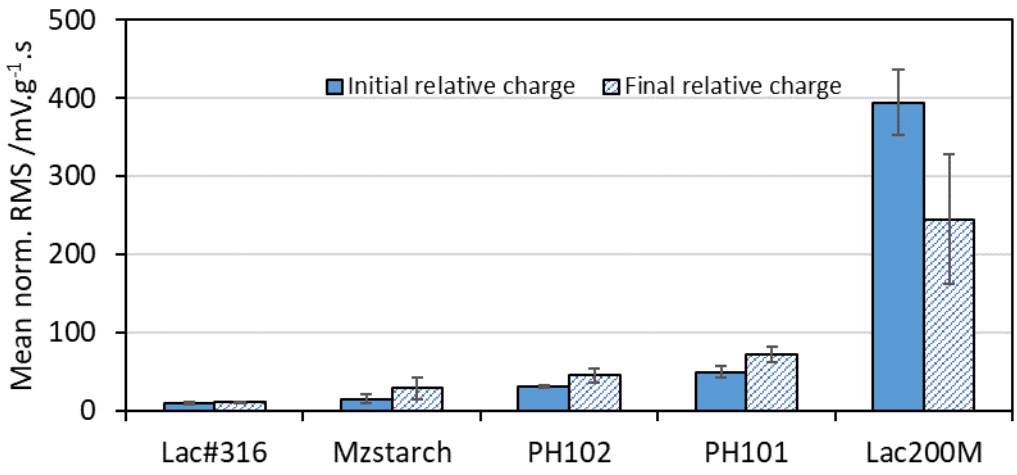

Fig. 5-11. Mean initial and final relative charges calculated for each powders (n=3).

Student's t-test was applied to assess whether both the initial and final relative charges between each powder were statistically different, where $p < 0.05$ (Table 5-3 and Table 5-4 respectively). Based on their initial relative charge measurements, all powders were shown to be statistically different, except for maize starch EP and Lactose #316 Fast flo. As well, based on their final relative charge measurements, all powders were statistically different except for maize starch EP and Avicel PH102 and maize starch EP and Lactose #316 Fast flo.

Table 5-3. Results from the student's t-test for the initial normalised RMS values. $p < 0.05$. Non-significant interactions are coloured white.

	Maize Starch	Avicel PH101	Lactose 200M	Lactose #316	Avicel PH102
Maize Starch		0.0034	0.0001	0.1819	0.0110
Avicel PH101	0.0034		0.0002	0.0008	0.0145
Lactose 200M	0.0001	0.0002		0.0001	0.0001
Lactose #316	0.1819	0.0008	0.0001		0.0001
Avicel PH102	0.0110	0.0145	0.0001	0.0001	

Table 5-4. Results from the student's t-test for the final normalised RMS values. $p < 0.05$. Non-significant interactions are coloured white.

	Maize Starch	Avicel PH101	Lactose 200M	Lactose #316	Avicel PH102
Maize Starch		0.0113	0.0114	0.0836	0.1712
Avicel PH101	0.0113		0.0233	0.0004	0.0253
Lactose 200M	0.0114	0.0233		0.0001	0.0145
Lactose #316	0.0836	0.0004	0.0082		0.0033
Avicel PH102	0.1712	0.0253	0.0145	0.0033	

The relative powder charge values as well as the chargeability of each powder was likely influenced by their bulk moisture content (Table 5-5) and particle size and shape characteristics (Fig. 5-12). Lactose #316 Fast flo, comprised of a mixture of large regular shaped and the finer irregular shaped particles due to fracture against the feeding mechanism. The low initial relative charge was likely related to the low initial chargeability of the freshly dosed particles which originally were spherical in shape. Spherical particles normally have a lower tendency to charge given that electrical charges are tend to distribute homogenously across their surfaces. On the other hand, for elongated particles, charges tend to concentrate at regions where the topography is uneven, thus resulting in a higher measured charge (Kaialy, et al. 2014; Kaialy 2016). The low final relative charge of Lactose #316 Fast flo was related to its aforementioned loss in chargeability due to the particles coating the screws.

Maize starch charged slightly more than Lactose #316 Fast flo, although less so compared to the microcrystalline celluloses and Lactose 200M EP, which was consistent to accounts in literature (Lumay, et al. 2019). In the case of maize starch, its higher bulk moisture content (12 %w/w) was thought to contribute to a lower resistivity than the microcrystalline celluloses and Lactose 200M EP, therefore rendering it more conductive by comparison (Choi, et al. 2017; Lumay, et al. 2019).

Avicel PH102 and PH101 were shown to be more chargeable compared to maize starch. Their chargeability may be related to their irregular particle shape and lower bulk moisture content (4.3 – 4.5 %w/w). Avicel PH101 NF was probably more chargeable than Avicel PH102 NF since the former comprised of a smaller nominal particle sizes (50 µm and 100 µm respectively) which are comparatively more susceptible to charging (Engers, et al. 2006).

Lactose 200M EP was by far the most chargeable powder, both during the onset and end of conveying. These observations were no doubt related to the low inherent moisture content (0.1 %w/w) coupled with the small nominal particle size of the constituent particles (75 µm). However, Lumay, et al. (2019), reported very similar charge densities between Avicel PH101 and Pharmatose 200M (a cohesive grade of lactose monohydrate), although these were charged and measured in a different manner compared to the materials used in this study (Lumay, et al. 2019).

An attempt was also made to explain the charging behaviour of Lactose 200M EP. It was thought that the gain in charge was coupled to the interaction between the cohesive nature of the powder and the confined nature of the barrel. Under these conditions, cohesive powders had a higher propensity to agglomerate into large plaque, which increased the overall surface the material contacting the barrel wall, thus allowing it to charge more. Also, Freeman (2007), stated that cohesive powders do not readily flow; requiring a constant input shear force in order to overcome its inertia and maintain flow (i.e. bulldozing action), (Freeman 2007). Due to this behaviour, it was expected that this powder would experience a greater degree of friction as it was forced along by the screws whilst dragging against the walls of the barrel, which may have allowed charge more compared to Avicel PH101 NF since increasing the degree of friction a particle experiences results in higher charging tendencies (Telko, et al. 2007). This behaviour may also account for maize starch EP's higher chargeability compared to Lactose #316 Fast flo despite its higher moisture content, since it compacted and flowed in a similar manner to Lactose 200M EP and thus would also be expected to experience and increased degree of friction. In order to further study these in-process charging effects, it may be beneficial to utilise DEM with integrated Coulomb's Law and electric field models to study the fundamental charging behaviour developed in particle flow systems (Tan, et al. 2019). This technique could possibly be used for validation in place of the Faraday Cup.

Table 5-5. Moisture content for each powder determined via oven-drying method and for Avicel PH101 NF determined via TGA.

Material	Measured moisture content /% w/w
Lactose #316 Fast Flo	0.4 ± 13 %
Lactose 200M EP	0.1 ± 42 %
Avicel PH102 NF	4.3 ± 4 %
Avicel PH101 NF	4.5 ± 4 %
Maize starch EP	12 ± 0.4 %

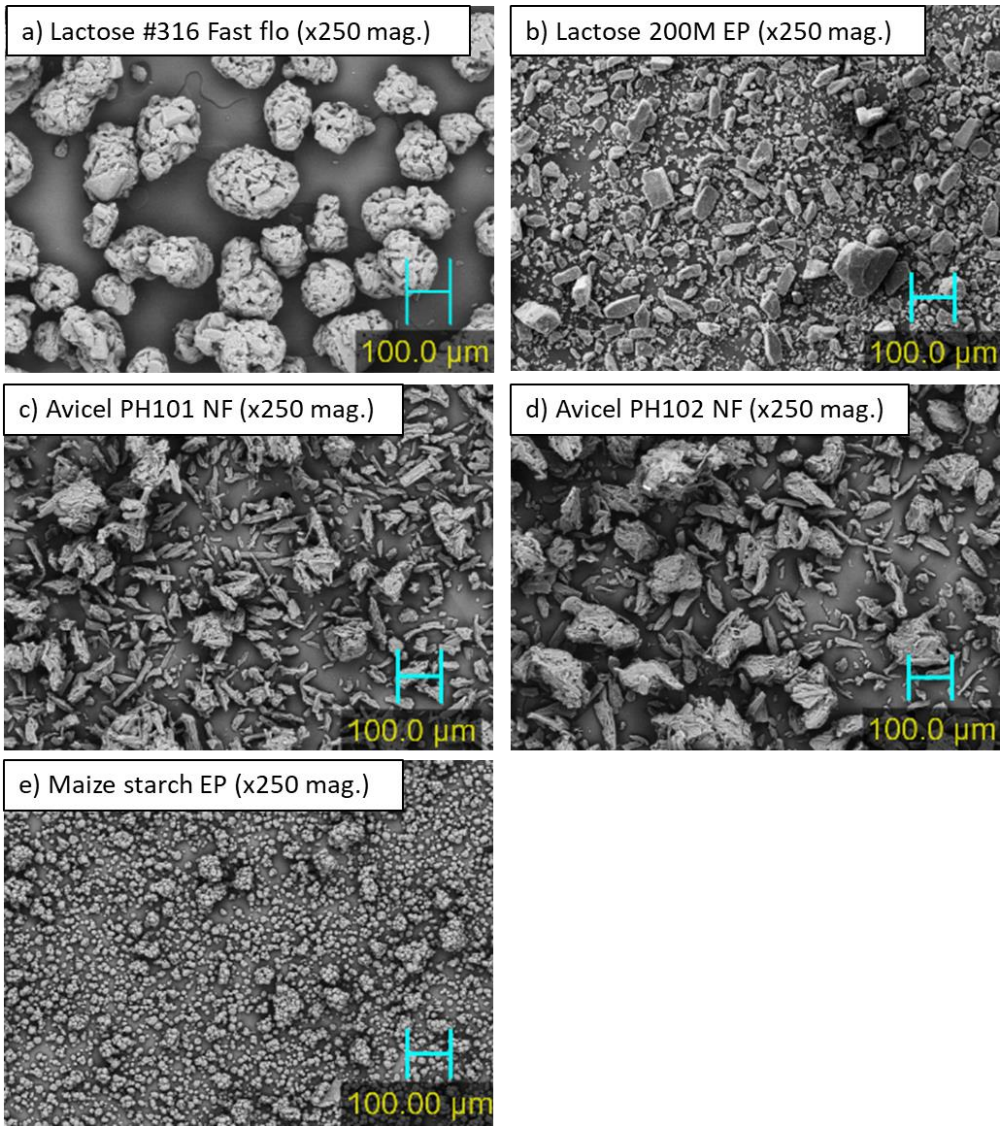

Fig. 5-12. SEM images of a) Lactose #316 Fast flo, b) Lactose 200M EP, c) Avicel PH101 NF, d) Avicel PH102 NF and e) maize starch EP.

Table 5-6, arranges the five powders based on their differences in order of their relative chargeability, although this is only applicable to conditions under which they were tested. In most instances, the charging exhibited by the powders measured in this study did not appear to impact their flow characteristics, as evidenced by their respective mass flow profiles. On the other hand, APIs, which were not studied, are usually more hydrophobic and smaller in particle size (to increase their aqueous solubility) and thus are more likely to exhibit adverse flow effects (Šupuk, et al. 2012). As a result, one would expect these materials to be more susceptible flow issues. Even still, some excipients may be susceptible to charging, as demonstrated by Lactose #316 Fast Flo, which in this study, underwent charge induced adhesion despite its low initial relative charge. Therefore, the capacity to detect the onset of charge induced adverse flow phenomena could prove invaluable for processes, especially those which handle expensive materials. Also, within the context of pharmaceutical formulation and development, there is also potential for the information obtained through dynamic charge measurements to contribute towards increase process knowledge and continuous process improvement as described by PAT framework (FDA 2004).

Table 5-6. Order of powder relative chargeability when conveyed using the twin-screw feeder at 40 rpm.

Relative charge magnitude	Material
High	Lactose 200M EP
	Avicel PH101 NF
	Avicel PH102 NF
	Maize starch EP
Low	Lactose #316 Fast flo

It should be made clear that these measurements were not able to indicate the specific charge of the powder, which is an indication of the total absolute charge present on the particles, whereas the relative charge measured in this study can vary depending on a number of factors. These include variation in the spatial sensitivity of the electrodes defined by their geometry and any in-homogeneity present within the solids distribution (i.e. how the particles are distribute with respects to the electrode wall), (Qian, et al. 2012). As well, the resistance and tolerance of the feedback resistors in the TIA, the signal amplification factor, and the data

processing method would have also impacted the relative charge measurement. Regardless, it would be beneficial to optimise the design of the EPFS, the measurement hardware and the data processing method so that the relative charge outputs are as reproducible as possible. This may be aided by modelling software and further experimentation (Xu, et al. 2012). It is also important to state the need to pair the EPFS with an in-line gravimetric measurement in order to determine the normalised RMS. This could be achieved with a loss-in-weight feeder which is adjusted to record the weight data or through integration with PAT which is able to quantify the powder mass flow rate in-line. PAT for mass flow rate may be obtained via inferential technique which combines solids concentration and velocity measurements, the latter of which coincidentally can be reliably obtained using electrostatic sensors (Carter, et al. 2005; Li, et al. 2015; Sun, et al. 2008; Wang, et al. 2016).

5.6. Conclusions

The dynamic powder charging characteristics of a number of pharmaceutical excipients conveyed using a volumetric twin-screw feeder were characterized using an EPFS. An electrostatic flow parameter was developed via normalization of the RMS of the electrostatic signal against the respective powder mass flow rate (in $mV.g^{-1}.s$), which was indicative of the relative powder charge under the conditions of flow. It was found that the powder charging characteristics were dependant on the material type and its interaction with the screw feeder. Avicel PH101 NF, Avicel PH102 NF and maize starch EP were observed to have gained charge against the stainless-steel feeding mechanism, whereas Lactose 200M EP and Lactose #316 Fast flo were shown to charge less over time. For the majority of the powders, the change in the relative powder charge did not impact their flow characteristics. However, Lactose #316 Fast flo demonstrated charge induced adhesion to the equipment, which was reflected by a sudden increased in charge (up to ~45 %) within its relative charging profile. Furthermore, using the initial and final relative charge values, a tribo-electric series was constructed, which indicated the relative chargeability of each powder for the given experimental conditions. Although it was not possible to determine the charge polarity and absolute charge using this technique, the relative charging measurements were useful in understanding how powders charge under the conditions of flow, which would not be easily obtained via the standard Faraday Cup method.

Future work should further investigate the applicability of this technique to a wider range of powders which were absent from this study, most notably API, conductive powders and

blends. The scope of this study also did not include a method for validating the relative charge measurements as this would have been unfeasible given that the standard Faraday Cup cannot be easily integrated into the powder flow regime without impeding the flow. A sampling method may be integrated into the flow, although this should not induce further charging (Shi, et al. 2017). Charge characterisation techniques should also be introduced, e.g. powder resistivity measurements (Murtomaa, et al. 2015). Although, at the time of writing, a standard technique for powder application does not yet exist.

Chapter 6. A first look into the application of an electrostatic powder flow sensor (EPFS) for the qualitative study of intermittent flow regime typically present within dense phase gravitational flows such as tablet-press hoppers.

6.1. Introduction

In the pharmaceutical industry, hoppers are employed for the delivery of powdered material into a variety of processes including continuous dispensing/feeding, milling, extrusion and tabletting (Prescott and Barnum 2000). Like most delivery mechanisms, the hopper should be able to achieve a uniform feed of powder into the process, either under the natural dense phase gravitational flow or with the aid of a shearing mechanism. The hopper flowability of a powder is dependent on its material properties as well as the powder's interaction with the hopper (i.e. its geometry and contact surface qualities). A powder that flows well will adopt a mass flow regime, where all particles are in motion and no stagnant regions are present, with particles that are fed into the hopper first are generally the first to leave and vice-versa (Ketterhagen, et al. 2009; Prescott and Barnum 2000). On the other hand, for a powder with poor hopper flowability, it will generally possess a higher propensity to develop stagnant flow zones within its bulk which can result in rat-holing and funnel flow regimes, or otherwise be susceptible to cohesive arch formation (Ketterhagen, et al. 2009; Prescott and Barnum 2000). These tendencies for these adverse effects to develop and hopper flowability may be predicted via rheological testing (i.e. shear cell and wall friction (Freeman 2007). As well, methodology originally developed by Jenike (1964), has to this day been widely incorporated into the design of hoppers. The procedure, which is based on the outputs of shear and wall friction testing (i.e. flow function FF, angle of internal friction φ and wall friction angle φ_w) as well as a hopper flow factor, can be used to determine the critical outlet diameter B in a hopper which facilitates gravitational flow without the formation of a cohesive arch (Equation 10).

Although it is possible to optimise hopper flow through rigorous design of the hopper, flowability issues may still arise should input variability in the formulation be present. In this case, it would not be economically feasible to design a hopper for every formulation variant.

Instead, one may monitor parameters which develop under the conditions of flow which can feedback information to the operator on in-process flow characteristics as well as the performance of the hopper flow. These parameters include but are not limited to the adopted flow regime; the particle/bulk velocity; the packing density distribution; etc. Numerical solutions such as DEM have also been use to model critical quantitative hopper discharge parameters such as particle/bulk mass flow rate (Govender, et al. 2018; Hou, et al. 2014; Ketterhagen and Hancock 2010; Liu, S. D., et al. 2014), velocity (Govender, et al. 2018; Hou, et al. 2014; Liu, et al. 2014; Zhang, T. F., et al. 2018; Zhao, Y., et al. 2019), particle size distribution across a bulk due to segregation (Xiao, et al. 2019; Zhang, et al. 2018), as well as qualitative observation of the hopper flow patterns (Govender, et al. 2018; Zhang, et al. 2018). DEM has also been used as a platform for Jenike's hopper design methodology (Ketterhagen, et al. 2009; Ketterhagen and Hancock 2010). However, a limitation to the technique is that large processing times are typically required for flow simulations, especially if they utilise broad distributions in particle size and shapes (Berger and Hrenya 2014).

Hopper flow characteristics can also be obtained experimentally, either within purpose-built hoppers or those coupled to a process. Here, the flow behaviour can be analysed whilst under the influence of the stress conditions that develop within the given system. However, analysis is challenging given the opacity of the hopper and the powder, as well as the restrictive nature of the hopper geometry. These factors also limit the accessibility for many PAT tools. These may either need to penetrate the hopper wall or otherwise require modifications made to the hopper so that they may interrogate the flow. Some tools can be engineered into the interior surface of the hopper but given their invasive nature this could propagate flow stagnation or deviation from the intended flow regime.

Some reports of experimental hopper flow analysis are reviewed as follows. Bacchuwar, et al. (2019), analysed bin discharge profiles, volume displacement and particle velocity via X-ray radiography of particles tagged using a KI solution, arranged between layers of non-tagged particles (Bacchuwar, et al. 2019). Whilst the tool could visualise the bin discharge profiles; it did not appear to be suitable for in-line application. For one, the particles required tagging with a sensitive compound, which may need to be proven safe for patient consumption and furthermore, cannot impact medicinal efficacy. Additionally, there is an uncertainty as to whether the tool could be applied to small particles (which comprise of some pharmaceutical

powders), since the authors utilised relatively large particles in their experiments (500-700 µm).

Ganesh, et al. (2017), calibrated hopper mass flow rate using an X-ray sensor, demonstrating robustness against a number of factors including: the presence of additives, tube diameter, signal averaging procedure and powder reprocessing (which induced changes in flow properties and bulk density), (Ganesh, et al. 2017). Whilst the authors anticipate integration of their sensor into tablet-press hopper flows, they had not accounted for the added complexity in the hopper flow pattern induced by a tablet press feeder.

Babout, et al. (2013), utilised an X-ray tomography system to obtain 2D radiograph and 3D tomography images of hopper discharge in funnel flow regimes (Babout, et al. 2013). From the radiographs, the authors were able to quantify the changing height and width of flowing and stagnant zones as a function of time in response to variations in packing density and hopper surface roughness. Although, further image processing was required in order to improve the contrast between these regions within loosely packed beds. Moreover, from the 3D images, the authors were able to study the shape of the flow boundaries and the differences in packing densities across the powder bed, although these were not obtainable for loosely packed powders. From an in-line perspective, a major limitation to 3D imaging was the excessive time required to scan the powder (17 minutes), further compounded by the need to halt the powder flow during scans. Moreover, from a pharmaceutical perspective, the authors only utilised a homogenous material (sand) for their measurements, therefore it is unknown how heterogeneous blends would impact the scan contrast.

Gentzler and Tardos (2009), utilised nuclear-magnetic-resonance (NMR) for the analysis of powder density and velocity fields in narrow and wide angled hoppers (Gentzler and Tardos 2009). The authors were able to analyse the particle velocity distribution as a function of the hopper width and the change in density as a function of hopper fill height, also capturing a flow regime transition (i.e. from funnel flow to mass flow). Finally, the velocity profiles were studied, indicating regions of active flow (nearer to the centre) and stagnant flow (nearer to the wall). It should be noted that this study was performed only using hoppers with small geometries and free-flowing powders. Therefore, it would be interesting for the applicability of this technology towards larger hoppers and powders with a wider range of flow properties to be assessed.

Grudzień, et al. (2018), measured silo flow discharge characteristics across three different hoppers via a non-invasive ECT technique, with comparisons against optical imaging and a commercial ECT system. Data was presented in the form of permittivity maps, which demonstrated high cut-offs in response to stagnant flow. The authors reported good agreement between the ECT estimated flow boundaries compared to those measured via optical imaging, although the ECT images tended to overestimate these boundaries by up to 10 % relative error. Moreover, the ECT technique was able to detect the asymmetry in the visualised flow, whereas the optical imaging could not. However, the technique possessed a low temporal resolution and analysis could only be performed on a steady-state dense phase flows. Furthermore, the applicability of this technique to conical hoppers is debatable given the curvature of a hopper wall. This could require suitable electrodes with similar curvature, thus impacting their electrode spatial sensitivity and by extension, the accuracy in the resulting ECT measurements.

Sielamowicz, et al. (2006), analysed the velocity fields that developed within amaranth seed flow via digital particle image velocimetry (DPIV) technique (Sielamowicz, et al. 2006). Active and stagnant flow zones were identified within the velocity vector fields due to different contrast. Moreover, these flow zones also exhibited geometric changes as a function of time with the hopper emptying (i.e. flow regime transition). Finally, the volumetric discharge flow rate was inferred based on the visual changes in hopper volume within the image sets, which was shown comparable to the mass flow rate measured via balance (accuracy > 1%). DPIV was limited by the need for a transparent hopper and a source of illumination in order to access the powder flow, which is both atypical and challenging within a pharmaceutical setting. Furthermore, the technique was only capable of accessing the 2D flow profile of the powder nearest to the wall, which was only a fraction of the entire batch.

As was evident by the reviewed literature, the challenges in accessing and measuring in-line hopper flow must be overcome and adapted towards by exploring alternative non-invasive measurement tools. Technologies based on the electrostatic induction of electrified particles for mass flow, velocity and solids concentration measurement have been widely documented within literature (Carter, et al. 2005; Qian, et al. 2014; Wang, et al. 2016; Yang, et al. 2019). Some authors have reported electrostatic signal sensitivity to flow regime. In one study, Qian, et al. (2014), utilised the variation in the induced electrostatic charge as an indicator of pulverised coal loading across the period of 24 hours within a power plant (Qian, et al. 2014).

On the other hand, Zhang, et al. (2012), utilised an electrostatic/capacitive sensor coupled with Hilbert-Huang transform algorithm in order to differentiate between roping and stratified regimes within pneumatically conveyed particles (Zhang, et al. 2012). Based on these applications, there may be an opportunity to derive qualities of the in-line hopper flow regime using electrostatic sensors.

This study describes a first look into the application of an electrostatic powder flow sensor (EPFS) for the qualitative analysis of powder flow characteristics within the outlet of a tablet-press hopper, with additional focus on differentiation between cohesive and non-cohesive powder flow. The study was divided into three parts. The first part focused on investigating the response of the electrostatic signal to the densified intermittent flow, which was performed using a densely packed powder loaded into a pipe. Due to the novelty of the application, the electrostatic data was interpreted based on established relationships between electrostatic parameters and powder flows described in literature. This experiment also permitted the use of a balance in order to obtain gravimetric data, which assisted in the interpretation of the electrostatic data. The second part of the study describes the application of the EPFS to the tablet-press hopper, with the aim of ascertaining whether a relationship existed between the electrostatic characteristics and the hopper flow behaviour. Additional factors such as turret speed and the degree of hopper fill were also investigated on the aforementioned characteristics. Finally, since it has been demonstrated in literature that the hopper flow regime is highly dependent on the powder cohesivity (Faqih, et al. 2007). Therefore, the effect of powder cohesivity on the hopper flow behaviour and electrostatic signal characteristics were also studied. These observations were supported using bulk and rheological property measurements obtained off-line using an FT4 Powder Rheometer. It should also be highlighted that due to the novelty of the application, the focal point of this study was on developing an understanding between the electrostatic characteristics with respects to the hopper flow behaviour, thus at this stage no focus was yet given to relationship between the electrostatic characteristics and the tablet quality attributes. Without a doubt, this would be a goal for a future study.

6.2. Materials

A free-flowing spray-dried grade of lactose monohydrate (#316 Fast flo, Foremost Farms) was used for the dense phase gravitational flow experiment. For the initial study of the hopper flow, a simple 2 kg blend (Blend A) was formulated with the intent to achieve good flow and

compression properties. The excipient ratios were 20 %w/w lactose monohydrate (200M EP, Blackburn distributions), 79.5 %w/w microcrystalline cellulose (M102 Ph. Eur Blue Diamond, Accent Microcell Private Ltd) and 0.5 %w/w magnesium stearate (supplied by De Montfort University, manufacturer unknown).

For the study of powder cohesivity on the electrostatic characteristics, three additional blends (B-D) were formulated using varying ratios of a free-flowing component (microcrystalline cellulose-M102) to a cohesive component (Lactose 200M EP), (see Table 6-1). Each powder/blend was stored under ambient conditions and used "as received".

Table 6-1. Blend excipient ratios for hopper flow cohesivity study. Bulk density was recorded during the shear testing procedure for n=3 samples using the FT4 Powder Rheometer (see Chapter 6.4).

	Blend excipient ratio (for 2 kg batch size)			**Mean bulk density (g/mL)**
	Microcrystalline cellulose-M102 (%w/w)	**Lactose 200M EP (%w/w)**	**Magnesium stearate (%w/w)**	
Blend A	79.5	20	0.5	0.45 ± 0.02 %
Blend B	69.5	30	0.5	0.48 ± 0 %
Blend C	59.5	40	0.5	0.5 ± 0.01 %
Blend D	39.5	60	0.5	0.56 ± 0.01 %

6.3. Methods

6.3.1. Moisture analysis

Moisture content of each blend was achieved via loss-on-drying method for lactose (British Pharmacopoeia Commission 2019d) at 80 °C for 3 hours, which was done to prevent the purging of the water of crystallisation. An oven drying method was employed (British Pharmacopoeia Commission 2019a), which was modified to include a cooling step after drying was completed. Each sample was cooled for 10 mins within a desiccator conditioned at ~ 0 %RH by means of activated 2.5 – 5.0 mm molecular sieve beads (Type 4A, Fisher Scientific). Once the samples were cooled, the weight after drying was recorded. The samples were twice re-dried for 3 hours each in order to ascertain any further moisture loss.

6.3.2. SEM imaging

SEM images for the three excipients and the four blends were obtained. Each sample of powder was sputtered coated with 15 nm of gold via rotary pump coater (Q150RS, Quorum). SEM images were recorded via EVO LS 15 model microscope (Zeiss) using an accelerated voltage of 20 kV.

6.3.3. Study of dense phase gravitational flow

The dense phase gravitational flow rig setup is identical to that shown in Fig. 3-1, which comprised of a cylindrical stainless-steel pipe, which possessed an axial length of 1000 mm and i.d. of ~19.1 mm. This pipe was suspended above a balance by a length of ~100 mm. The lab-scale EPFS was connected to the end of the pipe with a brass nozzle fixed at its outlet in an attempt to control the mass flow rate (where the aperture diameter x = 7.1, 10.1, 12.4, 14.3 and 16 mm). A flow stopper attached to the pipe controlled the onset and stop of the powder flow.

The pipe was filled to approximately one-hundred percent capacity with the Lactose #316 Fast flo powder with the flow stopper obstructing the outlet. This powder was gradually introduced using a funnel in order to achieve as homogenous a packing density as possible. The fill weight was ~140-150 g. A measurement run of 200 seconds was executed using the electrostatic / gravimetric measurement software. The flow stopper was released and the entirely of the powder was allowed to deposit from the pipe onto the balance via gravitational flow. Note that at this stage, the environmental conditions were not controlled or recorded.

6.3.4. Study of hopper flow in a tablet press

For the initial study of hopper flow in the tablet press, the blend was prepared within a customised intermediate bulk container (IBC) manufactured using stainless-steel. The IBC was mounted onto the arm of a blender (Type 1652, Apex Construction Ltd) via a customised holding fork and bracket. The individual blend excipients were added to the blender via doubling up technique, starting from the powder with the lowest bulk. The materials were then blended at 10 rpm for 10 minutes. The completed blend was dispensed into a polythene bag and stored under ambient conditions until used for hopper flow experiments.

Hopper flow/compression experiments were performed using a rotary tablet press (Piccola, Reva) equipped with five sets of 8 mm flat tipped punches and dies. The tablet-press hopper was conical shaped, concentric type and was manufactured from stainless-steel 316L. The

hopper interior surface finish was stated by the manufacturer (Ra = 0.15), although it was likely that the actual surface roughness was higher given the age of the tablet press. A fill-volume sensor was also present within the hopper interior, which served to terminate the tablet production when the powder fill reached below a minimum volume. For the purpose of this study, this feature was avoided by obscuring the sensor using a rubber cap (thus simulating a perpetually full hopper). A video camera was installed above the hopper in order to observe the reducing hopper fill level.

The tabletting-scale EPFS was inserted into the feeder and the hopper slotted into the sensor's top section. The top electrode of the EPFS was connected to Channel 2 on the TIA and vice-versa (so that the top electrode was indicated by Signal 1 in the data sets). Since at this stage there was a need to obtain the tablet weight / flow rate, the balance was installed on the floor beneath the tablet-press exit chute, which were linked using a narrow extension pipe so as to aid the transfer of tablets. Additionally, a cotton-wool lined container was mounted on the balance in order to dampen the impact of the falling tablets. Measures were also taken to ensure that the tablets were transferred to the balance on an individual basis. Firstly, a small aluminium baffle was attached to the feeder near tablet ejection zone, in order to prevent accumulation of tablets on the turret. Secondly, an extension fitting with a tapered outlet was attached to exit chute, designed to prevent multiple tablets entering the extension pipe at once. An image of the full experimental rig is shown in (Fig. 6-1).

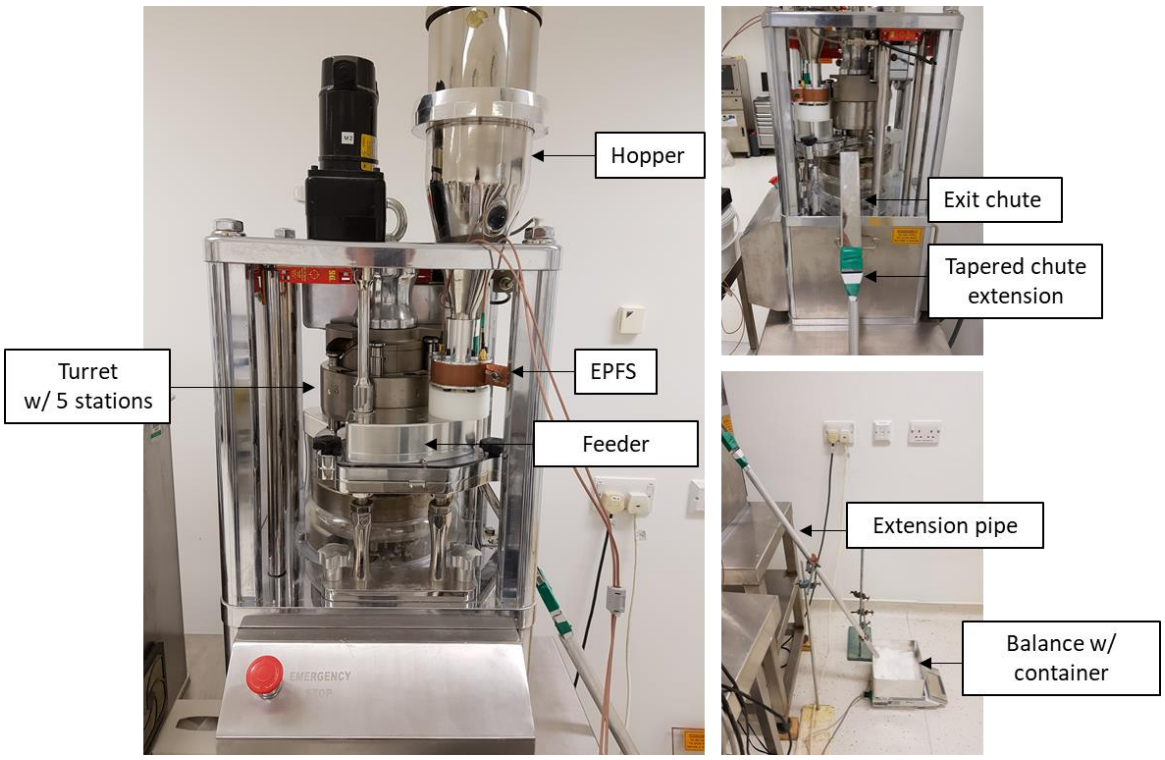

Fig. 6-1. EPFS/tablet press installation. The video camera is not present in these images.

The experimental procedure is described as follows. Firstly, the blend was dispensed into the hopper so that the top level of the powder bed completely obscured the fill-volume sensor. Subsequently, tablets were produced in order to establish the physical tablet characteristics by adjusting the compression force and tablet fill depth. For each blend, the mean tablet weight and thickness was recorded between 0.16 g – 0.17 g and 3.6 mm – 4.07 mm for twenty units respectively. The tablets were compressed to sufficient hardness so that they could resist fracture when transferred to the balance, although this parameter was not quantified. Once the physical tablet characteristics were established, an electrostatic/gravimetric measurement was prepared using the data acquisition software using a time window of 100 seconds. A video recording was initiated using the video camera, following which the measurement run was executed. After ~5-10 seconds the tablet press was switched on and allowed to operate in production mode for the entire measurement duration. Measurements were repeated three times for each blend at a pre-determined turret speed (10, 15, 20, 25 and 30 rpm) and constant feeder speed (15 rpm). Between measurements, the hopper was not refilled to track the progress of the hopper emptying in the video recordings. Experiments were performed in a room with laminar airflow and controlled conditions, with temperature and humidity recorded

using a probe (TinyTag, Gemini Dataloggers). The room temperature and humidity ranged from 20 – 21 °C and 42 – 62 % RH respectively.

6.4. Flowability analysis using the FT4 Powder Rheometer

The bulk and rheological properties of the four blends were characterised using the FT4 Powder Rheometer (Freeman Technology Ltd, United Kingdom). These included compressibility, permeability, shear cell and wall friction. These properties were relevant to hopper flow behaviour and were used to identify differences in the blend cohesivity (Prescott and Barnum 2000). Methodology for the compressibility and permeability tests can be found in (Section 4.3.2), whereas those used for the shear cell and wall friction tests are documented below.

a) **Shear cell test:** To a 25 mm x 15 mL powder sample, a normal stress of σ = 9 kPa was applied to achieve a pre-consolidated state. Afterwards, through the use of a 24 mm shear cell, the sample was pre-sheared to a critically consolidated state, also using a load σ = 9 kPa (Leturia, et al. 2014). The load was then reduced to a pre-determined value (σ = 7 kPa) and the shear stress (torque) required for the powder bed to fail was thus determined. These pre-shear / shear cycles were repeated, using reduced loads (σ = 3 – 6 kPa) for the latter, whilst pre-shear load was kept constant at 9 kPa. The incipient failure shear stress values were expressed as a function of the normal stress, which generated the material yield locus. Additionally, through the application) of Mohr's circle analysis (performed using FT4 Data Analysis software, Freeman), a number of parameters were derived from the yield locus including unconfined yield stress (UYS), major principle stress (MPS), cohesion and angle of internal friction (AIF) (Leturia, et al. 2014). Moreover, the flow function, which is used as an indicator of flowability, was derived from the ratio of the MPS and the UYS.
b) **Wall friction test:** To a 25 mm x 15 mL powder sample, a load of σ = 9 kPa was applied to achieve the pre-consolidated state. Afterwards, a coupon manufactured from stainless-steel 316 with a surface finish Ra = 0.28 µm, was gradually used to compress the sample to the pre-sheared critically consolidated state (where σ = 9 kPa). Using the same load, the coupon was slowly rotated until the shear stress overcame the resistance due to friction against the powder bed, thus achieving steady-state flow. This was repeated for a range of reduced loads (σ = 4 - 7 kPa). The steady-state shear stress values were expressed as a function of the normal stresses in order to yield the

wall friction yield locus. The angle at which the wall friction yield locus intersects the origin is termed the wall friction angle (WFA), an indicator of how well the material flows against the measured surface (Ketterhagen and Hancock 2010). Note, that the coupon used in this study was the nearest available in terms of surface roughness to that of the hopper interior.

Each test was thrice repeated per material, using fresh sample of powder for each. For the compressibility and permeability test, the vessels were cleaned using compressed air, paper towel and ethanol. However, for the shear and wall friction tests, it was critical that the vessels were properly cleaned to remove coated magnesium stearate on the vessel walls which would otherwise impact the shear results due to loss of friction. This was achieved by washing the vessels using warm soapy water and drying prior to subsequent testing. Also, it is important to note is that each bulk / rheological property test included the automated conditioning phase described in (Section 4.3.2).

6.5. Raw signal and data processing

Electrostatic data analysis was initially performed using software developed via Borland C++ and later in Microsoft Word. Fig. 6-2a-b, illustrates an example times series for the cumulative tablet weight and the raw electrostatic signal induced by the hopper flow in the tablet press respectively. Depending on the manner of how the electrostatic data was obtained, the raw signal comprised of two or three main components. For the dense phase gravitational flow experiments, this is comprised of the signal component generated due to inactive powder flow, as well the component (electrostatic spikes) generated in response to active powder flow. For the tablet-press experiments, the raw signal was low-pass filtered of frequency components >12 Hz using the method described in Section 2.4, in order to remove vibrational interference associated with the rotating turret. The filtered signal is shown in (Fig. 6-2c). The RMS of the electrostatic signal was also determined by taking the average deviation for the absolute value of electrostatic data points accumulated between two consecutive weighing points (i.e 20 Hz / 1 datum per 0.05 s). Fig. 6-2d, shows the filtered RMS, which was comparatively less dense in terms data compared to the original signal, allowing simple comparison between data regardless of charge polarity distribution. It should be confirmed here that the process of averaging did not impact the relative time placement of the discrete electrostatic spikes between the filtered raw signal and the RMS signal.

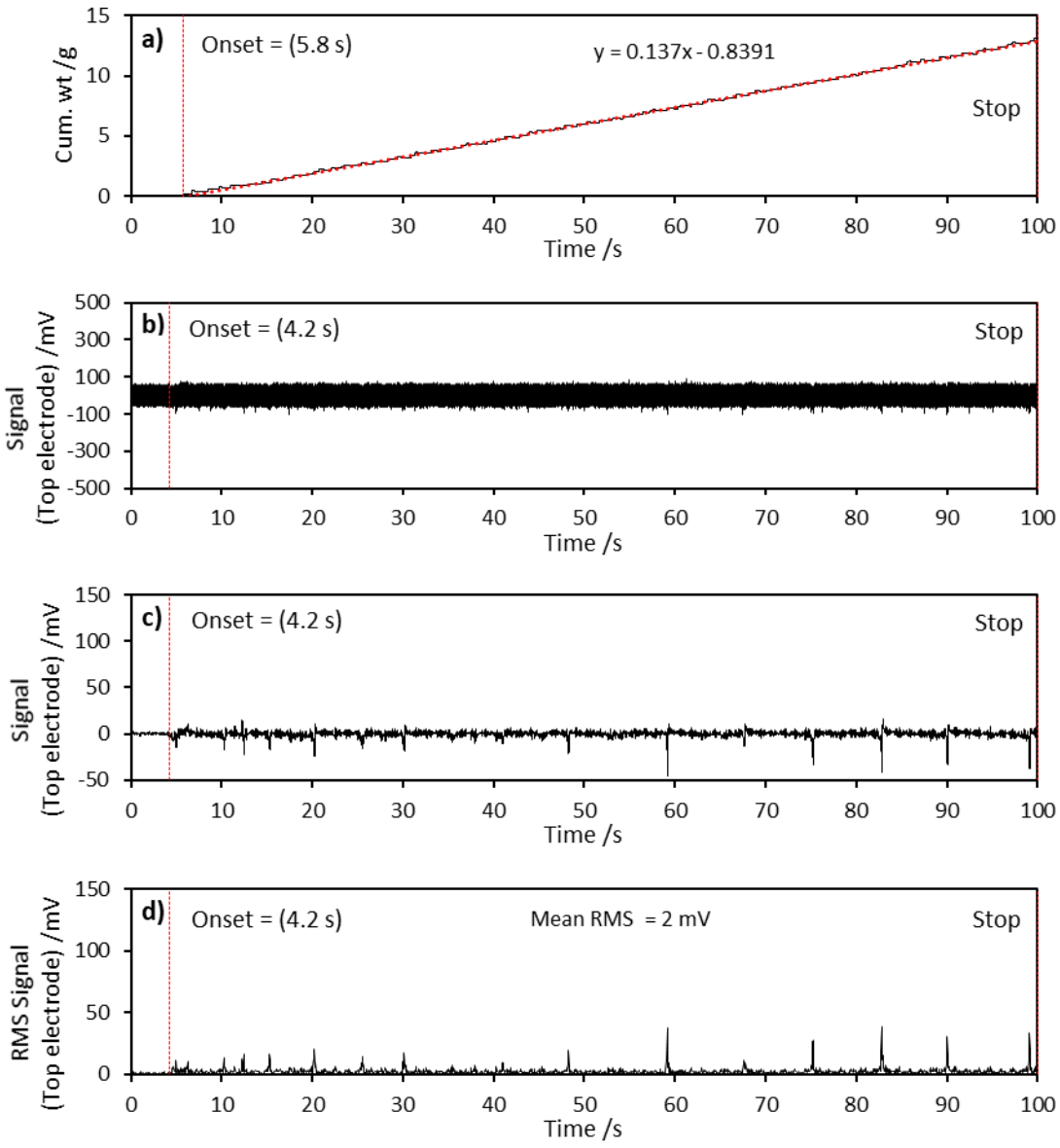

Fig. 6-2. Raw and processed data calculated for the same powder, which includes: a) the cumulative tablet weight; b) raw electrostatic signal; c) electrostatic signal with low-pass filter of 12+ Hz applied; d) RMS of the filtered electrostatic signal.

In order to confirm that the electrostatic spikes were coupled to powder flow in the hopper and not vibration due to the turret/feeder rotation or compression, electrostatic signals were recorded for Blend C, where the hopper filled with powder as well as when the hopper had emptied with powder. It should be noted that during the measurement of the latter, the feeder remained flooded and the turret remained in operation with tablets being produced. This was done to avoid damaging the tablet tooling. Fig. 6-3a-b, compares the electrostatic signal response to the filled hopper and empty hopper respectively. For the former, large amplitude spikes are were shown to develop within the electrostatic signal, whereas for the

latter, these spikes are not present and only the electrostatic background noise is visible. Since it is known that electrostatic signals were generated in response to moving charges, this confirmed that the large electrostatic spikes were coupled to the powder flow.

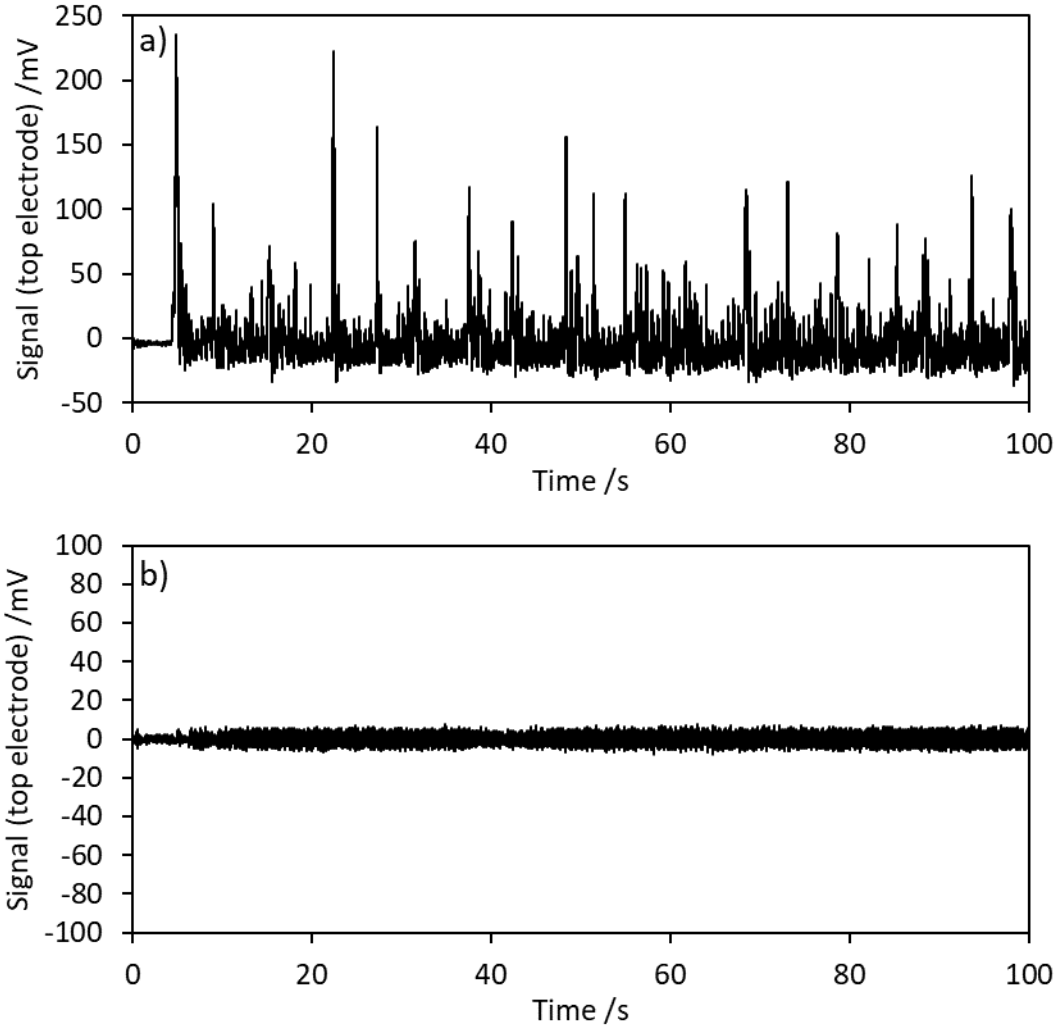

Fig. 6-3. Filtered electrostatic signals with applied low pass filter (12 Hz+) for Blend C, with the tablet press operating at turret speed of 20 rpm, in response to: a) powder flowing within the hopper, and b) zero powder flow due to empty hopper.

6.6. Results and discussion

6.6.1. Study of dense phase gravitational flow

Fig. 6-4a-c, shows the cumulative weight and electrostatic signals recorded for both electrodes, induced by the gravitational flow of Lactose #316 Fast flo through a nozzle aperture size of 7.1 mm. The cumulative weight profile (Fig. 6-4a), captured the mean mass flow rate (μ = 2.1 $g.s^{-1}$) of powder as the pipe gradually emptied from onset to finish. Although, analysing the cumulative weight in greater detail revealed that the flow rate decreased to 1.8 $g.s^{-1}$ at the ~76 s time point, when the pipe was near an emptied state. Fig. 6-4b-c, shows both RMS signals induced by the same flow of powder, which contained a number of discrete electrostatic spikes, each indicating a single downwards movement of powder within the pipe. Between each electrostatic spike were instances where the signal fell to a baseline state, which was thought to indicate stagnant flow. Therefore, it was surmised that the constant alternation between fluctuations and the baseline state were a result of sporadic acceleration and deceleration of the powder bed, likely due to the presence of a dynamic arch at the nozzle outlet base which continually yielded and reformed due to the pressure exerted by the bulk weight (Muite, et al. 2004; Uñac, et al. 2012). Notably, these RMS profiles were significantly different to those measured by in Chapter 3.5.1.1., which was thought to be the result of a change in flow regime to a more intermittent nature, facilitated by the larger nozzle diameters.

Similar to the observation described in Chapter 3.5.1.1., for the first 60 seconds, the individual electrostatic spikes were located at relatively similar time points when comparing both RMS signals. As explained previously, at higher pipe capacities velocity fields would have developed within the region localised to the outlet, whereas the remainder of the powder bed further up the pipe would have been expected to flow at a more homogenous velocity (Kumar, et al. 2020). As powder left the pipe, space was freed up within this region, allowing for the entire powder bed to shift downwards and reoccupy this space. This unified movement would have generated electrostatic spikes recorded by the electrode pair at the same time points.

After approximately 60 s, the electrostatic spikes were observed to have increased in their apparent frequency as well as reduced in their overall amplitude (mean RMS for 14.6-60 s and 60-78 s periods decreased by ~7.4 %), which was likely reflective of the aforementioned deviation in the powder mass flow rate at ~ 76 s. This change in mass flow rate was thought to be attributed to a transition from an intermittent mass flow regime to core flow regime. Here, as the pipe began to empty, the velocity field localised to the outlet would have extended to

affect the remainder of the powder bed, with the fastest moving particles located nearer to the pipe cross-section and the slowest nearer to the wall (Kumar, et al. 2020). As a result of smaller quantities of powder flowing past the individual electrodes each at different velocities, the electrostatic signals induced would have been smaller compared to the signals induced by the unified movement of total powder bed (i.e. lower mass flow rate inducing small signals vs higher mass flow rate inducing larger signals).

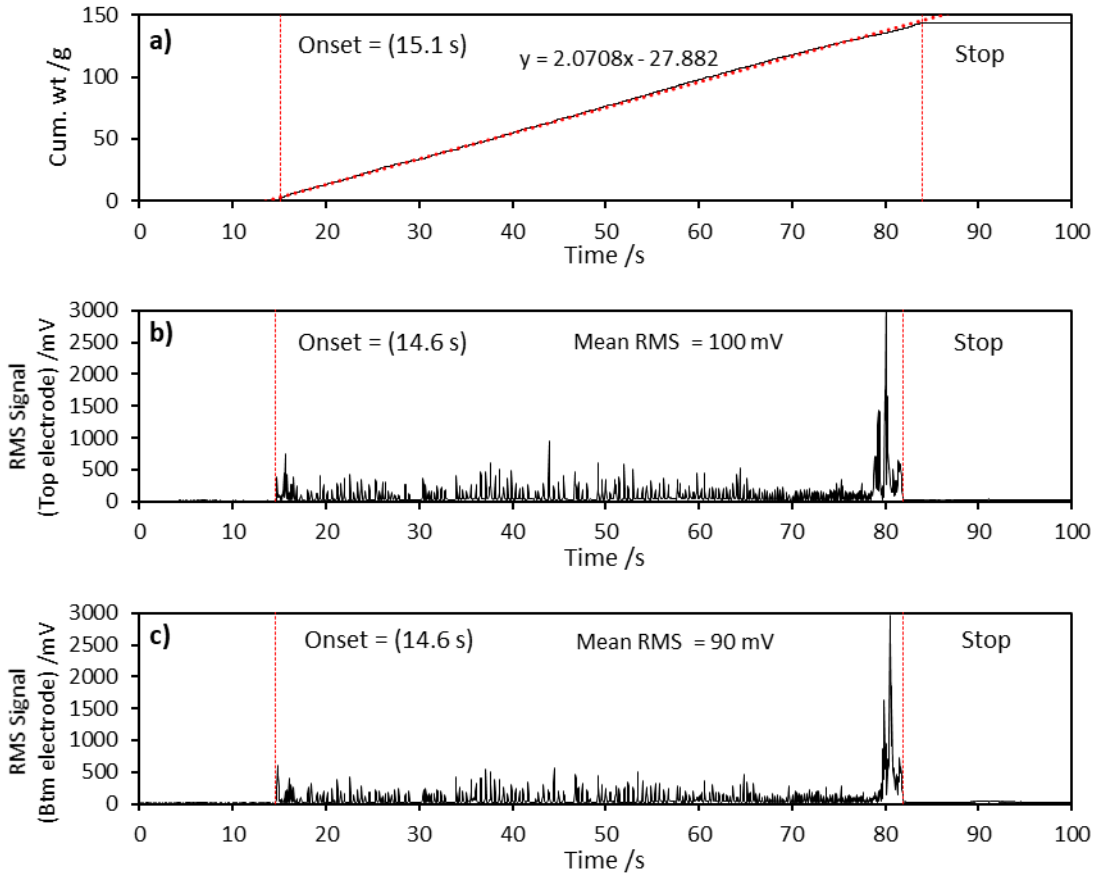

Fig. 6-4. Time series recorded for Lactose #316 Fast flo moving via dense phase gravitational flow regime through an aperture size of 7.1 mm. These include: a) the powder weight; b) RMS signal (top electrode); and c) RMS signal (bottom electrode).

The powder mass flow rate was then altered using the five nozzles with variable aperture sizes. The mean mass flow rate was determined by taking the gradient of the linear trendline regressed through the cumulative weight profiles between the flow onset and stop time points. Although, it should be noted that the mass flow rates were not necessarily consistent in all cases, particularly for the 10.1 mm and 12.4 mm nozzles, where a slight shift in the

gravitational mass flow rate was observed within middle of the measurement. Regardless , given that the intent was not to achieve a calibration, the accuracy in the calculated flow rate was inconsequential. Generally, an increase in the nozzle aperture size resulted in an exponential increase in the mass flow rate (Fig. 6-5), with maximum mass flow rate expected to be yielded at 19.1 mm aperture size.

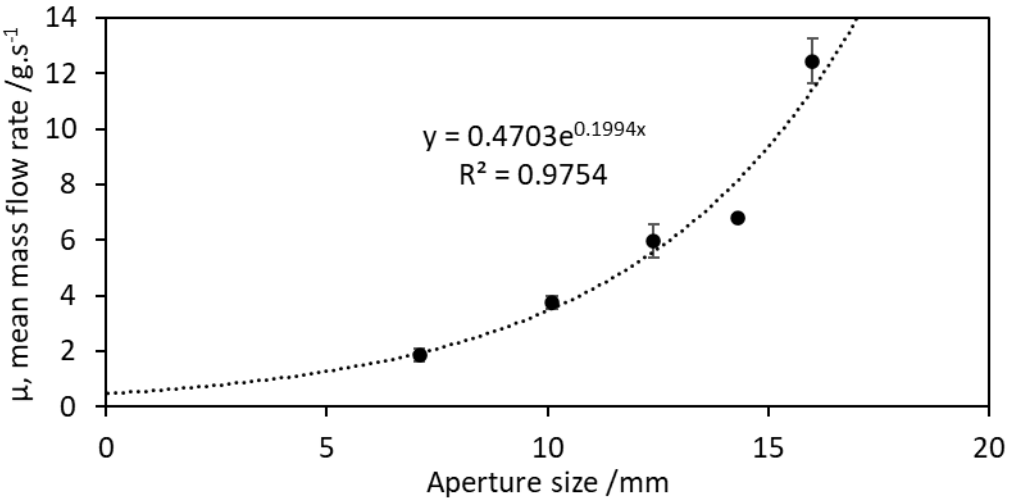

Fig. 6-5. Gravitational powder mass flow rate as a function of nozzle aperture size.

The impact of the increasing powder mass flow rate / nozzle aperture size was reflected within the associated RMS signals. The first sets of data per turret speed are shown in Fig. 6-6a-e, whereas the second and third sets are shown in Appendix 7 and Appendix 8. As expected, the period in the RMS signal associated with active powder flow was shown to decrease with increasing mass flow rate. By increasing the nozzle aperture size from 7.1 mm to 12.4 mm, the amplitudes of the individual electrostatic spikes were shown to drastically increase. In the case of the 12.4 mm nozzle, many of these individual spike amplitudes were shown to reach the measurement threshold of the electrostatic measurement system (i.e. 4 kV). However, for the two largest nozzles, this saturation of the EPFS was not observed and their signals showed similarity to the latter portion within the RMS signals recorded for flow through the smaller nozzles (i.e. low amplitude, high frequency electrostatic spikes).

For the three smallest nozzles, the increase in the overall electrostatic spike amplitude was obviously induced by the increased powder mass flow rate. However, as indicated by large

distinctions between the electrostatic spikes and the baseline of the RMS signal (Fig. 6-6c), it was evident that the intermittent nature of the flow regime was still present (Muite, et al. 2004). For the two largest nozzles, the lower individual electrostatic fluctuation amplitude and increased fluctuation frequency may have indicated a shift from intermittent mass flow regime to steady-state. Dense phase flow regimes can change when the pressure distribution on the loaded powder decreases (Ramírez, et al. 2010). In this case, this was evident by fewer or zero occasions where the RMS signal fluctuations dropped to the baseline level, which also implied flow was almost never stagnant (i.e. loss of intermittent flow regime). This was evident by the general lack of similarity in the electrostatic spikes between both top and bottom RMS profile for both the largest nozzles (Fig. 6-6d-e). This shift to steady-state flow was also observed and implied in Chapter 3.5.1.1., which was indicated by the RMS signals recorded for the dense phase flow of powder through largest nozzle (15 mm) (see Fig. 3-8g). However, to further substantiate these observations, the powder flow would need to be observed visually, which could be achieved using a clear pipe coupled with video recording, the latter of which was not integrated into these experiments. Otherwise, velocity distributions in the pipe can be studied using DEM.

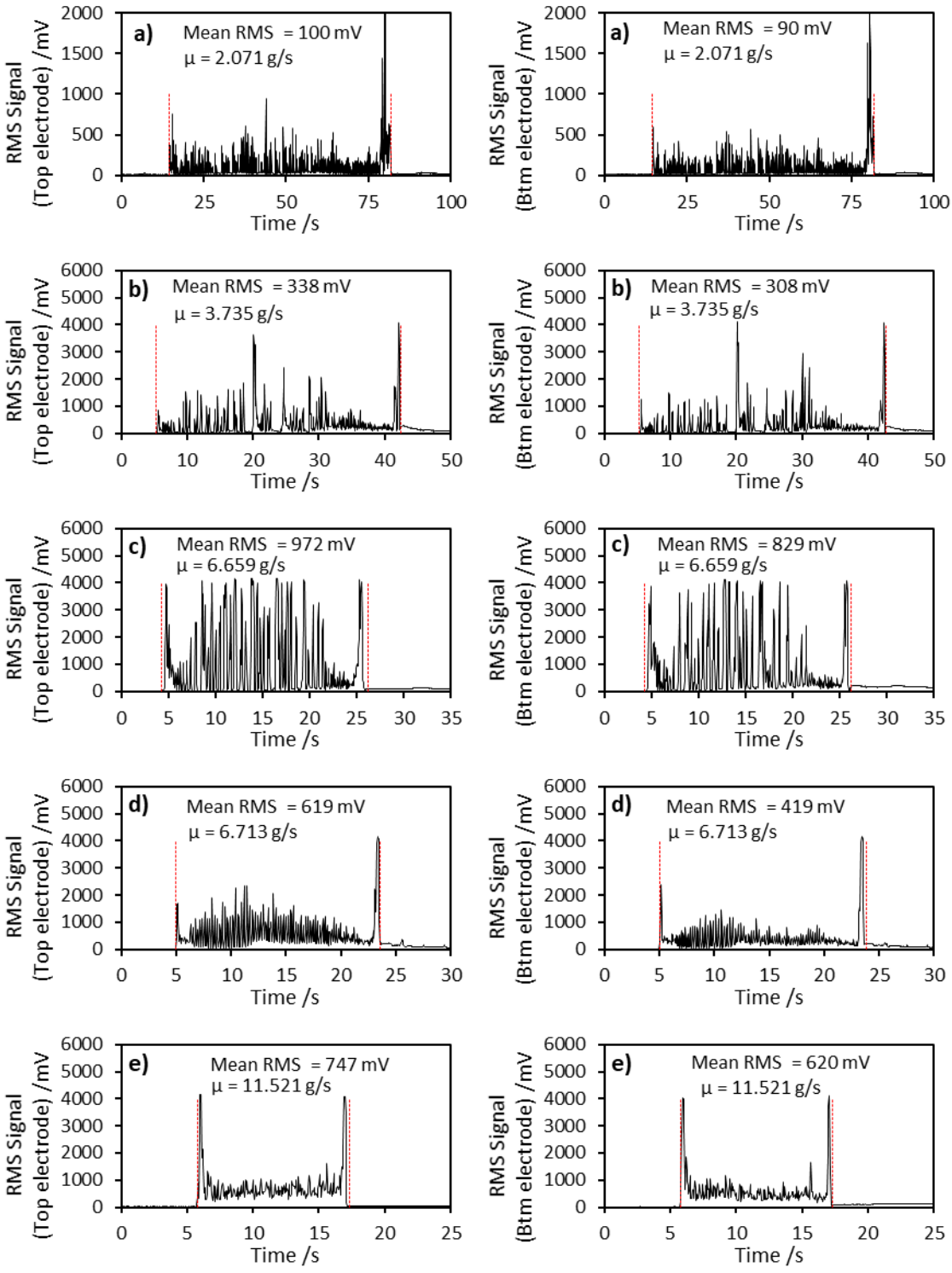

Fig. 6-6. First set of top and bottom RMS signals recorded for Lactose #316 Fast flo moving via dense phase gravitational flow regime through nozzles with aperture sizes of a) 7.1 mm, b) 10.1 mm, c) 12.4 mm, d) 14.3 mm and e) 16 mm. μ = the associated powder mass flow rate.

6.6.2. Blend bulk and rheological characteristics

Table 6-2, shows the flowability of each blend based on their bulk and rheological properties, arranged them in the order of their relative cohesivity. According to the similarities in their rheological properties (cohesion, UYS, MPS, AIF, FF and WFA), Blends A and B were expected to exhibit similar hopper flow behaviour to each other. Blend B exhibited a slightly higher compressibility and permeability result than Blend A, which is likely to be related to the increase in Lactose 200M EP content, however it is evident that these slight distinctions did not serve to impact their rheological similarities. The FF value is used as an indicator of how well a powder flows in a hopper. For Blends A and B, their FF values were greater than 10, which indicated "free-flowing" hopper flowability (Leturia, et al. 2014). Blend C was comparatively more cohesive than Blends A and B, evident by a 30 % increase in mean cohesion, 31 % increase in mean UYS, 4 % increase in mean MPS, 6 % increase in mean WFA, 12 % increase in mean CPS and a 40 % in mean PD. AIF remained relatively unchanged between blends, possibly suggesting that increase in relative friction due to increase in cohesive blend component was impeded by the effect of magnesium stearate coating the constituent particles. The FF value for Blend C lay in the upper region of the "easy-flowing" category (where 4 < FF < 10) (Leturia, et al. 2014). Therefore, it was expected for this blend to still flow well in the hopper. Blend D was more cohesive than Blend C, with a 75 % increase in mean cohesion, 70 % increase in mean UYS, 4 % increase in WFA, 25 % in mean CPS and 78 % increase in mean PD. FF value for Blend D lay within the lower region of the "easy-flowing" category, therefore it was expected to flow slightly worse than Blend C.

SEM images (Fig. 6-7a-d), show the differences between the cohesive/free-flowing component distributions between each blend, where the presence of microcrystalline cellulose-102 is indicated by the coarser particles and for Lactose 200M EP, the finer particles. Blends A and B appeared very similar in terms of the distribution of microcrystalline cellulose-102 particles to the Lactose 200M EP particles, which explained their rheological similarities. However, for Blends C and D, the Lactose 200M EP particles were observed in higher concentration which is why these blends tended to adopt poorer flow properties.

Table 6-3, shows the moisture contents of each blend determined at 3, 6 and 9-hour periods. Generally, the higher the Lactose 200M EP content within the blend, the lower the moisture content and vice-versa. This was due to Lactose 200M EP naturally possessing a higher

moisture content when compared to microcrystalline-cellulose (see Table 3-2 in Chapter 3.5.2.2).

Table 6-2. Bulk and rheological properties characterised for Blends A-D (n=3).

Blend (MCC-102/Lac200M/ MgSt)	**Cohesion /kPa**	**UYS /kPa**	**MPS /kPa**	**FF**	**AIF /º**	**WFA /º**	**CPS, /% @ 15.0 kPa**	**PD, /mBar @ 15.0 kPa**
A (79.5/20/0.5)	0.38 (± 0.09)	1.50 (± 0.37)	16.29 (± 0.43)	11.48 (± 2.62)	35.84 (± 0.49)	17.55 (± 1.07)	12.42 (± 0.17)	1.09 (± 0.02)
B (69.5/30/0.5)	0.38 (± 0.10)	1.51 (± 0.37)	16.19 (± 0.33)	11.55 (± 3.38)	36.68 (± 1.17)	17.51 (± 0.86)	15.98 (± 0.47)	1.43 (± 0.02)
C (59.5/40/0.5)	0.50 (± 0.04)	1.99 (± 0.2)	16.78 (± 0.47)	8.49 (± 0.63)	36.97 (± 1.06)	18.52 (± 0.63)	17.91 (± 0.1)	2 (± 0.02)
D (39.5/60/0.5)	0.87 (± 0.04)	3.39 (± 0.15)	16.44 (± 0.25)	4.85 (± 0.17)	35.81 (± 0.33)	19.24 (± 0.74)	22.44 (± 0.22)	3.55 (± 0.06)

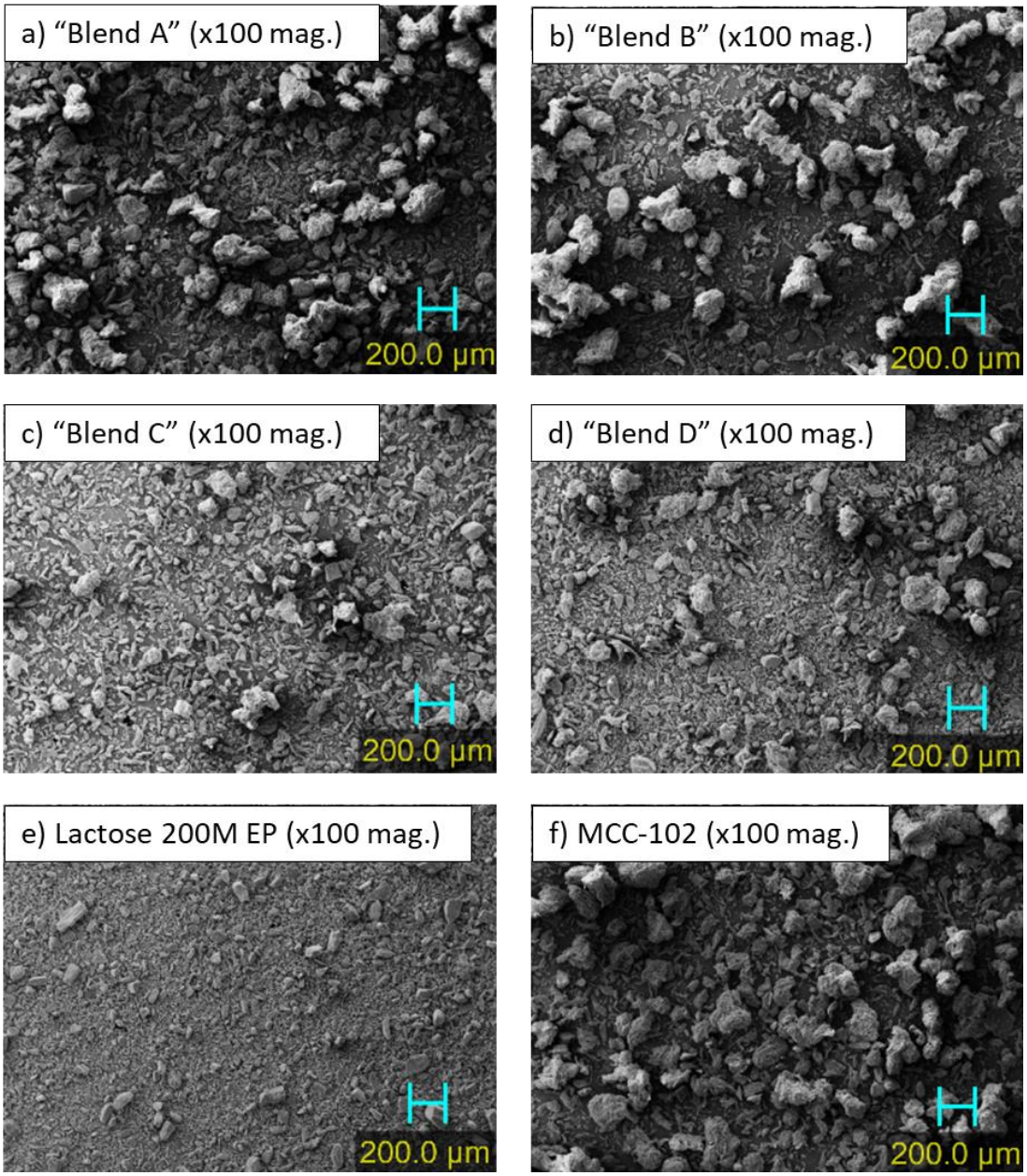

Fig. 6-7. SEM images of a-d) Blends A-D respectively and e) Lactose 200M EP and f) microcrystalline cellulose-102.

Table 6-3. Moisture contents for Blends A-D determined after 3, 6 and 9 hours using the oven-drying method (n=3).

Blend	Moisture content determined via oven-drying (% w/w)		
	After 3 hrs	**After 6 hrs**	**After 9 hrs**
Blend A MCC-102 / Lac200M / MgSt 79.5 %/ 20 %/ 0.5 %	3 ± 8.3 %	2.9 ± 18 %	2.9 ± 5.6 %
Blend B MCC-102 / Lac200M / MgSt 69.5 %/ 30 %/ 0.5 %	2.9 ± 12 %	3.1 ± 10 %	2.9 ± 17 %
Blend C MCC-102 / Lac200M / MgSt 59.5 %/ 40 %/ 0.5 %	2.1 ± 26 %	2.1 ± 22 %	2.2 ± 6.4 %
Blend D MCC-102 / Lac200M / MgSt 39.5 %/ 60 %/ 0.5 %	1.4 ± 8 %	1 ± 40 %	1.3 ± 12 %

6.6.3. Study of dense phase intermittent hopper flow

Fig. 6-8a-c, shows the response to the accumulation of tablets on the balance and the flow of Blend A within the hopper respectively, recorded whilst using a turret production speed of 10 rpm. For the gravimetric data, a fairly consistent tablet mass flow rate of 0.14 $g.s^{-1}$ was recorded by the balance. However, it was difficult to isolate the tablet weight per unit since the time taken for the recorded weight to stabilise due to the tablet impact was often longer than period between the weighing of two individual tablets in succession, which was especially true at higher turret speeds. Moreover, despite the inclusion of a baffle, there was a tendency for tablets to become trapped at the end of turret until the movement second tablet forced it down the chute, which resulted in an inconsistent tablet weighing frequency. It was also virtually impossible to link electrostatic data induced by a given flow of powder to its associated tablet weight characteristics since the powder spent an undefined period of time within the feeder that interfaced the hopper and turret. Therefore, moving ahead, the gravimetric data was simply used as an indication of the tablet mass flow rate and by extension, the hopper flow rate.

Similar to the gravitational flow experiment, the RMS signals induced by the tablet-press hopper flow comprised of a baseline and a number of discrete electrostatic fluctuations

separated by a period of ~5 - 10 seconds (Fig. 6-8b-c), once again confirming the presence of intermittent hopper flow regime, similar to the results reported by (Muite, et al. 2004). However, unlike the electrostatic data obtained for the previous experiment, there were only ~14 electrostatic fluctuations present within both RMS signals, which was attributed to a comparatively lower mass flow rate within the hopper. This was unsurprising given that the hopper flow was predominantly dictated by the gradual emptying of the feeder by the tabletting dies, which at low turret speeds was a slower process than the emptying of a pipe. Also, similarly to the gravitational flow experiments using smaller nozzles, the electrostatic fluctuations were shown to occur at almost identical time points in both the top and bottom RMS signals. Like before, these were likely induced by the sporadic downward movement of the entire powder bed within the hopper.

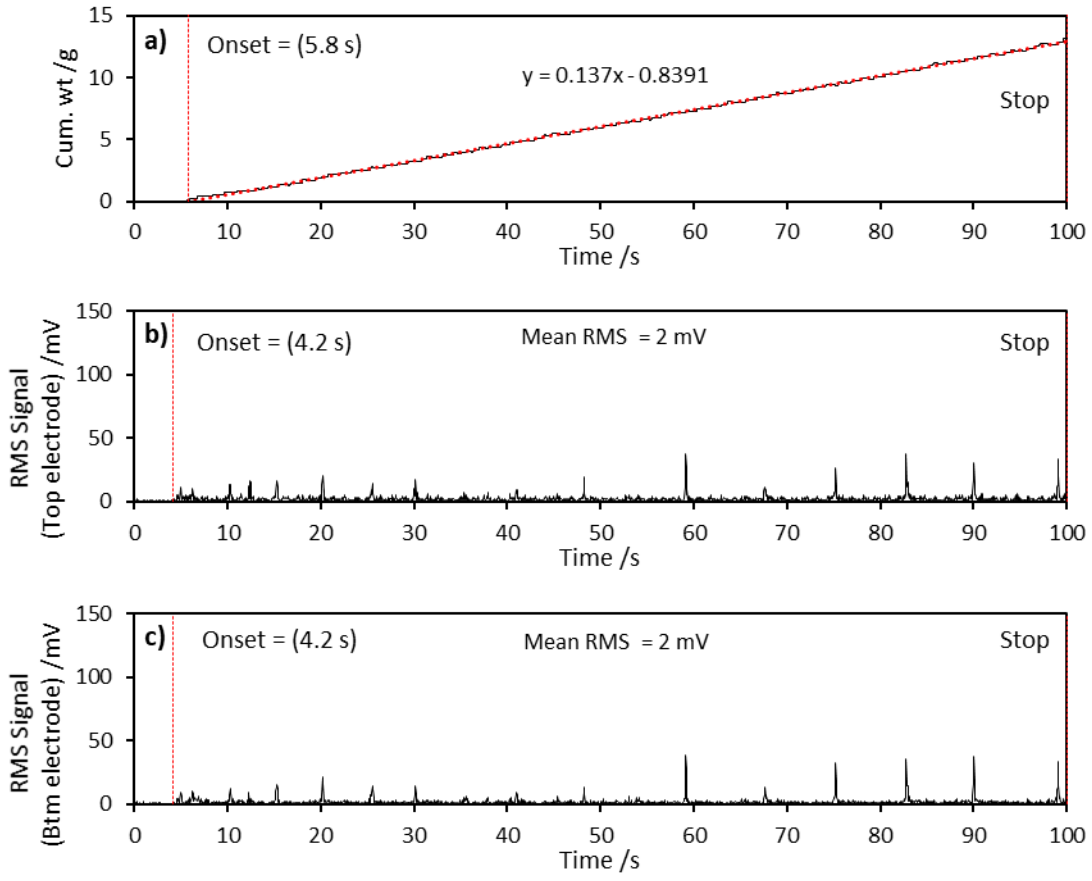

Fig. 6-8. a) Gravimetric and b) the filtered RMS data (for both electrodes) recorded in response to the accumulation of tablets on the balance and flow of powder in the hopper, for a tablet production run using a turret speed of 10 rpm and Blend A.

Fig. 6-9a-e, shows the top and bottom RMS signals generated in response to the increased turret speed during a tablet production run using Blend A. The second and third repeats are shown in Appendix 9 and Appendix 10. Blend A was able to flow through the hopper unimpeded as indicated by its high FF value. At a turret speed of 15 rpm, the associated RMS signal discrete fluctuation number, as well as their apparent frequency also increased. Like the experiment run at 10 rpm, the discrete fluctuations were temporally consistent between both signals and an intermittent flow regime was present. However, for turrets speed ≥20 rpm (Fig. 6-9c-e), the spikes present in both RMS signals became less discrete, noticeably lower in overall amplitude and temporarily inconsistent with each other. Like the pipe experiments, the hopper was not refilled (see Appendix 11), meaning that effects of the increasing velocity field across the powder bed due to hopper emptying would have been present (Kumar, et al. 2020).

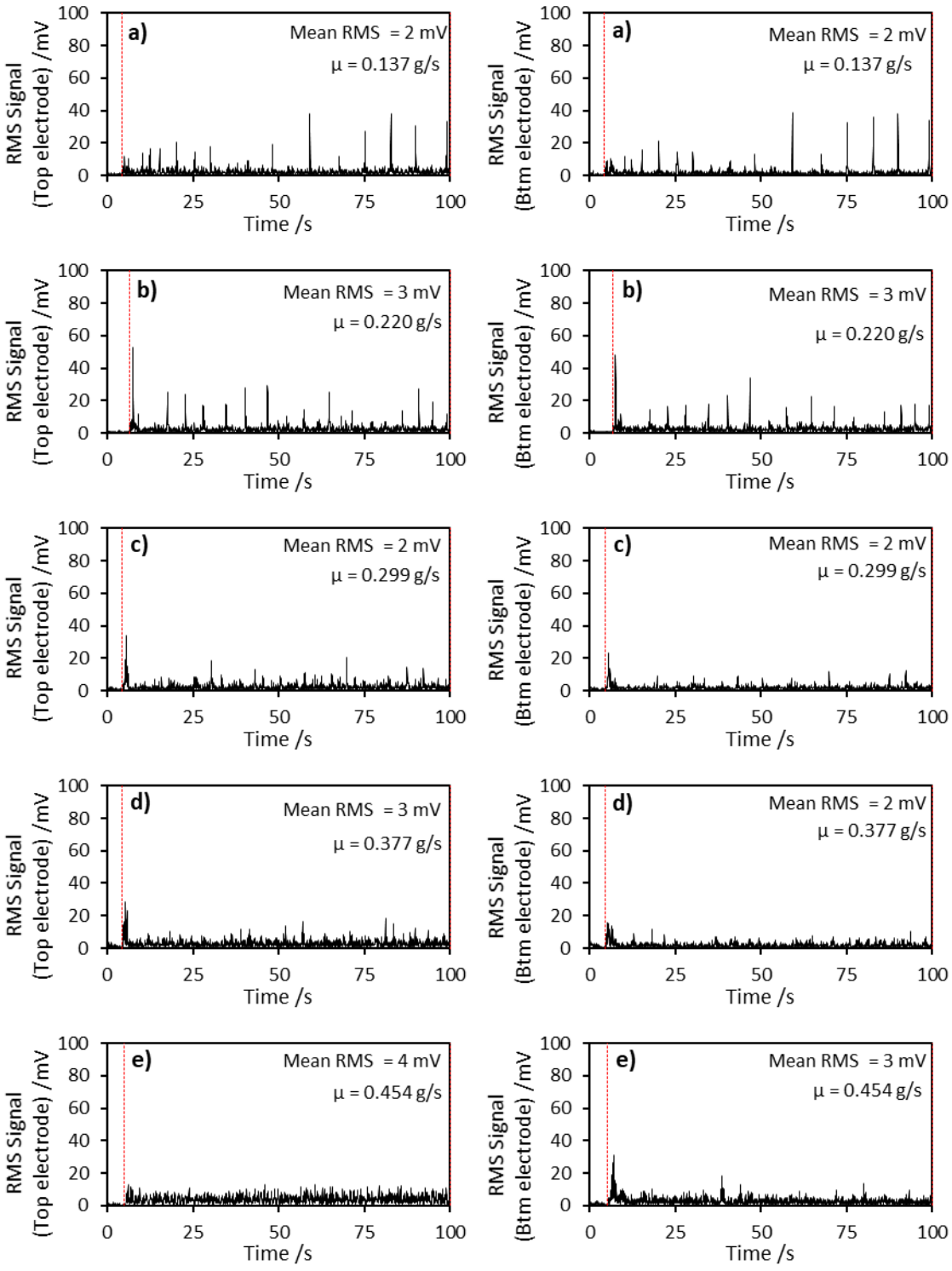

Fig. 6-9. First set of filtered RMS signals obtained from the top and bottom electrodes in response to the hopper flow of Blend A, whilst utilising turret speeds of, a) 10 rpm, b) 15 rpm, c) 20 rpm, d) 25 rpm and e) 30 rpm. μ = the associated tablet mass flow rate.

Fig. 6-10a-e, shows the first set RMS signals recorded for both the top and bottom electrodes induced by the hopper flow of Blend B at turret speeds between 10-30 rpm. The second and third set of repeats for this blend are shown in Appendix 12 and Appendix 13 respectively. Also, refer to Appendix 14 for images of the relative hopper fill level per turret speed. Like Blend A, Blend B was able to flow freely within the hopper, as indicated by its high FF value. At lower turret speeds, the hopper flow of Blend B also induced discrete spikes with temporal consistencies between both top and bottom electrostatic signals, thus indicating an intermittent flow regime, which was unsurprising given the rheological similarities to Blend A. However, unlike Blend A, Blend B also induced these discrete spikes even at the highest turret speeds, suggesting that the intermittent flow regime was persistent regardless of the turret speed/hopper mass flow rate. This effect was thought to be related an increased susceptibility to bulk consolidation due to the load of the powder bed bearing down on the powder near the hopper outlet (Ramírez, et al. 2010). Since Blend B exhibited a 29 % and 31 % increase in CPS and PD respectively with respects to Blend A, the former was further susceptible to compression at lower loadings and more so at higher loadings, whereas the higher PD value implied Blend B was less likely to aerate during flow (Prescott and Barnum 2000). Consequently, the further compressed state would have had a reduced propensity to yield, but when it did so, it was thought that the entire bulk would have moved downwards at once, as indicated by the RMS spikes located at similar time points.

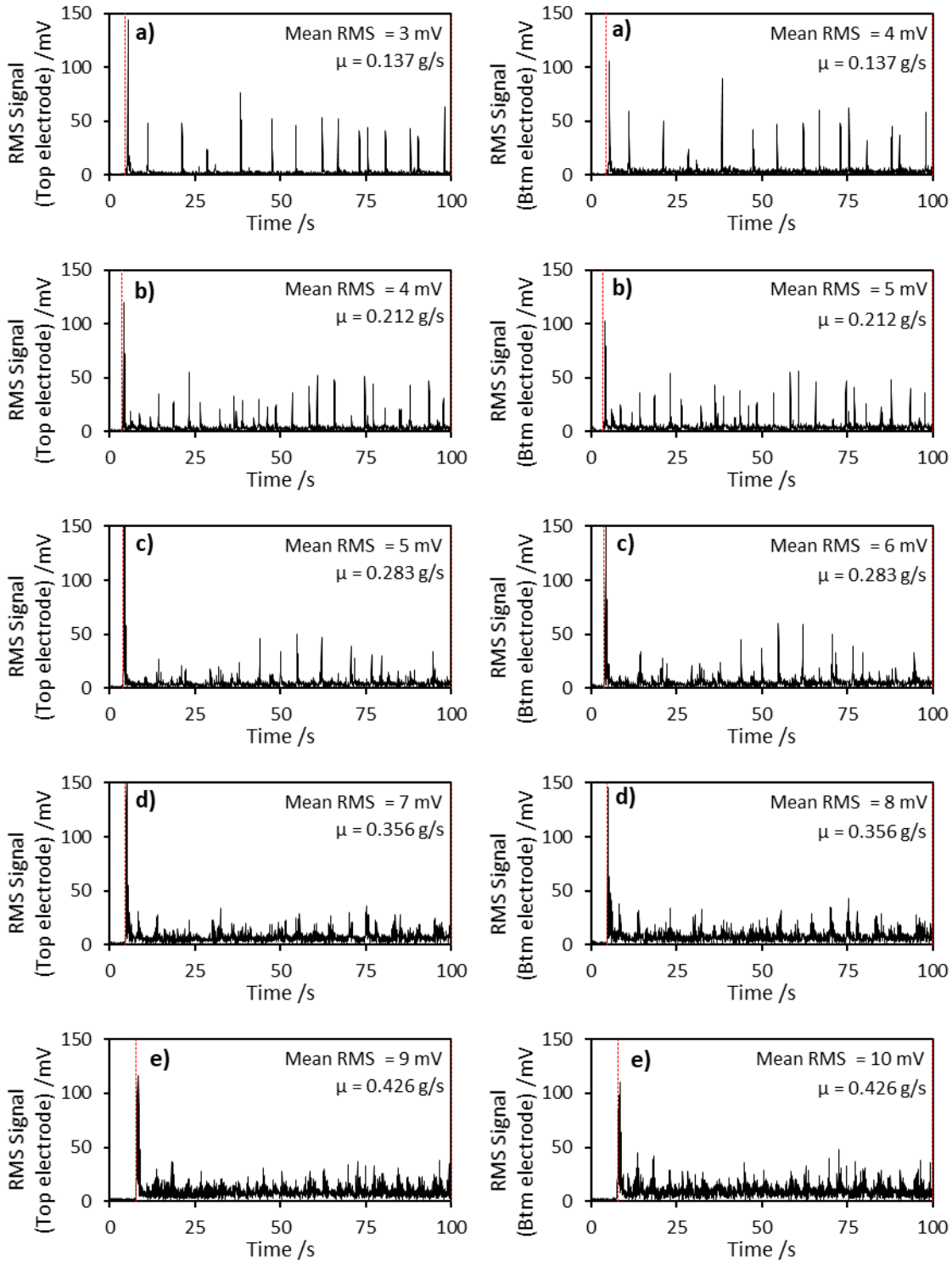

Fig. 6-10. First set of filtered RMS signals obtained from the top and bottom electrodes in response to the hopper flow of Blend B, whilst utilising turret speeds of, a) 10 rpm, b) 15 rpm, c) 20 rpm, d) 25 rpm and e) 30 rpm. μ = the associated tablet mass flow rate.

Fig. 6-11a-e, shows the first set RMS signals recorded for both the top and bottom electrodes induced by the hopper flow of Blend C, at incrementing turret speeds. The second and third repeat RMS signals can be found in Appendix 15 and Appendix 16. Also, images for the relative hopper fill level per turret speed are shown in Appendix 17. Compared to Blend A and Blend B, Blend C was more cohesive, as evident by its higher FF value, although it was still able to flow through the hopper unimpeded. As well, the RMS spikes recorded for this blend were stronger in magnitude, especially for the signals recorded for the bottom electrodes. Like Blend B, these RMS spikes were shown to occur at similar time points across each turret speed, once again suggesting the presence of an intermittent flow regime. Furthermore, this flow regime did not seem to alter with the emptying of the hopper and increasing turret speed due to the increased susceptibility of the blend consolidation and poor permeability (CPS = 17.91 kPa and PD = 2 mBar). The tendency for more cohesive powders (with lower flow indices) to adopt an intermittent flow regime has previously been reported by Faqih, et al. (2007), who performed an extensive study on the flow regimes adopted by a number of powders and blends within hoppers that possessed variable interior angles (Faqih, et al. 2007).

Finally, for Blend C, the mean RMS recorded by the bottom electrode was about 167 - 250 % greater than that recorded by the top electrode, a difference which was higher when compared to those recorded for Blend A and B. Since the RMS spikes still occurred at the similar time points between top and bottom electrodes, it is suggested that the mass flow rate between these two points remained the same. Instead, the disparity between the top and bottom RMS signals may be related to a change in powder density across the axial length of the sensing region. A possible explanation for this behaviour is illustrated in Fig. 6-12, which considers the powder nearer the top electrode vicinity existing in more a densified state but moving at a lower velocity, whereas powder nearer the bottom electrode vicinity existing in a less densified state but moving at a higher velocity, with the latter density induced by possible dilation of the powder bed beneath the sensing region due to freeing space in the feeder below. These behaviours would thus result in the powder bed moving at the same mass flow rate and inducing electrical currents at the same time points, with the faster moving powder inducing the higher current. Although, there may be a question as to whether such a drastic change in density would have truly been present across the 14 mm sensing region. This would require further investigation, possibly with the aid of DEM.

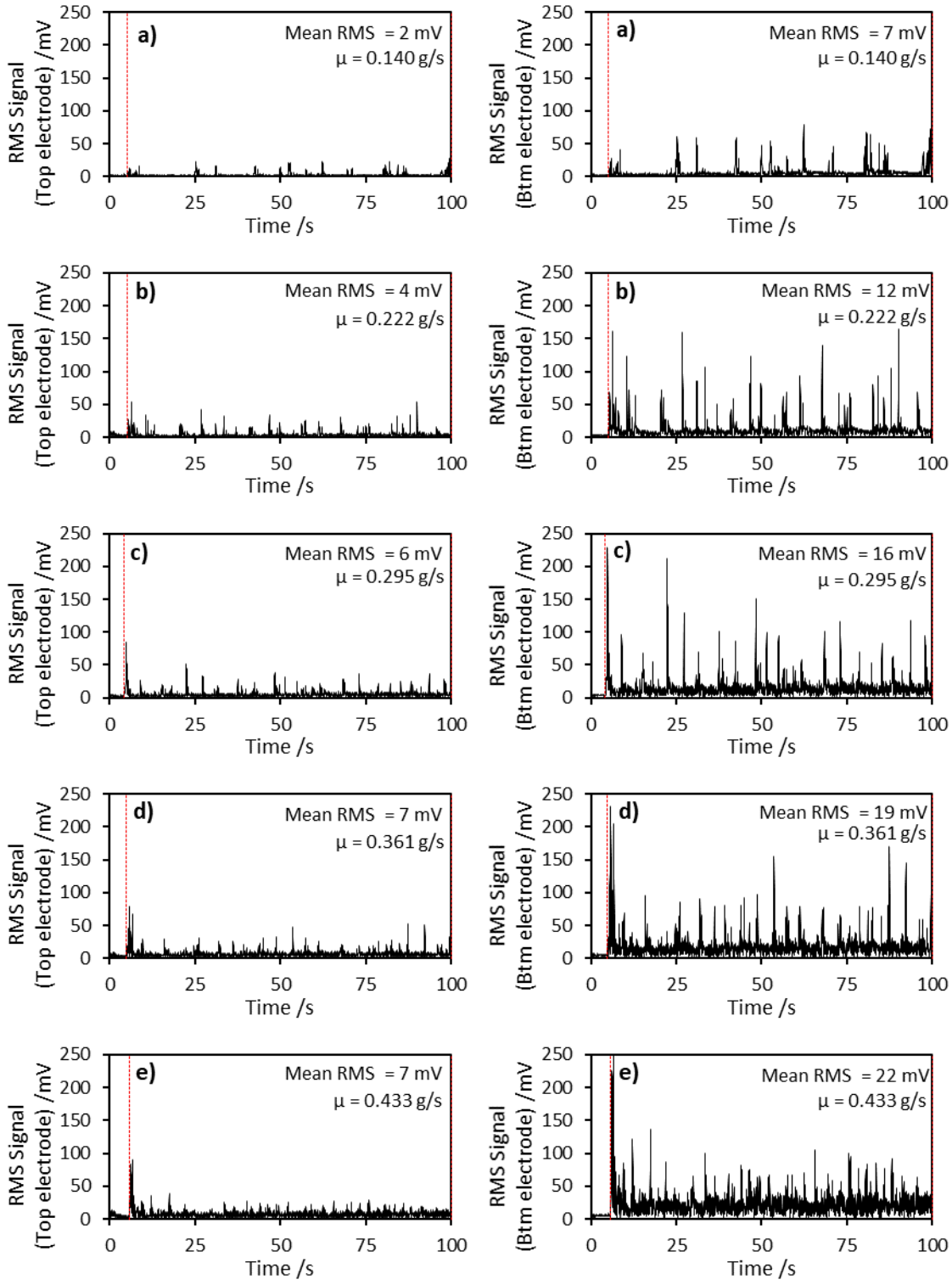

Fig. 6-11. First set of filtered RMS signals obtained from the top and bottom electrodes in response to the hopper flow of Blend C, whilst utilising turret speeds of, a) 10 rpm, b) 15 rpm, c) 20 rpm, d) 25 rpm and e) 30 rpm. μ = the associated tablet mass flow rate.

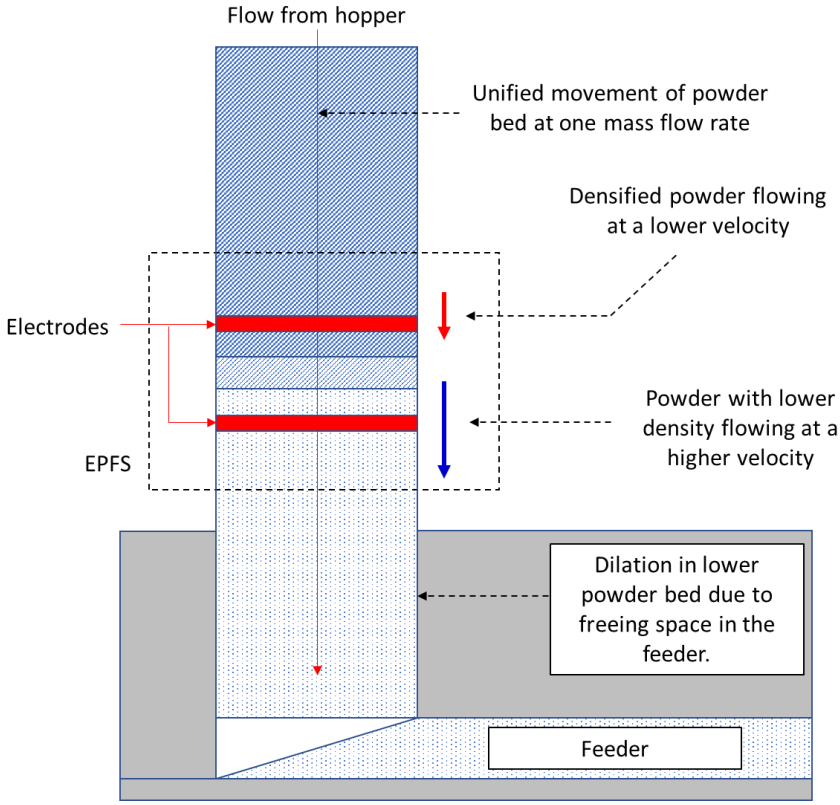

Fig. 6-12. Illustration for explaining the signal amplitude difference between the top and bottom electrodes for the electrostatic data recorded for Blend C.

Fig. 6-13, shows the RMS signals recorded in response to the hopper flow of Blend D at a turret speed of 10rpm only. However, it was shown that upon starting the tabletting operation, the powder was found to have formed a cohesive arch above the EPFS, meaning that no electrostatic signal was generated due to zero flow. The residual components in the signal were simply related to electrostatic background noise. Although this blend possessed the worst flowability of the four blends, it was still categorised as “easy-flowing” (FF = 4.85). In this case, it could be that the blockage may have been further propagated by consolidation, probably under its bulk weight, of which Blend D would have been the most susceptible (CPS = 22.4 %). Even so, this data was useful as it allowed the visualisation of the electrostatic response to powder blockage within the hopper, which otherwise would not have been detected by the fill-volume sensor.

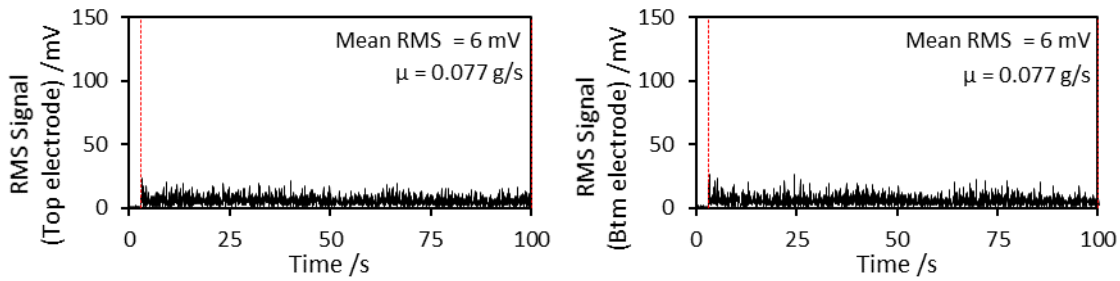

Fig. 6-13. Filtered electrostatic signals obtained from the top and bottom electrodes in response to the hopper flow of Blend D, whilst utilising turret speeds of 10 rpm only. μ = the associated tablet mass flow rate.

Fig. 6-14, shows additional RMS signals captured as the EPFS sensing region emptied of Blend C. Here, the RMS signal of a given electrode is shown to have dropped to a baseline value, which was related to the clearance of powder within its respective sensing region. This clearance time point was delayed between the bottom electrode signal and the top electrode signal, given that the powder clearance occurred within the top electrode sensing region initially. However, despite the emptying of powder in the hopper, the tablet mass flow rate was unaffected given that the feeder remained flooded. The ability to pre-emptively predict the emptying of powder prior to the tablet weight becoming impacted is valuable, although at this stage of the study, it was not possible to determine any effects on the tablet weight given the difficulties in obtaining a reliable in-line measurement for the latter. Nonetheless, the sensitivity to hopper emptying as well as blockage are valuable qualities should the EPFS potentially be applied as PAT for process control. Compared to the commercial fill-volume sensor installed in the tablet press, the EPFS not only possessed a smaller footprint, but was able to be installed at a lower region within the hopper in a non-intrusive manner, which was suitable for in-line application.

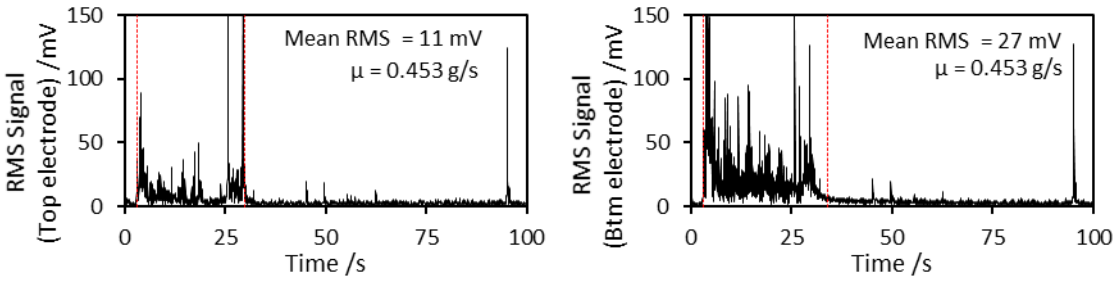

Fig. 6-14. Filtered electrostatic signals obtained from the top and bottom electrodes capturing the emptying of the EPFS of Blend C, whilst utilising turret speeds of 30 rpm only. μ = the associated tablet mass flow.

6.7. Conclusions

In this study, intermittent dense phase powder flow in two systems were qualitatively analysed using EPFS technology. Initially, gravitational flow of Lactose #316 Fast flo in a simple pipe experiment was studied in order to develop an understanding between the RMS signal output and the corresponding powder flow regime. Each fluctuation in the RMS signals was attributed to individual downwards movements of the powder bed within the pipe. At lower mass flow rates, the flow regime was thought to flow via intermittent mass flow regime, indicated by instances when the RMS spikes occurred at the same time points between both the top and bottom electrode RMS signals. This was caused by unified movement of powder bed with a volume at least equal to or greater than that of the EPFS sensing region. However, in the instances where RMS spikes became inconsistent across the signal pair, it was suggested that the powder began to flow between both electrodes at different velocities. When the pipe was full it was thought that a variable velocity distribution was present near the outlet, where particles nearer the cross-section of the pipe flowed at a higher velocity than those nearer to the wall (i.e. core flow), whereas the remaining powder within the pipe would have flowed at a more homogenous velocity. As the pipe emptied, the in-homogenous velocity field would have expanded across the height of the rest of the powder bed resulting in a core flow regime developed across the entire pipe. As a result, when the pipe became lower in fill capacity, the particles would have flowed at different velocities within the sensing region and thus would have induced RMS spikes at different time points between both electrodes.

In the second part of the study, hopper flow behaviour for four blends (A-D) in a tablet press was studied, with blend cohesivity and turret speed as input variables. At the lowest turret speeds and higher hopper fill levels, blends A-C adopted an intermittent flow regime.

Although, for the least cohesive blends (A and B) this flow regime became less intermittent as the turret speed was increased and the hopper fill level decreased. Although Blend B was less susceptible to this effect due to its high bulk compressibility. Blends C, which was more cohesive, maintained the intermittent flow regime regardless of the turret speed and hopper fill level, which was attributed to its increased susceptibility to consolidation. Blend D which was the most cohesive blend, failed to flow through the hopper due to cohesive arching at the hopper outlet, indicated by the absence of large RMS spikes. As well, the RMS signal demonstrated sensitivity to instances where the hopper emptied.

It is anticipated that with further development, this may be integrated into dense phase flow systems as PAT for the study of hopper flow behaviour to facilitate hopper and formulation design and for the monitoring of the in-line hopper flow regime during tabletting operations.

Future work should consider the gaps in this study. Firstly, the electrostatic observations with respects to the flow characteristics need to be validated, which could be achieved in bespoke transparent hoppers/pipe where flow patterns are captured via digital recording or using DEM tools. The sensing volume of the EPFS should also be optimized in order to interrogate a larger hopper volume and thus capture a greater degree of powder movement. This could include expansion of the EPFS interfacing the hopper and feeder. Another approach would be to install two or more electrodes along axial length of the outer hopper wall, although this would require modifications to be made to the hopper so that it is able to accommodate the electrodes along its wall without impeding the powder flow. As well, the TIA and measurement software would require redesigning. Once the EPFS design is optimized, focus should be further placed on the relationship between input variables and the output RMS signal characteristics and possibly even the downstream tablet CQAs.

Chapter 7. General conclusions and future work

7.1. General conclusions

Off-line measurements are not usually able to provide the information which allows the flow and charge properties exhibited in-process to be accurately predicted. However, in-line electrostatic sensors are one of the only examples of non-intrusive PAT which are sensitive to both properties. Therefore, experiments were conducted in order to study the flow and charging characteristics developed by powders under the conditions of flow by means of EPFS measurement.

A powder's in-line flow behaviour (e.g. flow properties, regime and pattern), were shown to be highly dependent on the interaction between its material properties and the shear and packing conditions of the process. Powders that could flow gravitationally under dense phase conditions tended to adopt an intermittent flow regime, whereas screw conveyed powders adopted the frequency characteristics of the screw feeding mechanism, resulting in a pulsatile flow pattern. Also, in each of these scenarios, the powder's cohesivity played a critical role in the development of the flow regime.

In the hopper, the increased powder cohesivity contributed to an elevated susceptibility to consolidation, resulting in a higher tendency for the material to adopt an intermittent flow regime, even at lower hopper fill levels. Compressibility and permeability bulk properties characterised using the FT4 Powder Rheometer described the susceptibility of the powder to consolidate under its own weight. Moreover, shear and wall friction properties partly indicated the powder's spontaneous flowability under the packing conditions within the hopper (Freeman 2007), although the consolidation in the latter were unknown. However, at this stage, these observations could not be coupled to the tablet weight characteristics.

On the other hand, in the screw feeder, the powder's cohesivity influenced its packing tendencies as well as its coupling to periodicity of the feeding mechanism upon deposition. Cohesive powders tended to form dense plaques which deposited randomly at the barrel terminal, whereas free-flowing particles which spilled easily from the feeder were shown to retain the periodicity of the feeding mechanism. In these instances, the powder compressibility and permeability were considered key properties which contributed to the bulk powder's ability to consolidate and occupy the free volume within the barrel. Measurements of cohesivity via FFT analysis of electrostatic signals were shown to following a similar rank

order in powder cohesivity as permeability, compressibility and specific energy properties characterised using the FT4 Powder Rheometer. It is thought that value of these outputs potentially lies in the realms of process and formulation design, since in-line bulk transfer parameters are known to be heavily dependent on the flow regime (Jaworski and Dyakowski 2001). These outputs may also provide an early inclination of as to whether the flowing material is deviating from its intended flow pattern which corresponds to consistent flow, due to change in the input variables.

In contrast, it was more challenging to quantify bulk transfer parameters such as mass flow rate against the electrostatic parameters. The relationship between the powder mass flow rate and RMS of the electrostatic signal was thought to be dependent on a number of factors: the nature of the flow regime with respects to the EPFS sensing volume; the consistency in the mass flow rate; and the magnitude and distribution of charges present on the powder. Under the dense phase gravitational flow regime, it was difficult to predict the mass flow rate given a change in gradient between both flow parameters at higher flow rate, which was attributed to a change in flow regime (i.e. increased dilation). Although, in the screw feeder a relatively linear relationship was expressed between both parameters for each powder, most likely because the screw mechanism induced shear conditions with greater consistency. However, RMS variability was still a presiding issue, evident by a standard deviation up to 36 %, which was due to the charge variation on the powders. This was more prevalent in low moisture lactose monohydrate powders compared to higher moisture content maize starch and microcrystalline cellulose powders. Although, this application was confirmed unfeasible, the ability for the EPFS to identify instability in the measured powder charge propagated a further study regarding the in-line analysis of powder charge, which will be elaborated on further in this section.

There were also attempts to calibrate the powder velocity against the powder mass flow rate in both dense and lean phase conditions. This was proven impossible in the former flow regime since the high powder density did not induce identical signals with a noticeable time delay required for cross-correlation. However, in lean phase, the velocity measurement was made possible due to the lower solids' concentration. It can be surmised that these are the minimum conditions required to measure velocity parameters for non-pneumatic flow regimes. The multiple cross-correlation technique was also able to obtain a velocity profile which is anticipated to be valuable for in-line analysis. Although, the average velocities were

shown to be immune to the powder mass flow rate, given that the propulsion exerted by the feeder had deteriorated during the gravitational deposition of the powder through air. However, the reproducibility in the average velocities for each powder was excellent (standard deviation < 2%) regardless of the mass flow rate. This opens future development of an integrated sensor, in combination with an independent measurement of solids concentration, so that the in-line powder mass flow rate may be inferred. Although as explained previously, it is confirmed that this would not be applicable to high density flow regimes such as those in hoppers.

As alluded to earlier, the in-line analysis of the dynamic powder charge was rendered possible by the sensitivity of the EPFS to the electrostatic charge variation and an in-line measurement of powder mass flow rate. The charging behaviours of the five pharmaceutical powders conveyed using the twin-screw feeder, were analysed using the RMS signal normalised against the mass flow rate, which provided a measure of the charge per gram per second. Maize starch EP and the microcrystalline cellulose powders were both shown to charge over time. Lactose 200M was shown to discharge, which was attributed to the coating of the screws and reduced particle-metal contacts. Lactose #316 Fast flo was shown to rapidly charge for a relatively short period of time due to particle fracture, which resulted in adhesion to the equipment. These behaviours would otherwise be difficult to capture in real-time using the standard Faraday Cup method. It should be re-emphasised that powder charging should be characterised under the conditions of flow in order to capture these exact behaviours, which at of the current time of writing, is only achievable using electrostatic sensors.

7.2. Future work

The novelty in this tool is clearly demonstrated by the applications reported in this work. Until now, electrostatic sensors had not been applied to flow regimes involving pharmaceutically relevant powders. It is anticipated that with further development, a dual-PAT approach may be possible, one which enables the in-line characterisation of both powder charge and flow properties. However, since scope of this study focused on investigating the relationship between the electrostatic characteristics and the flow / charge behaviour of the powders, there was no opportunity to validate the electrostatic outputs against reference techniques. Moreover, a number of characterisation techniques were not explored. Therefore, future work should focus on achieving the following goals:

- Incorporate particle sizing techniques, although it would be ideal for this technique to also be integrated in-line so as to capture the cohesive interactions such as agglomeration that occur in-process. This may be achievable using the commercial Eyecon$_2$ (Innopharma Labs), a technique based on digital imaging which is able to characterise particle size under the conditions of flow.
- Expand the cohesivity analysis using a wider range of powders with different flow properties. In doing so, identify the failure modes of the technology, e.g. maximum allowed flow concentration, material compatibility (such as conductive powders) and oversaturation of particle charges. It might also be beneficial to include shear cell testing, which may describe the yielding tendency of the powders at the free surface (i.e. the barrel terminal).
- It is suggested that numerical solutions such as DEM should also be applied in order to study the relationship between powder cohesivity and the screw feeder flow mechanism that is normally obstructed by the barrel. Coulomb's Law and electrical field models may also be incorporated into these simulations so that the fundamental charging behaviour involved developed during processing may be (Tan, et al. 2019).
- Validate the measured velocities using a reference technique. For these flow conditions, it might be possible to perform a simple velocity measurement by determining the time travelled by the particles / powder between the fields of view of two digital cameras.
- Explore combination technologies, which also utilise an independent measurement of solids concentration, in order to infer the in-line powder mass flow rate.
- Validate the charging behaviour observed using the EPFS technique. This would be a challenging task given that the standard method for charge measurement is the closed-ended Faraday Cup. A method would need to be developed in order to ensure that the sampling technique does not induce additional charge.
- It is suggested that the charging behaviour of powders can be characterised via measurements of resistivity (Murtomaa, et al. 2015), which may be possible using dielectric / impedance spectroscopy.
- Expand the relative charging analysis with applications made towards other processes such as blending.
- Study the intermittent flow regime present in dense phase using DEM as a means to validate the qualitative localised flow regime analysis achieved using the electrostatic

sensor. Furthermore, the applicability of the technique to other types of flow regimes such as mass and funnel flow should be investigated. Finally, a means to characterise the in-line tablet weight should be developed in order to ascertain whether changes in the hopper flow behaviour as indicated by the RMS also induces changes in the tablet weight.

References

Alam, M.A., Shi, Z., Drennen III, J.K., Anderson, C.A., 2017. In-line Monitoring and Optimization of Powder Flow in a Simulated Continuous Process Using Transmission Near Infrared Spectroscopy. International Journal of Pharmaceutics. doi: //doi.org/10.1016/j.ijpharm.2017.04.054.

Albion, K., Briens, L., Briens, C., Berruti, F., 2007. Flow regime determination in horizontal pneumatic transport of fine powders using non-intrusive acoustic probes. Powder Technology, 172, 157-166. doi: //doi.org/10.1016/j.powtec.2006.10.040.

Alkassar, Y., Agarwal, V.K., Behera, N., Jones, M.G., Pandey, R.K., 2019. Transient characteristics of fine powder flows within fluidized dense phase pneumatic conveying systems. Powder Technology, 343, 629-643. doi: https://doi.org/10.1016/j.powtec.2018.11.081.

Anand, A., Curtis, J.S., Wassgren, C.R., Hancock, B.C., Ketterhagen, W.R., 2009. Predicting discharge dynamics of wet cohesive particles from a rectangular hopper using the discrete element method (DEM). Chemical Engineering Science, 64, 5268-5275. doi: https://doi.org/10.1016/j.ces.2009.09.001.

Anand, A., Curtis, J.S., Wassgren, C.R., Hancock, B.C., Ketterhagen, W.R., 2008. Predicting discharge dynamics from a rectangular hopper using the discrete element method (DEM). Chemical Engineering Science, 63, 5821-5830. doi: https://doi.org/10.1016/j.ces.2008.08.015.

Babout, L., Grudzien, K., Maire, E., Withers, P.J., 2013. Influence of wall roughness and packing density on stagnant zone formation during funnel flow discharge from a silo: An X-ray imaging study. Chemical Engineering Science, 97, 210-224. doi: //doi.org/10.1016/j.ces.2013.04.026.

Bacchuwar, S., Vidyapati, V., Quan, K., Lin, C., Miller, J.D., 2019. Quantitative bin flow analysis of particle discharge using X-ray radiography. Powder Technology, 344, 693-705. doi: //doi.org/10.1016/j.powtec.2018.12.028.

Barratt, I.R., Yan, Y., Byrne, B., Bradley, M.S.A., 2000. Mass flow measurement of pneumatically conveyed solids using radiometric sensors. Flow Measurement and Instrumentation, 11, 223-235. doi: //doi.org/10.1016/S0955-5986(00)00022-4.

Baserinia, R., Sinka, I.C., Rajniak, P., 2016. Vacuum assisted flow initiation in arching powders. Powder Technology, 301, 493-502. doi: https://doi.org/10.1016/j.powtec.2016.03.051.

Beakawi Al-Hashemi, H.M., Baghabra Al-Amoudi, O.S., 2018. A review on the angle of repose of granular materials. Powder Technology, 330, 397-417. doi: https://doi.org/10.1016/j.powtec.2018.02.003.

Behjani, M.A., Motlagh, Y.G., Bayly, A., Hassanpour, A., 2019. Assessment of blending performance of pharmaceutical powder mixtures in a continuous mixer using Discrete Element Method (DEM). Powder Technology. doi: https://doi.org/10.1016/j.powtec.2019.10.102.

Benedetti, C., Abatzoglou, N., Simard, J.-., McDermott, L., Léonard, G., Cartilier, L., 2007. Cohesive, multicomponent, dense powder flow characterization by NIR. International Journal of Pharmaceutics, 336, 292-301. doi: //doi.org/10.1016/j.ijpharm.2006.12.014.

Bentham, A.C., Kwan, C.C., Boerefijn, R., Ghadiri, M., 2004. Fluidised-bed jet milling of pharmaceutical powders. Powder Technology, 141, 233-238. doi: https://doi.org/10.1016/j.powtec.2004.01.024.

Berger, K.J., Hrenya, C.M., 2014. Challenges of DEM: II. Wide particle size distributions. Powder Technology, 264, 627-633. doi: https://doi.org/10.1016/j.powtec.2014.04.096.

Beverloo, W.A., Leniger, H.A., van de Velde, J., 1961. The flow of granular solids through orifices. Chemical Engineering Science, 15, 260-269. doi: https://doi.org/10.1016/0009-2509(61)85030-6.

British Pharmacopoeia Commission, 2019a. Appendix IX D. Determination of Loss on Drying. British Pharmacopoeia.

British Pharmacopoeia Commission, 2019b. Appendix XVII E. Flowability. British Pharmacopoeia.

British Pharmacopoeia Commission, 2019c. Appendix XVII N. Powder Flow. British Pharmacopoeia.

British Pharmacopoeia Commission, 2019d. Lactose. British Pharmacopoeia.

British Pharmacopoeia Commission, 2019e. Maize Starch. British Pharmacopoeia.

British Pharmacopoeia Commission, 2019f. Microcrystalline Cellulose. British Pharmacopoeia.

British Standards Institute, 1996. BS7506-2: Methods for measurements in electrostatics. Part 2. Test methods.

British Standards Institute, 1995. BS7506-1: Methods for measurements in electrostatics. Part 1. Guide to basic electrostatics.

British Standards Institution, 1996. Methods for Measurements in electrostatics. Part 2. Test methods.

Brown, R.L., 1961. Minimum energy theorem for flow of dry granules through apertures. Nature, 191, 458-461.

Brown, R.L., Richards, J.C., 1970. Principles of Powder Mechanics: Essays on the Packing and Flow of Powders and Bulk Solids, 1st Ed., Pergamon Press Ltd.

Brown, R.L., Richards, J.C., 1965. Kinematics of the flow of dry powders and bulk solids. Rheological Acta, 4, 153.

Buckton, G., 2007. Solid-state propertiesIn: Aulton, M.E. (Ed.), Aulton's Pharmaceutics, the Design and Manufacture of Medicines, Churchill Livingstone Elsevier, Philadelphia, United States, pp. 110-115.

Calderón, C.A., Villagrán Olivares, M.C., Uñac, R.O., Vidales, A.M., 2017. Correlations between flow rate parameters and the shape of the grains in a silo discharge. Powder Technology, 320, 43-50. doi: https://doi.org/10.1016/j.powtec.2017.07.004.

Capece, M., Silva, K.R., Sunkara, D., Strong, J., Gao, P., 2016. On the relationship of inter-particle cohesiveness and bulk powder behavior: Flowability of pharmaceutical powders. International Journal of Pharmaceutics, 511, 178-189. doi: //dx.doi.org/10.1016/j.ijpharm.2016.06.059.

Carter, R.M., Yan, Y., Cameron, S.D., 2005. On-line measurement of particle size distribution and mass flow rate of particles in a pneumatic suspension using combined imaging and electrostatic sensors. Flow Measurement and Instrumentation, 16, 309-314. doi: //doi.org/10.1016/j.flowmeasinst.2005.03.005.

Cavinato, M., Artoni, R., Bresciani, M., Canu, P., Santomaso, A.C., 2013. Scale-up effects on flow patterns in the high shear mixing of cohesive powders. Chemical Engineering Science, 102, 1-9. doi: https://doi.org/10.1016/j.ces.2013.07.037.

Chan, E.L., Washino, K., 2018. Coarse grain model for DEM simulation of dense and dynamic particle flow with liquid bridge forces. Chemical Engineering Research and Design, 132, 1060-1069. doi: https://doi.org/10.1016/j.cherd.2017.12.033.

Chen, W., Roberts, A., Williams, K., Miller, J., Plinke, J., 2017. On uniaxial compression and Jenike direct shear testings of cohesive iron ore materials. Powder Technology, 312, 184-193. doi: https://doi.org/10.1016/j.powtec.2017.02.037.

Choi, K., Taghavivand, M., Zhang, L., 2017. Experimental studies on the effect of moisture content and volume resistivity on electrostatic behaviour of pharmaceutical powders. International Journal of Pharmaceutics, 519, 98-103. doi: //doi.org/10.1016/j.ijpharm.2017.01.005.

Chowdhury, F., Sowinski, A., Ray, M., Passalacqua, A., Mehrani, P., 2018. Charge generation and saturation on polymer particles due to single and repeated particle-metal contacts. Journal of Electrostatics, 91, 9-15. doi: //doi.org/10.1016/j.elstat.2017.11.004.

Cong, X., Guo, X., Gong, X., Lu, H., Dong, W., 2011. Experimental research of flow patterns and pressure signals in horizontal dense phase pneumatic conveying of pulverized coal. Powder Technology, 208, 600-609. doi: https://doi.org/10.1016/j.powtec.2010.12.027.

Cong, X., Guo, X., Lu, H., Gong, X., Liu, K., Sun, X., Xie, K., 2013. Flow patterns of pulverized coal pneumatic conveying and time-series analysis of pressure fluctuations. Chemical Engineering Science, 101, 303-314. doi: https://doi.org/10.1016/j.ces.2013.05.058.

Coombes, J.R., Yan, Y., 2015. Experimental investigations into the flow characteristics of pneumatically conveyed biomass particles using an electrostatic sensor array. Fuel, 151, 11-20. doi: //doi.org/10.1016/j.fuel.2014.11.048.

Cundall, P.A., Strack, O.D.L., 1979. A discrete numerical model for granular assemblies. Geotechnique, 29, 47-65. doi: 10.1680/geot.1979.29.1.47.

De Leersnyder, F., Peeters, E., Djalabi, H., Vanhoorne, V., Van Snick, B., Hong, K., Hammond, S., Liu, A.Y., Ziemons, E., Vervaet, C., De Beer, T., 2018. Development and validation of an in-line NIR spectroscopic method for continuous blend potency determination in the feed frame of a tablet press. Journal of Pharmaceutical and Biomedical Analysis, 151, 274-283. doi: https://doi.org/10.1016/j.jpba.2018.01.032.

De Leersnyder, F., Vanhoorne, V., Kumar, A., Vervaet, C., De Beer, T., 2019. Evaluation of an in-line NIR spectroscopic method for the determination of the residence time in a tablet press. International Journal of Pharmaceutics, 565, 358-366. doi: https://doi.org/10.1016/j.ijpharm.2019.05.006.

Deleuil, M., Chulia, D., Pourcelot, Y., 1998. Chapter 5: Particle and Powder Dynamics. 9.

Eckhoff, R.K., 2009. Understanding dust explosions. The role of powder science and technology. Journal of Loss Prevention in the Process Industries, 22, 105-116. doi: https://doi.org/10.1016/j.jlp.2008.07.006.

Eilbeck, J., Rowley, G., Carter, P.A., Fletcher, E.J., 2000. Effect of contamination of pharmaceutical equipment on powder triboelectrification. International Journal of Pharmaceutics, 195, 7-11. doi: //doi.org/10.1016/S0378-5173(99)00351-8.

Emery, E., Oliver, J., Pugsley, T., Sharma, J., Zhou, J., 2009. Flowability of moist pharmaceutical powders. Powder Technology, 189, 409-415. doi: //dx.doi.org/10.1016/j.powtec.2008.06.017.

Engers, D.A., Fricke, M.N., Storey, R.P., Newman, A.W., Morris, K.R., 2006. Triboelectrification of pharmaceutically relevant powders during low-shear tumble blending. Journal of Electrostatics, 64, 826-835. doi: //doi.org/10.1016/j.elstat.2006.02.003.

Faqih, A.N., Alexander, A.W., Muzzio, F.J., Tomassone, M.S., 2007. A method for predicting hopper flow characteristics of pharmaceutical powders. Chemical Engineering Science, 62, 1536-1542. doi: //doi.org/10.1016/j.ces.2006.06.027.

Fay, J., 1994. Introduction to Fluid Mechanics, The MIT Press, London, England.

FDA, 2004. Guidance for Industry: PAT—A Framework for Innovative Pharmaceutical Development, Manufacturing, and Quality Assurance.

Feng, H., Meng, A., Zhang, Y., Gong, Y., Li, Q., 2020. LDV measurements of particle fluctuation velocities in dilute gravity-driven gas-particle flows. Powder Technology, 360, 1368-1376. doi: https://doi.org/10.1016/j.powtec.2019.10.037.

Fitzpatrick, J.J., Barringer, S.A., Iqbal, T., 2004. Flow property measurement of food powders and sensitivity of Jenike's hopper design methodology to the measured values. Journal of Food Engineering, 61, 399-405. doi: https://doi.org/10.1016/S0260-8774(03)00147-X.

Fonteyne, M., Vercruysse, J., De Leersnyder, F., Besseling, R., Gerich, A., Oostra, W., Remon, J.P., Vervaet, C., De Beer, T., 2016. Blend uniformity evaluation during continuous mixing in a twin screw granulator by in-line NIR using a moving F-test. Analytica Chimica Acta, 935, 213-223. doi: https://doi.org/10.1016/j.aca.2016.07.020.

Fonteyne, M., Vercruysse, J., De Leersnyder, F., Van Snick, B., Vervaet, C., Remon, J.P., De Beer, T., 2015. Process Analytical Technology for continuous manufacturing of solid-dosage forms. TrAC Trends in Analytical Chemistry, 67, 159-166. doi: https://doi.org/10.1016/j.trac.2015.01.011.

Freeman Technology, 2010. W Instruction - Stability Method - W7011. 1-8.

Freeman Technology, 2007. W Instruction - Variable Flow Rate Method - W7012. 1-4.

Freeman, R., 2007. Measuring the flow properties of consolidated, conditioned and aerated powders — A comparative study using a powder rheometer and a rotational shear cell. Powder Technology, 174, 25-33. doi: //doi.org/10.1016/j.powtec.2006.10.016.

Freret-Lorgeril, V., Donnadieu, F., Eychenne, J., Soriaux, C., Latchimy, T., 2019. In situ terminal settling velocity measurements at Stromboli volcano: Input from physical characterization of ash. Journal of Volcanology and Geothermal Research, 374, 62-79. doi: https://doi.org/10.1016/j.jvolgeores.2019.02.005.

Fries, L., Antonyuk, S., Heinrich, S., Dopfer, D., Palzer, S., 2013. Collision dynamics in fluidised bed granulators: A DEM-CFD study. Chemical Engineering Science, 86, 108-123. doi: https://doi.org/10.1016/j.ces.2012.06.026.

Fu, F., Xu, C., Wang, S., 2018. Flow characterization of high-pressure dense-phase pneumatic conveying of coal powder using multi-scale signal analysis. Particuology, 36, 149-157. doi: //doi.org/10.1016/j.partic.2017.05.003.

Ganesan, V., Muthukumarappan, K., Rosentrater, K.A., 2008. Flow properties of DDGS with varying soluble and moisture contents using jenike shear testing. Powder Technology, 187, 130-137. doi: https://doi.org/10.1016/j.powtec.2008.02.003.

Ganesh, S., Troscinski, R., Schmall, N., Lim, J., Nagy, Z., Reklaitis, G., 2017. Application of X-Ray Sensors for In-line and Noninvasive Monitoring of Mass Flow Rate in Continuous Tablet Manufacturing. Journal of Pharmaceutical Sciences, 106, 3591-3603. doi: //doi.org/10.1016/j.xphs.2017.08.019.

Gao, H., Wang, X., Chang, Q., Yan, K., Liu, J., 2018. Particle charging and conveying characteristics of dense-phase pneumatic conveying of pulverized coal under high-pressure by N2/CO2. Powder Technology, 328, 300-308. doi: https://doi.org/10.1016/j.powtec.2018.01.018.

Garg, R., Galvin, J., Li, T., Pannala, S., 2012. Open-source MFIX-DEM software for gas–solids flows: Part I—Verification studies. Powder Technology, 220, 122-137. doi: https://doi.org/10.1016/j.powtec.2011.09.019.

Gentzler, M., Tardos, G.I., 2009. Measurement of velocity and density profiles in discharging conical hoppers by NMR imaging. Chemical Engineering Science, 64, 4463-4469. doi: //doi.org/10.1016/j.ces.2009.08.010.

Ghori, M.U., Šupuk, E., Conway, B.R., 2014. Tribo-electric charging and adhesion of cellulose ethers and their mixtures with flurbiprofen. European Journal of Pharmaceutical Sciences, 65, 1-8. doi: https://doi.org/10.1016/j.ejps.2014.08.010.

Girimonte, R., Bernardo, P., Minnicelli, A., Formisani, B., 2018. Experimental characterization of the cohesive behaviour of fine powders by the raining bed test. Powder Technology, 325, 373-380. doi: //doi.org/10.1016/j.powtec.2017.11.038.

Glor, M., 1985. Hazards due to electrostatic charging of powders. Journal of Electrostatics, 16, 175-191. doi: https://doi.org/10.1016/0304-3886(85)90041-5.

Govender, N., Wilke, D.N., Pizette, P., Abriak, N., 2018. A study of shape non-uniformity and poly-dispersity in hopper discharge of spherical and polyhedral particle systems using the Blaze-DEM GPU code. Applied Mathematics and Computation, 319, 318-336. doi: //doi.org/10.1016/j.amc.2017.03.037.

Hancock, B.C., 2019. The Wall Friction Properties of Pharmaceutical Powders, Blends, and Granulations. Journal of Pharmaceutical Sciences, 108, 457-463. doi: https://doi.org/10.1016/j.xphs.2018.10.019.

Hare, C., Zafar, U., Ghadiri, M., Freeman, T., Clayton, J., Murtagh, M.J., 2015. Analysis of the dynamics of the FT4 powder rheometer. Powder Technology, 285, 123-127. doi: https://doi.org/10.1016/j.powtec.2015.04.039.

Hastie, D.B., 2015. On the difficulties of sampling bulk powder blends in determining segregation propensity — A case study. Powder Technology, 286, 164-171. doi: https://doi.org/10.1016/j.powtec.2015.08.013.

Hertel, M., Schwarz, E., Kobler, M., Hauptstein, S., Steckel, H., Scherließ, R., 2018. Powder flow analysis: A simple method to indicate the ideal amount of lactose fines in dry powder inhaler formulations. International Journal of Pharmaceutics, 535, 59-67. doi: https://doi.org/10.1016/j.ijpharm.2017.10.052.

Hou, Q.F., Dong, K.J., Yu, A.B., 2014. DEM study of the flow of cohesive particles in a screw feeder. Powder Technology, 256, 529-539. doi: https://doi.org/10.1016/j.powtec.2014.01.062.

Hu, H.L., Xu, T.M., Hui, S.E., Zhou, Q.L., 2006. A novel capacitive system for the concentration measurement of pneumatically conveyed pulverized fuel at power stations. Flow Measurement and Instrumentation, 17, 87-92. doi: https://doi.org/10.1016/j.flowmeasinst.2005.11.001.

Humby, S., Tüzün, U., Yu, A.B., 1998. Prediction of hopper discharge rates of binary granular mixtures. Chemical Engineering Science, 53, 483-494. doi: https://doi.org/10.1016/S0009-2509(97)00326-6.

Hussain, T., Kaialy, W., Deng, T., Bradley, M.S.A., Nokhodchi, A., Armour-Chélu, D., 2013. A novel sensing technique for measurement of magnitude and polarity of electrostatic charge distribution across individual particles. International Journal of Pharmaceutics, 441, 781-789. doi: //doi.org/10.1016/j.ijpharm.2012.10.002.

ICH, 2009. Harmonised tripartite guideline. Pharmaceutical development Q8 (R2).

Jaworski, A.J., Dyakowski, T., 2001. Application of electrical capacitance tomography for measurement of gas-solids flow characteristics in a pneumatic conveying system. Meas. Sci. Technol., 12, 1109-1119. doi: 10.1088/0957-0233/12/8/317.

Jenike, A.W., 1964. Storage and flow of solids. Utah Eng. Exp. Station Bull., 53, 1-194.

Jenike, A.W., Leser, T., 1965. Proc. 4th Int. Congress Rheol., pp. 125-141.

Ji, S., Wang, S., Peng, Z., 2019. Influence of external pressure on granular flow in a cylindrical silo based on discrete element method. Powder Technology, 356, 702-714. doi: https://doi.org/10.1016/j.powtec.2019.08.083.

Jones, T.M., Pilpel, N., 1966. Some angular properties of magnesia and their relevance to material handling. Journal of Pharmacy and Pharmacology, 16, 182S-189S.

Kaialy, W., 2016. A review of factors affecting electrostatic charging of pharmaceuticals and adhesive mixtures for inhalation. International Journal of Pharmaceutics, 503, 262-276. doi: //doi.org/10.1016/j.ijpharm.2016.01.076.

Kaialy, W., Hussain, T., Alhalaweh, A., Nokhodchi, A., 2014. Towards a More Desirable Dry Powder Inhaler Formulation: Large Spray-Dried Mannitol Microspheres Outperform Small Microspheres. Pharmaceutical research, 31, 60-76. doi: 10.1007/s11095-013-1132-2.

Kanin, E.A., Osiptsov, A.A., Vainshtein, A.L., Burnaev, E.V., 2019. A predictive model for steady-state multiphase pipe flow: Machine learning on lab data. Journal of Petroleum Science and Engineering, 180, 727-746. doi: https://doi.org/10.1016/j.petrol.2019.05.055.

Karner, S., Anne Urbanetz, N., 2011. The impact of electrostatic charge in pharmaceutical powders with specific focus on inhalation-powders. Journal of Aerosol Science, 42, 428-445. doi: //doi.org/10.1016/j.jaerosci.2011.02.010.

Ketterhagen, W.R., Curtis, J.S., Wassgren, C.R., Hancock, B.C., 2009. Predicting the flow mode from hoppers using the discrete element method. Powder Technology, 195, 1-10. doi: //doi.org/10.1016/j.powtec.2009.05.002.

Ketterhagen, W.R., Hancock, B.C., 2010. Optimizing the design of eccentric feed hoppers for tablet presses using DEM. Computers & Chemical Engineering, 34, 1072-1081. doi: https://doi.org/10.1016/j.compchemeng.2010.04.016.

Koynov, S., Glasser, B., Muzzio, F., 2015. Comparison of three rotational shear cell testers: Powder flowability and bulk density. Powder Technology, 283, 103-112. doi: //doi.org/10.1016/j.powtec.2015.04.027.

Krantz, M., Zhang, H., Zhu, J., 2009. Characterization of powder flow: Static and dynamic testing. Powder Technology, 194, 239-245. doi: //doi.org/10.1016/j.powtec.2009.05.001.

Kretz, D., Callau-Monje, S., Hitschler, M., Hien, A., Raedle, M., Hesser, J., 2016. Discrete element method (DEM) simulation and validation of a screw feeder system. Powder Technology, 287, 131-138. doi: https://doi.org/10.1016/j.powtec.2015.09.038.

Kruggel-Emden, H., Simsek, E., Rickelt, S., Wirtz, S., Scherer, V., 2007. Review and extension of normal force models for the Discrete Element Method. Powder Technology, 171, 157-173. doi: https://doi.org/10.1016/j.powtec.2006.10.004.

Kumar, R., Gopireddy, S.R., Jana, A.K., Patel, C.M., 2020. Study of the discharge behavior of Rosin-Rammler particle-size distributions from hopper by discrete element method: A systematic analysis of mass flow rate, segregation and velocity profiles. Powder Technology, 360, 818-834. doi: https://doi.org/10.1016/j.powtec.2019.09.044.

Leturia, M., Benali, M., Lagarde, S., Ronga, I., Saleh, K., 2014. Characterization of flow properties of cohesive powders: A comparative study of traditional and new testing methods. Powder Technol., 253, 406-423. doi: //doi.org/10.1016/j.powtec.2013.11.045.

Li, J., Fu, F., Li, S., Xu, C., Wang, S., 2015. Velocity characterization of dense phase pneumatically conveyed solid particles in horizontal pipeline through an integrated electrostatic sensor. International Journal of Multiphase Flow, 76, 198-211. doi: //doi.org/10.1016/j.ijmultiphaseflow.2014.11.004.

Li, J., Kong, M., Xu, C., Wang, S., Fan, Y., 2015. An Integrated Instrumentation System for Velocity, Concentration and Mass Flow Rate Measurement of Solid Particles Based on Electrostatic and Capacitance Sensors. Sensors, 15, 31023-31035. doi: 10.3390/s151229843.

Li, J., Xu, C., Wang, S., 2012. Local particle mean velocity measurement using electrostatic sensor matrix in gas–solid two-phase pipe flow. Flow Measurement and Instrumentation, 27, 104-112. doi: //doi.org/10.1016/j.flowmeasinst.2012.05.005.

Li, Q., Rudolph, V., Weigl, B., Earl, A., 2004. Interparticle van der Waals force in powder flowability and compactibility. International Journal of Multiphase Flow, 280, 77-93. doi: //dx.doi.org/10.1016/j.ijpharm.2004.05.001.

Lim, J.H., Lee, Y., Shin, J.H., Bae, K., Han, J.H., Lee, D.H., 2014. Hydrodynamic characteristics of gas–solid fluidized beds with shroud nozzle distributors for hydrochlorination of metallurgical-grade silicon. Powder Technology, 266, 312-320. doi: https://doi.org/10.1016/j.powtec.2014.06.031.

Liu, L.X., Marziano, I., Bentham, A.C., Litster, J.D., E.T.White, Howes, T., 2008. Effect of particle properties on the flowability of ibuprofen powders. International Journal of Pharmaceutics, 362, 109-117. doi: https://doi.org/10.1016/j.ijpharm.2008.06.023.

Liu, L., Wang, K., Bai, B., 2020. Experimental study on flow patterns and transition criteria for vertical swirling gas-liquid flow. International Journal of Multiphase Flow, 122, 103113. doi: https://doi.org/10.1016/j.ijmultiphaseflow.2019.103113.

Liu, N., Zhou, J., Gao, M., Cheng, P., 2019. An experimental study on flow and heat transfer characteristics of binary hydrate slurries in a horizontal tube. International Communications in Heat and Mass Transfer, 102, 34-41. doi: https://doi.org/10.1016/j.icheatmasstransfer.2019.01.009.

Liu, S.D., Zhou, Z.Y., Zou, R.P., Pinson, D., Yu, A.B., 2014. Flow characteristics and discharge rate of ellipsoidal particles in a flat bottom hopper. Powder Technology, 253, 70-79. doi: //doi.org/10.1016/j.powtec.2013.11.001.

Lumay, G., Pillitteri, S., Marck, M., Monsuur, F., Pauly, T., Ribeyre, Q., Francqui, F., Vandewalle, N., 2019. Influence of mesoporous silica on powder flow and electrostatic properties on short and long term. Journal of Drug Delivery Science and Technology, 101192. doi: //doi.org/10.1016/j.jddst.2019.101192.

Ma, J., Yan, Y., 2000. Design and evaluation of electrostatic sensors for the measurement of velocity of pneumatically conveyed solids. Flow Measurement and Instrumentation, 11, 195-204. doi: //dx.doi.org/10.1016/S0955-5986(00)00019-4.

Matsusaka, S., Maruyama, H., Matsuyama, T., Ghadiri, M., 2010. Triboelectric charging of powders: A review. Chemical Engineering Science, 65, 5781-5807. doi: //doi.org/10.1016/j.ces.2010.07.005.

Matsusyama, T., Yamamoto, H., 2006. Impact charging of particulate materials. Chemical Engineering Science, 61, 2230-2238. doi: https://doi.org/10.1016/j.ces.2005.05.003.

Muite, B.K., Quinn, S.F., Sundaresan, S., Rao, K.K., 2004. Silo music and silo quake: granular flow-induced vibration. Powder Technology, 145, 190-202. doi: //doi.org/10.1016/j.powtec.2004.07.003.

Mukherjee, R., Mao, C., Chattoraj, S., Chaudhuri, B., 2018. DEM based computational model to predict moisture induced cohesion in pharmaceutical powders. International Journal of Pharmaceutics, 536, 301-309. doi: https://doi.org/10.1016/j.ijpharm.2017.12.001.

Murtomaa, M., Ojanen, K., Laine, E., 2002. Effect of surface coverage of a glass pipe by small particles on the triboelectrification of glucose powder. Journal of Electrostatics, 54, 311-320. doi: https://doi.org/10.1016/S0304-3886(01)00158-9.

Murtomaa, M., Peltonen, J., Salonen, J., 2015. One-step measurements of powder resistivity as a function of relative humidity and its effect on charging. Journal of Electrostatics, 76, 78-82. doi: //doi.org/10.1016/j.elstat.2015.05.016.

Nakayama, Y., 2018. Introduction to Fluid Mechanics, 2nd Ed., Elsevier Ltd, United Kingdom.

Nalluri, V.R., Kuentz, M., 2010. Flowability characterisation of drug–excipient blends using a novel powder avalanching method. European Journal of Pharmaceutics and Biopharmaceutics, 74, 388-396. doi: //doi.org/10.1016/j.ejpb.2009.09.010.

Nan, W., Ghadiri, M., Wang, Y., 2017a. Analysis of powder rheometry of FT4: Effect of air flow. Chemical Engineering Science, 162, 141-151. doi: https://doi.org/10.1016/j.ces.2017.01.002.

Nan, W., Ghadiri, M., Wang, Y., 2017b. Analysis of powder rheometry of FT4: Effect of particle shape. Chemical Engineering Science, 173, 374-383. doi: https://doi.org/10.1016/j.ces.2017.08.004.

Ndama, A.T., Guigon, P., Saleh, K., 2011. A reproducible test to characterise the triboelectric charging of powders during their pneumatic transport. Journal of Electrostatics, 69, 146-156. doi: //doi.org/10.1016/j.elstat.2011.03.003.

Nwose, E.N., Pei, C., Wu, C., 2012. Modelling die filling with charged particles using DEM/CFD. Particuology, 10, 229-235. doi: https://doi.org/10.1016/j.partic.2011.11.010.

Oldal, I., Keppler, I., Csizmadia, B., Fenyvesi, L., 2012. Outflow properties of silos: The effect of arching. Advanced Powder Technology, 23, 290-297. doi: https://doi.org/10.1016/j.apt.2011.03.013.

Pachón-Morales, J., Do, H., Colin, J., Puel, F., Perré, P., Schott, D., 2019. DEM modelling for flow of cohesive lignocellulosic biomass powders: Model calibration using bulk tests. Advanced Powder Technology, 30, 732-750. doi: https://doi.org/10.1016/j.apt.2019.01.003.

Pang, L., Shao, Y., Geng, C., Zhong, W., Liu, G., Liu, L., Tian, W., 2018. Measurement of solid mass flow rate by a non-intrusive microwave method. Powder Technology, 323, 525-532. doi: //doi.org/10.1016/j.powtec.2017.10.030.

Park, C.H., Park, J.K., Jeon, H.S., Chun, B.C., 2008. Triboelectric series and charging properties of plastics using the designed vertical-reciprocation charger. Journal of Electrostatics, 66, 578-583. doi: https://doi.org/10.1016/j.elstat.2008.07.001.

Peltonen, J., Murtomaa, M., Salonen, J., 2018. Measuring electrostatic charging of powders on-line during surface adhesion. Journal of Electrostatics, 93, 53-57. doi: https://doi.org/10.1016/j.elstat.2018.03.007.

Pillai, J.R., Bradley, M.S.A., Berry, R.J., 2007. Comparison between the angles of wall friction measured on an on-line wall friction tester and the Jenike wall friction tester. Powder Technology, 174, 64-70. doi: https://doi.org/10.1016/j.powtec.2006.10.024.

Pingali, K.C., Shinbrot, T., Hammond, S.V., Muzzio, F.J., 2009. An observed correlation between flow and electrical properties of pharmaceutical blends. Powder Technology, 192, 157-165. doi: https://doi.org/10.1016/j.powtec.2008.12.012.

Plumb, K., 2005. Continuous Processing in the Pharmaceutical Industry. Chemical Engineering Research and Design, 83, 730-738. doi: //dx.doi.org/10.1205/cherd.04359.

Prescott, J.K., Barnum, R.A., 2000. Flowability, Pharmaceutical Technology.

Qian, X., Huang, X., Yonghui, H., Yan, Y., 2014. Pulverized coal flow metering on a full-scale power plant using electrostatic sensor arrays. Flow Measurement and Instrumentation, 40, 185-191. doi: //doi.org/10.1016/j.flowmeasinst.2014.06.001.

Qian, X., Shi, D., Yan, Y., Zhang, W., Li, G., 2017. Effects of moisture content on electrostatic sensing based mass flow measurement of pneumatically conveyed particles. Powder Technology, 311, 579-588. doi: //doi.org/10.1016/j.powtec.2016.12.061.

Qian, X., Yan, Y., Shao, J., Wang, L., Zhou, H., Wang, C., 2012. Quantitative characterization of pulverized coal and biomass–coal blends in pneumatic conveying pipelines using electrostatic sensor arrays and data fusion techniques. Measurement Science and Technology., 23, 085307. doi: 10.1088/0957-0233/23/8/085307.

Qian, X., Yan, Y., Wang, L., Shao, J., 2015. An integrated multi-channel electrostatic sensing and digital imaging system for the on-line measurement of biomass–coal particles in fuel injection pipelines. Fuel, 151, 2-10. doi: //doi.org/10.1016/j.fuel.2014.11.013.

Ramírez, A., Nielsen, J., Ayuga, F., 2010. Pressure measurements in steel silos with eccentric hoppers. Powder Technology, 201, 7-20. doi: //doi.org/10.1016/j.powtec.2010.02.027.

Rowley, G., 2001. Quantifying electrostatic interactions in pharmaceutical solid systems. International Journal of Pharmaceutics, 227, 47-55. doi: https://doi.org/10.1016/S0378-5173(01)00784-0.

Rowley, G., Mackin, L.A., 2003. The effect of moisture sorption on electrostatic charging of selected pharmaceutical excipient powders. Powder Technology, 135, 50-58. doi: //dx.doi.org/10.1016/j.powtec.2003.08.003.

Ruiz-Carcel, C., Starr, A., Nsugbe, E., 2018. Estimation of powder mass flow rate in a screw feeder using acoustic emissions. Powder Technology, 336, 122-130. doi: //doi.org/10.1016/j.powtec.2018.05.029.

Samiei, L., Kelly, K., Taylor, L., Forbes, B., Collins, E., Rowland, M., 2017. The influence of electrostatic properties on the punch sticking propensity of pharmaceutical blends. Powder Technology, 305, 509-517. doi: https://doi.org/10.1016/j.powtec.2016.10.018.

Sarkar, S., Mukherjee, R., Chaudhuri, B., 2017. On the role of forces governing particulate interactions in pharmaceutical systems: A review. International Journal of Pharmaceutics, 526, 516-537. doi: https://doi.org/10.1016/j.ijpharm.2017.05.003.

Schulze, D., 2008. Powders and Bulk Solids
Behavior, Characterization, Storage and Flow, 1st Ed., Springer.

Shi, Q., Zhang, Q., Han, G., Zhang, W., Wang, J., Huang, Z., Yang, Y., Yang, Y., Wu, W., Yan, Y., 2017. Simultaneous measurement of electrostatic charge and its effect on particle motions by electrostatic sensors array in gas-solid fluidized beds. Powder Technology, 312, 29-37. doi: //doi.org/10.1016/j.powtec.2017.02.014.

Sielamowicz, I., Błoński, S., Kowalewski, T.A., 2006. Digital particle image velocimetry (DPIV) technique in measurements of granular material flows, Part 2 of 3-converging hoppers. Chemical Engineering Science, 61, 5307-5317. doi: //doi.org/10.1016/j.ces.2006.03.002.

Simonaho, S., Ketolainen, J., Ervasti, T., Toiviainen, M., Korhonen, O., 2016. Continuous manufacturing of tablets with PROMIS-line — Introduction and case studies from continuous feeding, blending and tableting. European Journal of Pharmaceutical Sciences, 90, 38-46. doi: //doi.org/10.1016/j.ejps.2016.02.006.

Singh, R., Román-Ospino, A.D., Romañach, R.J., Ierapetritou, M., Ramachandran, R., 2015. Real time monitoring of powder blend bulk density for coupled feed-forward/feed-back control of a continuous direct compaction tablet manufacturing process. International journal of pharmaceutics, 495, 612-625. doi: //doi.org/10.1016/j.ijpharm.2015.09.029.

Søgaard, S.V., Olesen, N.E., Hirschberg, C., Madsen, M.H., Allesø, M., Garnaes, J., Rantanen, J., 2017. An experimental evaluation of powder flow predictions in small-scale process equipment based on Jenike's hopper design methodology. Powder Technology, 321, 523-532. doi: //doi.org/10.1016/j.powtec.2017.08.006.

Soleimani, A., Hanratty, T.J., 2003. Critical liquid flows for the transition from the pseudo-slug and stratified patterns to slug flow. International Journal of Multiphase Flow, 29, 51-67. doi: https://doi.org/10.1016/S0301-9322(02)00124-6.

Staniforth, J.N., Aulton, M.E., 2007. Powder flowIn: Aulton, M.E. (Ed.), Aulton's Pharmaceutics, the Design and Manufacture of Medicines, Churchill Livingstone Elsevier, Philadelphia, United States, pp. 168-179.

Sun, M., Liu, S., Lei, J., Li, Z., 2008. Mass flow measurement of pneumatically conveyed solids using electrical capacitance tomography. Measurement Science and Technology, 19, 1-6.

Šupuk, E., Zarrebini, A., Reddy, J.P., Hughes, H., Leane, M.M., Tobyn, M.J., Timmins, P., Ghadiri, M., 2012. Tribo-electrification of active pharmaceutical ingredients and excipients. Powder Technology, 217, 427-434. doi: //doi.org/10.1016/j.powtec.2011.10.059.

Tallon, S., Davis, C.E., 1997. Use of the Attenuation of Acoustic Pulsed Waves for Concentration Measurement in Gas-Solid Pipe Flow. American Institute of Chemical Engineers, 136-140.

Tan, Z., Liang, C., Chen, X., Li, J., 2019. Comparisons of TFM and DEM-CFD simulation analyses on the influence mechanism of electrostatics on single bubble in gas-solid fluidized bed. Powder Technology, 351, 238-258. doi: https://doi.org/10.1016/j.powtec.2019.04.019.

Tangri, H., Guo, Y., Curtis, J.S., 2019. Hopper discharge of elongated particles of varying aspect ratio: Experiments and DEM simulations. Chemical Engineering Science: X, 4, 100040. doi: https://doi.org/10.1016/j.cesx.2019.100040.

Telko, M.J., Kujanpää, J., Hickey, A.J., 2007. Investigation of triboelectric charging in dry powder inhalers using electrical low pressure impactor (ELPI™). International Journal of Pharmaceutics, 336, 352-360. doi: https://doi.org/10.1016/j.ijpharm.2006.12.018.

Tirapelle, M., Santomaso, A.C., Hare, C., 2019. Dynamic ball indentation for powder flow characterization. Powder Technology. doi: https://doi.org/10.1016/j.powtec.2019.11.009.

Tiscar, J.M., Escrig, A., Mallol, G., Boix, J., Gilabert, F.A., 2019. DEM-based modelling framework for spray-dried powders in ceramic tiles industry. Part I: Calibration procedure. Powder Technology, 356, 818-831. doi: https://doi.org/10.1016/j.powtec.2019.08.053.

Tortora, P.R., Ceccio, S.L., Trujillo, S.M., O'Hern, T.J., Shollenberger, K.A., 2004. Capacitance measurements of solid concentration in gas–solid flows. Powder Technology, 148, 92-101. doi: https://doi.org/10.1016/j.powtec.2004.09.002.

Uñac, R.O., Vidales, A.M., Benegas, O.A., Ippolito, I., 2012. Experimental study of discharge rate fluctuations in a silo with different hopper geometries. Powder Technology, 225, 214-220. doi: //doi.org/10.1016/j.powtec.2012.04.013.

Vasilenko, A., Glasser, B.J., Muzzio, F.J., 2011. Shear and flow behavior of pharmaceutical blends — Method comparison study. Powder Technology, 208, 628-636. doi: https://doi.org/10.1016/j.powtec.2010.12.031.

Vercruysse, J., Toiviainen, M., Fonteyne, M., Helkimo, N., Ketolainen, J., Juuti, M., Delaet, U., Van Assche, I., Remon, J.P., Vervaet, C., De Beer, T., 2014. Visualization and understanding of the granulation liquid mixing and distribution during continuous twin screw granulation using NIR chemical imaging. European Journal of Pharmaceutics and Biopharmaceutics, 86, 383-392. doi: https://doi.org/10.1016/j.ejpb.2013.10.012.

Wahl, P.R., Fruhmann, G., Sacher, S., Straka, G., Sowinski, S., Khinast, J.G., 2014. PAT for tableting: Inline monitoring of API and excipients via NIR spectroscopy. European Journal of Pharmaceutics and Biopharmaceutics, 87, 271-278. doi: https://doi.org/10.1016/j.ejpb.2014.03.021.

Wang, S., Xu, C., Li, J., Ding, Z., Wang, S., 2016. An instrumentation system for multi-parameter measurements of gas-solid two-phase flow based on Capacitance-Electrostatic sensor. Measurement, 94, 812-827. doi: //doi.org/10.1016/j.measurement.2016.09.010.

Wang, Y., Koynov, S., Glasser, B.J., Muzzio, F.J., 2016. A method to analyze shear cell data of powders measured under different initial consolidation stresses. Powder Technology, 294, 105-112. doi: https://doi.org/10.1016/j.powtec.2016.02.027.

Wang, Y., Li, T., Muzzio, F.J., Glasser, B.J., 2017. Predicting feeder performance based on material flow properties. Powder Technology, 308, 135-148. doi: https://doi.org/10.1016/j.powtec.2016.12.010.

Ward, H.W., Blackwood, D.O., Polizzi, M., Clarke, H., 2013. Monitoring blend potency in a tablet press feed frame using near infrared spectroscopy. Journal of Pharmaceutical and Biomedical Analysis, 80, 18-23. doi: https://doi.org/10.1016/j.jpba.2013.02.008.

Watanabe, H., Ghadiri, M., Matsuyama, T., Ding, Y.L., Pitt, K.G., Maruyama, H., Matsusaka, S., Masuda, H., 2007. Triboelectrification of pharmaceutical powders by particle impact.

International Journal of Pharmaceutics, 334, 149-155. doi: //doi.org/10.1016/j.ijpharm.2006.11.005.

Weighardt, K., 1952. Some experiments on the flow of sand. Ingenieur-Archiv, 20, 109.

Whiting, J., Springer, A., Sciammarella, F., 2018. Real-Time Acoustic Emission Monitoring of Powder Mass Flow Rate for Directed Energy Deposition. Additive Manufacturing. doi: //doi.org/10.1016/j.addma.2018.08.015.

Wiesendorf, V., Werther, J., 2000. Capacitance probes for solids volume concentration and velocity measurements in industrial fluidized bed reactors. Powder Technology, 110, 143-157. doi: https://doi.org/10.1016/S0032-5910(99)00276-4.

Wong, J., Kwok, P.C.L., Chan, H., 2015. Electrostatics in pharmaceutical solids. Chemical Engineering Science, 125, 225-237. doi: //doi.org/10.1016/j.ces.2014.05.037.

Xiao, H., Fan, Y., Jacob, K.V., Umbanhowar, P.B., Kodam, M., Koch, J.F., Lueptow, R.M., 2019. Continuum modeling of granular segregation during hopper discharge. Chemical Engineering Science, 193, 188-204. doi: //doi.org/10.1016/j.ces.2018.08.039.

Xu, C., Li, J., Gao, H., Wang, S., 2012. Investigations into sensing characteristics of electrostatic sensor arrays through computational modelling and practical experimentation. Journal of Electrostatics, 70, 60-71. doi: https://doi.org/10.1016/j.elstat.2011.10.004.

Xue, J., Schiano, S., Zhong, W., Chen, L., Wu, C., 2019. Determination of the flow/no-flow transition from a flat bottom hopper. Powder Technology, 358, 55-61. doi: https://doi.org/10.1016/j.powtec.2018.08.063.

Yadav, I.K., Holman, J., Meehan, E., Tahir, F., Khoo, J., Taylor, J., Benedetti, A., Aderinto, O., Bajwa, G., 2019. Influence of material properties and equipment configuration on loss-in-weight feeder performance for drug product continuous manufacture. Powder Technology, 348, 126-137. doi: https://doi.org/10.1016/j.powtec.2019.01.071.

Yan, Y., 1996. Mass flow measurement of bulk solids in pneumatic pipelines. Measurement Science and Technology, 7, 1687-1706. doi: 10.1088/0957-0233/7/12/002.

Yanagida, K., Morita, T., Takeuchi, M., 2000. A new powder flow control system for electrostatic powder coating: a closed-loop-control system equipped with a capacitance sensor. Journal of Electrostatics, 49, 1-13. doi: https://doi.org/10.1016/S0304-3886(99)00070-4.

Yang, L., Hu, J., Bai, K., 2015. Capillary and van der Waals force between microparticles with different sizes in humid air. Journal of Adhesion Science and Technology, 30, 566-578.

Yang, Y., He, L., Sun, J., Huang, Z., Wang, J., Yang, Y., Huang, C., Huang, Z., 2019. Measurement and analysis of flow regimes transition by acoustic and electrostatic signals in vertical pneumatic conveying. Powder Technology, 352, 283-293. doi: //doi.org/10.1016/j.powtec.2019.04.024.

Ye, J., Guo, L., 2013. Multiphase flow pattern recognition in pipeline–riser system by statistical feature clustering of pressure fluctuations. Chemical Engineering Science, 102, 486-501. doi: https://doi.org/10.1016/j.ces.2013.08.048.

Yu, L.X., 2008. Pharmaceutical Quality by Design: Product and Process Development, Understanding, and Control. Pharmaceutical Research, 25, 781-791. doi: 10.1007/s11095-007-9511-1.

Zafar, U., Hare, C., Calvert, G., Ghadiri, M., Girimonte, R., Formisani, B., Quintanilla, M.A.S., Valverde, J.M., 2015. Comparison of cohesive powder flowability measured by Schulze Shear Cell, Raining Bed Method, Sevilla Powder Tester and new Ball Indentation Method. Powder Technology, 286, 807-816. doi: //doi.org/10.1016/j.powtec.2015.09.010.

Zafar, U., Hare, C., Hassanpour, A., Ghadiri, M., 2017. Ball indentation on powder beds for assessing powder flowability: Analysis of operation window. Powder Technology, 310, 300-306. doi: //doi.org/10.1016/j.powtec.2017.01.047.

Zakhvatayeva, A., Zhong, W., Makroo, H.A., Hare, C., Wu, C.Y., 2018. An experimental study of die filling of pharmaceutical powders using a rotary die filling system. International Journal of Pharmaceutics, 553, 84-96. doi: https://doi.org/10.1016/j.ijpharm.2018.09.067.

Zaki, M., Siraj, M.S., 2019. Study of a flat-bottomed cylindrical silo with different orifice shapes. Powder Technology, 354, 641-652. doi: https://doi.org/10.1016/j.powtec.2019.06.041.

Zhang, J., Cai, S., Li, Y., Zhu, H., Zhang, Y., 2016. Visualization study of gas–liquid two-phase flow patterns inside a three-stage rotodynamic multiphase pump. Experimental Thermal and Fluid Science, 70, 125-138. doi: https://doi.org/10.1016/j.expthermflusci.2015.08.013.

Zhang, J., Hu, H., Dong, J., Yan, Y., 2012. Concentration measurement of biomass/coal/air three-phase flow by integrating electrostatic and capacitive sensors. Flow Measurement and Instrumentation, 24, 43-49. doi: //doi.org/10.1016/j.flowmeasinst.2012.03.003.

Zhang, T.F., Gan, J.Q., Pinson, D., Zhou, Z.Y., 2018. Size-induced segregation of granular materials during filling a conical hopper. Powder Technology, 340, 331-343. doi: //doi.org/10.1016/j.powtec.2018.09.031.

Zhang, T.F., Gan, J.Q., Yu, A.B., Pinson, D., Zhou, Z.Y., 2019. Segregation of granular binary mixtures with large particle size ratios during hopper discharging process. Powder Technology, doi: https://doi.org/10.1016/j.powtec.2019.07.010.

Zhang, W., Cheng, X., Hu, Y., Yan, Y., 2018. Measurement of moisture content in a fluidized bed dryer using an electrostatic sensor array. Powder Technology, 325, 49-57. doi: https://doi.org/10.1016/j.powtec.2017.11.006.

Zhang, Z., Wang, Z., Gao, Y., Li, H., Wang, J., Sun, B., 2019. Experimental study on the effect of surfactants on the characteristics of gas carrying liquid in vertical churn and annular flows. Journal of Petroleum Science and Engineering, 180, 347-356. doi: https://doi.org/10.1016/j.petrol.2019.05.048.

Zhao, H., Zhao, Y., 2019. CFD–DEM simulation of pneumatic conveying in a horizontal channel. International Journal of Multiphase Flow, 118, 64-74. doi: https://doi.org/10.1016/j.ijmultiphaseflow.2019.06.003.

Zhao, Y., Yang, S., Zhang, L., Chew, J.W., 2019. Understanding the varying discharge rates of lognormal particle size distributions from a hopper using the Discrete Element Method. Powder Technology, 342, 356-370. doi: //doi.org/10.1016/j.powtec.2018.09.080.

Zhou, X., Nauka, E., Narang, A., Mao, C., 2020. Flow Function of Pharmaceutical Powders at Low-Stress Conditions Can Be Inferred Using a Simple Flow-Through-Orifice Device. Journal of Pharmaceutical Sciences. doi: https://doi.org/10.1016/j.xphs.2020.02.017.

Appendix

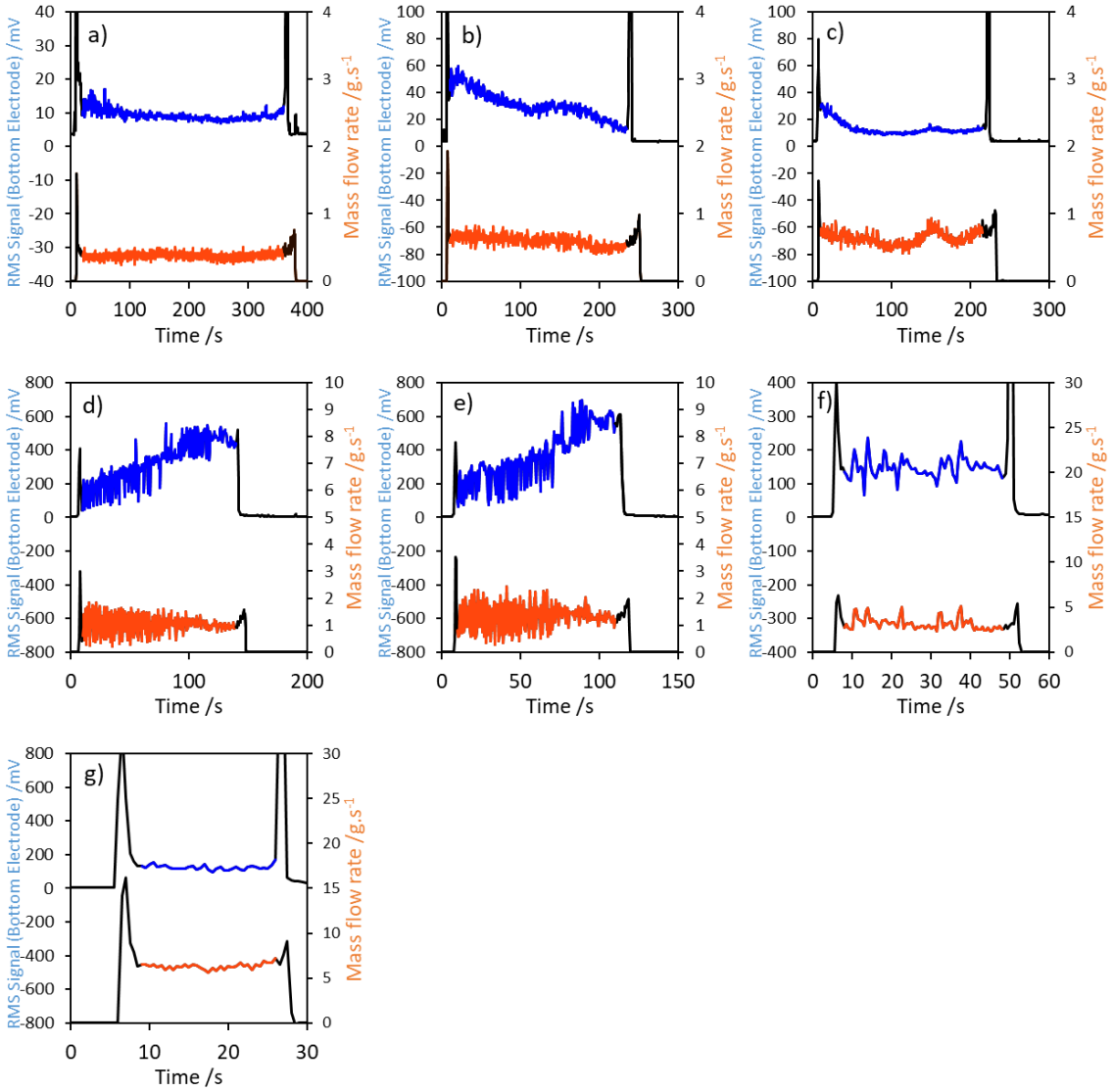

Appendix 1. Mass flow and RMS profiles recorded for the second runs of Lactose #316 Fast flo flowing through a pipe with nozzle apertures of: a) 4.2 mm; b) 4.5 mm; c) 4.8 mm; d) 5 mm; e) 5.4 mm; f) 10 mm; and g) 15 mm. The regions shaded in blue and orange represent the RMS and mass flow data respectively, which were recorded in response to active powder flow.

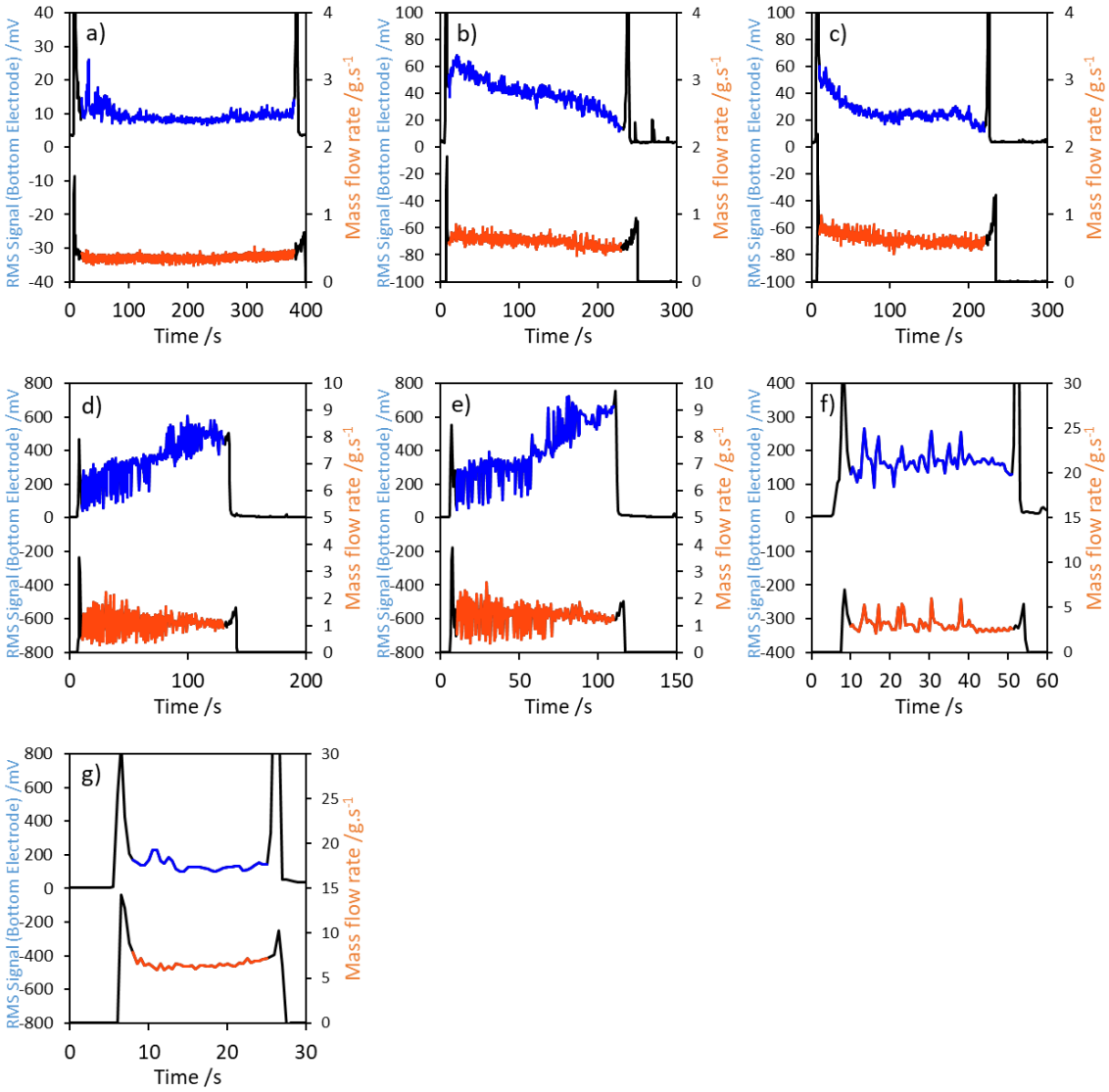

Appendix 2. Mass flow and RMS profiles recorded for the third runs of Lactose #316 Fast flo flowing through a pipe with nozzle apertures of: a) 4.2 mm; b) 4.5 mm; c) 4.8 mm; d) 5 mm; e) 5.4 mm; f) 10 mm; and g) 15 mm. The regions shaded in blue and orange represent the RMS and mass flow data respectively, which were recorded in response to active powder flow.

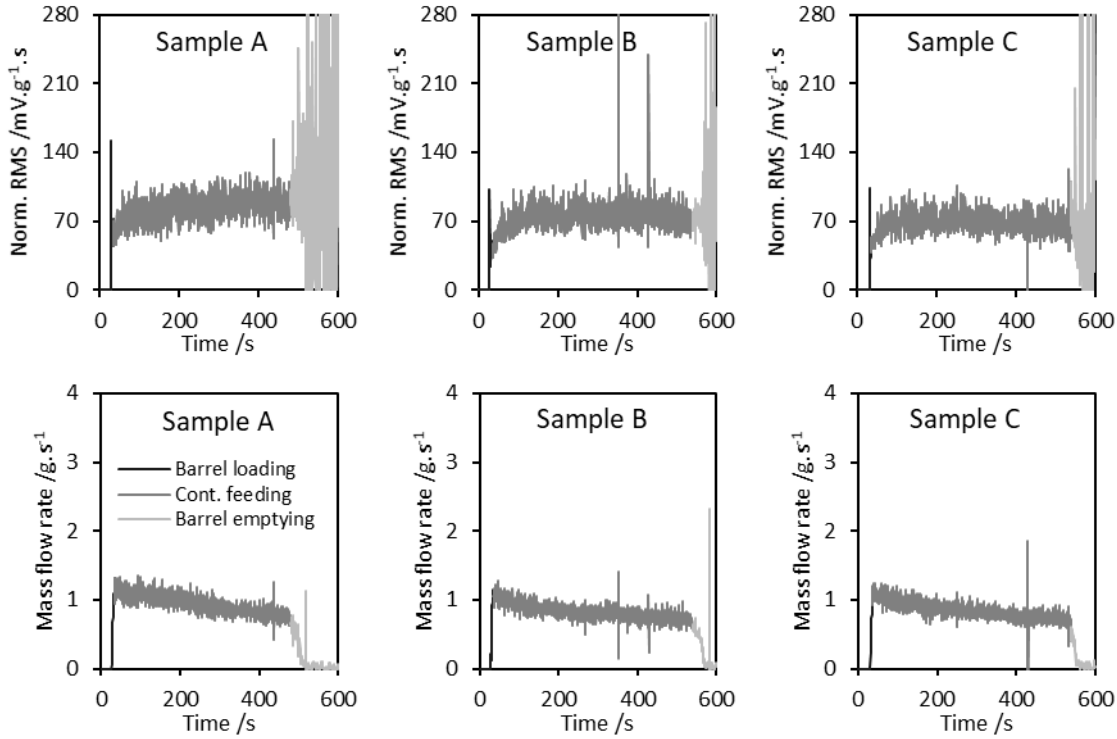

Appendix 3. (Top) Relative charging profiles and (Bottom) recorded for three samples of Avicel PH101 conveyed through a twin-screw feeder at 40 rpm.

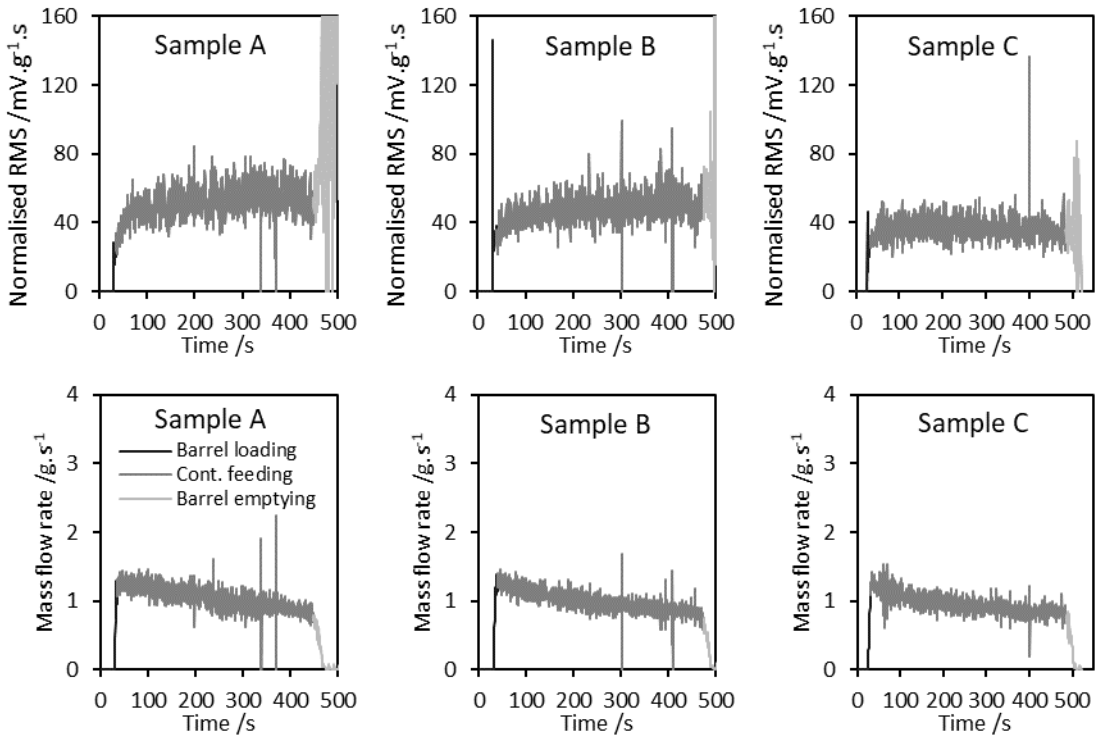

Appendix 4. (Top) Relative charging profiles and (Bottom) recorded for three samples of Avicel PH102 conveyed through a twin-screw feeder at 40 rpm.

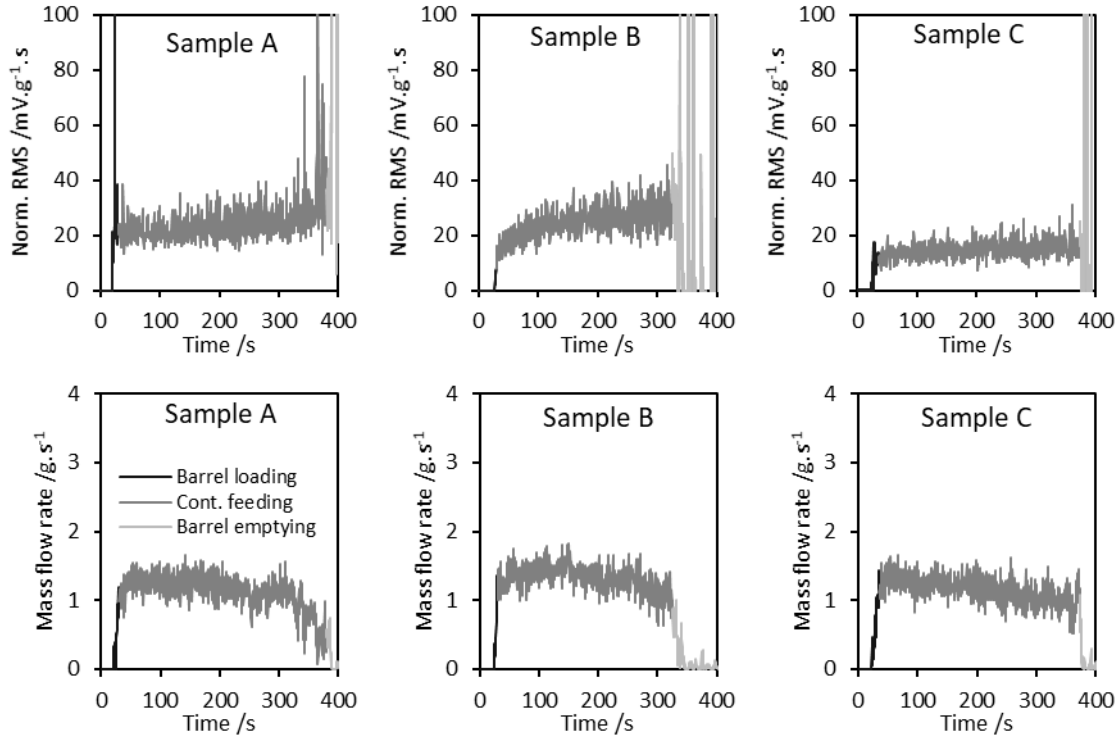

Appendix 5. (Top) Relative charging profiles and (Bottom) recorded for three samples of maize starch conveyed through a twin-screw feeder at 40 rpm.

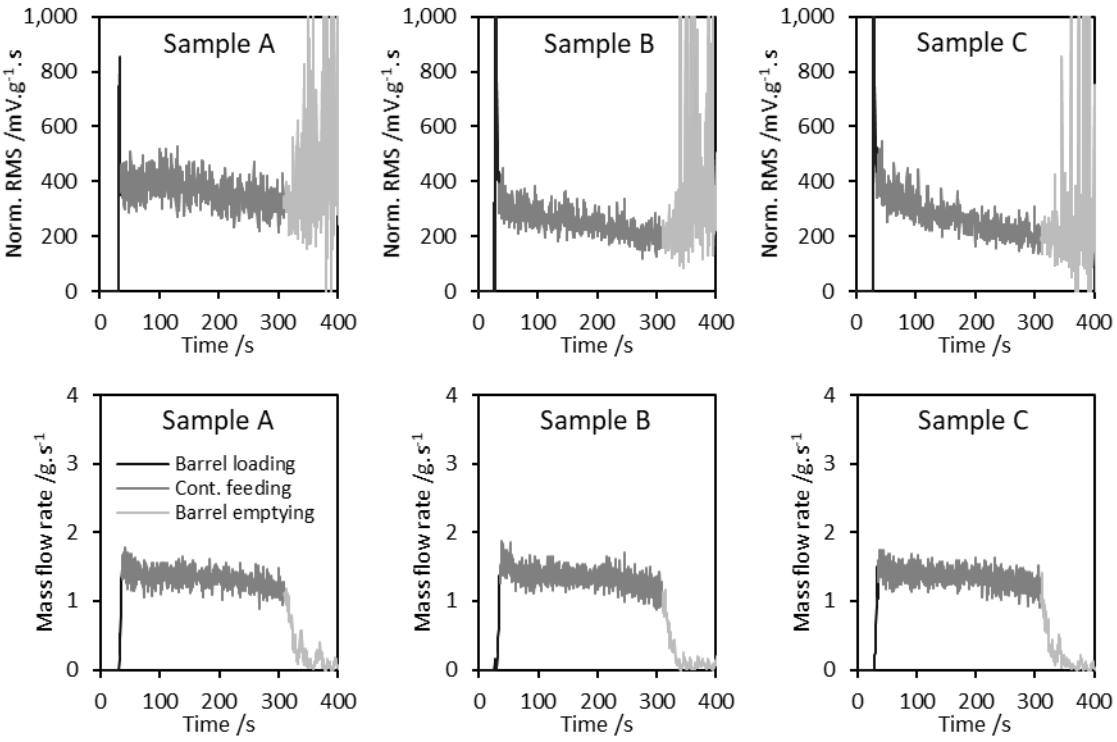

Appendix 6. (Top) Relative charging profiles and (Bottom) recorded for three samples of Lactose 200M conveyed through a twin-screw feeder at 40 rpm.

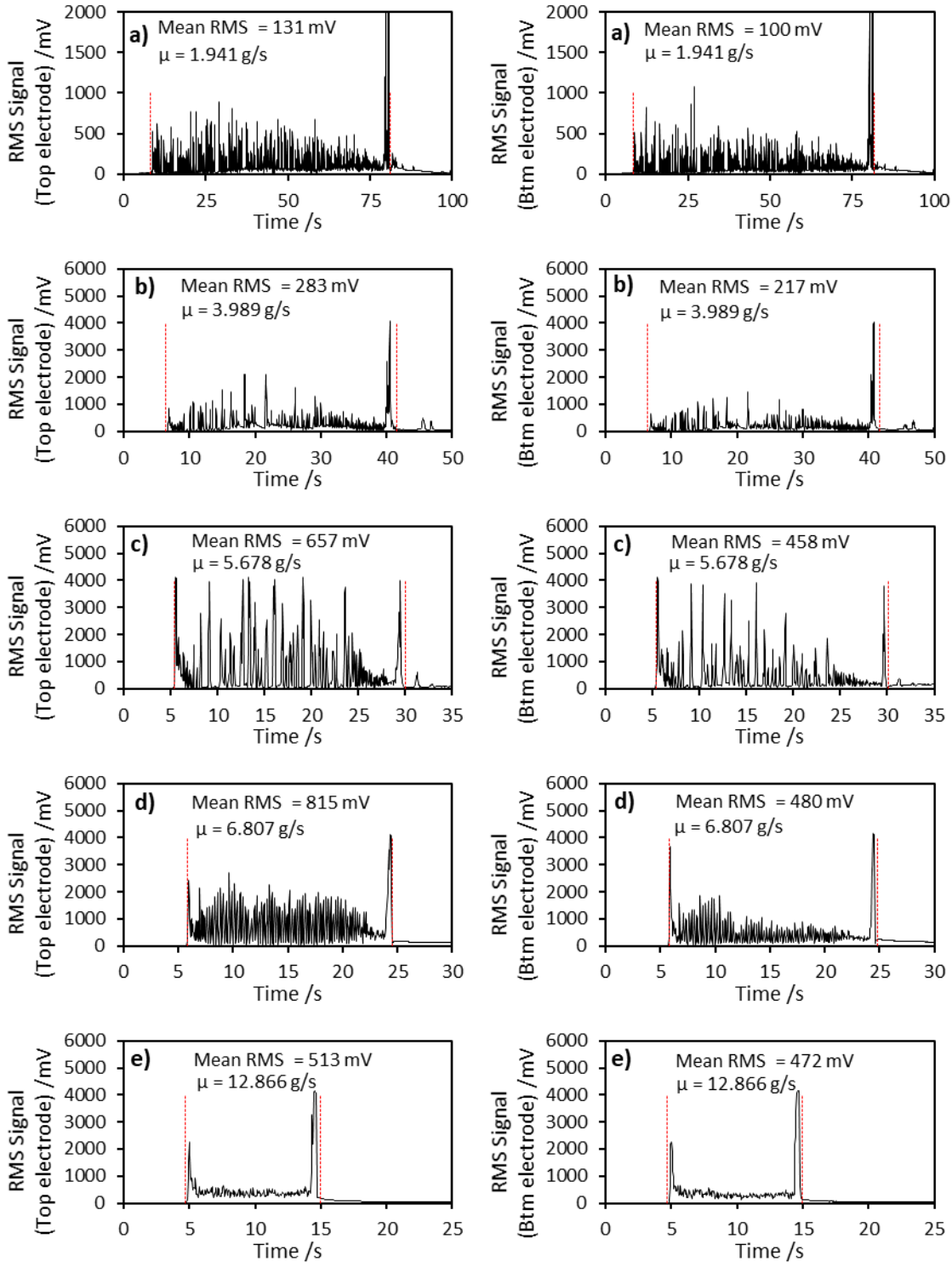

Appendix 7. Second set of top and bottom RMS signals recorded for Lactose #316 Fast flo moving via dense phase gravitational flow regime through nozzles with aperture sizes of a) 7.1 mm, b) 10.1 mm, c) 12.4 mm, d) 14.3 mm and e) 16 mm. μ = the associated powder mass flow rate.

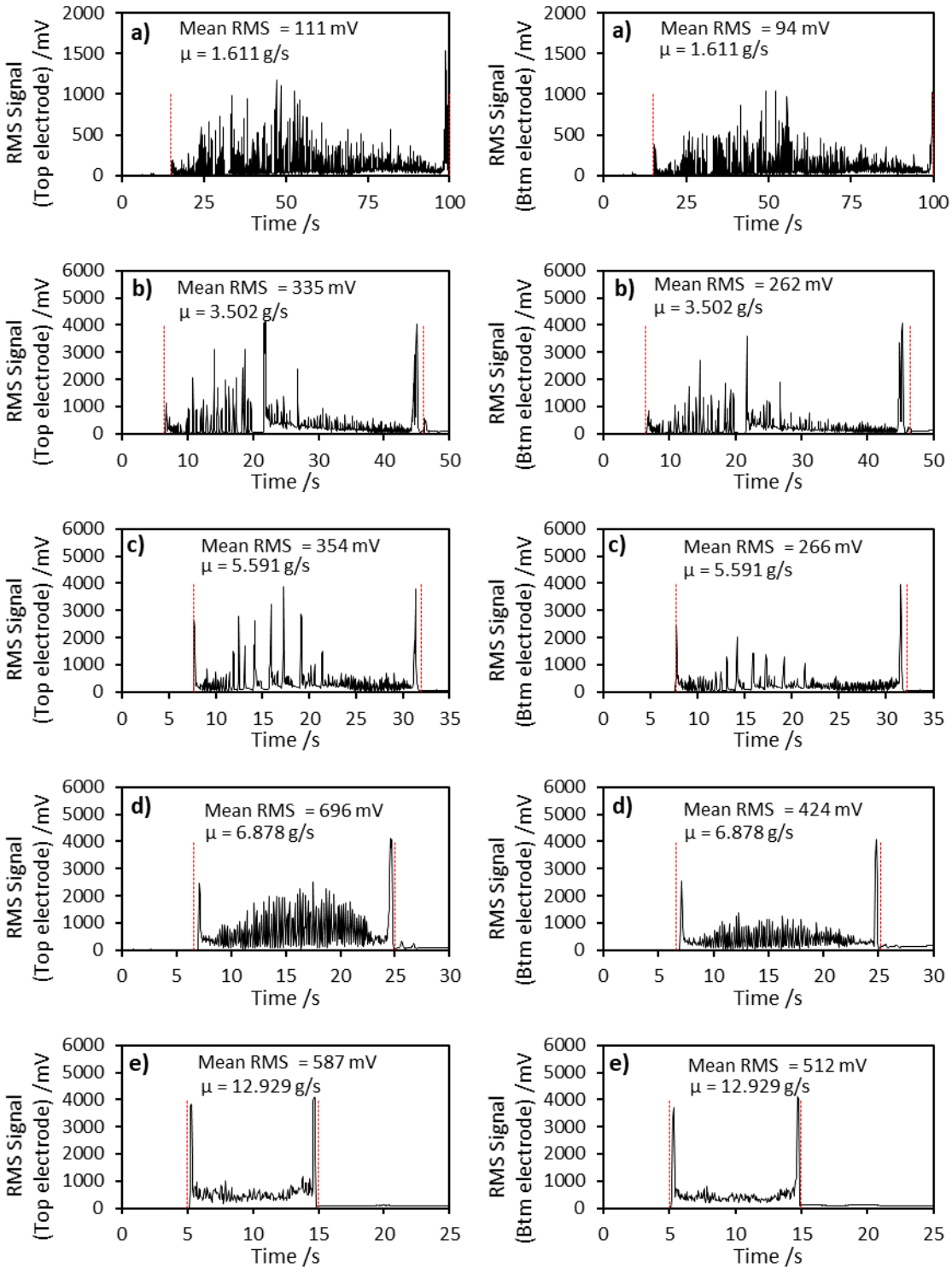

Appendix 8. Third set of top and bottom RMS signals recorded for Lactose #316 Fast flo moving via dense phase gravitational flow regime through nozzles with aperture sizes of a) 7.1 mm, b) 10.1 mm, c) 12.4 mm, d) 14.3 mm and e) 16 mm. μ = the associated powder mass flow rate.

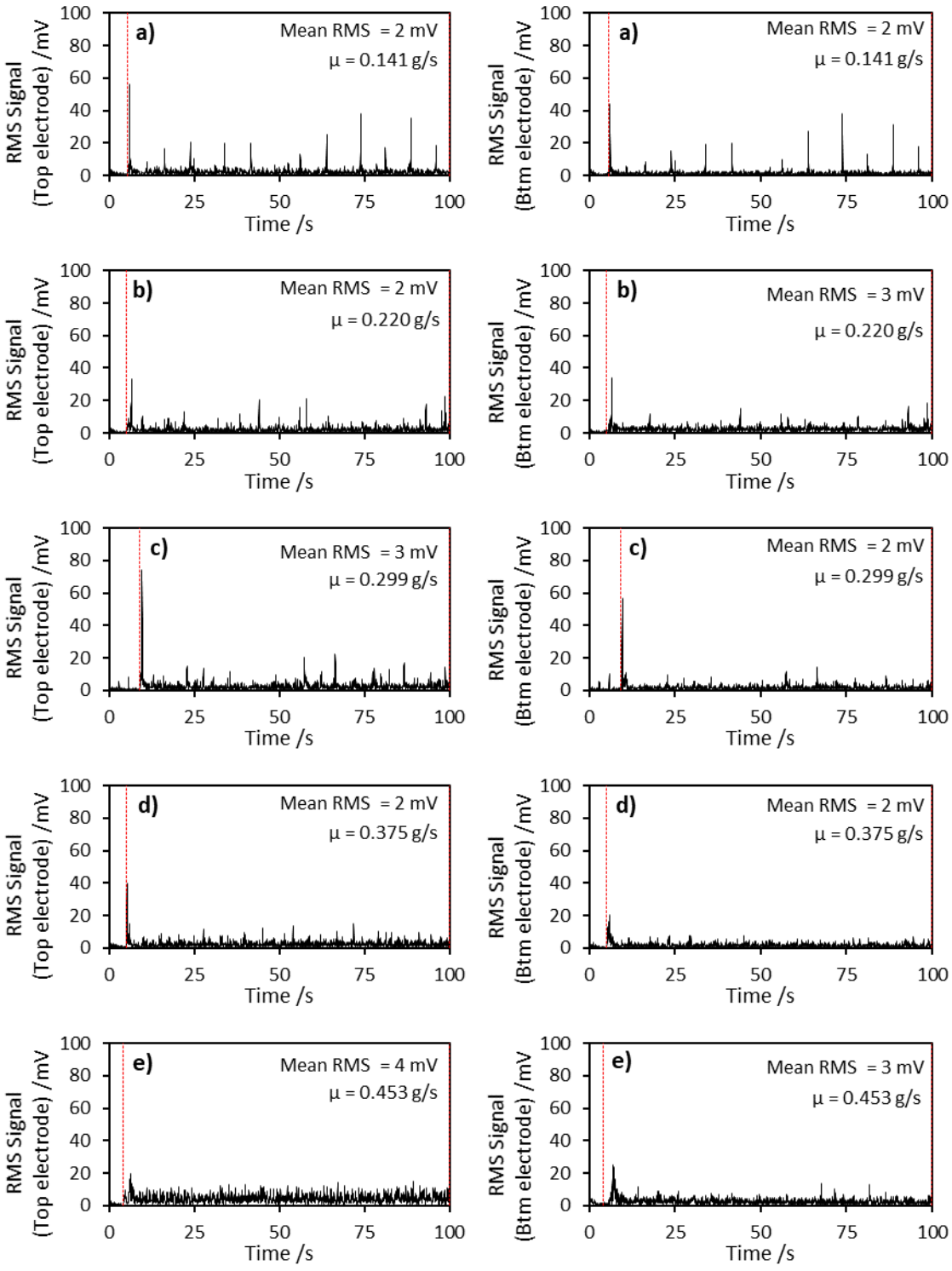

Appendix 9. Second set of filtered RMS signals obtained from the top and bottom electrodes in response to the hopper flow of Blend A, whilst utilising turret speeds of, a) 10 rpm, b) 15 rpm, c) 20 rpm, d) 25 rpm and e) 30 rpm. μ = the associated tablet mass flow rate.

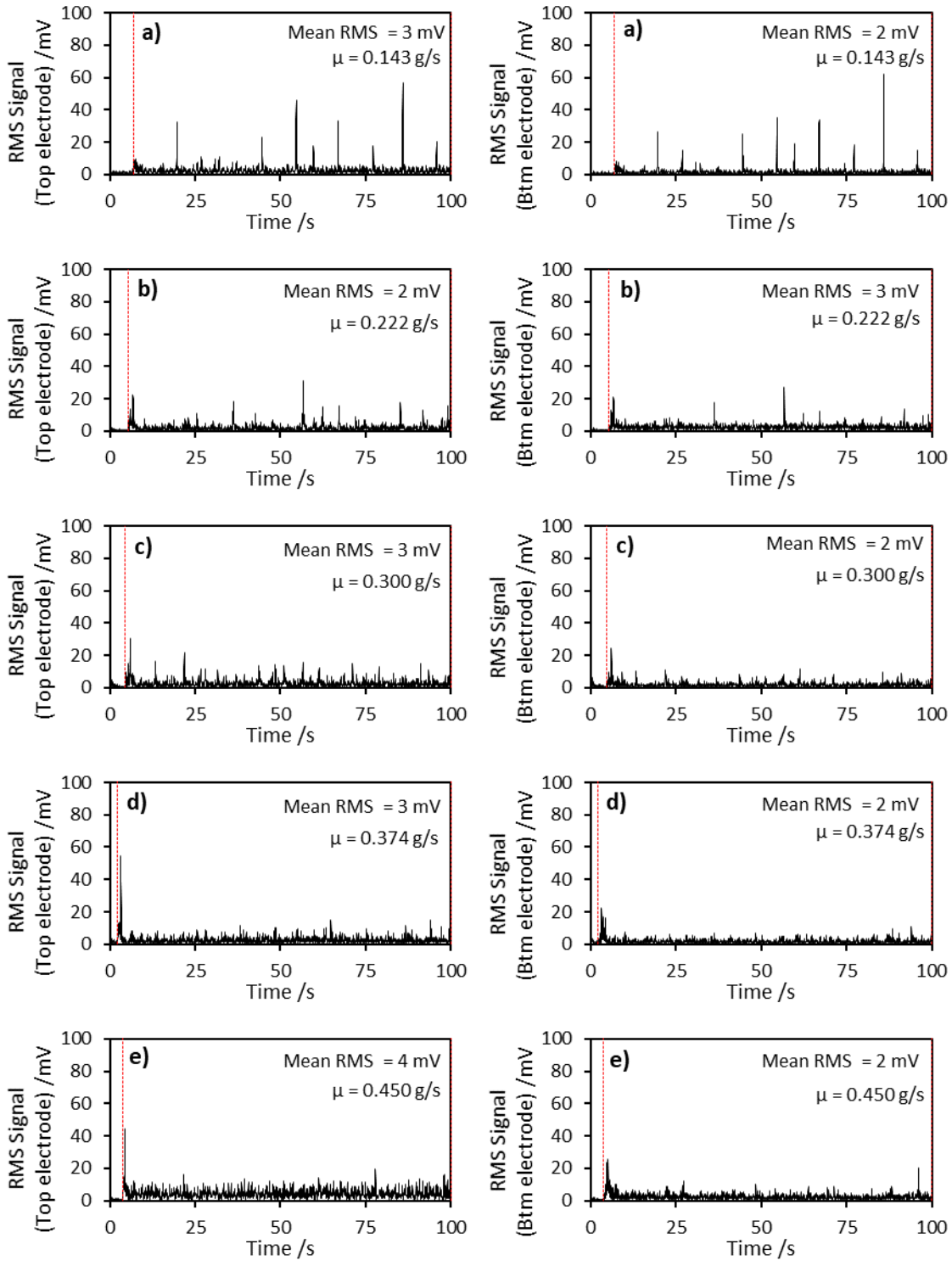

Appendix 10. Third set of filtered RMS signals obtained from the top and bottom electrodes in response to the hopper flow of Blend A, whilst utilising turret speeds of, a) 10 rpm, b) 15 rpm, c) 20 rpm, d) 25 rpm and e) 30 rpm. μ = the associated tablet mass flow rate.

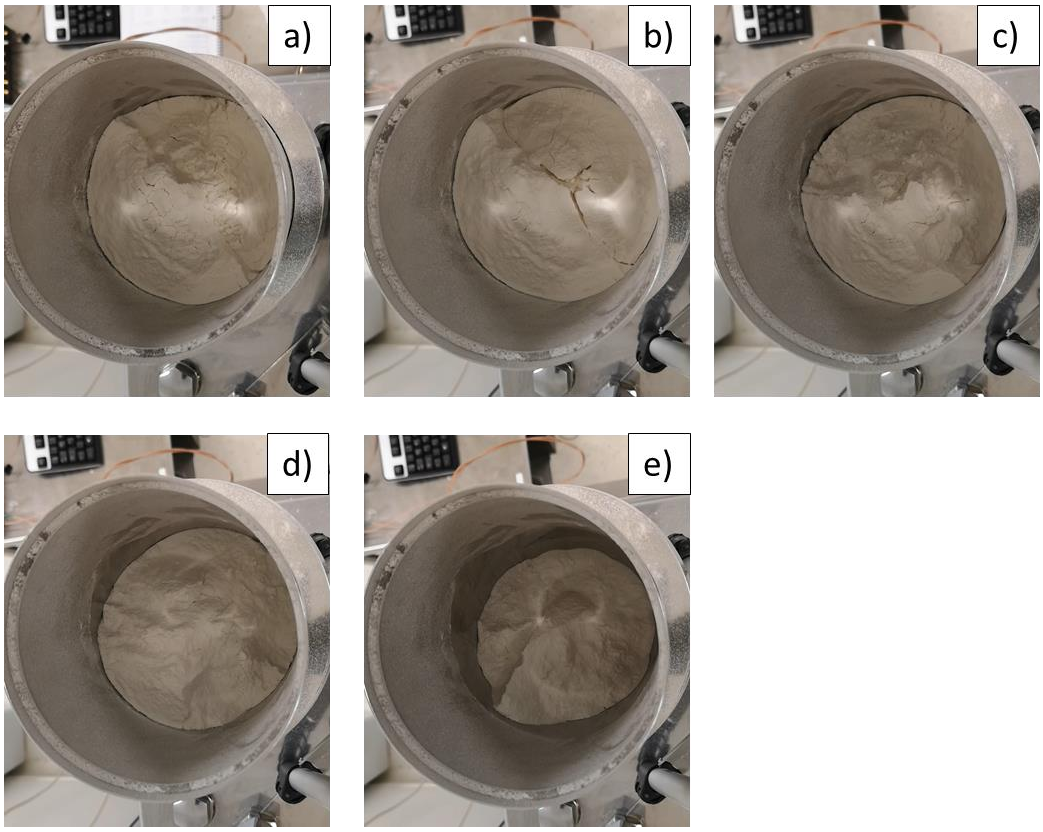

Appendix 11. Images of the initial powder bed level of Blend A prior to the start of hopper flow experiments at the following turret speeds, a) 10 rpm, b) 15 rpm, c) 20 rpm, d) 25 rpm and e) 30 rpm.

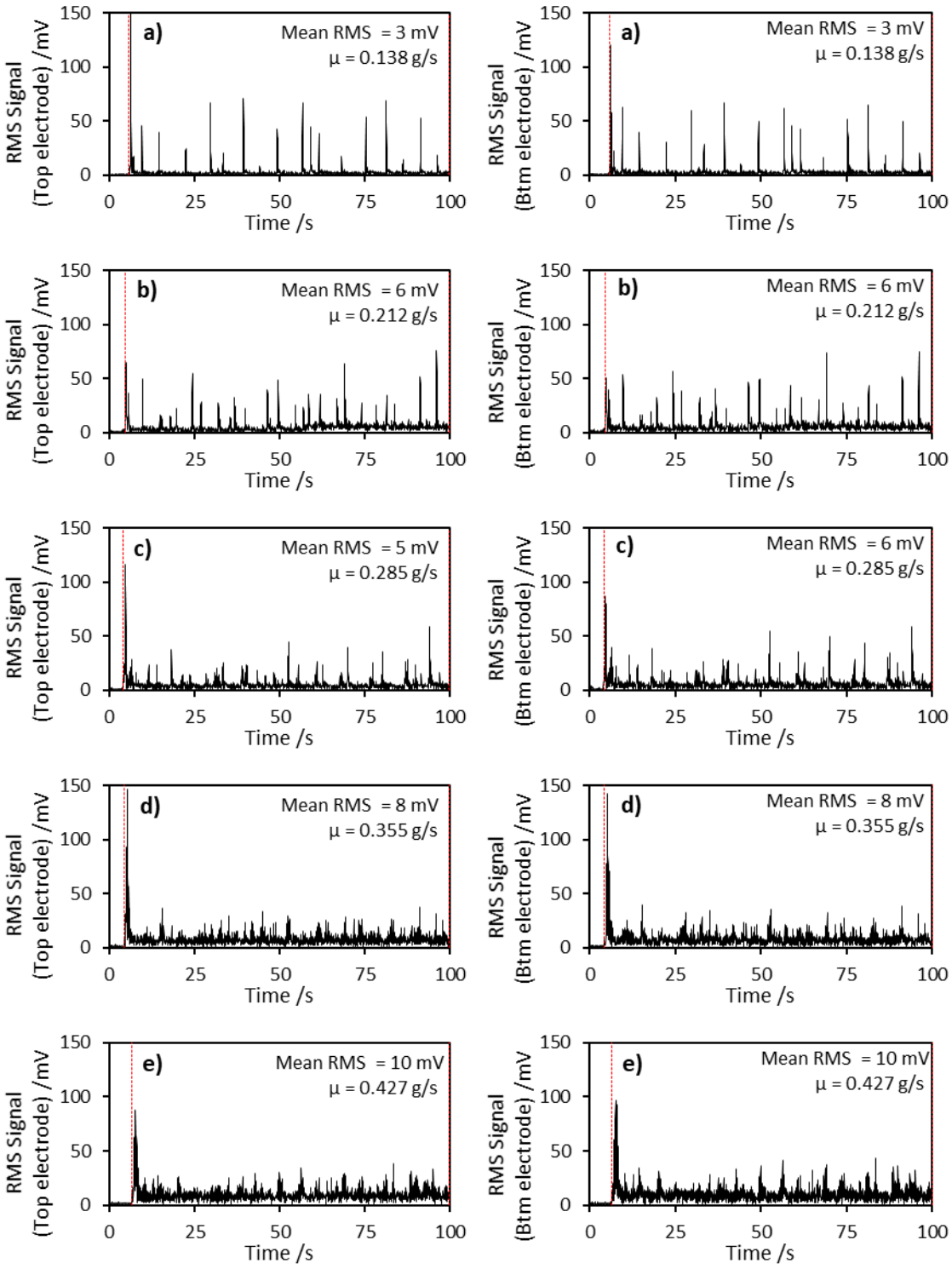

Appendix 12. Second set of filtered RMS signals obtained from the top and bottom electrodes in response to the hopper flow of Blend B, whilst utilising turret speeds of, a) 10 rpm, b) 15 rpm, c) 20 rpm, d) 25 rpm and e) 30 rpm. μ = the associated tablet mass flow rate.

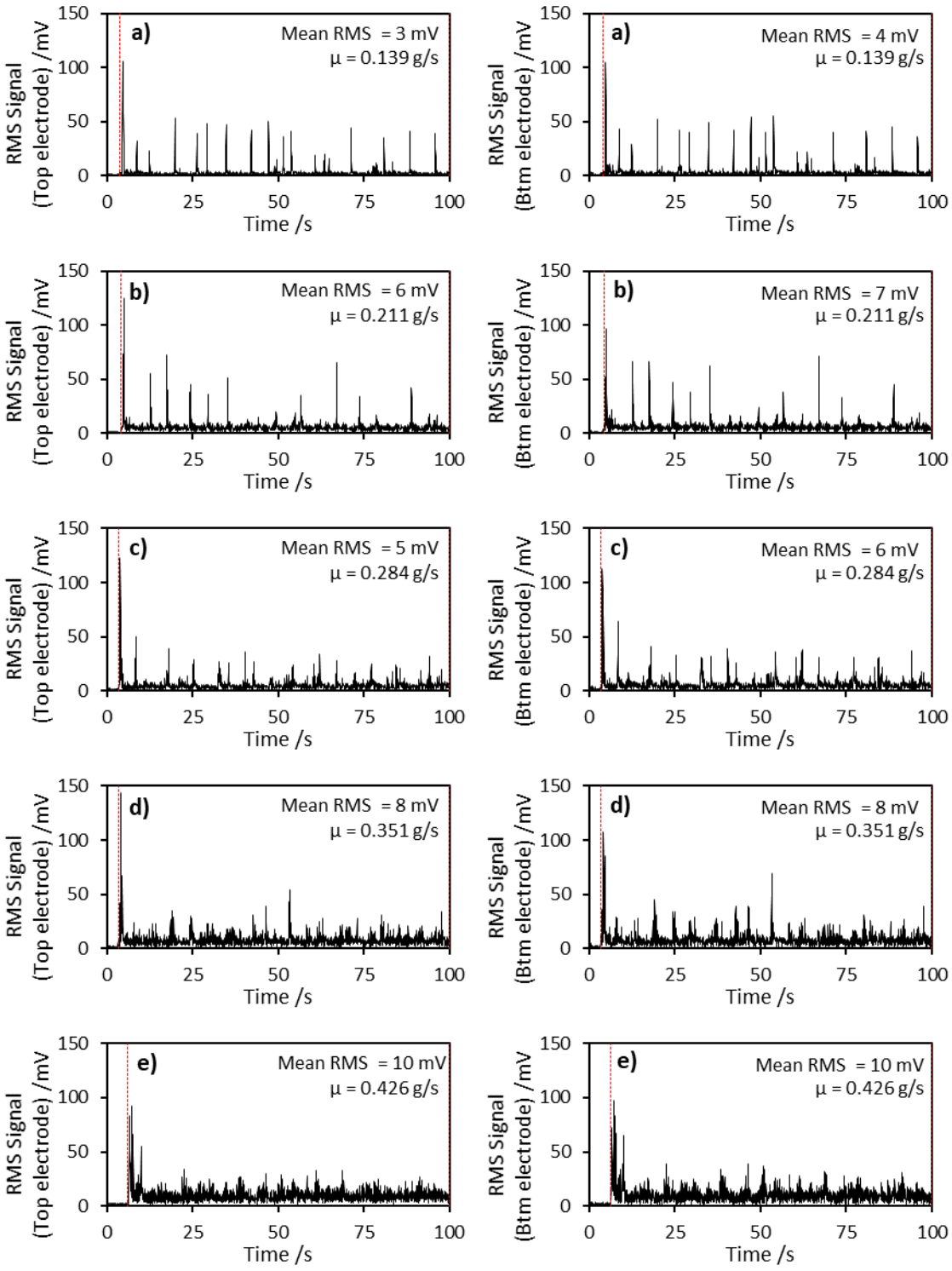

Appendix 13. Third set of filtered RMS signals obtained from the top and bottom electrodes in response to the hopper flow of Blend B, whilst utilising turret speeds of, a) 10 rpm, b) 15 rpm, c) 20 rpm, d) 25 rpm and e) 30 rpm. μ = the associated tablet mass flow rate.

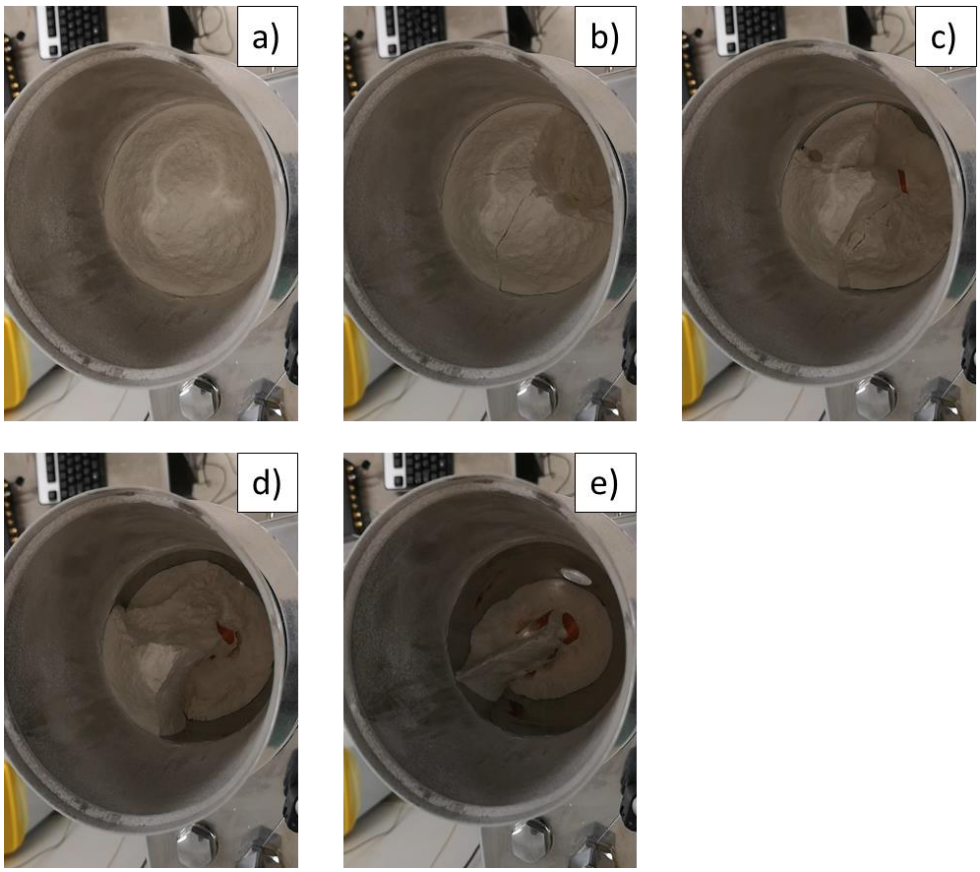

Appendix 14. Images of the initial powder bed level of Blend B prior to the start of hopper flow experiments at the following turret speeds, a) 10 rpm, b) 15 rpm, c) 20 rpm, d) 25 rpm and e) 30 rpm.

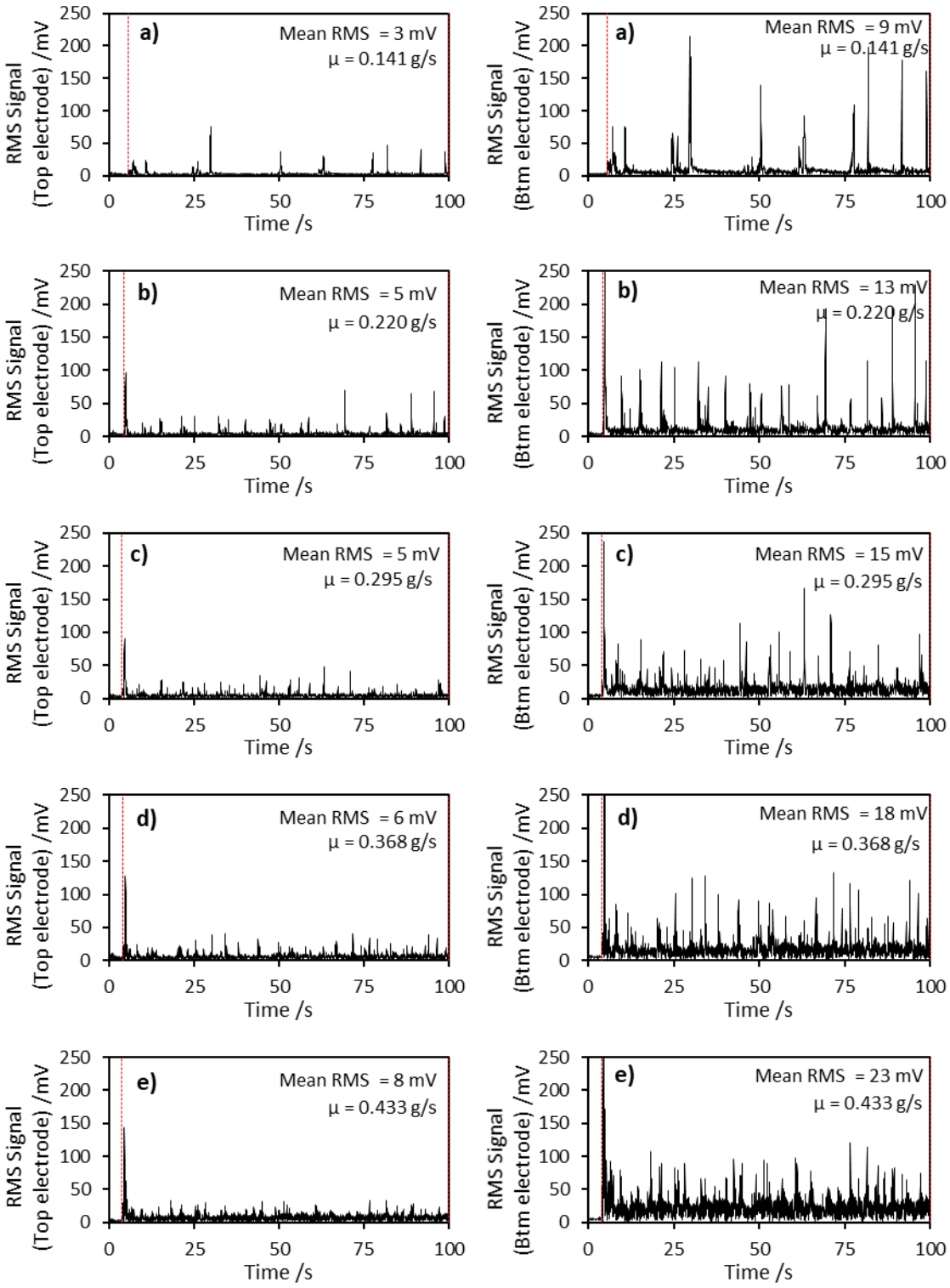

Appendix 15. Second set of filtered RMS signals obtained from the top and bottom electrodes in response to the hopper flow of Blend C, whilst utilising turret speeds of, a) 10 rpm, b) 15 rpm, c) 20 rpm, d) 25 rpm and e) 30 rpm. μ = the associated tablet mass flow rate.

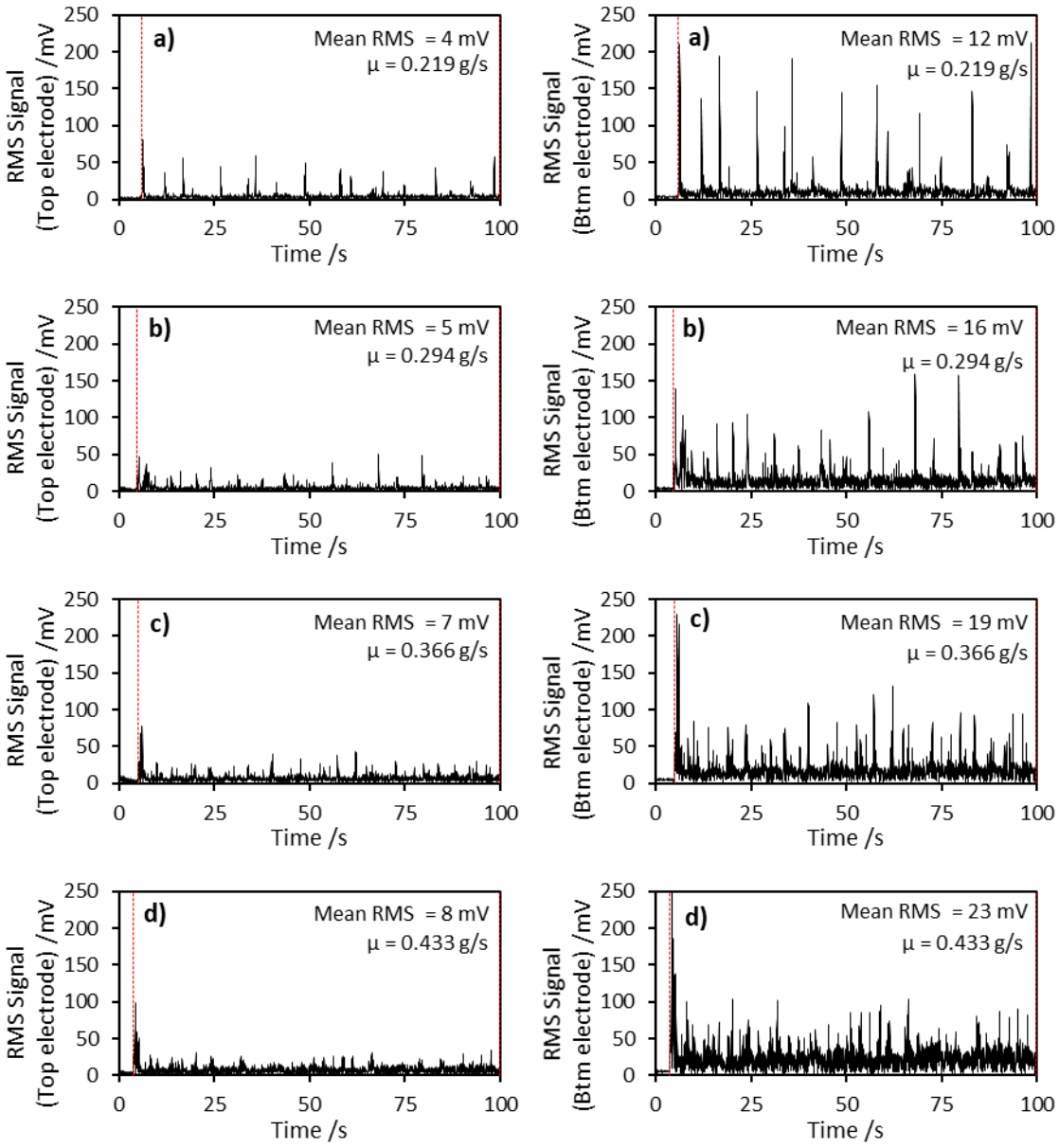

Appendix 16. Third set of filtered RMS signals obtained from the top and bottom electrodes in response to the hopper flow of Blend C, whilst utilising turret speeds of, a) 15 rpm, b) 20 rpm, c) 25 rpm, d) 30 rpm. μ = the associated tablet mass flow rate. Note. Third set of data at 10 rpm turret speed was not recorded.

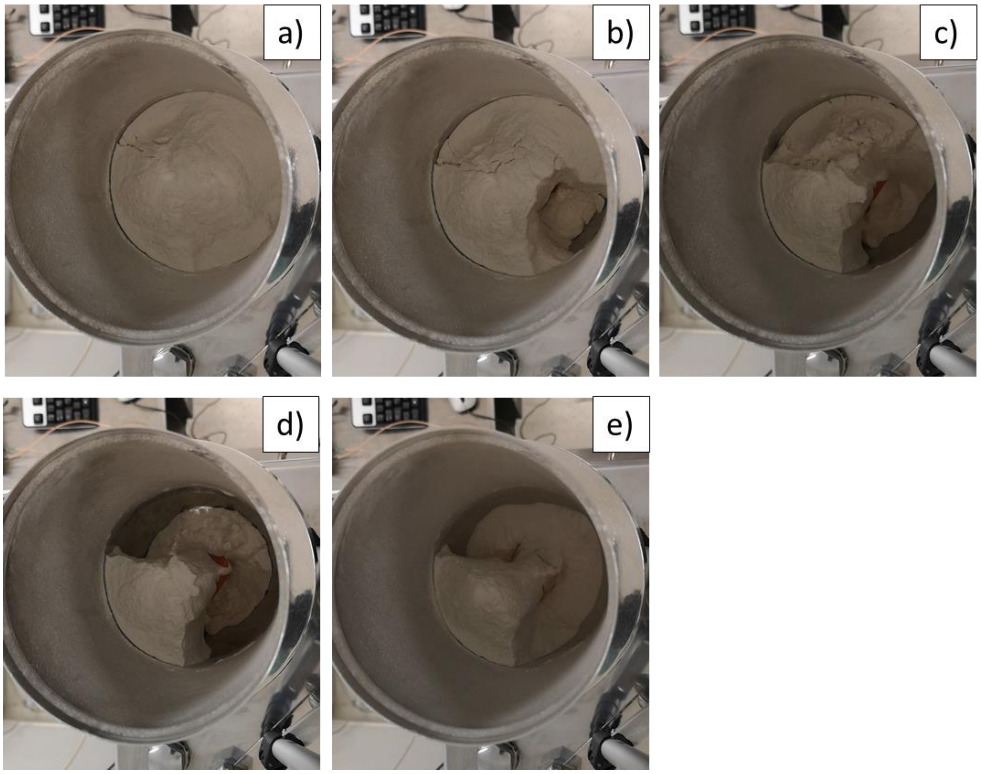

Appendix 17. Images of the initial powder bed level of Blend C prior to the start of hopper flow experiments at the following turret speeds, a) 10 rpm, b) 15 rpm, c) 20 rpm, d) 25 rpm and e) 30 rpm.